

14 March 2016

## Guide to technical specifications for STORM + PALM

Single Molecule Localisation techniques are complex and every stage of the procedure needs to be optimised. Here are a collection of papers detailing each step of the procedure.

- 1) Coverglass selection paper (NPL)
- 2) dSTORM original paper with details about which fluorophores to use
- 3) PALM resource paper with information about which fluorescent proteins are suitable
- 4) Localisation microscopy immunolabelling NPL paper about technical specification for STORM written in 2013 prior to publication of paper about use of Vectasheild as a simple STORM buffer.
- 5) Original paper about use of Nano-bodies which is a hybrid technique between STORM and PALM
- 6) Super-resolution software benchmarking paper detailing what to expect from different algorithms
- 7) My original paper about spinning disk super-resolution, this contains a discussion of the algorithms available at the time and considerations about when each one would be applicable.

Please be aware the SMLM field moves very fast. By the time you read these papers they may even be out of date. For these techniques it is essential to keep on top of the published literature as the techniques do date very quickly at present.

I will endeavour to update this document at reasonable intervals but have included the date on the cover page so people can be aware of when I last looked for these resources.

Ann

# Direct stochastic optical reconstruction microscopy with standard fluorescent probes

Sebastian van de Linde, Anna Löschberger, Teresa Klein, Meike Heidbreder, Steve Wolter, Mike Heilemann & Markus Sauer

Department of Biotechnology & Biophysics, Julius-Maximilians-University Würzburg, Würzburg, Germany. Correspondence should be addressed to M.S. (m.sauer@uni-wuerzburg.de).

Published online 16 June 2011; doi:10.1038/nprot.2011.336

**Direct stochastic optical reconstruction microscopy (dSTORM)** uses conventional fluorescent probes such as labeled antibodies or chemical tags for subdiffraction resolution fluorescence imaging with a lateral resolution of ~20 nm. In contrast to photoactivated localization microscopy (PALM) with photoactivatable fluorescent proteins, dSTORM experiments start with bright fluorescent samples in which the fluorophores have to be transferred to a stable and reversible OFF state. The OFF state has a lifetime in the range of 100 milliseconds to several seconds after irradiation with light intensities low enough to ensure minimal photodestruction. Either spontaneously or photoinduced on irradiation with a second laser wavelength, a sparse subset of fluorophores is reactivated and their positions are precisely determined. Repetitive activation, localization and deactivation allow a temporal separation of spatially unresolved structures in a reconstructed image. Here we present a step-by-step protocol for dSTORM imaging in fixed and living cells on a wide-field fluorescence microscope, with standard fluorescent probes focusing especially on the photoinduced fine adjustment of the ratio of fluorophores residing in the ON and OFF states. Furthermore, we discuss labeling strategies, acquisition parameters, and temporal and spatial resolution. The ultimate step of data acquisition and data processing can be performed in seconds to minutes.

## INTRODUCTION

The availability of efficient fluorescent probes and labeling methods has made fluorescence microscopy one of the most successful techniques for noninvasive three-dimensional biological and medical imaging. However, diffraction poses a historic limit on the resolution power of fluorescence microscopy and limits the minimal distance at which two objects can be unequivocally distinguished to about half of the wavelength of light<sup>1</sup>. For visible light in the far field, the spatial resolution is around 200–300 nm in the imaging plane<sup>2</sup> and, therefore, does not provide insight into cellular structures and multiprotein complexes with a size of a few tens of nanometers.

After the introduction of the first concept for fluorescence imaging beyond the resolution limit<sup>3–5</sup>, several methods have emerged that enable super-resolution imaging with optical resolution approaching molecular scale<sup>6</sup>. Among them are stimulated emission depletion using a nonlinear saturation process for the controlled de-excitation of fluorophores<sup>5,6</sup> and structured illumination microscopy<sup>7,8</sup>, in which a finely structured excitation pattern is used to demodulate high spatial frequencies that encode structural information beyond the diffraction limit. In parallel, alternative super-resolution imaging methods emerged that use precise position determination (localization) of individual fluorophores by evaluating their diffraction patterns in the imaging plane and, thus, are heavily dependent on the number of detected photons<sup>9–16</sup>. Ultimately, temporal separation of fluorophore emission<sup>17</sup> paved the way for single-molecule-based localization microscopy by stochastic photoswitching as in photoactivated localization microscopy (PALM)<sup>18</sup>, fluorescence PALM (FPALM)<sup>19</sup>, stochastic optical reconstruction microscopy (STORM)<sup>20</sup>, direct STORM (*d*STORM)<sup>21,22</sup>, spectral precision distance microscopy<sup>23–25</sup>, ground-state depletion microscopy followed by individual molecule return<sup>26</sup>, blink microscopy<sup>27,28</sup>, super-resolution optical fluctuation imaging<sup>29,30</sup> and related methods<sup>31,32</sup>.

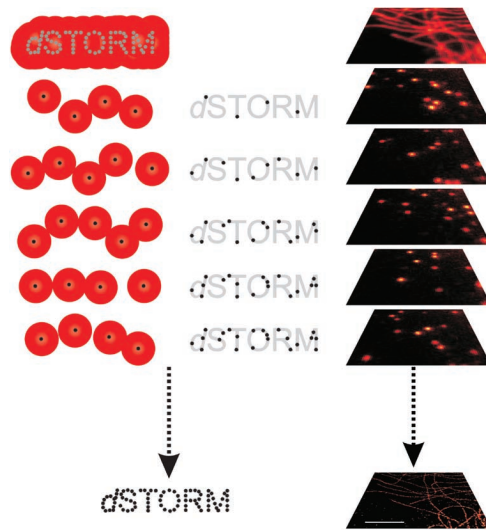
Microscopic methods that use single-molecule localization randomly read out the emission of individual fluorophores. This is achieved by transferring the majority of fluorophores to a reversible OFF state and by stochastic activation of individual fluorophores, for example, upon irradiation with light of appropriate wavelength and intensity and subsequent single-molecule fluorescence detection using a wide-field fluorescence microscope equipped with a sensitive CCD camera. If the probability of activation is sufficiently low, then the majority of activated fluorophores residing in their ON state are spaced further apart than the resolution limit and their positions can be precisely determined (localized) by fitting a point spread function (PSF) to the measured photon distributions<sup>9,14,15</sup>. This cycle of photoactivation and readout is repeated to record an image stack of thousands of images. A prerequisite to minimize artifacts in data analysis is that only a single fluorophore is emitting at any time within a diffraction-limited area. A super-resolution image is finally reconstructed from all single-molecule localizations (typically several ten thousands to millions of localizations; **Fig. 1**).

Common to all single-molecule-based localization microscopy methods is a need for fluorophores that can be photoactivated or reversibly photoswitched by irradiation with light. Such fluorophores have a fluorescent ON state, a nonfluorescent OFF state and a transition between these states. The most prominent variants are photoactivatable or photoconvertible fluorescent proteins (PA-FPs)<sup>33–35</sup>, as used in PALM and FPALM; standard organic fluorophores (*d*STORM)<sup>21,22</sup>; or pairs of organic fluorophores, that is, combinations of activator and reporter fluorophores (STORM)<sup>20</sup>. Even though all concepts are very similar and excellent reviews have already been published highlighting the strengths and limitations of the different methods<sup>6,34–38</sup>, *d*STORM with standard fluorescent probes warrants special attention because it differs from PALM and FPALM on several important points.

## PROTOCOL

**Figure 1** | The *d*STORM concept. The target molecule of interest is labeled with photoswitchable fluorophores. The top image on the right side shows labeled microtubules in a mammalian cell. At the beginning of the experiment, all fluorophores are transferred to the nonfluorescent OFF state upon irradiation with light of appropriate wavelength and intensity. Either spontaneously or photoinduced upon irradiation with a second laser wavelength, a sparse subset of fluorophores is reactivated. If the probability of activation is sufficiently low, then the activated fluorophores residing in their ON state are statistically spaced further apart than the resolution limit and their positions can be precisely determined. Repetitive activation, localization and deactivation allow a temporal separation of spatially unresolved structures in a reconstructed image (image below). Scale bar, 2  $\mu$ m.

- (1) PA-FPs<sup>18,19,39–41</sup> are genetically fused to target proteins and endogenously expressed in cells and organelles. Moreover, stable cell lines can be prepared that achieve protein-labeling efficiency of nearly 100%, a level impossible to achieve by chemical staining with synthetic fluorophores.
- (2) Furthermore, fluorescent proteins are smaller (a barrel with dimensions 2.4 nm  $\times$  4.2 nm)<sup>42</sup> than fluorophore-labeled antibodies, which are typically used in *d*STORM and STORM applications (the size of an IgG antibody is  $\sim$ 7–8 nm). Therefore, the density of fluorophores tagging a structure is generally lower compared with endogenously expressed PA-FPs. Whereas the smallest resolvable distance between two fluorophores determines the optical resolution, the structural interpretation of localization microscopy data is determined by the labeling density. According to information theory, the required density of fluorescent probes for super-resolution imaging has to be sufficiently high to satisfy the Nyquist-Shannon sampling theorem<sup>43</sup>. In essence, it states that the mean distance between neighboring localized fluorophores (the sampling interval) must be at least twice as fine as the desired resolution. For example, to resolve 20 nm structural features in one dimension, a fluorophore must be localized at least every 10 nm. Extended to a two-dimensional structure, this corresponds to a labeling density of  $\sim$ 10<sup>4</sup> fluorophores per  $\mu$ m<sup>2</sup> and translates to 600 fluorophores present within a diffraction-limited area with a diameter of  $\sim$ 250 nm. Only one of these 600 fluorophores should reside in its fluorescent state at any time of the experiment, thus implying that the lifetime of the OFF state has to be at least 600 times longer than the lifetime of the fluorescent ON state. Here it must be pointed out that, in practice, the density of fluorescent spots should be substantially lower to enable reliable spot finding and fitting.
- (3) On the contrary, PA-FPs as used in PALM show a lower photostability and brightness than standard organic fluorophores<sup>44</sup>. The number of detectable photons of PA-FPs is typically a few hundred photons before they bleach, whereas synthetic fluorophores can emit more than 1,000 photons per cycle<sup>22,45</sup>. This has a direct consequence on the localization precision: for negligible background fluorescence and detector noise, the localization precision depends only on the number of collected photons  $N$  and on the standard deviation of the PSF ( $\sigma$ ), and can be approximated by  $\sigma/N^{14,15}$ . Another issue is that PA-FPs need to be photobleached before a next subset can be activated. To maximize the number of detected photons from each PA-FP, the frame rate should be adjusted to the average photobleaching time under the applied experimental

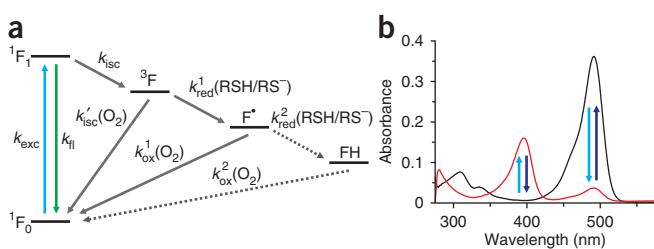


conditions. Typical frame rates used for PA-FP in PALM and FPALM experiments are 10–25 Hz<sup>33,34,40,41</sup>.

From this point of view, *d*STORM is advantageous because small organic fluorophores survive moderate excitation conditions for longer time periods (i.e., they have a higher photostability), emit thousands of photons and their photoswitching rates can be controlled by external means<sup>21,22</sup>. Thus, the time the fluorophores reside in the ON and OFF states can be sensitively adjusted. Furthermore, a large number of commercially available fluorescent probes spanning the entire visible spectral range<sup>22</sup> can be directly used as photoswitches in aqueous solvents simply by adding millimolar concentrations of reducing thiols. Therefore, *d*STORM has been used successfully to study the number, distribution and density of cellular or membrane proteins in fixed cells<sup>46–50</sup> and the *in vitro* dynamics of molecular motor proteins<sup>51</sup>. Appropriate reducing conditions inside a living cell (all cells contain reducing agents such as glutathione (GSH)) enable live-cell *d*STORM, which has been used to study the distribution and dynamics of core histone proteins<sup>52,53</sup> applying real-time data analysis<sup>54</sup>. This opens the potential to combine *d*STORM with (F)PALM to perform multicolor super-resolution imaging experiments in living cells, profiting from orthogonal labeling strategies. In summary, the tunability of photoswitching allows frame rates of 10–1,000 Hz at excitation intensities between 0.5 and 50 kW cm<sup>−2</sup> such that data acquisition takes only seconds to a few minutes. *d*STORM is not restricted to biological samples; it could, in principle, also be used to study, for example, polymers or other nonbiological, optically transparent samples that can be labeled with fluorescent probes and measured in aqueous solvents in the presence of thiols.

Even though (F)PALM and *d*STORM experiments using PA-FPs and standard fluorescent probes, respectively, can be performed under similar experimental conditions, for example, in the presence of millimolar concentrations of reducing GSH in living cells, the initial situation of a super-resolution imaging experiment is completely different. PA-FPs are essentially nonfluorescent at the beginning of the experiment, allowing the number of fluorescent molecules, i.e., the density of fluorescent molecules, to be tightly controlled by the irradiation intensity of a 405 nm laser. In contrast, one of the key steps of single-molecule-based localization microscopy with synthetic organic fluorophores is the efficient transfer of the fluorophores

**Figure 2** | Reversible photoswitching of Alexa Fluor and ATTO dyes in the presence of thiols. (a) The fluorophore is either cycled between its singlet ground and excited state emitting fluorescence photons or can undergo intersystem crossing with rate  $k_{isc}$  upon irradiation. The triplet state ( $^3F$ ) can react with molecular oxygen to recover the singlet ground state and produce singlet oxygen or react with the thiolate with rate  $k_{red}$  to form the radical anion of the fluorophore ( $F^*$ ) and the corresponding thiyl radical. The radical anion can be oxidized by oxygen with rate  $k_{ox}$  to recover the singlet ground state. Because radical anions of most rhodamine and oxazine derivatives show pronounced absorption at  $\sim 400$  nm irradiation, for example, at 405 nm promotes recovery of the fluorescent form (i.e., OFF- and ON-switching are photoinduced). Whereas the thiyl radicals formed react efficiently with molecular oxygen to produce superoxide radicals and hydrogen peroxides, the fluorophore radical anion is very unreactive and survives for up to several seconds even in the presence of molecular oxygen. Fluorophores such as ATTO 655 and ATTO 680 accept a second electron to the fully reduced leuco-form (FH). Oxidation of FH with oxygen also recovers the ON state. (b) Absorption spectra of Alexa Fluor 488 in PBS (pH 9.3) in the presence of 100 mM MEA. After irradiation at 488 nm (light blue), the absorption at 488 nm decreases and the radical anion absorbing maximally around 400 nm appears. The fluorescent state is recovered spontaneously or by direct excitation of the radical anion at  $\sim 400$  nm (dark blue). The stability (lifetime) of the radical anion is mainly determined by the oxygen concentration and can easily exceed several hours<sup>62</sup>.



to a reversible, relatively stable OFF state at the beginning of the experiment<sup>20–28</sup>. In other words, a bright fluorescent sample has to be turned ‘dim’ by increasing the irradiation intensity in a way that ensures that only a sparse subset of fluorophores remains fluorescent. The challenge of the procedure is twofold because damage of the sample and photobleaching of the fluorophores must be avoided. These considerations show that the photoswitching mechanism is of central importance for *d*STORM.

### The photoswitching mechanism

*d*STORM takes advantage of the fact that standard fluorophores (most Alexa Fluor and ATTO dyes) belong to the class of rhodamine and oxazine dyes, and are photoreduced in the presence of potent electron donors such as aromatic amines (e.g., guanosine or tryptophan)<sup>55–57</sup>. In other words, the electronically excited fluorophore is reduced upon collision or contact with guanosine or tryptophan. Thiols such as  $\beta$ -mercaptoethylamine (MEA) or GSH are generally weaker electron donors than aromatic amines<sup>58,59</sup>. Their reduction efficiency increases up to pH  $\sim 9$  because the thiolate anion ( $RS^-$ ) is the reducing species<sup>60,61</sup>. Nevertheless, quenching of the first excited singlet state (fluorescence quenching) of rhodamine and oxazine dyes with a lifetime of a few nanoseconds by thiols is negligible. The triplet state, however, is energetically stabilized and has a lifetime of several microseconds in air-equilibrated aqueous solutions. Therefore, the triplet state is also quenched by millimolar concentrations of MEA or GSH (Fig. 2). As a result, the triplet state of commercially available ATTO and Alexa Fluor dyes is reduced on irradiation in the presence of millimolar quantities of thiols in aqueous solvents, and the corresponding dye radical anion and thiyl radical is formed<sup>62</sup>.

Whereas thiyl radicals efficiently react with molecular oxygen by the formation of superoxide radicals and hydrogen peroxide<sup>58,59</sup>, rhodamine radical anions are more stable to oxidation and survive for several hundred milliseconds to seconds in the presence of molecular oxygen (naturally present at concentrations of 200–250  $\mu$ M in aqueous solutions at room temperature (20 °C))<sup>22,28,47,49</sup>. On removal of oxygen, rhodamine dyes can be easily trapped in their radical anion state for several hours<sup>62</sup>. On the other hand, thiazine and oxazine dyes such as methylene blue and ATTO 655 or ATTO 680 show a higher electron affinity<sup>56</sup>. Hence, the semireduced fluorophore radicals ( $F^*$ ) are intermediary reaction products that accept a second electron in the presence of thiols, forming the corresponding fully reduced leuco dye (FH; Fig. 2a)<sup>62–65</sup>.

The fundamental mechanism of *d*STORM, that is, photoinduced formation of intermediate radical anions for most Alexa Fluor and ATTO dyes in aqueous solvents in the presence of millimolar concentrations of thiols, can be easily shown by ensemble absorption and electron paramagnetic resonance experiments<sup>62</sup>. To close the photoswitching cycle, the fluorescent state of the fluorophores is recovered upon oxidation by molecular oxygen (Fig. 2). Both processes, reduction of the triplet state by thiols and oxidation of the intermediate reduced state by oxygen, are facilitated on irradiation. Excitation of the fluorescent form pumps the fluorophore into the triplet state, which is reduced by the thiolate, and direct excitation of the radical anion (all radical anions show a pronounced absorbance at  $\sim 400$  nm)<sup>62</sup> at 405 nm facilitates recovery of the fluorescent form (Table 1). As animal cells contain oxygen as well as millimolar concentrations of GSH<sup>66</sup>, *d*STORM can also be performed in living cells<sup>52,53</sup>.

In this respect, it is interesting to relate the mechanistic considerations of rhodamine and oxazine photoswitching to the first class of fluorophores used for *d*STORM imaging, i.e., carbocyanine fluorophores. Photoswitching of carbocyanines such as Cy5, Cy5.5, Cy7 or Alexa Fluor 647, 680 and 700 is performed under identical conditions for all of these fluorophores, but the reversibility of photoswitching is dramatically improved when the oxygen concentration is reduced by application of an enzymatic oxygen scavenging system<sup>67,68</sup>. The reason for this is that cyanine fluorophores are far more easily oxidized than rhodamine or oxazine derivatives<sup>56</sup>. In addition, oxygen removal increases the stability or lifetime of the generated semireduced radical anions absorbing at  $\sim 500$  nm<sup>69</sup>. The recently observed formation of a thiol adduct in cyanine dyes<sup>70</sup> might well be explained by a follow-up reaction, similar to the photoinduced formation of stable leuco dyes in the case of thiazine and oxazine dyes<sup>62</sup>. Table 1 summarizes all standard fluorophores used successfully so far in reversible ensemble and single-molecule photoswitching experiments according to the *d*STORM concept. Most of the fluorophores listed show remarkably stable nonfluorescent OFF states that absorb at shorter wavelengths, in the range of 350–550 nm, and survive the entire photocycle several times with only minimal photobleaching.

For *d*STORM experiments in fixed cells (Table 1), the sample is embedded in aqueous buffer (e.g., PBS (pH 7.4)) in the presence of 10–200 mM thiol (MEA). For cyanine fluorophores, the application of an oxygen scavenging system significantly improves photoswitching. After proper sample alignment by fluorescence imaging under

# PROTOCOL

**TABLE 1** | Standard organic fluorophores and experimental conditions for *d*STORM.

Fluorophore	ON state $\lambda_{\text{abs}}/\lambda_{\text{em}}$ (nm)	OFF state $\lambda_{\text{abs}}$ 350–550 nm	Experimental conditions	Reference
Alexa Fluor 488	491/517	✓	100 mM MEA, pH 7.4, <1 kW cm <sup>-2</sup> at 488 nm 100 mW MEA, pH 8.0, 5 kW cm <sup>-2</sup> at 488 nm	22 62
Dy 505	500/525	✓	100 mM MEA, pH 9.3, <1 W cm <sup>-2</sup> at 488 nm <sup>a</sup>	62
Rhodamine 123	500/518	✓	100 mM MEA, pH 9.3, <1 W cm <sup>-2</sup> at 488 nm <sup>a</sup>	62
ATTO 488	501/523	✓	100 mM MEA, pH 9.3, <1 W cm <sup>-2</sup> at 488 nm <sup>a</sup>	62
SNAP-Cell 505	504/532	✓	0.5–2 kW cm <sup>-2</sup> b Used for live-cell <i>d</i> STORM	53
Rhodamine 6G	526/556	✓	200 mM MEA, pH 10.2, <1 W cm <sup>-2</sup> at 514 nm <sup>a</sup>	62
ATTO 520	516/538	— <sup>c</sup>	100 mM MEA, pH 7.4, 3 kW cm <sup>-2</sup> at 514 nm 100 mM MEA, pH 7.4, 1–2 kW cm <sup>-2</sup> at 514 nm 1.5 kW cm <sup>-2</sup> b Used for live-cell <i>d</i> STORM	22 49 22
Dy 530	535/556	✓	100 mM MEA, pH 9.3, <1 W cm <sup>-2</sup> at 514 nm <sup>a</sup>	62
ATTO 532	532/553	✓	100 mM MEA, pH 9.3, <1 W cm <sup>-2</sup> at 514 nm <sup>a</sup>	62
Alexa Fluor 532	532/552	✓	200 mM MEA, pH 10.2, <1 W cm <sup>-2</sup> at 514 nm <sup>a</sup> 100 mM MEA, pH 7.4, 1.5 kW cm <sup>-2</sup> at 514 nm	62 22
SNAP-Cell TMR-Star	554/580	✓	0.5–2 kW cm <sup>-2</sup> b Used for live-cell <i>d</i> STORM	53
ATTO 565	563/592	✓	200 mM MEA, pH 12.1, 1 W cm <sup>-2</sup> at 568 nm <sup>a</sup>	62
			100 mM MEA, pH 7.4, 1–2 kW cm <sup>-2</sup> at 568 nm	22, 49
Alexa Fluor 568	572/600	✓	200 mM MEA, pH 10.2, <1 W cm <sup>-2</sup> at 568 nm <sup>a</sup> 100 mM MEA, pH 7.4, 1.5 kW cm <sup>-2</sup> at 568 nm	62 22
ATTO 590	594/624	— <sup>c</sup>	200 mM MEA, pH 7.4, 4 kW cm <sup>-2</sup> at 568 nm	22
Alexa Fluor 647	649/670	✓ <sup>e</sup>	50 mM MEA, pH 7.4, 1–2 kW cm <sup>-2</sup> at 647 nm <sup>d</sup> 50 mM MEA, pH 7.4, 35–50 kW cm <sup>-2</sup> at 647 nm <sup>d</sup>	21, 46 54
Cy5	649/670	✓ <sup>e</sup>	50 mM MEA, pH 7.4, 1–2 kW cm <sup>-2</sup> at 647 nm <sup>d</sup>	21
ATTO 655	663/684	✓ <sup>e</sup>	10 mM GSH/MEA, pH 7.4, 2–3 kW cm <sup>-2</sup> at 647 nm 10–100 mM MEA, pH 7.4, 1–2 kW cm <sup>-2</sup> at 647 nm	47 49
TMP-ATTO 655			1.5 kW cm <sup>-2</sup> b Used for live-cell <i>d</i> STORM 5 kW cm <sup>-2</sup> b Used for live-cell <i>d</i> STORM	22 52
ATTO 680	680/700	— <sup>c</sup>	10 mM GSH/MEA, pH 7.4, 2–3 kW cm <sup>-2</sup> at 647 nm 10–100 mM MEA, pH 7.4, 1–2 kW cm <sup>-2</sup> at 647 nm 1.5 kW cm <sup>-2</sup> b Used for live-cell <i>d</i> STORM	47 49 22
ATTO 700	700/719	— <sup>c</sup>	10–100 mM MEA, pH 7.4, 1–2 kW cm <sup>-2</sup> at 647 nm 1.5 kW cm <sup>-2</sup> b Used for live-cell <i>d</i> STORM	49 22

<sup>a</sup>Determined in ensemble experiments. <sup>b</sup>Used for live-cell *d*STORM. <sup>c</sup>Not determined. <sup>d</sup>Oxygen is removed by an enzymatic oxygen scavenging system. <sup>e</sup>The fluorescent state can be recovered upon excitation at 350–550 nm. The radical anion absorption spectrum has not been determined in bulk experiments.

low excitation conditions ( $< 0.1 \text{ kW cm}^{-2}$ ), the excitation intensity is increased to 5–30  $\text{kW cm}^{-2}$  until the majority of fluorophores are switched off to enable precise single-molecule localization (Fig. 3). This step requires typically only a few seconds.

As the triplet yield and subsequent photoinduced formation of nonfluorescent reduced fluorophore intermediates depends linearly on the excitation intensity, the thiol concentration and the pH of the solvent<sup>21,22,62</sup> are available as parameters to optimize the transfer of the majority of fluorophores to their nonfluorescent stable OFF state.

For subsequent data acquisition, the excitation intensity is tuned to ensure that the lifetime of the ON state equals one to four times the acquisition time of the electron-multiplying charged-coupled device (EMCCD) camera. For live-cell *d*STORM, the excitation intensity has to be lowered to  $\leq 5 \text{ kW cm}^{-2}$  to avoid cellular damage. At higher intensities, photoinduced fluorophore and thiyl radical formation and subsequent production of reactive oxygen species is enhanced<sup>62</sup>. However, for fixed cells or other samples, the excitation intensity can be kept high (up to 50  $\text{kW cm}^{-2}$ ) to reduce the lifetime of the fluorescent ON state to a few milliseconds, enabling frame rates of up to 1 kHz (ref. 54). Without another irradiation wavelength for direct excitation of the reduced intermediates, the lifetime or stability of the OFF state is only controlled by the redox property of the fluorophore

itself and the oxygen concentration. Independent of the laser excitation intensity, typically between 500 and 5,000 photons are detected from the ON state of all fluorophores listed in Table 1, corresponding to an expected localization precision of  $< 10 \text{ nm}$  (ref. 14).

Alternatively, “push-pull fluorophores”<sup>71,72</sup> and rhodamine amides<sup>73,74</sup> can be used for single-molecule-based localization microscopy. Photochromic rhodamine amides can be photoactivated by irradiation with light in the UV at  $\sim 375 \text{ nm}$  or by two-photon excitation at  $\sim 750 \text{ nm}$ .

#### Adjustment of photoswitching rates

The formation of stable OFF states and tunable transition rates are the key requirements in super-resolution imaging, and they have a direct influence on the achievable optical resolution<sup>40,75–77</sup>. In *d*STORM, photoswitchable organic fluorophores have to be converted (reduction of the triplet state by thiols) at a rate  $k_{\text{OFF}}$  to a nonfluorescent OFF state (stable radical anions) at the beginning of the experiment to ensure single-molecule localization. The fluorescent state is repopulated on oxidation at a rate  $k_{\text{ON}}$ . These photoswitching rates, i.e., the inverse of the lifetimes of the ON state  $\tau_{\text{ON}}$  and OFF state  $\tau_{\text{OFF}}$ , directly control the density of fluorescent probes and thus have a critical influence on the quality of a super-resolution image (Fig. 4).

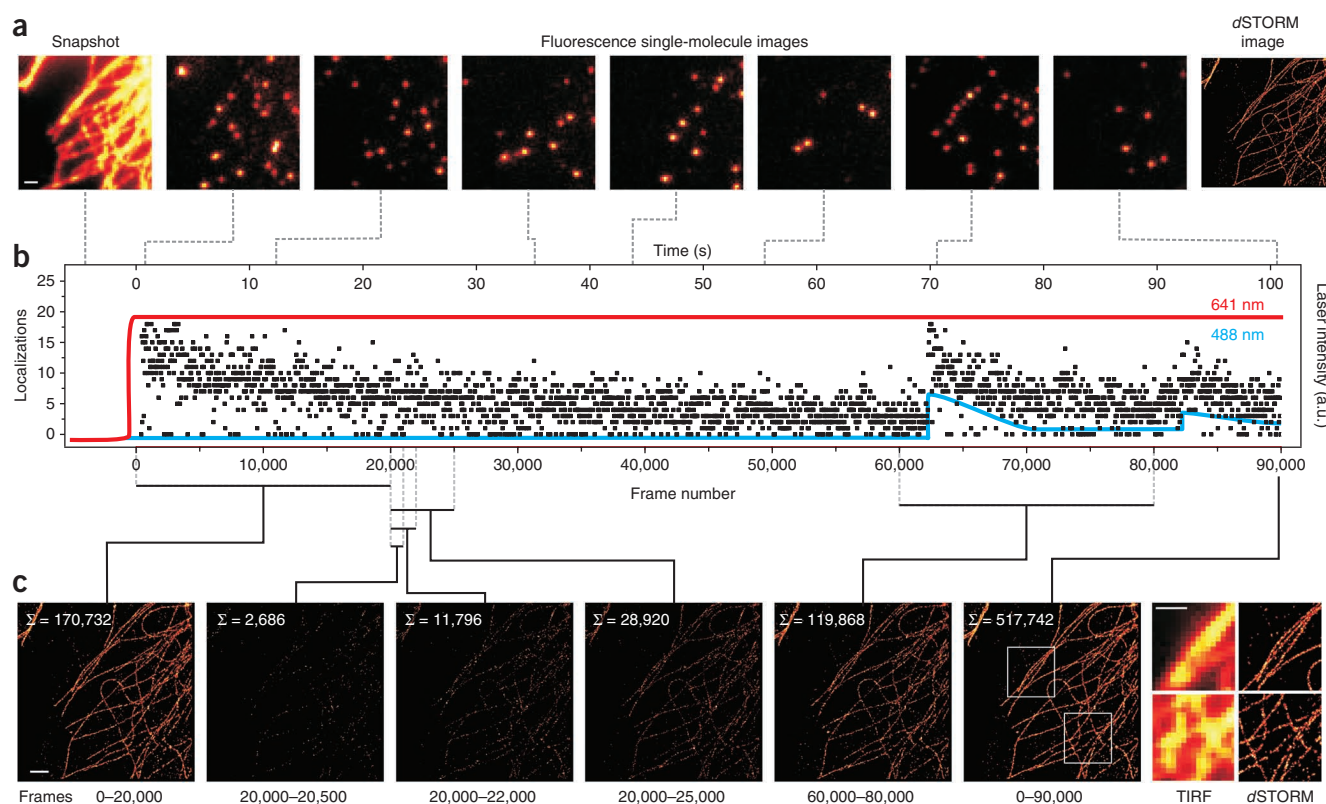
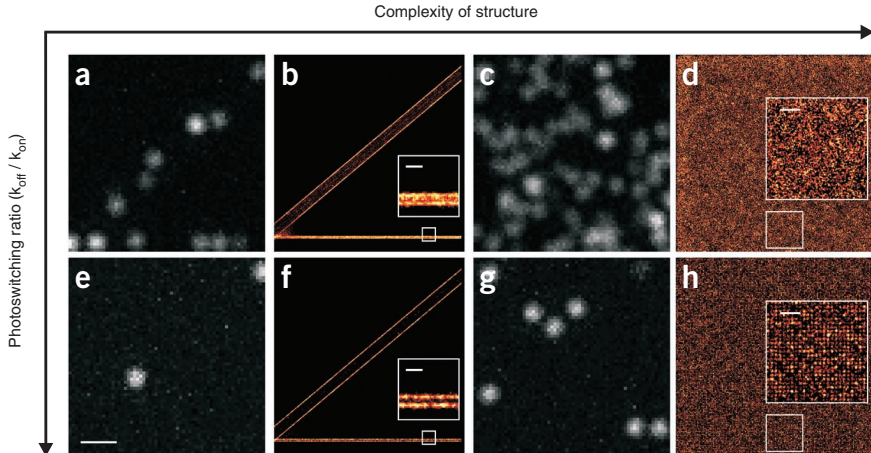


**Figure 3 |** *d*STORM acquisition procedure exemplified for Alexa Fluor 647-labeled β-tubulin in a COS-7 cell. (a,b) A fluorescence image of the structure is measured at low excitation intensity (a) ( $< 0.1 \text{ kW cm}^{-2}$  see red line in b). In the next step, higher irradiation intensity is applied to transfer the majority of fluorophores into a nonfluorescent OFF state until a sufficiently low spot density is reached. Finally, a super-resolved image is reconstructed from all localizations. (b) Number of localizations per image frame (approximately ten, corresponding to  $\sim 0.1 \text{ spots per } \mu\text{m}^2$ ) plotted against the frame number and time, respectively. The images were acquired with a frame rate of 885 Hz at an excitation intensity of 30  $\text{kW cm}^{-2}$  at 641 nm and additional irradiation at 488 nm (blue line) with 0–0.5  $\text{kW cm}^{-2}$ . Direct excitation of the OFF state at 488 nm increases the number of fluorophores residing in the ON state and has to be carefully controlled. (c) Image reconstruction showing that a highly resolved image can already be reconstructed from 20,000 images corresponding to a total acquisition time of  $\sim 20 \text{ s}$ . The structure cannot be fully resolved after analysis of  $< 2,000$  frames. Σ, the number of localizations used to reconstruct the *d*STORM image. Scale bars, 1  $\mu\text{m}$ .

## PROTOCOL

**Figure 4** | Simulated data demonstrating the influence of the ratio of photoswitching rates,  $r$ , on different complexities. With increasing complexity of the imaged structure, the number of fluorophores present per area increases. The photoswitching ratio is mainly determined by the stability of the OFF state. (a–h) Images shown in a, c, e and g are snapshots from the localization microscopy stacks from which the reconstructed super-resolution images b, d, f and h were generated. Panels b and f show pairs of lines separated by 300 and 50 nm with a fluorophore attached every 8.5 nm, whereas d and h show a lattice with 40 nm spacing. (a–d) Images were simulated with  $r = 250$ . (e–h) Images were simulated with  $r = 3,000$ . It becomes clear that the necessary photoswitching ratio depends strongly on the structure imaged; when the photoswitching ratio is too low (c,d) more than one fluorophore may fluoresce per diffraction-limited area and subsequent fitting of the PSF can result in false localizations and image artifacts<sup>75</sup>. On the contrary, high photoswitching ratios result in a small number of localizations per image and thus prolong the acquisition time unnecessarily. Note that the density of fluorescence emissions is roughly the same for the images shown in a and g, even though they are simulated for different values of  $r$ . Scale bars, 1  $\mu\text{m}$  for e (valid for all images); 100 nm for insets in b and f; and 200 nm for insets in d and h.



For a more detailed discussion, we introduce the ratio of switching rates as  $r = k_{\text{OFF}}/k_{\text{ON}} = \tau_{\text{OFF}}/\tau_{\text{ON}}$ . High values of  $r$  assure a low number of fluorophores in the ON state and, therefore, that single fluorophores are localized as individuals. OFF state lifetimes of photoswitchable synthetic fluorophores have been reported to vary from 10 to 100 ms<sup>26–28,77</sup> to several seconds<sup>22,28,47,49,52,62,77</sup>. For metastable OFF states with short  $\tau_{\text{OFF}}$  high irradiation intensities should be applied to reduce  $\tau_{\text{ON}}$  and to generate a sufficiently high ratio  $r$ . For very stable OFF states with long lifetimes of several seconds, a sufficient high ratio  $r$  can be achieved applying only a low irradiation intensity, which is an important prerequisite for live-cell applications. For fixed cells, however,  $\tau_{\text{ON}}$  can be further shortened by applying higher irradiation intensities to increase  $r$  and the imaging speed (i.e., the frame rate). Currently, only small areas of a sample can be imaged on a  $128 \times 128$  pixel chip with the highest possible imaging speed of an EMCCD camera of  $\sim 1$  kHz, that is, the chip readout time currently limits the acquisition speed for investigation of larger areas or whole cells.

dSTORM offers several possibilities to vary  $r$  through fine adjustment of  $\tau_{\text{ON}}$  and  $\tau_{\text{OFF}}$  enabling super-resolved imaging of cellular structures with different complexity and fluorophore densities in fixed and living cells<sup>22,52,53,62</sup>. The first-order rate constants for OFF- and ON-switching ( $k_{\text{OFF}}$  and  $k_{\text{ON}}$ , respectively) follow a linear dependence on the excitation intensities. Whereas  $k_{\text{OFF}}$  is controlled by the singlet-state excitation intensity, the intersystem crossing yield and the concentration of thiolate,  $k_{\text{ON}}$  is determined by the radical excitation intensity and the concentration of molecular oxygen<sup>22,62</sup>.

Using a laser with a maximum power of  $\sim 100$  mW,  $k_{\text{OFF}}$  can be easily controlled over one order of magnitude. The concentration of the reducing thiolate ( $\text{RS}^-$ ) can be increased by both the concentration of thiol added and the pH (between pH 6 and 9) of the solvent and enables the adjustment of  $k_{\text{OFF}}$  over approximately two orders of magnitude<sup>22</sup>. On the contrary,  $k_{\text{ON}}$  can be increased (at least one order of magnitude) by direct excitation of the radical anions at, for example, 405 nm, whereas  $k_{\text{ON}}$  can be reduced by several orders of magnitude by depleting oxygen from the buffer by an oxygen scavenging system (on efficient removal of oxygen,

the lifetime of the radical anions can approach several hours in ensemble experiments)<sup>62</sup>. Tuning both rates  $k_{\text{OFF}}$  and  $k_{\text{ON}}$  allows arbitrary control of the photoswitching ratio  $r$  over several orders of magnitude. Thus,  $r$  can be adjusted to match the required conditions for super-resolution imaging of different cellular structures. A suitable  $r$  is determined by the complexity of the structure but should be (as a rule of thumb) adjusted such that  $\sim 0.1$ –1.0 fluorophores are simultaneously active per  $\mu\text{m}^2$  to ensure the localization of single emitters. For live-cell dSTORM, manipulating  $k_{\text{OFF}}$  and  $k_{\text{ON}}$  is limited to the laser intensities for both the fluorescence readout and the radical anion, respectively, whereas the excitation intensities should be kept low to avoid cellular damage. Here it should be pointed out that the optical resolution is mainly determined by the full width at half maximum (FWHM) of the PSF and photon statistics and not by the photoswitching rates. The photoswitching rate determines the fluorophore density required to extract meaningful structural information in single-molecule-based localization microscopy experiments.

## Experimental design

**Fluorescence microscope setup.** To determine the position of single fluorophores, the fluorescence signal (given by the number of fluorescence photons detected) should be very high, whereas the background (background fluorescence and detector noise) should be as low as possible<sup>14</sup>. Optimal results can be achieved by single-molecule fluorescence imaging with high signal-to-background ratio using an inverted fluorescence microscope equipped with an oil-immersion objective, with a high numerical aperture ( $\text{NA} \geq 1.45$ ) operated in objective-type total internal reflection fluorescence (TIRF) microscopy mode (Fig. 5). TIRF microscopy limits fluorophore excitation to a thin evanescent field (100–200 nm) and minimizes background light. Three-dimensional or whole-cell imaging can be realized using a wide-field configuration, at the expense of a lower signal-to-background ratio and a lower precision in single-molecule localization. An interesting approach is the illumination by a highly inclined and thin beam that allows axial sectioning (highly inclined and laminated optical sheet, HILO)<sup>78</sup>.

Multiline excitation can experimentally be realized in two principal ways (Fig. 5a): (excitation option I) a multiline argon-krypton gas ion laser (for example, Coherent's Innova 70C), emitting at 488, 514, 568 and 647 nm in combination with a 405 nm diode laser (for example, the Cube diode laser 405–100C (Coherent)); or (excitation option II) single-line semiconductor lasers emitting at 405, 488, 532, 568, 640 and 660 nm (for example, sapphire 488LP with an output power of 100 mW (Coherent)). Laser lines are combined by suitable dichroic mirrors (from Chroma, Semrock, or AHF analysentechnik) and/or selected by an acousto-optical tunable filter (e.g., acousto-optical tunable filter (AOTF) from AAOptics) and coupled into the microscope objective using an appropriate polychromatic mirror. Laser beams might be spatially filtered using a high-power single-mode fiber. A lens or a pair of lenses (L1 and L2) is introduced in the excitation path to focus the laser on the back focal aperture of the high-numerical oil-immersion objective (e.g., PlanApo 60 $\times$ , NA 1.45; Olympus) to ensure homogeneous excitation of a  $50 \times 50 \mu\text{m}^2$  area. The focal length of the lenses can be changed to adjust the size of the illuminated area and the excitation intensity. A mirror (M1) mounted on a lateral translation stage is needed for TIRF applications (Fig. 5a).

As shown exemplarily in Table 1, excitation intensities in the range of  $1\text{--}5 \text{ kW cm}^{-2}$  have to be applied for readout and photoswitching at frame rates of 10–100 Hz. For excitation of the intermediate radical anions at 405 nm, excitation intensities well below  $1 \text{ kW cm}^{-2}$  (e.g.,  $<0.1 \text{ kW cm}^{-2}$ )<sup>53,62</sup> are sufficient. Irradiation of cells with 405 nm might increase autofluorescence. Furthermore, irradiation of already excited fluorophores at 405 nm promotes photobleaching of organic fluorophores. Both problems can be faced by alternating the excitation for readout and photoswitching, triggering the AOTF or the semiconductor lasers directly.

The fluorescence light in the detection path is filtered using suitable bandpass filters (Chroma, Semrock or AHF analysentechnik) and imaged with an EMCCD (e.g., Andor Ixon DU897) with quantum yields of 80–90% in the visible range. The CCD chip collects the incoming photons in pixels with a typical size in the range of  $16 \mu\text{m} \times 16 \mu\text{m}$  to  $24 \mu\text{m} \times 24 \mu\text{m}$ . To preserve most of the position information in the fluorescence signal data, a pixel size of  $\sim 2.3 \times$  smaller than the Abbe resolution limit of the optical system is generally used. Thus, for visible light, the fluorescence signal should be imaged ensuring a pixel size of  $80\text{--}160 \text{ nm}$  (typically  $\sim 100 \text{ nm}$ ) using appropriate additional

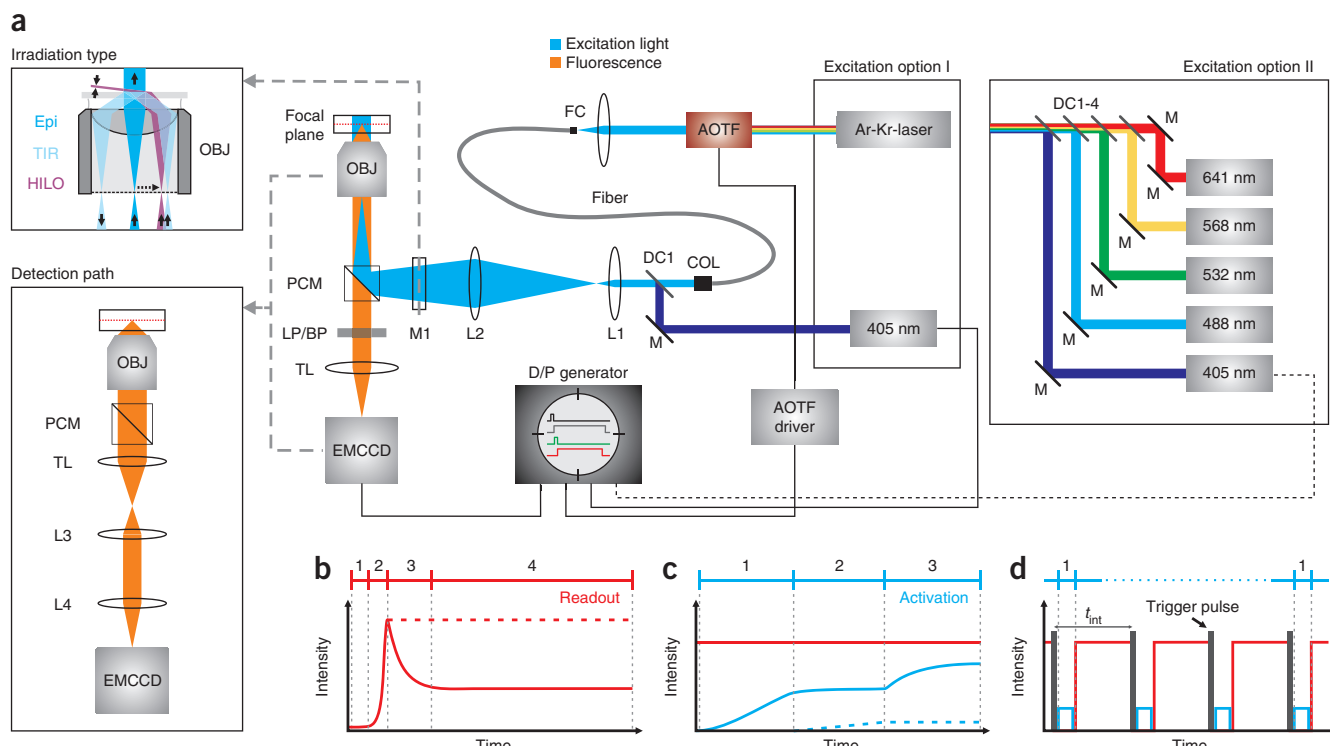


**Figure 5** | Scheme of experimental setup for single-molecule based localization microscopy with standard synthetic fluorophores. (a) The laser setup can consist of an Ar-Kr-laser providing laser lines at 488, 514, 568 and 647 nm and a 405 nm diode laser (excitation option I) or different semiconductor lasers sequentially combined by suitable dichroic mirrors (DC1-4; excitation option II). Irradiation wavelengths are selected by an AOTF, coupled into a single-mode fiber using standard fiber couplers, and focused on the back focal aperture of a high numerical aperture oil-immersion objective by a polychromatic mirror (PCM) using a lens or a pair of appropriate lenses (e.g., L1 with  $f = 25 \text{ mm}$  and L2 with  $f = 120 \text{ mm}$ ) located near the back port of the microscope. A movable mirror (M1) can be introduced in order to achieve TIRF or inclined illumination (HILO)<sup>78</sup> (scheme is not to scale). Fluorescence light is collected by the same objective, spectrally filtered by long-pass and/or bandpass filters (LP/BP) and imaged on an EMCCD camera. Additional lenses are arranged (tubus lens (TL), L3 and L4) in the detection path to ensure a pixel size of  $\sim 100 \text{ nm}$ . A potential lens configuration for the detection path is depicted. A delay and pulse generator (D/P generator) triggered by the camera is used to control alternating irradiation through the AOTF. (b) Course of irradiation intensity (red) used for fluorescence readout and photoswitching of fluorophores. (c) To control the number of 'active' fluorophores residing in the ON state, additional irradiation at 405 nm (blue) can be applied to directly excite the radical anions and ensure photoinduced recovery of the fluorescent ON state. Dashed lines show alternative irradiation schemes. (d) Alternating excitation scheme (integration time,  $t_{\text{int}}$ ) to minimize photobleaching in two-color experiments.

## PROTOCOL

lenses. Finally, a video sequence containing several thousands of images is recorded.

To minimize stage drift of the microscope setup, the excitation intensities of the two lasers should be adjusted to enable *d*STORM experiments with acquisition times as short as possible. However, especially in live-cell experiments, light-induced cellular damage must be minimized, thus requiring that the experiments are performed using lower excitation intensity. Therefore, acquisition times of a few minutes must be accepted for complex structures. To check for lateral drift, fluorescent beads or semiconductor nanocrystals that do not photobleach during the experiment can be immobilized at low density and their positions can be determined as a function of time. By generating histograms of the *x* and *y* position of single beads or nanocrystals, and by determining the standard deviation of the distributions in *x* and *y*, lateral drift can be monitored. Axial drift is directly reflected by blurring of the PSFs of individual beads. Whereas lateral drift can be corrected during post-processing of the images, axial drift has to be corrected online during acquisition with an active feedback loop. Alternatively, a nosepiece stage (e.g., IX2-NPS, Olympus) can be used to minimize the distance change between the specimen and the objective.

*d*STORM can be expanded to three dimensions by applying various experimental concepts. The generation of a double-helical PSF<sup>79</sup>, interferometric approaches<sup>80</sup> and virtual volume super-resolution microscopy<sup>45</sup> have achieved impressive axial resolutions, but these can be challenging to set up for nonexperts. The 3D super-resolution imaging based on introducing defocusing, i.e., dual- or multifocal-plane imaging or astigmatism, is easier to implement but achieves a comparable lower axial resolution of ~50–80 nm (refs. 81,82). Alternatively, an axial resolution of ~50 nm has been achieved, combining spatial-modulated illumination with single-molecule localization microscopy<sup>23</sup>. Aside from the considerations of microscopic configurations, 3D imaging has consequences for the density of fluorophores emitting concurrently. The excitation volume is considerably larger than in 2D imaging, but the information is still recorded with a 2D detector. Large and asymmetrical photon distributions are recorded, which complicate PSF fitting and result in a lower localization precision. This reduces the number of simultaneously recordable single molecules in one imaging frame, and requires longer image stacks to achieve the same localization statistics. In addition, achieving a high 3D fluorophore labeling density remains challenging, especially for live-cell applications.

**Data analysis.** Data processing described in this protocol uses the recently introduced open access software (*rapid*STORM) for single-molecule-based localization microscopy<sup>54</sup>. The original fluorescence images are compressed to a single super-resolved image in three stages: first, probable locations of fluorophore emissions are extracted from each fluorescence image. Second, a small area around each probable location is cut out from the image and the pixels within are fitted with a model of the PSF to localize fluorophore emission. Third, all localizations are combined into a single, super-resolution image. For the first step, the input image is usually smoothed to find the pixels with the highest intensity values. Several algorithms have been suggested for smoothing<sup>54</sup>, and the use of a simple average mask (moving average) with a diameter of roughly one FWHM (full width at half maximum) of the PSF has been proven to be very fast and robust. In the smoothed image, pixels with the highest values correspond to pixels in which most

photons were detected in the PSF-sized neighborhood. Extraction of pixels with the highest values using a local maximum filter algorithm (the Neubeck algorithm is suited especially for 16-bit data)<sup>83</sup> delivers the most probable fluorophore position.

In the second stage, a small local window (diameter roughly two FWHM of the PSF) is fitted with a PSF model, most commonly a 2D Gaussian function with a fixed covariance matrix plus constant background. Thus, four free parameters have to be fitted to the data: amplitude, center in X, center in Y and background. The two center coordinates give the high-precision estimate of the fluorophore's position (localization). The amplitude gives an estimate of the number of photons and is used to discriminate between background noise and real fluorescence emissions. A reasonable value that can be used here is 15 times the background noise standard deviation. When implementing the fitting procedure, computational care should be taken to optimize for speed. Most importantly, the partial derivatives of the model function needed by most fitting procedures should be computed analytically. Here the GNU Scientific Library<sup>84</sup> provides a suitable fitting procedure.

All single-molecule coordinates that were determined by fitting PSF in all source images are combined to a super-resolved image. Experience has shown that simply binning or linearly interpolating the resulting localizations and then running a weighted histogram normalization<sup>85</sup> with a power of 0.3 results in good images. However, the super-resolution image produced by the algorithm outlined above is not always the best choice for further analysis, that is, often it is beneficial to use the set of localizations gained in the second step for further analysis. Examples include super-resolution tracking<sup>41,86</sup>, clustering<sup>50,87</sup> and precision estimation in super-resolution imaging<sup>38,46</sup>.

Furthermore, it has to be considered that two or more fluorophores can be fluorescent at the same time within a diffraction-limited area with a diameter of ~250 nm. To avoid these so-called multifluorophore localizations, a photon threshold can be applied and the geometry of the PSF can be taken into account, as overlapping PSFs of multiple emitters produce an unsymmetrical signal distribution. However, as fluorescence intensity is a poor parameter for the quantification of individual fluorophores, false localizations are always present in super-resolved images. The number of artificial or false localizations depends on the labeling density and the sample structure, but it can be kept low with appropriate control of the number of fluorophores residing in the fluorescent state and becomes higher when the photoswitching rates are set inappropriately, i.e., for low *r* values (Fig. 4)<sup>75</sup>.

Furthermore, it is important to mention an advantage of concepts such as *d*STORM (that use reversible photoswitches) over concepts that use PA-FPs that can be localized only once. Using *d*STORM, structural information is not lost when a two- or multi-fluorophore event is recognized and discarded from further analysis because it is likely that the same fluorophore is localized again individually. In addition, even for inappropriately set photoswitching rates, a structure can be resolved as long as every fluorophore is localized individually at least once and the error-rate for discarding multi-fluorophore events (which increases with decreasing *r* values) is kept low. When using PA-FPs, two-spot events can occur stochastically; alternatively, if the irradiation intensity for activation is set too high, then the localization information is irretrievably lost or a false localization is made.

**Fluorescence labeling.** The study of cellular structure and function *in vivo* and *in vitro* with super-resolution microscopy requires efficient labeling strategies to introduce suitable fluorescent probes. The most elegant way to specifically label proteins in cells is the coexpression of a fusion protein that can be photoactivated. Fusion proteins are very successfully used to study localization of proteins, dynamic processes and protein–protein interactions in cells<sup>88–90</sup>. Photoswitchable synthetic fluorophores are much smaller than fusion proteins but require a chemical labeling procedure.

Reliable and commonly used procedures to specifically label target biomolecules in fixed cells with organic fluorophores are labeled antibodies, DNA oligonucleotides or small specifically binding peptides such as phalloidin and Lifeact<sup>91</sup>.

In this protocol, the examples used are: (i) labeling of microtubules with antibodies, in which the fluorescent label is on the secondary antibody (**Fig. 6a–d**); and (ii) labeling of actin with fluorescently labeled phalloidin.

In particular, for immunofluorescence staining, a wealth of probes labeled with Alexa Fluor and ATTO fluorophores are commercially available. Whereas DNA oligonucleotides and peptides are stoichiometrically labeled with fluorophores, commercially available antibodies often carry more than one, i.e., typically two to six fluorophores, rendering appropriate photoswitching more difficult. To increase specificity, proteins are usually labeled indirectly, that is, with a first primary antibody against the antigen and a second antibody directed against the first antibody. Compared with standard IgG antibodies with a size of  $\geq 7$  nm,  $F(ab')_2$  fragments are slightly smaller and more specific (in this protocol both,  $F(ab')_2$  fragments and IgG antibodies have been used). Because the label size affects the achievable labeling density and resolution, smaller fluorescent probes are recommended. Furthermore, it must be considered that the resolution of *d*STORM easily approaches  $\sim 20$  nm in lateral direction, i.e., the size of fluorescent probes used to label the target structure (for example, antibodies) influences the measured size. For example, microtubules have a diameter of  $\sim 25$  nm, as determined by electron microscopy, whereas *d*STORM experiments with indirectly stained microtubules measured a diameter of 40–50 nm (ref. 21).

For start-up experiments, we recommend Alexa Fluor 647 or Cy5, and Alexa Fluor 488 for fixed cells. Alexa Fluor 647 or Cy5 should be used for single-color *d*STORM. Photoswitching can be performed at very high excitation intensities, allowing *d*STORM acquisition times of only a few seconds, which is especially interesting to study dynamics under *in vitro* conditions<sup>51</sup>. Reactivation of fluorophores by irradiation of the OFF state at 488, 514 or 532 nm does not induce strong damage or photobleaching and can be applied simultaneously with the readout wavelength at 641 or 647 nm. Oxygen removal increases the reliability of photoswitching. Various fluorescently labeled secondary antibodies and other probes such as phalloidin are commercially available (see MATERIALS).

Alexa Fluor 488 can also be purchased as antibody or phalloidin conjugate. Radical anions absorb at around 400 nm, enabling reactivation of the fluorescent state by irradiation with a 405-nm laser diode. In contrast to Cy5 or Alexa Fluor 647, photoreactivation at 405 nm increases autofluorescence and promotes photobleaching. Therefore, an alternating excitation scheme with short reactivation pulses is recommended.

In addition, the *d*STORM method enables live-cell super-resolution imaging, profiting from the intracellular redox system

(including GSH at mM concentrations) and oxygen to operate several organic fluorophores as photoswitches inside a living cell.

For *in vivo* labeling of cells, the target protein needs to be modified (tagged) so that an appropriate fluorescent molecule—one that permeates cell membranes—can bind to it with high specificity. The tetracysteine tag reacts with arsenical fluorophores to form stable and highly fluorescent complexes<sup>92</sup>. Alternative approaches include the SNAP-tag that allows labeling of fusion proteins of human  $O^6$ -alkylguanine-DNA alkyltransferase with  $O^6$ -benzylguanine derivatives<sup>93,94</sup> or the HALO-tag<sup>95</sup>. The trimethoprim (TMP)-tag<sup>96–98</sup> is based on the high-affinity noncovalent interaction between *Escherichia coli* dihydrofolate reductase (eDHFR) and TMP. Recently, it has been shown that the TMP-tag method can be used successfully for live-cell *d*STORM with ATTO dyes achieving a resolution of  $\sim 20$  nm<sup>52</sup>. On the other hand, commercial SNAP-tag kits also use reversibly photoswitchable rhodamine fluorophores, such as tetramethylrhodamine (TMR), as  $O^6$ -benzylguanine conjugates and can therefore also be used for live-cell *d*STORM<sup>53</sup>. Because cells naturally contain the ‘redox cocktail’, thiol (GSH) and oxygen, at appropriate concentrations, the *d*STORM method is widely applicable for *in vivo* multicolor super-resolution imaging experiments also in combination with PA-FPs.

For live-cell experiments, cells are usually stained with photoswitchable fluorophores according to the protocol of the chemical tag used (typically for 30 min, applying  $0.1$ – $2\text{ }\mu\text{mol l}^{-1}$  concentrations of fluorescent substrates) at  $\sim 1$  d after transfection with the vector of interest. However, for the successful application of chemical tags for *d*STORM in living cells, several facts have to be carefully considered. First, the transfection and labeling efficiency with chemical tags varies strongly, depending on the cell type used<sup>53</sup>. Therefore, the optimal substrate concentration has to be identified experimentally. Second, nonspecific adsorption of fluorescent substrates to glass surfaces, cellular membranes and structures, respectively, can strongly increase the background signal, especially when applied at high concentrations ( $\geq 1\text{ }\mu\text{M}$ ).

Low transfection efficiencies result in a high concentration of unbound fluorophore conjugates and increased nonspecific labeling because unbound fluorophore conjugates can diffuse out of cells. Nonspecific adsorption might be of minor importance, especially for low fluorophore concentrations in ensemble standard fluorescence imaging experiments, but seriously deteriorates the identification and appropriate localization of individual fluorophores at the single-molecule level. This is due to the fact that nonspecifically adsorbed fluorophores produce a higher background signal because they stay fluorescent (in the absence of thiols outside of cells), whereas the majority of specifically bound fluorophores is transferred to the stable OFF state upon irradiation. To minimize nonspecific adsorption effects, the cell density can be increased to effectively reduce the interspace between cells before labeling. Alternatively, and much more efficiently, cells can be trypsinized and transferred into a new chamber well after labeling<sup>52</sup> or the surface can be blocked efficiently by treating the surface with the amino acid glycine before the experiment (see PROCEDURE for more details; **Fig. 6e,f**)<sup>53</sup>. For live-cell *d*STORM, SNAP-Cell TMR-Star, SNAP-Cell 505 and TMP-ATTO 655 work reliably.

If applied appropriately, *d*STORM enables the observation of dynamic processes in living cells that move with velocities of up to several  $\text{nm s}^{-1}$  (ref. 52). In general, the achievable resolution in *d*STORM movie sequences of dynamic processes is, besides other

## PROTOCOL

**Figure 6** | *d*STORM images of fixed COS-7 and living HeLa cells. (a–d) Microtubules were stained with Alexa Fluor 647 antibodies, (experimental conditions: 20–30 kW cm<sup>-2</sup> at 641 nm, 0–0.5 kW cm<sup>-2</sup> at 532 nm, frame rate: 0.4–1 kHz, 15,000–20,000 frames). (a,b) Tubulin structures are not continuously resolved (especially in b). Possible reasons are a low antibody concentration that has been applied in immunocytochemistry staining or fixation artifacts. (c) The super-resolved microtubule structure is background dominated. The background stems either from unspecific binding of antibodies, fixation artifacts or from tubulin monomers in the cell. (d) A typical *d*STORM image of a cellular structure with good contrast and negligible unspecific binding of antibodies. Standard fluorescence images are shown for comparison in the upper left or right corner. (e–h) Human histone protein H2B of a living HeLa cell stained with SNAP-Cell 505. (g,h) Standard wide-field fluorescence image (g) and *d*STORM image (h) of H2B core histones with high contrast measured using the following experimental parameters: irradiation at 488 nm with 2 kW cm<sup>-2</sup>; frame rate, 31.5 Hz; 4,000 frames. (e) A single-molecule image showing nonspecific background signals outside of the nucleus that can be dramatically reduced (f) by glycine coating of the Lab-Tek chambers. Scale bars, 2 μm for a–d; 5 μm for e–h.

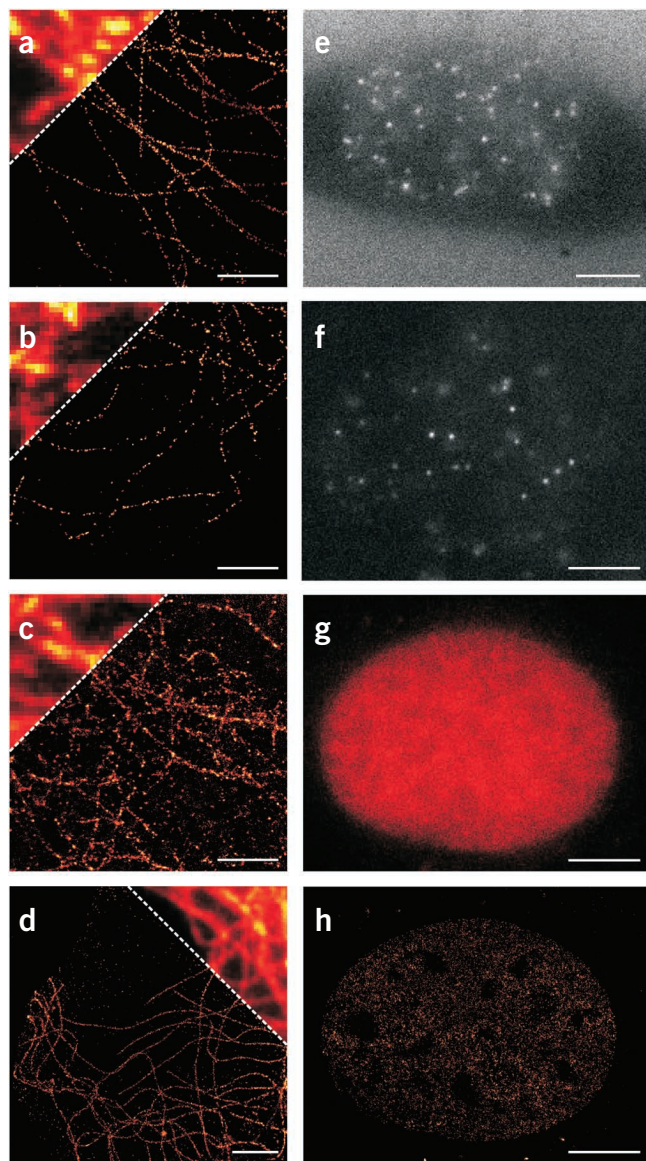
parameters, mainly determined by the movement velocity of the fluorescent signals. In reference 52, nucleosome and chromatin movement has been studied by *d*STORM in living cells, with a camera frame rate of 50 Hz, and super-resolution images have been reconstructed from 500 frames, respectively, corresponding to a temporal resolution of 10 s. As the velocity is only a few nanometers per second, a super-resolution image can be reconstructed every 10 s.

Whether or not a dynamic process can be temporally resolved is mainly controlled by two parameters: the complexity of the structure and its labeling density, and the photoswitching rates controlled by the irradiation intensity. In the cellular environment, ON state lifetimes of a few tens of milliseconds (typically 10–50 ms) require imaging frame rates of 20–100 Hz. The lifetime of the OFF state varies from several hundred milliseconds to a few seconds (0.5–10 s), corresponding to  $r = 50$ –1,000. For low labeling densities, as in studies of the dynamics of filaments or protein complexes, with only 10–50 fluorophores per diffraction-limited area, *d*STORM imaging with a speed only determined by the irradiation intensity is possible. Under these conditions, super-resolution imaging at spatial resolutions of ~20 nm and temporal resolutions of 0.1–1 s is possible<sup>51</sup>. On the other hand, the temporal resolution decreases for more complex structures, with high labeling densities of  $\geq 300$  fluorophores per diffraction-limited area, unless the excitation intensity is dramatically increased.

## MATERIALS

## REAGENTS

- Specific primary antibodies (e.g., mouse anti-β-tubulin antibody; Sigma, Invitrogen)
- Secondary antibodies (e.g., goat anti-mouse Alexa Fluor 647 antibody; Invitrogen, cat. no. A-21237)
- Specific drug molecules (e.g., Alexa Fluor 647 phalloidin; Invitrogen, cat. no. A22287), Alexa Fluor 488 phalloidin (Invitrogen, cat. no. A12379)
- ATTO and Alexa Fluor fluorophores for labeling of antibodies (e.g., ATTO 655 NHS)
- Growth medium RPMI 1640, (GIBCO, cat. no. 31870-025) supplemented with 10% (vol/vol) FCS, 2 mM L-glutamine, 100 u ml<sup>-1</sup> penicillin and 100 μg ml<sup>-1</sup> streptomycin
- Phenol red-free growth medium (e.g., RPMI 1640, GIBCO, cat. no. 32404-014) supplemented with 10% (vol/vol) FCS, 2 mM L-glutamine, 100 u ml<sup>-1</sup> penicillin and 100 μg ml<sup>-1</sup> streptomycin



To compare *d*STORM and (F)PALM, a protein genetically labeled with PA-FPs can be additionally labeled in fixed cells using standard fluorescent probes (e.g., antibodies).

- Glycine (2 M in ddH<sub>2</sub>O; Roth, cat. no. 2002722)
- PBS (PAA, cat. no. H15-002)
- Lipofectamine 2000 (Invitrogen, cat. no. 11668-019)
- Trypsin-EDTA (PAA, cat. no. L-11-004)
- pSNAP-H2B control plasmid (NEB, cat. no. N9179S)
- SNAP-Cell TMR-Star (NEB, cat. no. S9105S)
- SNAP-Cell 505 (NEB, cat. no. S9103S)
- Mammalian expression vector of H2B-eDHFR and corresponding TMP-ATTO655 tag
- Amaxa Nucleofector System (Lonza)
- HeLa (DSMZ, cat. no. ACC 75)
- Lab-Tek II chambered cover glass (Nunc, cat. no. 155409)
- Paraformaldehyde in PBS (4% (wt/vol), PFA; USB, cat. no. 19943)
- **! CAUTION** It is poisonous. Wear appropriate protective equipment and avoid contact with skin or eyes.

- Triton X-100 (Sigma)
  - Tween-20 (Sigma)
  - Sytox Blue or Hoechst dyes for DNA labeling in double staining experiments
  - Quantum dots for calibration and drift control (QD525, QD655; Invitrogen Q10141MP resp. Q10121MP)
  - BSA (Sigma)
  - Normal goat serum (NGS, Sigma)
  - Immersion oil (Carl Zeiss)
  - Antibodies (F(ab')<sub>2</sub>) fragments for labeling; Sigma, Invitrogen)
  - NAP-5 column for purification of labeled antibodies and fragments (Sephadex G25 DNA grade; GE Healthcare)
  - Mercaptoethylamine (MEA; Sigma); MEA can be purchased as hydrochloride (MEA-HCl; slightly acidic, has to be adjusted with KOH) or pure (alkaline, adjustment with HCl) **! CAUTION** HCl / NaOH is corrosive, wear appropriate protective equipment and avoid contact with skin or eyes.
  - Glutathione (GSH; Sigma)
  - Oxygen scavenger system (It consists of 0.5 mg ml<sup>-1</sup> glucose oxidase (Sigma), 40 µg ml<sup>-1</sup> catalase (Roche Applied Science), 10% (wt/vol) glucose in phosphate buffer (pH 7.4).)
  - DMSO
- EQUIPMENT**
- Optical table, vibration isolated (Linos / Qioptiq)
  - Inverted fluorescence microscope (IX-71, Olympus)
  - Oil-immersion objective (60×, PlanApo 1.45 NA, Olympus)
  - Objective for alignment (×10; Carl Zeiss, Olympus)
  - Irradiation lasers (see EXPERIMENTAL DESIGN)
    - 641 nm (Cube 640-100C, Coherent)
    - 643 nm (iBeam smart, Optica)
    - 405 nm (Cube 405-100C, Coherent)
    - 532 nm (Nano250; Linos / Qioptiq)
    - 488 nm (Sapphire 488 LP, Coherent)
    - 568 nm (Sapphire 568 LP, Coherent)
    - Argon-krypton laser (Innova 70C, Coherent)
  - Acousto-optical tunable filter (AOTF, AAOptics) for laser line selection
  - Delay and pulse generator (Stanford Research Systems)
  - Neutral density filter to adjust laser intensity (Edmund Optics)
  - Single-mode fiber (Linos)
  - Fiber coupler (Linos)
  - Lenses (Linos, Thorlabs, Edmund Optics)
  - Polychromatic mirror (Semrock, Chroma, AHF Analysentechnik)
    - HC 410/504/582/669, Semrock
    - HC 560/659, Semrock
  - Dichroic mirrors for laser coupling (Semrock, Chroma, AHF Analysentechnik)
    - LaserMUX (Semrock / AHF Analysentechnik)
    - LaserMUX 375-405R
    - LaserMUX 473-491R, 1064R
    - LaserMUX 514-543R
    - LaserMUX 561-594R
    - LaserMUX 633-647R
  - Band-pass / long-pass filters to spectrally separate fluorescence signal (Semrock, Chroma, AHF Analysentechnik)
    - HQ 535/50
    - HC 582/75
    - ET700/75
    - RazorEdge 647 Long-pass filter
  - Laser clean-up filter (Semrock, Chroma, AHF Analysentechnik)
    - Laser clean-up filter z 640/10
    - Laser clean-up filter z 488/10
    - Laser clean-up filter z 405/10
  - Electron multiplying, back-illuminated, cooled, charged-coupled device camera (Ixon; Andor) with high quantum yield and low readout and background noise
    - Large Chip (Ixon DU897, 512 × 512 pixels with 16 µm pixel size, Andor)
    - Ultrafast acquisition speed (Ixon DU860; 128 × 128 pixels with 24 µm pixel size, Andor)
  - Reticle for calibration and validation of final magnification (Carl Zeiss)
  - Software to control camera (Andor Solis, Andor)
  - Software for image analysis<sup>54</sup>
  - Cover slips

## REAGENT SETUP

**Sample for calibration and drift control** Semiconductor nanocrystals (so-called quantum dots (QDs)) can be dried on a bare cover slip at single-molecule concentration. This calibration sample is used to verify that the microscope setup is properly aligned and enables the detection of single molecules with high signal-to-background ratio. The use of QD655 is advantageous because they are efficiently excited by the various irradiation lasers used in *d*STORM, i.e., 405, 488, 532, 568 and 641 nm (ref. 99).

**Cell culture** Any cell type is compatible with *d*STORM. Adherent cells such as HeLa or fibroblast cells offer the additional advantage that movement of the sample is minimized. Grow cells at 37 °C and 5% CO<sub>2</sub> in RPMI 1640 medium supplemented with 10% (vol/vol) FCS and split every other day.

**Fluorescence labeling of antibodies** ATTO or Alexa Fluor fluorophores can be purchased as NHS derivatives and labeled to IgG antibodies or F(ab')<sub>2</sub> fragments according to standard coupling protocols given by the supplier. Conjugates are purified on a gel filtration column (e.g., NAP-5, Sephadex G-25 DNA Grade, GE Healthcare). The degree of labeling of antibodies or F(ab')<sub>2</sub> fragments is determined by absorption spectroscopy using the extinction coefficient of fluorophore and protein (absorption of the fluorophore at 280 nm has to be considered; determine correction factor at 280 nm (CF<sub>280</sub>)). To facilitate photoswitching of the 'antibody' as fluorescent probe, the degree of labeling should be kept at one or two fluorophores per antibody.

**Immunocytochemistry** For *in vitro* immunofluorescence labeling, cells must be fixed with PFA, formaldehyde, methanol or glutaraldehyde and permeabilized. Various fixation protocols can be used for the preparation of samples used for *d*STORM imaging. However, different fixatives do influence the spatial organization of cellular structures<sup>100</sup>. This is becoming more apparent in methods with superior resolution, and should be taken into account in data interpretation. If adherent cells are to be investigated, they are grown according to standard culture procedures in chambered cover glasses with a thickness of 130 µm (e.g., Lab-Teks, Nunc). Furthermore, chambered cover glasses are advantageous because the volume for any labeling or washing step is predetermined by the chamber dimensions (1 ml maximum). Ideally, the cellular structure is well conserved because of the crosslinking of proteins by the fixative. However, one should be aware that the concentration of fixative, the incubation time and the permeabilization reagent (e.g., Triton X-100, a nonionic surfactant) can influence the sample and should thus carefully be selected and applied. Finally, after fixation and permeabilization, a blocking buffer such as BSA in PBS or NGS is used to reduce unspecific binding and background signals.

After fixation, permeabilization and blocking, cells are sequentially stained with primary and secondary antibodies. Owing to their high specificity, staining is often accomplished in only 30 min. For proteins with high cellular density, we recommend using different antibody dilutions. Chambered cover glasses (e.g., Lab-Tek II chambered cover glass, Nunc) with eight wells are excellently suited to probe different concentrations of antibodies. After each staining step, washing steps are indispensable to remove unbound antibodies. Washing should be applied by purging and keeping the cells in PBS containing a surfactant such as Tween-20. Stained cells can be stored in PBS (pH 7.4) at 4 °C protected from light for several days until imaging. A postfixation step can be helpful to enable longer storage but is not mandatory. A complete label protocol for fixation and staining of mammalian cells is described in the PROCEDURE. The protocol given can be modified on demand according to different requirements of labels and target proteins (see manufacturer's instructions), but it works properly for the staining of cellular microtubules or actin filaments.

**Live-cell labeling with chemical protein tags** Grow cells in Lab-Tek II chambered cover glass. To avoid nonspecific adsorption of fluorophores on the cover glass, it is recommended to coat it with glycine (2 M glycine solution for 30–60 min) before use. Transfect ~2 × 10<sup>6</sup> cells, with the tag-vector coding the protein of interest (e.g., pSNAP-H2B control plasmid) according to the protocol of the supplier using, for example, electroporation with the Amaxa Nucleofector System. Incubate cells overnight to allow expression of the fusion protein. Prepare stock solutions of the tagged substrates TMP-ATTO 655, SNAP-Cell TMR-Star or SNAP-Cell 505 (benzyl guanine Rhodamine Green) in DMSO. Dilute the stock solutions in RPMI 1640 medium supplemented with 10% (vol/vol) FCS without phenol red to final concentrations of 0.1–2 µmol l<sup>-1</sup>. Fluorescence labeling of cells is

## PROTOCOL

performed—after removal of medium and one optional washing step (PBS or medium)—by adding medium containing the tag substrates at various concentrations. After incubation for typically 20–30 min, followed by several washing steps to remove unreacted substrate, cells are imaged in phenol red-free medium or PBS. For further background reduction, labeled cells can be detached from the glass surface by trypsinization (0.25%) at 37 °C and transferred into cleaned, new Lab-Tek II wells. Allow cells to reattach for 1–3 h before imaging. To prove that cells do not show apparent ill defects after imaging (i.e., they have normal growth and cell division), let them grow at 37 °C and 5% CO<sub>2</sub> in medium overnight and check the condition of cells. **Co-staining to verify specific labeling** For nuclear co-staining, cells must be fixed with PFA or formaldehyde and permeabilized with Triton X-100. Hoechst 33258 or Sytox Blue is used to label DNA. When Sytox Blue is used, incubate with RNase before staining to reduce background. After washing, image cells on a standard laser-scanning microscope (LSM).

### EQUIPMENT SETUP

**Construction of dSTORM microscope** To minimize sample drift, the dSTORM setup should be mounted on a vibration-isolated optical table. The lasers should be arranged as depicted in **Figure 5a**, allowing their superposition by suited dichroic mirrors. Passing an acousto-optical tunable filter (AOTF) for wavelength selection, the laser beams can be coupled into a single-mode fiber to optimize superposition. In case of diode lasers, AOTF and fiber coupling are optional. The laser beams are focused on the back focal aperture of the oil-immersion objective using lenses L1 (e.g.,  $f_1 = 25$  mm) and L2 (e.g.,  $f_2 = 120$  mm; **Fig. 5a**). Take care that the laser beams are perfectly aligned with the optical axis. This can be achieved using irises and steering mirrors in the beam path, so that the beam has two independent points of adjustment to enable control of the position and angle of the beam. Use a movable mirror to attain TIRF or inclined excitation of the sample. The fluorescence light collected by the same objective is spectrally filtered using appropriate bandpass filters and projected on an EMCCD camera mounted outside the side or base port of the microscope. In standard inverted microscopes, a tubus lens is introduced by the manufacturer enabling direct attachment of the EMCCD camera. To generate an effective

pixel size of ~100 nm, additional lenses (e.g., L3 and L4) can be inserted into the detection path.

**Controlling the photoswitching ratio** The lifetime of the ON state can be decreased to match the frame rate of the camera by increasing the irradiation intensity, thiol concentration (1–200 mM) and the pH value of the solvent (pH ~6.0–9.0). The lifetime of the OFF state can be shortened by direct irradiation of the radical anions at ~400 nm (ref. 62) or addition of oxidizing agents<sup>101</sup>, whereas the prolongation of the lifetime of the OFF state succeeds by oxygen removal (e.g., purging with nitrogen or application of an oxygen scavenging system)<sup>67,68</sup>. As shown in **Figure 5b** (numbers correspond to figure labels), at step one of the experiment (1) the irradiation intensity for fluorescence readout is kept low (~0.1 kW cm<sup>-2</sup>) to select an appropriate sample area for dSTORM, and a standard wide-field fluorescence image is recorded for later comparison. In the next step (2) the majority of fluorophores has to be switched to the OFF state applying a relatively high irradiation intensity of 5–30 kW cm<sup>-2</sup> for a few seconds. Once the desired density of fluorescence signals is achieved, the irradiation intensity is again decreased to typically 1–5 kW cm<sup>-2</sup> (3) to match the camera frame rate. Dependent on the sample, additional direct excitation of the radical anions is not necessary and the irradiation intensity of the readout laser can be kept constant throughout the experiment (4). For other samples, additional irradiation at 405 nm is required to activate enough fluorophores (**Fig. 5c**). Here the intensity of the activation laser can be increased slowly with proceeding acquisition time (1–3) to ensure a constant number of fluorophores residing in the ON state (see also **Fig. 3**). As simultaneous irradiation with the readout and the activation laser induces photobleaching in some fluorophores, we recommend alternating laser pulses (**Fig. 5d**). For example, the trigger signal of the EMCCD camera (a repetitive signal generated for every new frame) is used to generate a pulse scheme for readout and activation using a delay and pulse generator. At the beginning of a frame, a short activation pulse (1) reactivates a subset of fluorophores residing in their nonfluorescent OFF state. The length of the activation pulse and intensity determine the number of reactivated molecules. After the activation pulse, the readout laser line is triggered for fluorescence readout and photoswitching of activated fluorophores until the next frame starts.

## PROCEDURE

### Fluorescence labeling ● TIMING 2–3 d

1| At 2–3 d before experiments, transfer cells into Lab-Tek II chambered cover glass. For fixed cells and antibody labeling, follow the steps in option A (the labeling of microtubules with antibodies is used as an example). For labeling of actin filaments with phalloidin, see option B. For live-cell experiments, follow the steps in option C.

#### (A) Fixed cells

- (i) Wash cells with PBS, add PFA to a final concentration of 4% (wt/vol) and incubate for 10 min at room temperature (20 °C). **! CAUTION** Wear appropriate protective equipment and avoid contact with skin or eyes. After two washing steps with PBS (incubate in each case for 5 min), remove PBS and add 200 µl Triton X-100 at a concentration of 0.5% (vol/vol) in PBS to each chamber and incubate again for 10 min. Wash twice with PBS.
- (ii) Prepare the blocking buffer. Use NGS as blocking buffer if secondary antibody stems from goat. Dilute NGS in PBS to a final concentration of 5% (vol/vol). Alternatively, use BSA in PBS at a final concentration of 5% (wt/vol) as blocking buffer.
- (iii) Remove the fixing solution and add blocking buffer (e.g., 150 µl) to each chamber and incubate for 30 min at room temperature (20 °C).
- (iv) Dissolve antibody in blocking buffer at different concentrations, e.g., dilute mouse anti-β-tubulin antibody (2 mg ml<sup>-1</sup>) 1:100, 1:200, 1:500 and 1:1,000. Add different concentrations to different chambers after removing the former solution and incubate for 30–60 min at room temperature (20 °C).
- (v) Exchange the antibody solution in each chamber with 0.1% (vol/vol) Tween-20 in PBS and incubate for 5 min at room temperature (20 °C). Repeat this step twice.
- (vi) Add secondary fluorescently labeled antibody dissolved in blocking buffer (200 µl) to each sample at different concentrations and incubate for 30–60 min in the dark at room temperature (20 °C). For example, dilute goat anti-mouse Alexa Fluor 647 F(ab')<sub>2</sub> antibody (2 mg ml<sup>-1</sup>) 1:100, 1:200, 1:500 and 1:1,000 (final concentration) and add the different concentrations to similarly diluted primary antibody (Step 4).

### ? TROUBLESHOOTING

- (vii) For optional nuclear co-staining for LSM experiments, add 20  $\mu$ l of a 10  $\mu$ g ml<sup>-1</sup> Hoechst 33258 solution (in PBS) during the last 10 min of incubation with secondary antibody.
- (viii) Exchange the antibody solution in each chamber with 0.1% (vol/vol) Tween-20 in PBS and incubate for 5 min at room temperature (20 °C). Repeat this step twice.
- (ix) (optional) For postfixation, fix cells for 5 min using 4% (wt/vol) PFA in PBS and wash three times with PBS. Store cells in PBS at 4 °C.
- (x) Before imaging, add MEA to achieve a final thiol concentration of 10–200 mM (Table 1). When working with cyanine fluorophores (Cy5, Cy5.5, Cy7 and Alexa Fluor 647, 680, 700) additional removal of oxygen by application of an oxygen scavenging system (0.5 mg ml<sup>-1</sup> glucose oxidase, 40  $\mu$ g ml<sup>-1</sup> catalase, 10% (wt/vol) glucose) is recommended. If such a system is used, seal the chamber with a cover slip or a thin silicon sheet (press-to-seal).

#### ?

#### TROUBLESHOOTING

#### (B) Labeling actin with phalloidin in fixed cells

- (i) Wash cells with PBS, add PFA to a final concentration of 4% (wt/vol) and incubate for 10 min at room temperature (20 °C).
- ! CAUTION** Wear appropriate protective equipment and avoid contact with skin or eyes. After two washing steps with PBS (incubate in each case for 5 min), remove PBS and add 200  $\mu$ l Triton X-100 at a concentration of 0.5% (vol/vol) in PBS to each chamber and incubate again for 10 min. Wash twice with PBS.
- (ii) Prepare the blocking buffer. Use BSA in PBS at a final concentration of 5% (wt/vol) as blocking buffer.
- (iii) Remove the fixing solution and add blocking buffer (e.g., 150  $\mu$ l) to each chamber and incubate for 30 min at room temperature (20 °C).
- (iv) After blocking the fixed and permeabilized cells, label actin filaments by adding Alexa Fluor 488–phalloidin or Alexa Fluor 647–phalloidin (stock solution 1  $\mu$ mol l<sup>-1</sup>), diluted in PBS to a volume of 10<sup>-7</sup> to 10<sup>-9</sup> mol per liter (typically, 10<sup>-8</sup> mol per liter). Incubate for 30–60 min in the dark at room temperature (20 °C).

#### ?

#### TROUBLESHOOTING

- (v) Exchange phalloidin solution by 0.1% (vol/vol) Tween-20 in PBS in each chamber and incubate for 5 min at room temperature (20 °C). Repeat this step twice. Store cells in PBS at 4 °C.
- (vi) (optional) For postfixation, fix cells for 5 min using 4% (vol/vol) PFA in PBS and wash three times with PBS. Store cells in PBS at 4 °C.
- (vii) Before imaging, add MEA to achieve a final thiol concentration of 10–200 mM (Table 1). When working with cyanine fluorophores (Cy5, Cy5.5, Cy7 and Alexa Fluor 647, 680, 700), additional removal of oxygen by application of an oxygen scavenging system (0.5 mg ml<sup>-1</sup> glucose oxidase, 40  $\mu$ g ml<sup>-1</sup> catalase, 10% (wt/vol) glucose) is recommended. If such a system is used, seal the chamber with a cover slip or a thin silicon sheet (press-to-seal).

#### ?

#### TROUBLESHOOTING

#### (C) Live cells

- (i) Block the surface of the cover glass with 2 M glycine for 30–60 min.
- (ii) Transfer cells into Lab-Tek II chambered cover glass.
- (iii) At 1 d after transfer, transfect cells with a tag-vector encoding the protein of interest according to the protocol given by the supplier. For example, to label the core protein H2B with TMP-ATTO 655, transfet cells with the H2B-eDHFR plasmid by electroporation and incubate cells overnight in growth medium<sup>52</sup>.
- (iv) Dilute stock solution of fluorescent substrates (e.g., TMP-ATTO 655, SNAP-Cell TMR-Star and SNAP-Cell 505) in phenol red-free growth medium to 0.1–2  $\mu$ mol per liter.
- (v) Wash cells once with PBS or medium at room temperature (20 °C) before adding different concentrations of fluorescent substrates (e.g., 0.2, 0.5, 1 and 2  $\mu$ mol per liter). Incubate at 37 °C and 5% CO<sub>2</sub> for 20–30 min.
- (vi) Wash cells three times with 0.1% (vol/vol) Tween-20 in PBS or with medium without phenol red. Add phenol red-free medium or PBS before imaging at room temperature (20 °C). For optional nuclear co-staining experiments by LSM go to Step 1C(vii).
- (vii) Repeat Step 1B(i) if cells are not fixed. For nuclear co-staining use Hoechst 33258 or Sytox Blue. If Sytox Blue is used, incubate in PBS containing 10 mg RNase for 30–60 min at 37 °C. After a washing step, add Sytox Blue to a final concentration of 500 nM and incubate for 30 min before washing with PBS. Hoechst 33258 is added without blocking at a concentration of 2–5  $\mu$ g ml<sup>-1</sup> in PBS for 10 min. Wash three times with PBS before imaging on a LSM.

#### Microscope setup

#### ● TIMING 0.5–1 h

- 2| Turn on lasers, adjust to a low laser power (1–2 mW) and block beams using appropriate shutters in the excitation path. Allow gas lasers to warm up for 20 min.

## PROTOCOL

**3** Measure laser power in focus after the polychromic mirror before entering the objective. Determine homogeneously irradiated area imaging the fluorescence signal of a fluorophore or QD solution ( $\sim 10^{-8}$  M) on the EMCCD camera to calculate the irradiation intensity in  $\text{kW cm}^{-2}$ .

**! CAUTION** Always exercise laser safety precautions when aligning lasers.

**4** Use appropriate dichroic mirrors and bandpass filter to select the desired irradiation wavelength and block stray light.

**! CAUTION** To avoid eye damage, never look through the oculars without having confirmed that filter combinations are compatible with the lasers in use.

**5** Align the camera using the  $\times 10$  objective and a reticle by centering the image on the display and bringing it into focus applying a low lamp intensity. Change to an imaging oil-immersion objective and determine pixel size using a micrometer scale.

**6** Use the oil-immersion objective and overlay laser beams using the calibration sample (QDs) to verify that single molecules can be imaged with the setup. Single QDs can be easily identified by their size (resulting in a diffraction-limited PSF) and their irradiation intensity-dependent blinking.

**7** To control the irradiation profile of the different lasers, use the oil-immersion objective and excite a concentrated QD655 solution or a densely coated QD655 surface. The emission profile recorded on the EMCCD camera should be independent of the irradiation laser used. Use the camera software to obtain a snapshot of the different irradiation profiles to calculate the excitation intensity. If necessary, adjust laser alignment using steering mirrors in the irradiation path.

### ? TROUBLESHOOTING

**8** Move mirror M1 (Fig. 5a) to achieve TIRF using a QD calibration sample (i.e., QDs adsorbed on a bare cover slip). If TIRF or HILO (highly inclined and laminated optical sheet) is accomplished, the signal-to-background ratio increases substantially.

**! CAUTION** Lower the gain of the camera to prevent damage of the chip when moving from epi-illumination to TIRF because the irradiation intensity increases strongly.

**9** To find the optimal conditions for imaging, move the beam completely out of the sample, then move slowly back into TIRF until the fluorescence intensity and signal-to-background ratio achieve their maximum values. If necessary, adjust the focus so that the sample is in the focal plane again.

**10** To achieve inclined illumination<sup>78</sup>, image the fluorescently labeled sample (i.e., a cell) by epi-illumination. While moving the mirror toward TIRF geometry at a certain point, the incident laser beam is highly inclined by a large refraction and is laminated as a thin optical sheet at the specimen side. Inclined illumination is optimal when fluorescence signals inside the nucleus of a living cell can be imaged with a high signal-to-background ratio.

### ? TROUBLESHOOTING

#### Data acquisition ● TIMING 0.1–10 min

**11** Select a cell by the oculars using transmitted light and find the focal plane. Switch to camera and fluorescence mode, remove the shutter from the laser to be used or select appropriate wavelength by the AOTF. After proper sample alignment by fluorescence imaging under low excitation conditions ( $< 0.1 \text{ kW cm}^{-2}$ ), reduce the area of the camera chip by software (binning) to accelerate data acquisition and reduce data volume.

### ? TROUBLESHOOTING

**12** Prepare the camera software to take a kinetic series of 4,000–100,000 frames dependent on the labeling density and complexity of the structure. We recommend starting with 5,000–10,000 frames and optimize the number by inspection of the quality of reconstructed *d*STORM images.

**13** Increase irradiation intensity to 5–30  $\text{kW cm}^{-2}$  for a few seconds to transfer the majority of fluorophores to the OFF state so that only a sparse subset of fluorophores resides in the ON state in each image (Fig. 3). For super-resolution imaging in living cells, use irradiation intensities of 0.5–5  $\text{kW cm}^{-2}$ . For fixed cells, higher irradiation intensities can be applied (e.g., up to 50  $\text{kW cm}^{-2}$ ) to increase photoswitching rates and frame rates up to 1 kHz.

**14** Reduce integration time so that one fluorophore is visible only for about one to four frames at a time. If necessary, adjust the focus to ensure that the spots show a symmetric PSF, indicating that they are in the focal plane. The camera gain can also be adjusted to yield a better signal-to-background ratio.

**15** Ensure an optimal fluorophore density (i.e., 0.05–1 fluorophore per  $\mu\text{m}^2$ ) (Fig. 3a). If fluorophore density is too low, use additional direct excitation of intermediate radical ions at 405 nm to activate fluorophores (typically, use 0.01–0.1 kW  $\text{cm}^{-2}$  at 405 nm). For cyanine fluorophores 488, 514 or 532 nm light can be used alternatively for activation. Sometimes the intensity of the activation laser has to be increased with proceeding acquisition time to activate a constant number of fluorophores (Fig. 5c). Ideally, the activation laser is used only in short pulses of a length of a few micro- to milliseconds to reduce autofluorescence, cell damage and photobleaching of fluorophores (Fig. 5d).

#### ? TROUBLESHOOTING

**16** Start data acquisition with a frame rate of 10–100 Hz.

#### Data analysis ● TIMING 0.1–10 min

**17** Estimate an amplitude threshold and a PSF covariance matrix from your data. A good estimate for the threshold is 15 times the background noise s.d. The covariance matrix can be estimated by fitting Gaussian functions to a number of visually well-separated spots and averaging their covariance matrices.

#### ? TROUBLESHOOTING

**18** To generate a super-resolved image bin localization, select a pixel size to determine the distance of bins and an intensity transfer function to determine the intensity assigned to a given number of localizations. A pixel size of 10–20 nm and a histogram normalization with a weight of 0.3 usually gives good results.

#### ? TROUBLESHOOTING

#### ? TROUBLESHOOTING

Troubleshooting advice can be found in Table 2.

**TABLE 2** | Troubleshooting table.

Step	Problem	Possible reason	Solution
1A(vi), 1B(iv)	High background fluorescence	Blocking missed/failed	Modify blocking protocol, always use fresh serum (e.g., BSA, NGS)
	High background in reconstructed images	Antibody or probe degraded	Use new freshly prepared antibodies or probes
		Fixation artifacts	Modify fixation protocol
		Permeabilization is too strong	Modify permeabilization protocol
		Blocking missed/failed	Modify blocking protocol, always use fresh serum (e.g., BSA, NGS)
	Low fluorescence intensity	pH is incompatible with antibody–antigen or probe binding	Check pH; pH should be in the range of 6–9
			Apply postfixation Step 6
1A(x), 1B(vii)	Cyanine fluorophores do not show reversible photoswitching	pH of buffer is too low	Check pH and increase to pH 7–9
		MEA concentration is too low	Increase MEA concentration up to 100 mM
		Oxygen was not efficiently removed	Use fresh oxygen scavenging system
7, 10	Lateral or axial drift	Immersion oil is contaminated	Remove immersion oil, clean objective and replace with fresh, clean immersion oil
			Dry all slices and Lab-Teks before imaging
			Discard or seal leaky Lab-Teks
	Spots appear dim	Integration time does not match $\tau_{\text{on}}$	Increase integration time

(continued)

## PROTOCOL

TABLE 2 | Troubleshooting table (continued).

Step	Problem	Possible reason	Solution
11	Spots appear elliptical	Electron multiplying is set too low Singlet state quenching by reducing agent	Apply higher irradiation intensity Change to highly inclined illumination Increase electron multiplying gain Decrease amount of reducing agent
	Transfected cells are hard to find	Lenses are misaligned	Decrease pH of the solvent Align optical components
	High background signal in live-cell experiments	Low transfection efficiency	Use a different cell line that guarantees higher transfection rates Use a different transfection reagent or use stable transfected cells
	Cellular structures appear blurred	Nonspecific adsorption of fluorophore substrates on cover glass Low density of cells High concentration of unbound substrate due to low transfection efficiency Leakage of substrate due to necrotic cells	Block surface by coating with glycine or trypsinize and transfer cells to new cover glass Increase cell density Improve transfection efficiency and use lower substrate concentration
	High background from other image planes	Lateral or axial sample drift	Image cells immediately after last washing step, reduce exposure time under nonphysiological conditions (e.g., room temperature); work quickly Verify sample drift using the calibration sample and realign focal plane Change immersion oil
	Fluorophores do not recover	Movement of target molecules in living cells Dense, three-dimensional structure	Increase irradiation intensity as much as possible to shorten total acquisition time and increase temporal resolution Check TIRF or highly inclined illumination
	High fluorophore density during <i>d</i> STORM acquisition	Fluorophores are switched off very efficiently Fluorophores are photobleached Enzymes in oxygen scavenger system are degraded Reducing agent is degraded pH of the solvent is too low/high Probes are degraded Fluorescent probes, e.g., antibodies, have a high degree of labeling (DOL)	Use activation laser (405 nm for rhodamine dye radicals, 488/514/532 nm for cyanines) Reduce intensity of readout laser Apply oxygen scavenger system Reduce excitation intensity Alternate activation and readout laser Use freshly prepared enzyme solution or frozen working aliquots Always use freshly prepared MEA solution or frozen working aliquots Check pH; pH should be in the range of 6–9 Use new antibodies/fluorophores Purchase antibodies with low DOL (~1) Label antibodies with lower DOL (~1) Increase irradiation intensity
		Too many fluorophores reside in their fluorescent ON state	

(continued)

TABLE 2 | Troubleshooting table (continued).

Step	Problem	Possible reason	Solution
	Fluorophore density too low during <i>d</i> STORM acquisition	The camera integration time is too long Label density is too low	Stop activation of fluorophores Use antibodies with lower DOL Reduce camera integration time to match $\tau_{on}$ Increase label density Activate more fluorophores by increasing the irradiation intensity at 405 nm (rhodamines) or 488/514/532 nm (cyanines)
17,18	Randomly scattered localizations all over the image Noncontinuous structures in reconstructed images in fixed cells Number of localizations is too small Structures in reconstructed image are biased or blurred, especially in crossing areas	Threshold level is too low Acquired image stack is too short Antibody is degraded Fixation artifacts Initial threshold is set too high Acquired frames do not contain enough fluorescent spots Label density of structures is too low Inappropriate thresholds <i>d</i> STORM imaging was done with inappropriate photoswitching rates	Increase threshold stepwise by 10% Increase the number of frames Use freshly prepared antibodies Repeat or modify fixation protocol Reduce initial threshold Increase activation irradiation intensity Repeat experiment with higher label density Increase asymmetry threshold Increase lower photon threshold and set/decrease upper photon threshold Perform imaging with enhanced photoswitching rates by tuning excitation and activation intensity and/or pH and reducing agent concentration Reduce label density

### ● TIMING

Step 1, Fluorescence labeling: starting with cell growth, transfection or fixation, approximately 2–3 d  
 Steps 2–10, Microscope setup: for experts, only a few minutes (but with less experience, it takes up to 1 h)  
 Steps 11–16, Data acquisition: 0.1–10 min, depending on the labeling density/complexity of the structure and photoswitching ratio (i.e., the applied irradiation intensity)  
 Steps 17 and 18, Data analysis: can theoretically be run in parallel on a standard PC. However, finding an optimal threshold can sometimes take a few minutes (0.1–10 min)

### ANTICIPATED RESULTS

**Figure 3** shows results anticipated when imaging  $\beta$ -tubulin in fixed cells with fluorescently labeled antibodies. The data presented underscore the importance of additional excitation of the radical anions at shorter wavelengths in order to control the number of fluorophores residing in the ON state and demonstrate exemplarily the influence of the number of localizations or frames used on the quality of the reconstructed *d*STORM image. Live-cell *d*STORM images of the core histone protein H2B in eukaryotic cell lines can be performed with TMP-tags<sup>52</sup> and SNAP-tags<sup>53</sup>, and some anticipated results are shown in **Figure 6**. The results demonstrate the importance of the efficient reduction of nonspecific binding of fluorophores to cellular structures and to the cover slip. Whereas the two SNAP-tags tested so far (SNAP-Cell 505 and SNAP-Cell TMR-Star) can be used successfully for *d*STORM in HeLa and COS-7 cells, other cell lines, such as mouse 3T3 and mouse C2C12 cells, show different behavior (i.e., specific labeling of nuclear structures is influenced by the fluorophore used)<sup>53</sup>.

## PROTOCOL

**ACKNOWLEDGMENTS** We gratefully acknowledge support from G. Wiebusch, B. Vogel, U. Endesfelder, T. Holm and S. Proppert. We thank V.W. Cornish and R. Wombacher for providing the TMP substrates and the H2B-eDHFR plasmid. This work was supported by the Biophotonics and the Systems Biology Initiative (FORSYS) of the German Ministry of Research and Education (BMBF).

**AUTHOR CONTRIBUTIONS** S.v.d.L., A.L., T.K., M. Heidbreder, S.W., M. Heilemann and M.S. conceived and designed the experiments; S.v.d.L., A.L., T.K., M. Heidbreder and S.W. performed the experiments; M. Heilemann and M.S. supervised the project; and M. Heilemann, S.v.d.L. and M.S. wrote the paper.

**COMPETING FINANCIAL INTERESTS** The authors declare no competing financial interests.

Published online at <http://www.natureprotocols.com/>.

Reprints and permissions information is available online at <http://www.nature.com/reprints/index.html>.

1. Abbe, E. Beiträge zur Theorie des Mikroskops und der mikroskopischen Wahrnehmung. *Arch. Mikrosk. Anat.* **9**, 413–487 (1873).
2. Born, M. & Wolf, E. *Principles of Optics: Electromagnetic Theory of Propagation, Interference and Diffraction of Light* (Cambridge University Press, 1997).
3. Betzig, E. & Trautman, J.K. Near-field optics: microscopy, spectroscopy, and surface modification beyond the diffraction limit. *Science* **257**, 189–195 (1992).
4. Hell, S. & Stelzer, E.H.K. Fundamental improvement of resolution with a 4Pi-confocal fluorescence microscope using two-photon excitation. *Opt. Commun.* **93**, 277–282 (1992).
5. Hell, S.W. & Wichmann, J. Breaking the diffraction resolution limit by stimulated emission: stimulated-emission-depletion fluorescence microscopy. *Opt. Lett.* **19**, 780–782 (1994).
6. Hell, S.W. Far-field optical nanoscopy. *Science* **316**, 1153–1158 (2007).
7. Gustafsson, M.G. Surpassing the lateral resolution limit by a factor of two using structured illumination microscopy. *J. Microsc.* **198**, 82–87 (2000).
8. Kner, P., Chhun, B.B., Griffis, E.R., Winoto, L. & Gustafsson, M.G. Super-resolution video microscopy of live cells by structured illumination. *Nat. Methods* **6**, 339–342 (2009).
9. Bobroff, N. Position measurement with a resolution and noise limited instrument. *Rev. Sci. Instrum.* **57**, 1152–1157 (1986).
10. Betzig, E. Proposed method for molecular optical imaging. *Opt. Lett.* **20**, 237–239 (1995).
11. Bornfleth, H., Sätzler, K., Eils, R. & Cremer, C. High-precision distance measurements and volume-conserving segmentation of objects near and below the resolution limit in three-dimensional confocal fluorescence microscopy. *J. Microsc.* **189**, 118–136 (1998).
12. Lacoste, Th.D. *et al.* Ultrahigh-resolution multicolour colocalization of single fluorescent probes. *Proc. Natl Acad. Sci. USA* **97**, 9461–9466 (2000).
13. Heilemann, M. *et al.* High-resolution colocalization of single dye molecules by fluorescence lifetime imaging microscopy. *Anal. Chem.* **74**, 3511–3517 (2002).
14. Thompson, R.E., Larson, D.R. & Webb, W.W. Precise nanometer localization analysis for individual fluorescent probes. *Biophys. J.* **82**, 2775–2783 (2002).
15. Yildiz, A. *et al.* Myosin V walks hand-over-hand: single fluorophore imaging with 1.5-nm localization. *Science* **300**, 2061–2065 (2003).
16. Qu, X., Wu, D., Mets, L. & Scherer, N.F. Nanometer-localized multiple single-molecule fluorescence microscopy. *Proc. Natl Acad. Sci. USA* **101**, 11298–11303 (2004).
17. Lidke, K.A., Rieger, B., Jovin, T.M. & Heintzmann, R. Superresolution by localization of quantum dots using blinking statistics. *Opt. Exp.* **13**, 7052–7062 (2005).
18. Betzig, E. *et al.* Imaging intracellular fluorescent proteins at nanometer resolution. *Science* **313**, 1642–1645 (2006).
19. Hess, S.T., Girirajan, T.P. & Mason, M.D. Ultra-high resolution imaging by fluorescence photoactivation localization microscopy. *Biophys. J.* **91**, 4258–4272 (2006).
20. Rust, M.J., Bates, B. & Zhuang, X. Sub-diffraction-limit imaging by stochastic optical reconstruction microscopy (STORM). *Nat. Methods* **3**, 793–795 (2006).
21. Heilemann, M. *et al.* Subdiffraction-resolution fluorescence imaging with conventional fluorescent probes. *Angew. Chem. Int. Ed.* **47**, 6172–6176 (2008).
22. Heilemann, M., van de Linde, S., Mukherjee, A. & Sauer, M. Super-resolution imaging with small organic fluorophores. *Angew. Chem. Int. Ed.* **48**, 6903–6908 (2009).
23. Lemmer, P. *et al.* SPDM: light microscopy with single-molecule resolution at the nanoscale. *Appl. Phys. B* **93**, 1–12 (2008).
24. Baddeley, D. *et al.* Light-induced dark states of organic fluochromes enable 30 nm resolution imaging in standard media. *Biophys. J.* **96**, L22–L24 (2009).
25. Gunkel, M. *et al.* Dual color localization microscopy of cellular nanostructures. *Biotechnol. J.* **4**, 927–938 (2009).
26. Fölling, J. *et al.* Fluorescence nanoscopy by ground-state depletion and single-molecule return. *Nat. Methods* **5**, 943–945 (2008).
27. Steinhauer, C., Forthmann, C., Vogelsang, J. & Tinnefeld, P. Superresolution microscopy on the basis of engineered dark states. *J. Am. Chem. Soc.* **130**, 16840–16841 (2008).
28. Vogelsang, J., Cordes, T., Forthmann, C., Steinhauer, C. & Tinnefeld, P. Controlling the fluorescence of ordinary oxazine dyes for single-molecule switching and superresolution microscopy. *Proc. Natl Acad. Sci. USA* **106**, 8107–8112 (2009).
29. Dertinger, T., Colyer, R., Iyer, G., Weiss, S. & Enderlein, J. Fast background-free 3D superresolution optical fluctuation imaging (SOFI). *Proc. Natl Acad. Sci. USA* **106**, 22287–22292 (2009).
30. Dertinger, T., Heilemann, M., Vogel, R., Sauer, M. & Weiss, S. Super-resolution optical fluctuation imaging with organic dyes. *Angew. Chem. Int. Ed.* **49**, 9441–9443 (2010).
31. Flors, C. *et al.* A stroboscopic approach for fast photoactivation-localization microscopy with dronpa mutants. *J. Am. Chem. Soc.* **129**, 13970–13977 (2007).
32. Flors, C., Ravarani, C.N. & Dryden, D.T. Super-resolution imaging of DNA labeled with intercalating dyes. *Chemphyschem* **10**, 2201–2204 (2009).
33. Gould, T.J., Verkushava, V.V. & Hess, S.T. Imaging biological structures with fluorescence photoactivation localization microscopy. *Nat. Protoc.* **4**, 291–308 (2009).
34. Shroff, H., White, H. & Betzig, E. Photoactivation localization microscopy (PALM) of adhesion complexes. *Curr. Protoc. Cell Biol.* **41**, 4.21.1–4.21.27 (2008).
35. Ji, N., Shroff, H., Zhong, H. & Betzig, E. Advances in the speed and resolution of light microscopy. *Curr. Opin. Neurobiol.* **18**, 605–616 (2008).
36. Hell, S.W. Microscopy and its focal switch. *Nat. Methods* **6**, 24–32 (2009).
37. Huang, B., Bates, M. & Zhuang, X. Super-resolution fluorescence microscopy. *Annu. Rev. Biochem.* **78**, 993–1016 (2009).
38. Heilemann, M. Fluorescence microscopy beyond the diffraction limit. *J. Biotechnol.* **149**, 243–251 (2010).
39. Lippincott-Schwartz, J. & Patterson, G.H. Fluorescent proteins: a cell biologist's user guide. *Methods Cell Biol.* **85**, 45–61 (2008).
40. Shroff, H., Galbraith, C.G., Galbraith, J.A. & Betzig, E. Live-cell photoactivated localization microscopy of nanoscale adhesion dynamics. *Nat. Methods* **5**, 417–423 (2008).
41. Manley, S. *et al.* High-density mapping of single-molecule trajectories with photoactivated localization microscopy. *Nat. Methods* **5**, 155–157 (2008).
42. Ormo, M. *et al.* Crystal structure of the Aequorea Victoria green fluorescent protein. *Science* **273**, 1392–1395 (1996).
43. Shannon, C.E. Communication in the presence of noise. *Proc. Inst. Radio Eng.* **37**, 10–21 (1949).
44. Shaner, N.C. Improving the photostability of bright monomeric orange and red fluorescent proteins. *Nat. Methods* **5**, 545–551 (2008).
45. Tang, J., Akerboom, J., Vaziri, A., Looger, L.L. & Shank, S.V. Near-isotropic 3D optical nanoscopy with photon-limited chromophores. *Proc. Natl Acad. Sci. USA* **107**, 10068–10073 (2010).
46. van de Linde, S., Sauer, M. & Heilemann, M. Subdiffraction-resolution fluorescence imaging of proteins in the inner mitochondrial membrane with photoswitchable fluorophores. *J. Struct. Biol.* **164**, 250–254 (2008).
47. van de Linde, S., Kasper, R., Heilemann, M. & Sauer, M. Photoswitching microscopy with standard fluorophores. *Appl. Phys. B* **93**, 725–731 (2008).
48. Heilemann, M., Dedecker, P., Hofkens, J. & Sauer, M. Photoswitches: key molecules for subdiffraction-resolution fluorescence imaging and molecular quantification. *Laser Photon. Rev.* **3**, 180–202 (2009).
49. van de Linde, S. *et al.* Multicolor photoswitching microscopy for subdiffraction-resolution fluorescence imaging. *Photochem. Photobiol. Sci.* **8**, 465–469 (2009).
50. Owen, D.M. *et al.* PALM imaging and cluster analysis of protein heterogeneity at the cell surface. *J. Biophotonics* **3**, 446–454 (2009).
51. Endesfelder, U., van de Linde, S., Wolter, S., Sauer, M. & Heilemann, M. Subdiffraction-resolution fluorescence microscopy of myosin-actin motility. *Chemphyschem* **11**, 836–840 (2010).
52. Wombacher, R. *et al.* Live cell super-resolution imaging with trimethoprim conjugates. *Nat. Methods* **7**, 717–719 (2010).
53. Klein, T. *et al.* Live-cell dSTORM with SNAP-tag fusion proteins. *Nat. Methods* **8**, 7–9 (2011).

54. Wolter, S. *et al.* Real-time computation of subdiffraction-resolution fluorescence images. *J. Microsc.* **237**, 12–22 (2010).
55. Beaumont, P.C., Johnson, D.G. & Parsons, B.J. Excited state and free radical properties of rhodamine dyes in aqueous solution: a laser flash photolysis and pulse radiolysis study. *J. Photochem. Photobiol.* **107**, 175–183 (1997).
56. Doose, S., Neuweiler, H. & Sauer, M. Fluorescence quenching by photoinduced electron transfer: a reporter for conformational dynamics of macromolecules. *Chemphyschem* **10**, 1389–1398 (2009).
57. Görner, H. Oxygen uptake induced by electron transfer from donors to the triplet state of methylene blue and xanthene dyes in air-saturated aqueous solution. *Photochem. Photobiol. Sci.* **7**, 371–376 (2008).
58. Burner, U., Jantschko, W. & Obinger, C. Kinetics of oxidation of aliphatic and aromatic thiols by myeloperoxidase compounds I and II. *FEBS Lett.* **443**, 290–296 (1999).
59. Burner, U. & Obinger, C. Transient-state and steady-state kinetics of the oxidation of aliphatic and aromatic thiols by horseradish peroxidase. *FEBS Lett.* **411**, 269–274 (1997).
60. Madej, E. & Wardman, P. The oxidizing power of the glutathione thiyl radical as measured by its electrode potential at physiological pH. *Arch. Biochem. Biophys.* **462**, 94–102 (2007).
61. Wardmann, P. Reduction potentials of one-electron couples involving free radicals in aqueous solution. *J. Phys. Chem. Ref. Data* **18**, 1637–1755 (1989).
62. van de Linde, S. *et al.* Photoinduced formation of reversible dye radicals and their impact on super-resolution imaging. *Photochem. Photobiol. Sci.* **10**, 499–506 (2011).
63. Michaelis, L., Schubert, M.P. & Granick, S. Semiquinone radicals of thiazines. *J. Am. Chem. Soc.* **62**, 204–211 (1940).
64. Heineken, F.W., Bruin, M. & Bruin, F. ESR investigation of some thiazine and oxazine dye radicals. *J. Chem. Phys.* **37**, 1479–1482 (1962).
65. Kottke, T., van de Linde, S., Sauer, M., Kakorin, S. & Heilemann, M. Identification of the product of photoswitching of an oxazine fluorophore using FT-IR difference spectroscopy. *J. Phys. Chem. Lett.* **1**, 3156–3159 (2010).
66. Sies, H. Glutathione and its role in cellular functions. *Free Radic. Biol. Med.* **27**, 916–921 (1999).
67. Benesch, R.E. & Benesch, R. Enzymatic removal of oxygen for polarography and related methods. *Science* **118**, 447–448 (1953).
68. Rasnik, I., McKinney, S.A. & Ha, T. Nonblinking and long-lasting single-molecule fluorescence imaging. *Nat. Methods* **3**, 891–893 (2006).
69. Lenhard, J.R. & Cameron, A.D. Electrochemistry and electronic spectra of cyanine dye radicals in acetonitrile. *J. Phys. Chem.* **97**, 4916–4925 (1993).
70. Dempsey, G.T. *et al.* Photoswitching mechanism of cyanine dyes. *J. Am. Chem. Soc.* **131**, 18192–18193 (2009).
71. Lord, S.J. *et al.* A photoactivatable push-pull fluorophore for single-molecule imaging in live cells. *J. Am. Chem. Soc.* **130**, 9204–9205 (2008).
72. Lee, H.D. *et al.* Superresolution imaging of targeted proteins in fixed and living cells using photoactivatable organic fluorophores. *J. Am. Chem. Soc.* **132**, 15099–15101 (2010).
73. Fölling, J. *et al.* Photochromic rhodamines provide nanoscopy with optical sectioning. *Angew. Chem. Int. Ed.* **46**, 6266–6270 (2007).
74. Bossi, M. *et al.* Multicolor far-field fluorescence nanoscopy through isolated detection of distinct molecular species. *Nano Lett.* **8**, 2463–2468 (2008).
75. van de Linde, S., Wolter, S., Heilemann, M. & Sauer, M. The effect of photoswitching kinetics and labeling densities on super-resolution fluorescence imaging. *J. Biotechnol.* **149**, 260–266 (2010).
76. Cordes, T. *et al.* Resolving single-molecule assembled patterns with superresolution blink-microscopy. *Nano Lett.* **10**, 645–651 (2010).
77. Vogelsang, J. *et al.* Make them blink: probes for super-resolution microscopy. *Chemphyschem* **11**, 2475–2490 (2010).
78. Tokunaga, M., Imamoto, N. & Sakata-Sogawa, K. Highly inclined thin illumination enables clear single-molecule imaging in cells. *Nat. Methods* **5**, 159–161 (2008).
79. Pavani, S.R. *et al.* Three-dimensional, single-molecule fluorescence imaging beyond the diffraction limit by using a double-helix point spread function. *Proc. Natl Acad. Sci. USA* **106**, 2995–2999 (2009).
80. Shtengel, G. *et al.* Interferometric fluorescent super-resolution microscopy resolves 3D cellular ultrastructure. *Proc. Natl Acad. Sci. USA* **106**, 3125–3130 (2009).
81. Juette, M.F. *et al.* Three-dimensional sub-100 nm resolution fluorescence microscopy of thick samples. *Nat. Methods* **5**, 527–529 (2008).
82. Huang, B., Wang, W.Q., Bates, M. & Zhuang, X.W. Three-dimensional super-resolution imaging by stochastic optical reconstruction microscopy. *Science* **319**, 810–813 (2008).
83. Neuback, A. & van Gool, L. Efficient non-maximum suppression. in *ICPR '06: Proceedings of the 18th International Conference on Pattern Recognition*. Hong Kong, pp 850–855 (IEEE Computer Society, 2006).
84. Galassi, M. *et al.* *Gnu Scientific Library: Reference Manual* (Network Theory, 2003).
85. Yaroslavsky, L.P. *Digital Picture Processing*. (Springer, 1985).
86. Thomann, D., Dorn, J., Sorger, P.K. & Danuser, G. Automatic fluorescent tag localization II: improvement in super-resolution by relative tracking. *J. Microsc.* **211**, 230–248 (2003).
87. Hess, S.T. *et al.* Dynamic clustered distribution of hemagglutinin resolved at 40 nm in living cell membranes discriminates between raft theories. *Proc. Natl Acad. Sci. USA* **104**, 17370–17375 (2007).
88. Zhang, J., Campbell, R.E., Ting, A.Y. & Tsien, R.Y. Creating new fluorescent probes for cell biology. *Nat. Rev. Mol. Cell Biol.* **3**, 906–918 (2002).
89. Lippincott-Schwartz, J. & Patterson, G.H. Development and use of fluorescent protein markers in living cells. *Science* **300**, 87–91 (2003).
90. Miyawaki, A., Sawano, A. & Kogure, T. Lighting up cells: labelling proteins with fluorophores. *Nat. Cell Biol.* **5**, S1–S7 (2003).
91. Riedl, J. *et al.* Lifeact: a versatile marker to visualize F-actin. *Nat. Methods* **5**, 605–607 (2008).
92. Griffin, B.A., Adams, S.R. & Tsien, R.Y. Specific covalent labeling of recombinant protein molecules inside live cells. *Science* **281**, 269–272 (1998).
93. Keppler, A. *et al.* A general method for the covalent labeling of fusion proteins with small molecules *in vivo*. *Nat. Biotechnol.* **21**, 86–89 (2003).
94. Keppler, A., Pick, H., Arrivoli, C., Vogel, H. & Johnsson, K. Labelling of fusion proteins with synthetic fluorophores in live cells. *Proc. Natl Acad. Sci. USA* **101**, 9955–9959 (2004).
95. Los, G.V. *et al.* HaloTag: a novel protein labeling technology for cell imaging and protein analysis. *ACS Chem. Biol.* **3**, 373–382 (2008).
96. Miller, L.W. & Cornish, V.W. Selective chemical labeling of proteins in living cells. *Curr. Opin. Chem. Biol.* **9**, 56–61 (2005).
97. Miller, L.W., Cai, Y., Sheetz, M.P. & Cornish, V.W. *In vivo* protein labelling with trimethoprim conjugates: a flexible chemical tag. *Nat. Methods* **2**, 255–257 (2005).
98. Gallagher, S. *et al.* An *in vivo* covalent TMP-tag based on proximity-induced reactivity. *ACS Chem. Biol.* **7**, 547–556 (2009).
99. Michalet, X. *et al.* Quantum dots for live cells, *in vivo* imaging, and diagnostics. *Science* **307**, 538–544 (2005).
100. Robinson, R.W. & Snyder, J.A. An innovative fixative for cytoskeletal components allows high resolution in colocalization studies using immunofluorescence techniques. *Histochem. Cell. Biol.* **122**, 1–5 (2004).
101. Vogelsang, J. *et al.* A reducing and oxidizing system minimizes photobleaching and blinking of fluorescent dyes. *Angew. Chem. Int. Ed.* **47**, 5465–5469 (2008).

# Localisation Microscopy Immunolabelling Guide

## Aim of guide –

The intention is to highlight additional labelling considerations for localisation microscopy (dSTORM/STORM/GSDIM) and how they affect super-resolution image quality. Many of the principles also apply to other affinity binding approaches such as fluorescent ligand-receptor reagents, e.g. EGF-EGFR, and phalloidin staining of actin. For the sake of brevity, this guide will refer to STORM and antibodies, although most of the guide should be applicable to other localisation microscopy and immunolabelling and affinity binding approaches. The final page contains some references to published protocols. This list is not comprehensive and is intended to be a starting point from which to work. These protocols will not necessarily be ideal for your experimental systems.

This guide assumes that you are already familiar with fluorescence microscopy and immunolabelling approaches. STORM imaging requires high contrast bright fluorophore signal against a minimal background. The better this contrast, the better the resolution. So whilst autofluorescence is still a problem it will not manifest itself directly in the final image. Non-specific labelling, i.e. where there is antibody-fluorophore bound to the sample, but not specifically to the epitope, will still be imaged by STORM. Image filtering based on intensity and or noise may not be a good way to remove this signal as specific labelling at high resolution will also be removed.

Fixation, Permeabilisation, Quenching & Blocking	2
Label Size	3
Labelling Density	4-6
Fluorophore Choice	7
Protocol References	8

# Fixation, Permeabilisation, Quenching & Blocking

## Fixation

Some antibodies only bind when their target epitope has been fixed with particular protocols. Some fixation protocols can cause autofluorescence or other artefacts. Also, fixation can cause some types of fine cellular substructural details to be lost, for example fine tubules. These sorts of fine structures are more easily resolvable with STORM, so this may need to be considered when interpreting images.

## Permeabilisation

Required for disrupting membranes which allows antibody access to internal cellular structures. Therefore permeabilisation may affect high resolution membrane imaging results, if for example you have used lipid or integral membrane labelling approaches.

## Quenching

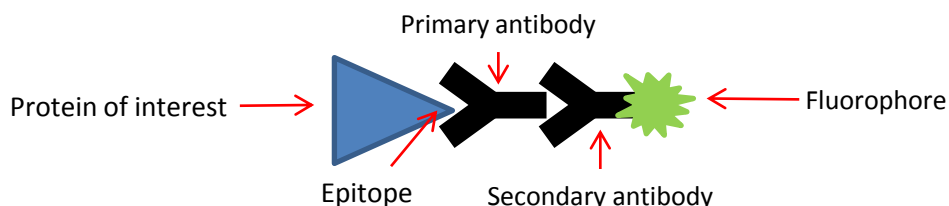
Reduces autofluorescence in the sample leading to improved contrast. This may help to increase the number of localisations and the resolution in resulting super-resolution images.

## Blocking

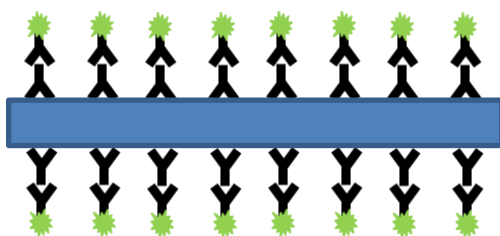
Reduces the amount of non-specific binding of the antibody to the sample. Antibodies should only be bound to their specific epitopes; however, it is possible for lower affinity non-specific binding to occur. This will usually be a relatively low abundance compared with specific labelling; however, it will be imaged by STORM with high resolution. This may be more of an issue in STORM images as low density areas are usually displayed with relatively high contrast compared with traditional fluorescence imaging techniques.

## Label Size

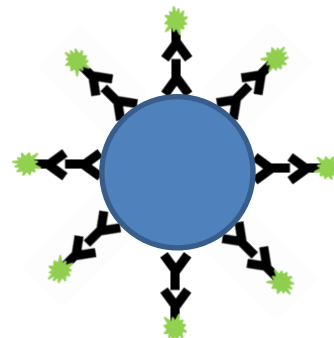
Effective resolution can be improved by reducing the distance between the epitope and the fluorophore. As much as 20 nm of distance can be introduced when using primary and secondary antibody approaches:



With a diffraction-limited resolution of 200 nm this labelling distance may only comprise 10% of the observed “blurring” whereas with localisation microscopy techniques providing up to 20 nm resolution, this becomes far more significant. Labelling distance should be considered when planning experiments and then analysing and interpreting super-resolution images. It may be worth considering approaches that reduced label size such as directly conjugating fluorophore to the primary antibody. Alternatives to traditional antibody labelling include, Fab fragments, nanobodies, aptamers and genetically encoded tags such as SNAP and HaLo.



This filament with a diameter of 10 nm and 15 nm additional labelling distance would end up with an apparent diameter of 40 nm



This vesicle with a diameter of 50 nm and 15 nm additional labelling distance would end up with an apparent diameter of 80 nm

## Labelling Density

### Incubation times

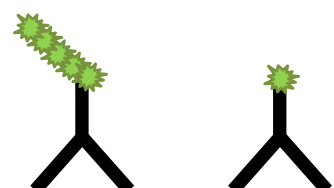
Typical incubation times are 30 to 60 minutes at room temperature. Longer incubation times will increase the chances of both specific and non-specific binding. High affinity specific binding (to the protein of interest) will occur more quickly than low affinity non-specific binding (to other cell structures and the cover glass). Optimum incubation times may vary, depending on the antibody and labelling conditions, such as blocking.

### Antibody concentration

Normally the aim should be to use a concentration of antibody that just saturates the available binding sites, i.e. all of the proteins of interest in the sample get tagged with antibody. The resulting super-resolution image will hopefully then report on the positions of a sufficient number of these molecules to be representative. Increasing the concentration beyond saturating is likely to lead to non-specific binding, which should be avoided. Therefore it is recommended to do titrations of antibody concentrations. Commercial secondary antibodies should normally be used in a range of 1:500 to 1:1000 dilution. Polyclonal antibodies will usually lead to higher specific labelling densities than monoclonals. They may also be more prone to non-specific labelling artefacts.

### Degree of labelling

Commercial fluorescent reagents, such as secondary antibodies, usually have more than 1 fluorophore molecule per antibody. Typically they are conjugated so that there are 3-8 fluorophore molecules per antibody. This information can usually be found on the product tube or data sheet and may be expressed as DoL or as moles. Ideally for localisation microscopy this ratio should be 1:1. There are a number of protocols and references which describe how to perform custom fluorophore-antibody conjugations.

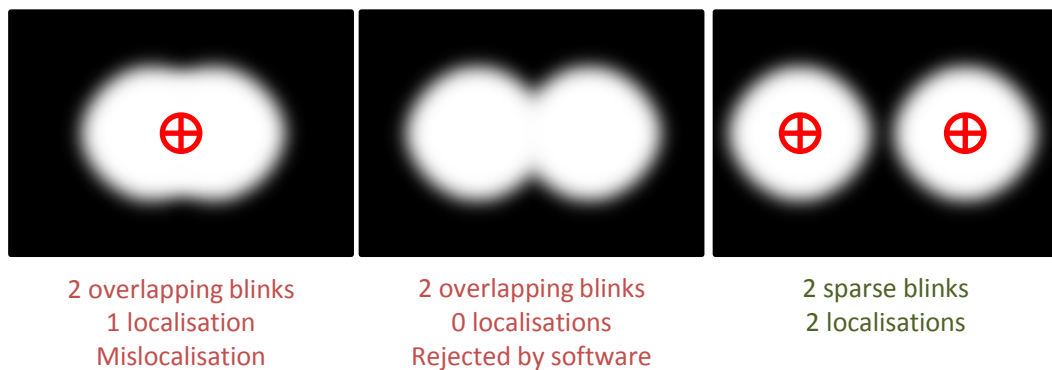


Left: DoL of 5 (5 dyes per antibody)

Right: DoL of 1 (1 dye per antibody)

## Blinking density (high density problem)

When performing localisation microscopy with an algorithm that is fitting single molecule positions, only one fluorophore molecule should be “switched on” within a diffraction limited area in a given frame. In other words, there should be 200-300 nm space between neighbouring simultaneous “blinks”. The more dense the number of fluorophore molecules the higher the chance there is of having overlapping blinks (non-sparse) data. Possible outcomes where there are 2 simultaneous blinks in close proximity when using a single fitting algorithm:



### The density of the fluorophore molecules is dependent on:

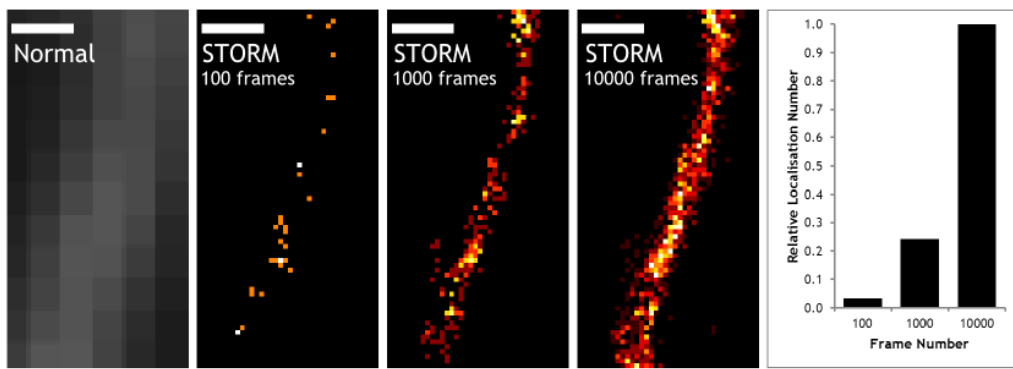
- Labelling saturation (proportion of molecules of interest bound with antibody) - Ideally saturated unless the underlying structure is very dense. Reducing incubation times, label concentration or mixing with unlabelled antibodies may help to reduce density.
- Density of underlying structure of interest - If it is very dense it may be necessary to use a sub-saturating labelling strategy
- Degree of labelling (fluorophore-antibody ratio) - Ideally 1

### The probability of an overlapping blink is dependent on:

- The density of the fluorophore molecules (see above)
- The buffer conditions (fluorophore environment)
- The acquisition settings (eg. exposure time)
- Illumination conditions (eg. laser power, illumination angle)
- The fluorophore (different fluorophores have different chemistries)

## Sparse labelling (low density problem)

The fluorescent labelling density must be at least twice the intended resolution of the image, ie. similar to the localisation precision. For example if you are imaging a structure with 40 nm lateral resolution (approximately 20 nm localisation precision) you will need a label spacing of 20 nm or less. If the labelling density is lower than this the resulting images will appear “pointillist” (punctate):



▲ Fluorescently labelled actin filament (Phalloidin-Alexa 647). Scale bars are 200 nm. STORM pixel size is 15 nm. Normal pixel size is 100 nm. Graph and STORM images show effect of increasing frame number used to reconstruct final image.

Low density labelling (sub-saturating concentrations) may occur if the antibody concentrations is too low, the incubation time is too short, inappropriate fixation conditions are used that destroy the epitope or if the epitope on the protein of interest is masked by other proteins.

In addition to sample preparation problems, pointillist (punctate) images can also be a result of problems with:

- Dye choice - poor characteristics for STORM
- Buffer conditions – wrong buffer choice or problem with buffer
- Illumination conditions (laser power and illumination angle)
- Camera settings (exposure time, frame number)
- Image reconstruction – inappropriate algorithm settings and thresholds
- Visualising the data with a scatter plot method or very small pixels

# Fluorophore Choice

## Fluorophore selection

In practise the behaviour of the fluorophores depends on the illumination conditions and the chemical environment, ie. buffer. The optimum conditions may vary between fluorophores. Characteristics to consider include:

- Brightness – the more photons emitted per fluorophore “blink” the better the resolution.
- Duty cycle – the proportion of time a fluorophore spends in the “on” state. Therefore on dense samples it is necessary to have as low a number as possible to ensure sparse, non-overlapping blinks. On low density samples this can be higher. In other words, the duty cycle number determines the maximum sample labelling density before overlapping blinks become a consideration.

## Example photoswitchable dye combinations

Far red - Cy5 or Alexa 647

Red - Alexa 555 or Alexa 568 or Cy3B

Green - Atto 488

All of these fluorophores photoswitch in standard oxygen scavenging buffers, such as glucose oxidase with 100 mM MEA. They can all be illuminated with an appropriate single laser line which can create the blinking signal required for STORM, for example Alexa 568 with a 561 nm laser. The best resolutions have been achieved with Cy5 and Alexa 647. Green dyes tend not to perform as well as red and far red dyes. Other fluorophore combinations are possible, however, they may not offer the same resolution or work in the same buffer conditions.

*For more details on photoswitchable dye performance see Dempsey et al., Nature Methods, 2012.*

*In addition to using reversibly switchable dyes (as above) it's also possible to use probes (dyes and fluorescent proteins) which can be activated and inactivated using photoactivation strategies of illuminating with 2 or more wavelengths of light to generate sparse blinking signals.*

## References

### Dyes, fluorescent proteins & photochemistry

Dempsey, Vaughan, Chen, Bates, Zhuang, Evaluation of fluorophores for optimal performance in localization-based super-resolution imaging, *Nature Methods*, 2012, [doi:10.1038/nmeth.1768](https://doi.org/10.1038/nmeth.1768)

Van de Linde, Loschberger, Klein, Heibreder, Wolter, Heilemann, Sauer, Direct stochastic optical reconstruction microscopy with fluorescent probes, *Nature Protocols*, 2011, [doi:10.1038/nprot.2011.336](https://doi.org/10.1038/nprot.2011.336)

Bates, Dempsey, Chen, Zhuang, Multicolor Super-Resolution Fluorescence imaging via Multi-Parameter Fluorophore Detection, *Chem Phys Chem*, 2011, [doi:10.1002/cphc.201100735](https://doi.org/10.1002/cphc.201100735)

Folling, Bossi, Bock, Medda, Wurm, Hein, Jakobs, Eggeling, Hell, Fluorescence nanoscopy by ground-state depletion and single-molecule return, *Nature Methods*, 2008, [doi:10.1038/nmeth.1257](https://doi.org/10.1038/nmeth.1257)

### Alternative labelling strategies

Dellagiacoma, Lukinavicius, Bocchio, Banala, Geissbuhler, Marki, Johnsson, Lasser, Targeted Photoswitchable Probe for Nanoscopy of Biological Structures, *Chem Bio Chem*, 2010, [doi:10.1002/cbic.201000189](https://doi.org/10.1002/cbic.201000189)

Lee, Lord, Iwanaga, Zhan, Xie, Williams, Wang, Bowman, Goley, Shapiro, Twieg, Rao, Moerner, Superresolution Imaging of Targeted Proteins in Fixed and Living Cells Using Photoactivatable Organic Fluorophores, *Journal of the American Chemical Society*, 2010, [doi:10.1021/ja1044192](https://doi.org/10.1021/ja1044192)

Ries, Kaplan, Platonova, Eghlidi, Ewers, A simple, versatile method for GFP-based- super-resolution microscopy via nanobodies, *Nature Methods*, 2012, [doi:10.1038/nmeth.1991](https://doi.org/10.1038/nmeth.1991)

Opazo, Levy, Byrom, Schafer, Geisler, Groemer, Ellington, Rizzoli, Aptamers as potential tools for super-resolution microscopy, *Nature Methods*, 2012, [doi:10.1038/nmeth.2179](https://doi.org/10.1038/nmeth.2179)

*This list is intended to provide some examples of labelling strategies and is not intended to be comprehensive.*

# A simple, versatile method for GFP-based super-resolution microscopy via nanobodies

Jonas Ries, Charlotte Kaplan, Evgenia Platonova, Hadi Eghlidi & Helge Ewers

**We developed a method to use any GFP-tagged construct in single-molecule super-resolution microscopy. By targeting GFP with small, high-affinity antibodies coupled to organic dyes, we achieved nanometer spatial resolution and minimal linkage error when analyzing microtubules, living neurons and yeast cells. We show that in combination with libraries encoding GFP-tagged proteins, virtually any known protein can immediately be used in super-resolution microscopy and that simplified labeling schemes allow high-throughput super-resolution imaging.**

The single-molecule localization-based super-resolution imaging techniques such as photoactivated localization microscopy (PALM) and stochastic optical reconstruction microscopy<sup>1–4</sup> (here referred to as ‘single-molecule nanoscopy’) require specific and efficient delivery of bright fluorophores into close proximity of the target structure without adding substantial background. Present labeling techniques usually involve a tradeoff between these properties. Bright organic dyes can be delivered via antibodies, but their large size displaces the dye from the target in a ‘linkage error’ of ~10 nm, and highly specific antibodies are available only for some proteins. Methods based on photoactivatable fluorescent proteins or enzymatic labeling schemes demand the generation of new fusion constructs, which should be characterized and may not be functional.

We demonstrate a simple, efficient and versatile method that optimizes several labeling parameters and can be used with any of the thousands of functionally tested GFP constructs available. We used very small and high-affinity camelid antibodies (nanobodies) to GFP<sup>5</sup> to deliver bright organic fluorophores to GFP-tagged proteins for use in single-molecule nanoscopy.

Organic dyes are conventionally delivered to target structures via antibodies, which are ~150 kDa, ~10 nm in size and of varying affinity. In contrast, the 13-kDa anti-GFP nanobodies are smaller (1.5 nm × 2.5 nm) and have a high affinity for GFP (0.59 nM; ref. 5; **Supplementary Fig. 1**) and several of its

isoforms. Nanobody-mediated targeting of organic dyes to GFP-fusion constructs would combine the molecular specificity of genetic tagging with the high photon yield of organic dyes and minimal linkage error.

We covalently coupled anti-GFP nanobodies to Alexa Fluor 647 (AF647) and added them to MDCK cells expressing GFP anchored via glycosylphosphatidylinositol to the plasma membrane (GPI-GFP). The nanobodies bound to transfected cells readily at low concentrations but did not bind to untransfected cells (**Supplementary Fig. 1**). Labeled nanobodies exhibited highly specific and saturable binding at about 0.6 nanobodies per GFP (Online Methods).

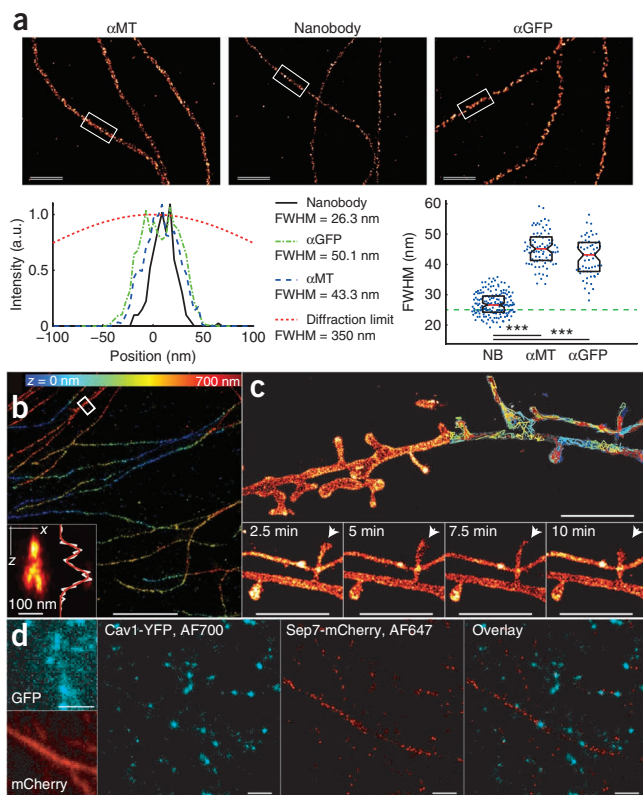
Under specific buffer conditions, many organic dyes become photoswitchable<sup>6,7</sup>. This fact is the basis for several single-molecule nanoscopy approaches<sup>2–4</sup>. To compare the nanobody-based approach to established methods, we labeled microtubules in fixed Ptk2 cells that stably expressed tubulin-YFP with AF647-anti-GFP nanobodies and imaged these cells by single-molecule nanoscopy. Individual microtubules were densely labeled with a full-width half maximum (FWHM) of 26.9 nm ± 3.7 nm (s.d.) (**Fig. 1a**), compatible with a microtubule diameter of 25 nm. This was significantly less (**Fig. 1a**) than what we achieved in parallel experiments using AF647-coupled secondary antibodies to detect microtubules either via anti-GFP (42.7 nm ± 7.0 nm) or anti-tubulin (45.6 nm ± 5.8 nm) antibodies, suggesting that the use of nanobodies led to minimal linkage error.

We next used the bright AF647-anti-GFP nanobodies for three-dimensional single-molecule nanoscopy with the bi-plane method<sup>8</sup>, which requires thousands of detected photons for good axial resolution. Nanobody-mediated labeling of microtubules in Ptk2 cells allowed us to resolve crossing microtubules with an axial separation of ~100 nm (**Fig. 1b**).

The use of bright labels not only increased localization precision (statistics in **Supplementary Fig. 2**), but also allowed the high frame rates required for imaging dynamic (live) samples. To realize this advantage, we transiently expressed GPI-GFP in primary hippocampal rat neurons and detected it via AF647-anti-GFP nanobodies. Single-particle tracking PALM (sptPALM)<sup>9</sup> allowed us to follow the trajectories of hundreds of molecules in the neuronal plasma membrane. We assembled a time series of super-resolution images and detected dynamic changes in the neuronal morphology over time (**Fig. 1c**).

Next, we used nanobodies for dual-color imaging. We realized this approach by using anti-GFP nanobodies labeled with Alexa Fluor 700 (AF700) and anti-RFP nanobodies (that also recognize monomeric (m)Cherry) labeled with AF647. We then labeled CV-1 cells expressing Septin7-mCherry and Caveolin1-YFP with these labels and could image both structures with high resolution and specificity (**Fig. 1d**).

**Figure 1 | Single-molecule nanoscopy by detection of GFP via nanobodies.** (a) Reconstructed super-resolution images obtained using different labeling strategies for microtubules in fixed Ptk2 cells stably expressing tubulin-YFP.  $\alpha$ MT, mouse anti-tubulin antibody plus secondary anti-mouse antibody labeled with AF647; nanobody, anti-GFP nanobody labeled with AF647; and  $\alpha$ GFP, mouse anti-GFP antibody plus secondary anti-mouse antibody labeled with AF647. Intensity profiles of microtubules were calculated from regions as indicated in the reconstructed super-resolution images, and the FWHM was determined by fitting with a Gaussian. Measured FWHM of microtubules from at least 60 line segments and three samples per labeling method. Boxes denote median values  $\pm$  quartiles, (\*\*\*, NB versus MT:  $P = 3.8 \times 10^{-52}$ ; and NB versus GFP:  $P = 2.7 \times 10^{-25}$ ; Mann-Whitney-test). Green dashed line indicates microtubule diameter. (b) Three-dimensional single-molecule nanoscopy of microtubules labeled with AF647-anti-GFP nanobodies. Inset, reconstructed  $x$ - $z$  image and  $z$  profile of a microtubule bundle denoted by the box. Distance between the peaks was 110 nm. FWHM of the top peak was 87 nm. (c) Live-cell super-resolution microscopy of cultured hippocampal neurons expressing GPI-GFP, labeled with AF647-anti-GFP nanobodies. Overlaid on the cumulative super-resolution image are single-molecule tracks obtained with sptPALM. Individual frames from super-resolution time-lapse imaging are shown. Arrows, areas with nanometer-scale morphological changes. For each time point subsets of 10,000 frames were used for reconstruction. (d) Dual-color super-resolution microscopy of a CV-1 cell expressing Caveolin-YFP and Septin7-mCherry labeled with AF700-anti-GFP and AF647-anti-RFP nanobodies, respectively. Scale bars, 2  $\mu$ m (single line) and 500 nm (double line) unless labeled otherwise.



Our labeling scheme made possible single-molecule nanoscopy of any GFP-tagged construct with minimal effort and hence could allow for high-throughput super-resolution imaging from libraries encoding GFP-tagged proteins (GFP-fusion libraries). To test this

possibility, we used a haploid *Saccharomyces cerevisiae* genomic library that encodes GFP-tagged proteins under the endogenous promoters<sup>10</sup> and developed a simple labeling scheme for AF647-anti-GFP nanobodies.

Yeast cells are generally immunostained after digestion of the cell wall, which generates spheroblasts and compromises cellular morphology. As this may affect the organization and localization of intracellular structures and is labor-intensive, we

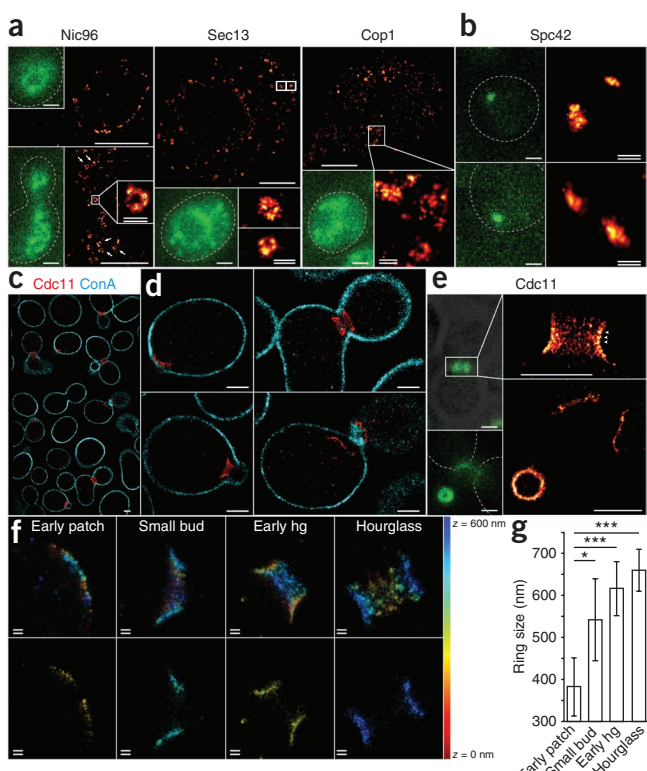


**Figure 2 | Single-molecule nanoscopy of proteins from a budding yeast GFP-fusion construct library.** (a) Reconstructed super-resolution images of Nic96-GFP, Sec13-GFP and Cop1-GFP. (b) Super-resolution images of the spindle pole body protein Spc42-GFP. (c) Dual-color reconstructed super-resolution images of a population of yeast cells expressing Cdc11-GFP stained with AF647-anti-GFP nanobodies (red) and the cell wall labeled with AF700-ConA (cyan). (d) Reconstructed dual-color super-resolution images visualizing the different organizational stages of Cdc11-GFP structures during the cell cycle. (e) Reconstructed super-resolution images of the yeast septin Cdc11-GFP, which localizes to a characteristic hourglass-shaped and later ring-like structure around the mother-bud neck. Dot-like structures are marked by arrowheads. (f) Reconstructed three-dimensional super-resolution images of the development of the bud-neck yeast septin structure over time. The central opening is visible in 200-nm-thick  $z$ -dimension sections. Hg, hourglass. Depth is color-coded from 0 to 600 nm. In a,b,e conventional wide-field images of the GFP fluorescence are shown in green. Owing to lack of optical sectioning, these wide-field fluorescence images might show higher background and lower contrast than state-of-the-art confocal or deconvoluted images. Scale bars, 1  $\mu$ m (single line) and 100 nm (double line). (g) Quantification of the diameter of the opening of the septin structure in the indicated stages ( $n = 9, 36, 20$  and  $18$  images analyzed for early patch, small bud, early hourglass (hg) and hourglass, respectively; error bars, s.d.; \* $P = 3.4 \times 10^{-5}$ , \*\*\* $P = 5.4 \times 10^{-7}$  (early patch versus hg),  $P = 1.5 \times 10^{-7}$ , (early patch versus hg), Mann-Whitney test).

## BRIEF COMMUNICATIONS

hypothesized that the small nanobodies might penetrate the cell wall of fixed, intact yeast cells after membrane permeabilization and developed a simple labeling scheme that would not require such a treatment.

As proof of principle, we analyzed structures of ~100 nm in size whose features are known, but have not been resolved by fluorescence microscopy so far, such as nuclear pores or coated vesicles. When we incubated fixed and permeabilized cells expressing GFP-tagged proteins in such structures with AF647-anti-GFP nanobodies and imaged them by single-molecule nanoscopy, we found that the nuclear pore complex component Nic96 localized to ring-like structures of ~70 nm diameter (Fig. 2a). When we imaged the COPII subunit Sec13, which forms cargo vesicles between the endoplasmic reticulum and the Golgi apparatus, we observed ring-like structures with diameters around 90 nm. The coatomer Cop1 yielded similar structures. To verify the suitability of our technique as a high-throughput method, we labeled another 20 GFP-tagged proteins from the library and performed single-molecule nanoscopy (Supplementary Fig. 3). Of these, the spindle pole body protein Spc42, which localizes to one diffraction-limited spot in the GFP channel, could be resolved to an elongated structure of  $108\text{ nm} \pm 20\text{ nm}$  length (Fig. 2b). In an analysis of 80 cells, we often (in 25 cells) found two structures about  $115\text{ nm} \pm 32\text{ nm}$  apart in the diffraction-limited spot. One of the structures usually appeared larger, suggesting the formation of a second spindle pole body (Supplementary Fig. 4).

Next we investigated the septin Cdc11-GFP, a molecule important in cell division<sup>11</sup> in more detail. When we incubated fixed and permeabilized cells with AF647 anti-GFP nanobodies and labeled the cell wall with the lectin concanavalin A coupled to AF700 (ConA-AF700), we could image both the cell wall and the septin structure in dual-color single-molecule nanoscopy<sup>12</sup> (Fig. 2c). We visualized the different organizational states of Cdc11-GFP-labeled structures during the cell cycle (Fig. 2d). During the hourglass structural state, we could resolve Cdc11-labeled point-like structures along the bud neck that resembled lateral cuts through periodic filaments (Fig. 2e; 13 of 21 structures investigated) in agreement with earlier observations using electron microscopy<sup>13</sup>.

How this septin ring is first assembled at the future bud site is unclear but it may involve a patch of septins<sup>14</sup> or a ring<sup>15</sup>. The resolution of conventional microscopy does not allow a quantitative investigation of this structure. When we synchronized cells and imaged them by single-molecule nanoscopy at different time points after release, we consistently observed holes in the center of even the earliest Cdc11 patches that increased in diameter with time (Supplementary Fig. 5). We then classified the structures according to their progression during the cell cycle (Fig. 2f) and quantified the size of the central opening. In the first structures (early patch) we observed, the central opening was  $382\text{ nm} \pm 70\text{ nm}$  ( $n = 9$ ) in diameter and this widened for hourglass structures to  $659\text{ nm} \pm 50\text{ nm}$  ( $n = 18$ , Fig. 2g). We concluded that nanobody labeling allows quantitative analysis of previously inaccessible structures in this important model organism.

We demonstrated here a simple, robust and versatile labeling scheme that enables the immediate use of any GFP-tagged molecule in yeast, tissue culture or neurons in single-molecule nanoscopy. Similar approaches combining GFP-tagging with

nanobodies may be generally useful for fluorescence microscopy and other applications such as immuno-electron microscopy or single-particle tracking. The small size and high affinity of the nanobodies allows for specific labeling in regions that are inaccessible to antibodies. Furthermore, compared with antibodies, the consistent affinity of nanobodies to GFP may allow for more comparable and quantitative labeling between different molecules. Although nanobodies have several advantages, in principle, the presented approach could also be realized using Fab fragments of anti-GFP antibodies. Our technique would be especially powerful in combination with the many available GFP knock-in mice.

GFP-tagged genomic libraries exist for several organisms, and our simple labeling protocol opens the door to high-throughput localization-analysis of entire proteomes at the nanoscopic level. Especially appealing is the yeast GFP-fusion library demonstrated here, as the constructs are expressed from the endogenous promoter in haploid strains. As a result, all molecules of a given protein are GFP-tagged, and our approach may allow for quantitative super-resolution microscopy in yeast cells and detection of molecules that are expressed in very low amounts.

## METHODS

Methods and any associated references are available in the online version of the paper.

*Note: Supplementary information is available in the online version of the paper.*

## ACKNOWLEDGMENTS

This work was supported by a Marie Curie Intra-European Fellowship (J.R.) the National Center for Competence in Biomedical Imaging and the National Center for Competence in Research 'Neural Plasticity and Repair'. We thank Y. Barral and members of the Barral laboratory for useful discussions, help with yeast strains and access to the yeast genomic GFP-fusion library, R. Dechant for help with elutriation and M. Stoeber for help with Amaxa transfection.

## AUTHOR CONTRIBUTIONS

H. Ewers conceived of the project; J.R., C.K., E.P. and H. Ewers designed experiments; J.R., C.K., E.P., H. Eghlidi & H. Ewers performed and analyzed experiments; H. Ewers and J.R. wrote the paper.

## COMPETING FINANCIAL INTERESTS

The authors declare no competing financial interests.

Published online at <http://www.nature.com/doifinder/10.1038/nmeth.1991>. Reprints and permissions information is available online at <http://www.nature.com/reprints/index.html>.

1. Betzig, E. *et al. Science* **313**, 1642–1645 (2006).
2. Rust, M.J., Bates, M. & Zhuang, X. *Nat. Methods* **3**, 793–795 (2006).
3. Heilemann, M. *et al. Angew. Chem. Int. Edn. Engl.* **47**, 6172–6176 (2008).
4. Fölling, J. *et al. Nat. Methods* **5**, 943–945 (2008).
5. Rothbauer, U. *et al. Nat. Methods* **3**, 887–889 (2006).
6. Bates, M., Blosser, T.R. & Zhuang, X. *Phys. Rev. Lett.* **94**, 108101 (2005).
7. Heilemann, M., Margeat, E., Kasper, R., Sauer, M. & Tinnefeld, P. *J. Am. Chem. Soc.* **127**, 3801–3806 (2005).
8. Juette, M.F. *et al. Nat. Methods* **5**, 527–529 (2008).
9. Manley, S. *et al. Nat. Methods* **5**, 155–157 (2008).
10. Huh, W.-K. *et al. Nature* **425**, 686–691 (2003).
11. Hartwell, L.H. *Exp. Cell Res.* **69**, 265–276 (1971).
12. Baddeley, D. *et al. PLoS ONE* **6**, e20645 (2011).
13. Byers, B. & Goetsch, L. *J. Cell Biol.* **69**, 717–721 (1976).
14. Cid, V.J., Adamková, L., Sánchez, M., Molina, M. & Nombela, C. *Microbiology* **147**, 1437–1450 (2001).
15. Chen, H., Howell, A.S., Robeson, A. & Lew, D.J. *Biol. Chem.* **392**, 689–697 (2011).

## ONLINE METHODS

**Cell culture.** Ptk2 cells stably expressing tubulin-YFP were maintained in phenol-red free DMEM (Invitrogen) supplemented with 10% FCS (Labforce), Glutamax (Invitrogen) and 500 µg/ml G418 (Invitrogen). Cells were plated on 18 mm round coverglass and after 24 h were permeabilized for 5 min at 37 °C in 0.25% Triton X-100 in BRB80 (80 mM PIPES, 1 mM MgCl<sub>2</sub> and 1 mM EGTA, pH 6.8). They were then fixed in methanol at -20 °C and washed in BRB80. Cells were blocked in BRB80 with 1% BSA and 4% horse serum and incubated for 30 min with 250 ng/ml AF647-labeled nanobodies. Buffer for single-molecule nanoscopy measurements in Ptk2 cells is based on that in ref. 3: 150 mM Tris-HCl, 60 mM β-mercaptoethylamine (Sigma), 1% v/w glucose, 0.5 mg/ml glucose oxidase (Sigma) and 40 µg/ml catalase (Sigma).

**Neuronal cell culture.** Cultures of hippocampal neurons were from E18 Sprague-Dawley rats. Embryos were removed and placed in ice-cold HBSS, decapitated and brains put into a new dish containing ice-cold HBSS. Both cerebral hemispheres were removed and freed from their meninges. The hippocampi were dissected and collected in fresh HBSS. After 15 min incubation in prewarmed trypsin (Invitrogen), neurons were singularized by pipetting up and down in a 1,000-µl pipette tip, plated at a density of 2–3 × 10<sup>5</sup> cells/dish on poly(lysine)-precoated cover slips and kept in neurobasal medium (Invitrogen) at 37 °C in 5% CO<sub>2</sub>. After 3 d, cytarabine was added to 5 µM. Neurons were transfected using Lipofectamine (Life Technologies) as described previously<sup>16</sup>. All live cell microscopy was performed in extracellular solution (ECS; 145 mM NaCl, 5 mM KCl, 2 mM CaCl<sub>2</sub>, 1 mM MgCl<sub>2</sub>, 10 mM HEPES and 10 mM glucose) supplemented with 0.2% bovine serum albumin at pH 7.4, and osmolarity was adjusted to that of the cellular medium. For single-molecule nanoscopy measurements, the solution was supplemented with 200 mM HEPES, 30 mM β-mercaptoethylamine (MEA), 0.5% (v/w) glucose, 0.25 mg/ml glucose-oxidase and 20 µg/ml catalase.

**Poly(lysine)-coating of coverglass.** Coverslips were incubated overnight in HNO<sub>3</sub>, washed six times in ddH<sub>2</sub>O and dried overnight in an oven at 250 °C. Four coverslips were placed in 6-cm dishes and coated with 200 µl of 1 mg/ml poly(lysine) solution (MW 30,000–70,000, Sigma), incubated for 3 h at 37 °C and afterwards washed three times in ddH<sub>2</sub>O.

**Preparation of yeast strains for single-molecule nanoscopy.** Standard methods and media were used to cultivate yeast cells<sup>17</sup>. Yeast strains are listed below.

Overnight cultures were diluted to OD 0.2 in 5 ml of yeast rich medium (yeast extract peptone dextrose; YPD) in a 50 ml Falcon tube and grown for 3 h at 30 °C. Cells were spun down for 4 min at 2,800 g and resuspended in 200 µl ddH<sub>2</sub>O. A 50 µl drop of cell suspension was pipetted onto concanavalin A-coated coverglass. The suspension was allowed to settle down for 15 min, remaining liquid was taken away and cells were fixed for 15 min in 4% paraformaldehyde (PFA), 2% sucrose in phosphate-buffered saline (PBS). The fixation was stopped by two washes for 15 min in PBS with 50 mM NH<sub>4</sub>Cl.

Subsequently, cells were blocked and permeabilized by gently shaking for 30 min in PBS with 0.25% Triton X-100, 5% BSA and 0.004% NaN<sub>3</sub> in 1× PBS. After blocking, the cells were labeled for 90 min in 100 µl of nanobody solution (10 µM labeled nanobody,

0.25% Triton X-100, 1% BSA and 0.004% NaN<sub>3</sub> in 1× PBS). Cells were then washed for 5 min by gently shaking in PBS. Depending on the quality of the staining, more washing steps were performed before mounting the cover slip onto the sample holder. Buffer for localization microscopy was the same as for Ptk2 cells. For Tub1 staining, in all steps BRB80 buffer was used instead of PBS.

**Dual-color labeling of yeast cells for single-molecule nanoscopy.** For dual-color labeling of yeast cells, coverslips were washed one time after the nanobody labeling step for 5 min in 1× PBS. The ConA-labeled with AF700 was diluted to 70 nM in a solution containing 1% BSA and 0.04% NaN<sub>3</sub> in PBS. Coverslips were transferred onto Parafilm again and incubated for 30 min in 100 µl secondary staining solution. Subsequent washing steps were performed as mentioned above.

**Dual-color labeling with nanobodies.** For dual color labeling of mammalian cells, cells were washed three times with BRB80, fixed in 4% PFA in BRB80 for 15 min at room temperature. Coverslips were then incubated for 15 min in BRB80 with 50 mM NH<sub>4</sub>Cl and then permeabilized in BRB80 with 0.25% Triton-X100 for 5 min. Cells were washed three times for 5 min in BRB80 and then incubated for 30 min in 4 drops of Image-it FX (Invitrogen). Cells were blocked for 45 min in BRB80 with 1% BSA and 4% horse serum and then labeled with 50 ng/ml of AF647-anti-RFP and AF700-anti-GFP nanobodies. Buffer for localization measurements was 150 mM Tris-HCl pH 8.8, 1.5% β-mercaptoethanol, 0.5% (v/w) glucose, 0.25 mg/ml glucose oxidase and 20 µg/ml catalase.

**Preparation of concanavalin A coverglass.** Round 18-mm-diameter cover slips (Assistent) were placed in a Petri dish with ddH<sub>2</sub>O and washed twice with ddH<sub>2</sub>O. Then they were submerged in 70% ethanol for at least 5 min. The required amount of cover-glass was air-dried and placed on Parafilm. A 20-µl drop of a 2 mg/ml concanavalin A solution (ConA, C7275, Sigma-Aldrich) was distributed onto each cover slip and spread with a pipette tip to cover it completely. The coverglass was left at room temperature to let the ConA attach and after 30 min the rest of the ConA solution was taken away. To dry the ConA completely, the glass was incubated for 1 h at 37 °C.

**Synchronization of yeast cells.** Cell-cycle synchronization was performed with a JE-5.0 elutriation rotor in an Avanti-J20 XP centrifuge (Beckmann). A 600-ml yeast culture was grown to OD = 1 for 3 h at 30 °C and was flooded into the funnel-shaped chamber of the rotor with a starting flow rate of 18 ml/min and a centrifuge speed of 2,000 r.p.m. As the chamber filled up with cells, the flow rate and centrifuge speed were adjusted to establish a sharp border in between the differently sized cells as monitored through the observation window. Cells were finally separated in the flow chamber at a flow rate of 6 ml/min and 3,000 r.p.m. The G1 fraction was collected with an initial flow rate of 11 ml/min that increased to 13 ml/min at the end. Homogeneity of the fraction was controlled by microscopy of cell samples.

We collected 300 ml of synchronized G1 cells and immediately concentrated them by filtering. Cells were resuspended in 50 ml YPD medium and incubated at 30 °C on a shaker (120 r.p.m.). Seven milliliters of yeast culture was fixed in a ratio 1:1 with 8% paraformaldehyde and 4% sucrose in 1× PBS at time points 0 min,

2 min, 5 min, 10 min, 15 min and 25 min. Fixation was performed for 15 min at room temperature, cells were washed once in 3 ml PBS with 50 mM NH<sub>4</sub>Cl by gently shaking for 30 min and then stored in 1× PBS at 4 °C. Mounting and staining was performed as described in the protocol above.

**Preparation of labeled nanobodies.** Nanobodies were purchased from Chromotek as GFP-Trap and RFP-Trap. For labeling, 50 µl of the 1 mg/ml solution were dialyzed into 0.2 M NaHCO<sub>3</sub>, pH 8.2 in a mini-dialysis unit (Pierce, molecular weight cutoff = 3,500 Da). Succinimidyl-esters of Alexa Fluor 647 and Alexa Fluor 700 (Invitrogen) were dissolved at 10 mg/ml in DMSO, stored at –80 °C and for labeling added to fivefold molar excess to the nanobodies. The mixture was incubated for 1–2 h at 25 °C. Excess dye was removed via buffer exchange into PBS using Zeba desalting columns (Pierce, molecular weight cutoff = 7,000 Da), and the solution was stored at 4 °C.

**Preparation of labeled concanavalin A.** Concanavalin A was dissolved at 2 mg/ml in 0.2 M NaHCO<sub>3</sub>, pH 8.2 and incubated for 1 h with a fivefold molar excess of Alexa Fluor 700 succinimidyl-ester (Invitrogen). Excess dye was removed by a desalting column (Amersham).

**Optical setup.** Single-molecule nanoscopy was performed with a custom-built microscope. A 473 nm laser (100 mW) and a 647 nm laser (150 mW, both lasers from Pusch OptoTech) were mode-cleaned with a pinhole and focused onto the back-focal plane of a total internal reflection fluorescence (TIRF) objective (numerical aperture (NA) 1.49, 60×; Olympus) for highly inclined plane illumination. Emission light was filtered by a 700/75 and a 675/50 band pass (AHF) and focused by a 500 mm tubus lens onto the chip of a back-illuminated electron-multiplying charge-coupled device (EM-CCD) camera (Evolve, Photometrics) that was water-cooled to –85 °C. Images were acquired with MicroManager<sup>18</sup>.

For 3D localization, the emission was split by a nonpolarizing 50:50 beam splitter cube and focused by two tube lenses onto different parts of the camera. The position of the tube lenses was adjusted to result in a difference in focal planes of  $\Delta z = 400$  nm.

For dual-color imaging, two 700/75 nm band-pass filters were used. A dichroic (LP 690, AHF) split the emission into two channels, which were imaged onto two parts of the CCD chip.

Focusing was done by moving the objective with a piezo objective positioner (MIPOS, Piezo Systems Jena). A focus lock was implemented by an electronic feedback loop (LabView, National Instruments) based on the total internal reflection of a red laser at the cover slip and its detection by a quadrant photodiode; the  $z$  stability was better than  $\pm 10$  nm over several hours. The lateral drift was typically smaller than 50 nm/h; a drift-correction was implemented on the level of the analysis software (see below). For live-cell imaging, the temperature was stabilized to 35 °C with a proportional-integral controller by heating the bottom plate of the encapsulated microscope.

**Determination of labeling efficiencies.** The labeling efficiency of the nanobodies with Alexa Fluor dyes was determined by absorption spectroscopy after removing excessive dye two times

as described above. Typical labeling efficiencies were around  $\epsilon = 0.6$  AF647 molecules per nanobody.

Binding efficiencies of the nanobodies (NB) to GFP were determined in the following way. A mixture of GFP and AF647 in PBS, 1% BSA, 0.005% Tween was prepared and their concentrations C<sup>0</sup><sub>GFP</sub> and C<sup>0</sup><sub>AF647</sub> were measured by absorption spectroscopy. Calibration images in the AF647 and the GFP channel (I<sup>0</sup><sub>AF647</sub>, I<sup>0</sup><sub>GFP</sub>) on this solution were taken under conditions identical to the later measurements. Images of nanobody-labeled structures (MDCK cells expressing GPI-GFP) were normalized pixel-wise by the calibration images and low-pass filtered. The labeling ratio in each pixel was then determined according to: NB/GFP =  $(1/\epsilon)(I_{AF647}/I_{AF647}^0)(I_{GFP}/I_{GFP}^0)(C_{AF647}^0/C_{GFP}^0)$ .

Labeling efficiencies were around 0.6 NB/GFP, both for labeling performed before and after fixation.

**Single-molecule measurements.** The samples were mounted in a custom-made holder, the measurement chamber was filled with 200 µl of the respective buffer, and the chamber was mounted on the microscope. We used an exposure time of 25 ms (15 ms for live-cell imaging) and an electron multiplier gain of 300. Imaging laser intensity at 642 nm was 5 kW/cm<sup>2</sup> (2.5 kW/cm<sup>2</sup> for live-cell imaging); the activation laser was automatically adjusted to keep the average number of localizations per frame constant (maximum intensity 0.25 kW/cm<sup>2</sup>). Typically 20,000–100,000 frames were acquired.

**Localization analysis.** Localization analysis was performed as described before<sup>19</sup>. Briefly, pixel counts were converted to photons by subtracting the constant offset and multiplying by the inverse gain. Approximate locations of bright spots in each image were determined by smoothing, nonmaximum suppression and thresholding. Selected regions of interest were fitted by a pixelized Gaussian function and a homogeneous photonic background with a maximum likelihood estimator (MLE) for Poisson distributed data using a freely available, fast GPU fitting routine<sup>20</sup> on a GeForce GTX275 (Nvidia). Lateral drift was corrected based on the imaged features: blocks of typically 5,000 frames were used to reconstruct one PALM image. Displacements among all reconstructed images were determined by image correlation and fitting of the maximum with an elliptical Gaussian. Displacements corresponding to each time point were averaged using a robust estimator, interpolated by a spline and used to correct the position of each localization. From the variation of the spline, we estimate that the residual error for the corrected positions was about 2 nm.

For fixed cells, localization bursts with a distance smaller than 90 nm in consecutive frames (interrupted by not more than two frames) were grouped into a single localization. Finally, localizations with an uncertainty of  $\sigma_{\max} > 10$  nm (15 nm for live-cell imaging) were discarded.

For 3D localization, the axial position of the fluorophores was inferred from the measured sizes  $\sigma_1$  and  $\sigma_2$  of the single-molecule images using a calibration with 40 nm fluorescent beads (TransFluoSpheres 488/645, Invitrogen). To this end, localizations in the two channels originating from one molecule had to be linked. This was achieved by calculating an approximate shift between the two channels by cross-correlating the images, linking the brightest molecules in each frame, which were then used to calculate an affine transformation between the two channels.

This transformation was used to map the positions of channel 2 onto channel 1. Finally, all molecules were linked and their axial position was calculated. Even higher axial localization precision can in principle be achieved by using an experimental PSF for data fitting<sup>21</sup> instead of a Gaussian.

For dual-color imaging, the transformation between the two channels was calculated using all AF647 localizations, which were visible in both channels. Subsequently, for each localization, background-corrected intensities from corresponding regions in the two channels were compared to assign the proper identity of the label.

For the images in **Figures 1** and **2**, the localization data were rendered using a Gaussian with a width according to the localization precision of the respective localization, determined from the fitted number of photons and background. Line profiles (**Fig. 1a**) were obtained by binning the localizations inside the selected region along the cross-section in intervals of 4 nm. The FWHM (**Fig. 1a,b**) was determined by fitting a Gaussian to the binned data. All analysis software was written in Matlab (Mathworks).

**Yeast strains and proteins.** All yeast strains were obtained from a yeast GFP-fusion library<sup>10</sup> (Invitrogen). In this study we investigated the localization of the yeast proteins Cdc11, Nic96, Bfr2, Spc42, Bud3, Pmp1, Rox3, Htx3, Sir2, Kar3, Nop2, Pma1, Tub1, Snf7, Cdc14, Cop1, Erg6, Sec13, Sur7, Tom20, Vma2, Nic96, Mep2, Hho1, Ilv6 and Fet3, which we selected for their distinct localization pattern according to ref. 6. Detailed information can be obtained from <http://www.yeastgenome.org/> and in the **Supplementary Note**.

16. Kaech, S. & Banker, G. *Nat. Protoc.* **1**, 2406–2415 (2006).
17. Amberg, D.C., Burke, D. & Strathern, J.N. *Methods in Yeast Genetics*. (Cold Spring Harbor Laboratory Press, 2005).
18. Edelstein, A., Amodaj, N., Hoover, K., Vale, R. & Stuurman, N. *Curr. Protoc. Mol. Biol.* 14.20 (2010).
19. Schoen, I., Ries, J., Klotzsch, E., Ewers, H. & Vogel, V. *Nano Lett.* **11**, 4008–4011 (2011).
20. Smith, C.S., Joseph, N., Rieger, B. & Lidke, K.A. *Nat. Methods* **7**, 373–375 (2010).
21. Juette, M.F. & Bewersdorf, J. *Nano Lett.* **10**, 4657–4663 (2010).

# Quantitative evaluation of software packages for single-molecule localization microscopy

Daniel Sage<sup>1</sup>, Hagai Kirshner<sup>1</sup>, Thomas Pengo<sup>2</sup>, Nico Stuurman<sup>3,4</sup>, Junhong Min<sup>5</sup>, Suliana Manley<sup>6</sup> & Michael Unser<sup>1</sup>

The quality of super-resolution images obtained by single-molecule localization microscopy (SMLM) depends largely on the software used to detect and accurately localize point sources. In this work, we focus on the computational aspects of super-resolution microscopy and present a comprehensive evaluation of localization software packages. Our philosophy is to evaluate each package as a whole, thus maintaining the integrity of the software. We prepared synthetic data that represent three-dimensional structures modeled after biological components, taking excitation parameters, noise sources, point-spread functions and pixelation into account. We then asked developers to run their software on our data; most responded favorably, allowing us to present a broad picture of the methods available. We evaluated their results using quantitative and user-interpretable criteria: detection rate, accuracy, quality of image reconstruction, resolution, software usability and computational resources. These metrics reflect the various tradeoffs of SMLM software packages and help users to choose the software that fits their needs.

We have conducted a large-scale comparative study of software packages developed in the context of SMLM, including recently developed algorithms. We designed realistic data that are generic and cover a broad range of experimental conditions and compared the software packages using a multiple-criterion quantitative assessment that is based on a known ground truth.

Our study is based on the active participation of developers of SMLM software. More than 30 groups have participated so far, and the study is still under way. We provide participants access to our benchmark data as an ongoing public challenge. Participants run their own software on our data and report their list of localized particles for evaluation. The results of the challenge are accessible online and updated regularly.

SMLM was demonstrated in 2006, independently by three research groups<sup>1–3</sup>, and has enabled subsequent breakthroughs in diverse fields<sup>4,5</sup>. SMLM can resolve biological structures at the nanometer scale (typically 20 nm lateral resolution), circumventing Abbe's diffraction limit. At the cost of a relatively simple setup<sup>6,7</sup>, it has opened exciting new opportunities in life science research<sup>8,9</sup>.

The underlying principle of SMLM is the sequential imaging of sparse subsets of fluorophores distributed over thousands of frames, to populate a high-density map of fluorophore positions. Such large data sets require automated image-analysis algorithms to detect and precisely infer the position of individual fluorophore, taking advantage of their separation in space and time.

The acquired data cannot be visualized directly; further computerized image-reconstruction methods are required. These typically comprise four steps: preprocessing, detection, localization and rendering. Preprocessing reduces the effects of the background and noise; detection identifies potential molecule candidates in each frame; localization performs a subpixel refinement of the initial position estimates, usually by fitting a point-spread function (PSF) model; and rendering turns the detected molecule positions into a high-resolution map of molecule densities. The performance of the overall processing pipeline contributes to the quality of the super-resolved image<sup>10</sup>.

The current literature describes more than 25 image-analysis software packages that process SMLM data. Each has its own characteristics, set of parameters, accessibility and terminology<sup>10,11</sup>. Moreover, these packages are often validated using different data. In the absence of guidance, end users face a difficult choice in deciding which software is most suitable for them. The lack of a standardized methodology for conducting performance analysis and the need for reference benchmark data constitute the gap that we address in this work.

Our synthetic data imitate microtubule structures. The data consist of thousands of images with labeling densities that span well over an order of magnitude. The model of image formation accounts for the stochastic nature of the emission rate of the fluorophores, the characteristics of the optical setup, and various sources of noise. As in real data, it also includes inhomogeneous excitation, autofluorescence and readout electron-multiplying noise from the detector, typically an electron-multiplying charge-coupled device (EMCCD).

Our benchmark criteria were designed to objectively measure computational performance in terms of time and quality. Our evaluation effort is more comprehensive than previous work<sup>12</sup> in benchmarking a large number of software packages, in synthesizing

<sup>1</sup>Biomedical Imaging Group, Ecole Polytechnique Fédérale de Lausanne (EPFL), Lausanne, Switzerland. <sup>2</sup>Center for Genomic Regulation, Barcelona, Spain.

<sup>3</sup>Howard Hughes Medical Institute, University of California (UCSF), San Francisco, California, USA. <sup>4</sup>Department of Cellular and Molecular Pharmacology, UCSF, San Francisco, California, USA. <sup>5</sup>Department of Bio and Brain Engineering, Korea Advanced Institute of Science and Technology (KAIST), Daejeon, Republic of Korea.

<sup>6</sup>Laboratory of Experimental Biophysics, EPFL, Lausanne, Switzerland. Correspondence should be addressed to D.S. (daniel.sage@epfl.ch).

RECEIVED 22 AUGUST 2014; ACCEPTED 17 APRIL 2015; PUBLISHED ONLINE 15 JUNE 2015; DOI:10.1038/NMETH.3442

## ANALYSIS

data closer to biological reality, and in including a rich set of evaluation criteria such as detection rate, accuracy, image quality, resolution and software usability.

A byproduct of our work is an extensive and annotated list of software packages (<http://bigwww.epfl.ch/smlm/software/>), which should prove a resource not only to practitioners but also to developers because it helps identify which aspects of existing software may be in need of further development.

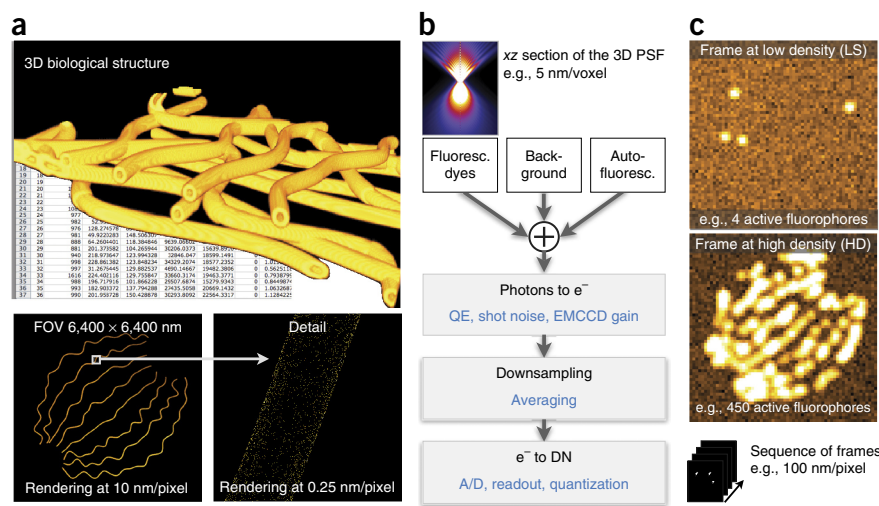
## RESULTS

### Bio-inspired data

We designed our synthetic data to be as similar as possible to images derived from real cellular structures. A key element is their continuous-domain description, as opposed to a spatially discrete model. For instance, we simulate microtubules by means of three-dimensional (3D) paths that are defined on the continuum (Fig. 1a), making it possible to render digital images at any scale. We typically choose a scale of 5 nm per pixel. Our synthetic model takes many parameters into account, among them sample thickness, random activation, laser power, variability of the excitation laser, the lifetime of the fluorophores, autofluorescence, several sources of noise, pixelation, analog-to-digital conversion and the PSF of the microscope (Fig. 1b). Our PSF model is made up either of classical Gaussian-based 3D functions or of the more realistic Gibson-Lanni formulation that benefits from a fast and accurate implementation<sup>13</sup>. Because multiple-frame events are rare in the data of interest, we tuned the lifetime model to favor single-frame events. We rely primarily on these ground-truth data for our objective evaluation of algorithms.

To accommodate the intended uses of the available software, we chose to image the same synthetic sample using different imaging modes: long sequence (LS) and high density (HD). The LS data are low-density sequences of about 10,000 frames each, and the HD data are high-density sequences of about 500 frames that include overlapping PSFs (Fig. 1c). Independently of the imaging mode, we changed the degree of difficulty of the data by modifying the contribution of autofluorescence, the amount of acquisition noise and the thickness of the sample (see Online Methods) to create datasets LS1-3 and HD1-3 (in order of increasing difficulty).

**Figure 1 |** Construction of the bio-inspired data. (a) Top, 3D structure simulating biological microtubules. Every single fluorophore event is uniquely identified and stored; collectively, they constitute the ground-truth localizations which can be rendered at any temporal and spatial scale (lower panels). (b) Each fluorophore is considered a point source and convolved with a 3D PSF. Combined with background and autofluorescence of the structure, the convolved image determines the number of photons at each pixel. These photons are then transformed into a number of electrons based on quantum efficiency (QE), shot noise and the EMCCD parameters. The image is reduced to the desired camera resolution, for example, 100 nm/pixel. Finally, these values are fed to an electron-to-DN converter (digital number, taking into account the readout noise and the quantization level). (c) These operations are repeated to obtain long sequence (LS) of low-density frames or short sequence of high-density (HD) frames.



We generated training data and disclosed them together with the true locations of the fluorophores, allowing participants to tune their software. We also generated contest data and delivered them without ground-truth information. We assessed every algorithm on the basis of the contest data. We make these data available at <http://bigwww.epfl.ch/smlm/datasets/>; the collection is already used by developers<sup>14-19</sup>.

### Quantitative assessment metrics

The core task faced by participants in our study is the 2D localization of single molecules. To rate the performance of their software, we defined multiple criteria (Online Methods) that highlight different aspects of SMLM algorithms: detection rate, accuracy, image quality, resolution, usability (USA) and execution runtime (TIME). Other preprocessing or postprocessing steps, such as drift correction and rendering, were excluded from our analysis to better provide an unbiased comparison based primarily on the localization performance.

### Detection rate and localization accuracy

The detection rate and localization accuracy are based on the pairing between the molecules localized by the participants and the molecules from the ground truth. These criteria do not depend on any rendering mechanism.

The detection rate quantifies the framewise fidelity and the completeness of the set of localizations with respect to the ground truth, measured in our case by a Jaccard index. We found that the detection rate (JAC) correlates with the level of difficulty.

The localization accuracy (ACC) is measured by the root-mean-square error (RMSE) of matched localizations. We found that this averaged 21.05 nm and 32.13 nm for LS1 and LS2, respectively. This is consistent with the Cramér-Rao lower bound predicted according the definition of uncertainty given by Rieger *et al.*<sup>20</sup>. The detection rate and localization accuracy of each software are documented in Figure 2 and in Supplementary Figures 1 and 2.

### Image quality and image resolution

Ultimately, the data representation favored by SMLM practitioners is not a list of localizations but a rendered image<sup>10</sup> (Supplementary Data 1 and Supplementary Videos 1-6).

**Figure 2** | Accuracy versus detection rate for each tested software. Scatter plots show high-density (HD) data above and long sequence data below. Efficiency lines (Eff. lines) are computed from the five results at the boundary of the field with high JAC and/or low ACC. The length of the bars is proportional to the grade, from 0 (poor) to 5 (good). Grades above 3.5 are written in the corresponding bar. The grades of the three data sets are given here for the detection rate, JAC1–JAC3; for the localization accuracy, ACC1–ACC3; for the image quality assessment, SNR1–SNR3; and for the image resolution, FRC1–FRC3. The grades of the computational time (TIME) and usability (USA) are reported in light gray bars.

We used two image-based criteria in our assessment: image quality (signal-to-noise ratio, SNR) and image resolution (Fourier ring correlation, FRC<sup>21</sup>). Methods afflicted by issues such as sampling artifacts or a low detection capacity at the image border are characterized by a low SNR. Conversely, a high SNR is often indicative of a successful tradeoff between detection rate and accuracy.

## Software efficiency

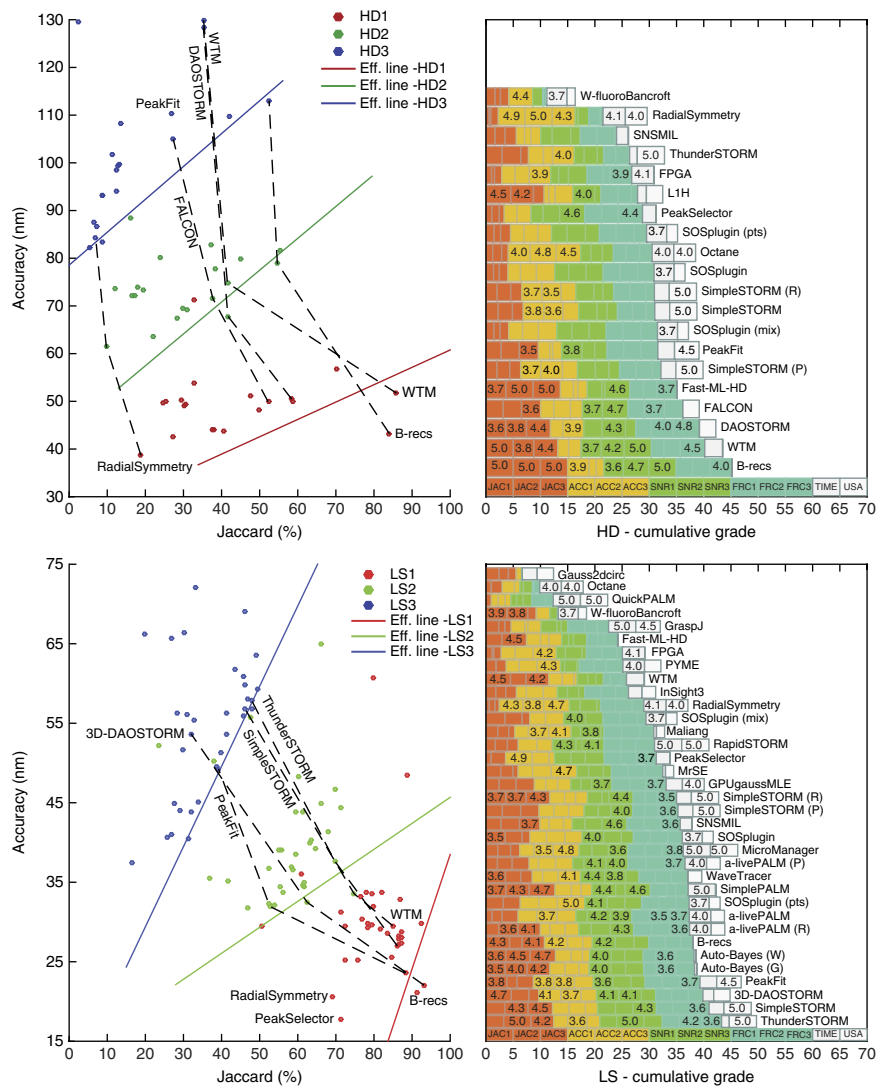
In a retrospective analysis, we identified the five best methods, in terms of the tradeoff between accuracy and detection rate for each dataset. We defined a linear regression that fits the best methods in a plot of ACC versus JAC, and call it an efficiency line (Fig. 3). The distance of the (JAC, ACC) coordinate for each software to such a line indicates the performance of the software.

The level of difficulty increases from LS1 to LS3, as evidenced by the average performance (JAC, ACC), which was (79.58%, 29.98 nm) for LS1, (55.64%, 41.91 nm) for LS2 and (35.64%, 55.82 nm) for LS3. These findings are consistent with our engineering of the data to have increasing levels of noise, as the theory predicts that the presence of noise leads to an increase in the uncertainty of the location of a particle. Likewise, the detection rate is also affected by noise; single molecules with lower emission rate and deeper axial position are more difficult to detect.

## Algorithms

Our study includes more than 30 packages (Table 1), covering a large proportion of the SMLM software currently available. Aside from a few that do not fit our validation framework because their SMLM reconstruction is based on deconvolution without explicit localization<sup>22</sup>, most packages have a similar architecture. However, a detailed analysis reveals fundamental differences.

Within the detection step, methods as diverse as low-pass filtering, band-pass filtering, watershed, and wavelet transform, to name a few, are deployed. The parameters of these preprocessing operations need to be determined in an *ad hoc* fashion. In some cases, we found that they cannot be set by the user; even when



they can be, often there is no calibration procedure provided. Most algorithms isolate candidate pixels by applying a threshold to identify potential local extrema, but each software uses different methods for determining the threshold value: level of noise, spot brightness, PSF size and/or particle density.

Over two-thirds of the participating packages carry out the localization step by means of a fitting with a Gaussian function. Other algorithms use an arbitrary PSF instead; DAOSTORM and SimpleSTORM use a measured PSF. Distinctively, the two packages MrSE and RadialSymmetry exploit the radial symmetry of the PSF.

We have identified three groups of localization methods and indicated their performance in Table 2. In Generation 1, the basic methods perform localization by means of center of mass (QuickPALM), triangularization (fluoroBancroft) or linear regression (Gauss2dcir). Although very fast, these methods often fail to reconstruct HD data. Generation 2 is the largest group of methods, including about two-thirds of all softwares submitted thus far. They are characterized by the use of iterative localization algorithms such as maximum-likelihood estimators (MLE) or least-squares minimizers (LS). Previous works compare the LS or MLE algorithm in detail<sup>10,23</sup>. Generation 3 comprises advanced methods, often unpublished. They improve

**Figure 3** | Rendering of software results versus ground truth at various scales. Every participant in the challenge received a detailed report on the performance of their software, including renderings as shown; the particular instance here corresponds to the PeakFit software. Long-sequence data (LS), columns 1–3: full field of view (FOV), medium (zoom1), and high (zoom2) magnification. High-density data (HD), columns 4–6. The white frames in FOV indicate the regions displayed in zoom1, while the frames in zoom1 are themselves expanded in zoom2. Rows 1–4: simulated data. The red channel represents the rendering of the ground truth and the green channel the localizations of the tested software. Row 5: real data with unknown ground truth.

the detection rate while keeping a high localization accuracy. This group includes minimum mean squared error (MMSE)/maximum *a posteriori* probability (MAP) approaches (B-recs), a method with high-quality interpolation (simpleSTORM), a template-matching technique (WTM), a mean-shift approach (simplePALM)

and packages that exploit the radial symmetry (RadialSymmetry and MrSE). Detailed information on the software packages is in **Supplementary Notes 1** and **2**.

### Usability and computation time

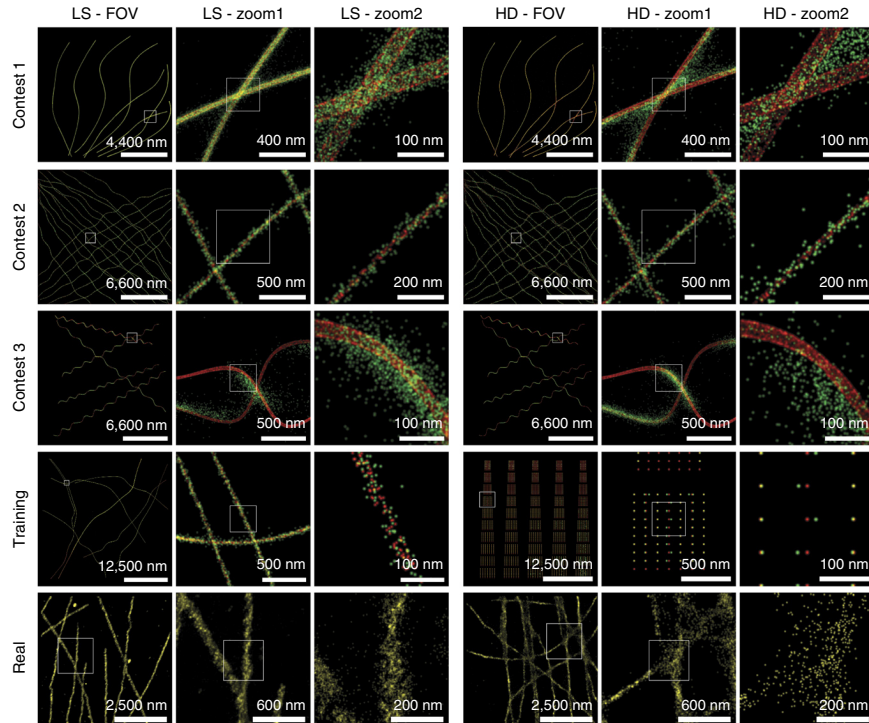
End users require that software packages be accessible, easy to use and fast. Although these aspects are subjective, they are important enough to justify their inclusion in our study. To score them, we prepared a questionnaire for the participants. We combined the accessibility score with a usability score that covers quality of documentation and user-friendliness. The open-source software ImageJ/Fiji and the versatile platform Matlab are the most highly represented frameworks hosting SMLM packages.

Finding the accurate position of millions of fluorophores is a heavy computational task. We observed that the four packages that use specialized hardware accelerators (a graphics processor unit, GPU, or field-programmable gate array, FPGA) reduce their runtimes by an order of magnitude, sometimes reconstructing a super-resolution image in less than a minute.

### Benchmarking reporting and ranking

We returned to every participant a benchmark report that includes renderings at different scales (Fig. 3) and quantitative measures (Fig. 4). In particular, the bottom left curve of Figure 4 illustrates how the proximity of fluorophores,  $d_{NN}$ , influences the performance of the software. In this specific case, the rate of detection improves from about half—when  $d_{NN}$  is below the FWHM of the PSF—to near perfection when  $d_{NN}$  is sufficient high.

To coalesce our six criteria for a single ranking, we computed the final score as the weighted sum of relative grades from 0 to 5, as presented in Table 2. We gave a greater weight to the objective criteria JAC, ACC, SNR and FRC than to the subjective criteria USA and TIME. With our particular choice of weights, the ranking for the LS data is as follows, starting from



the best results: ThunderSTORM, SimpleSTORM and PeakFit. For the HD data, it is B-recs, WTM and DAOSTORM.

### DISCUSSION

The accuracy of single-molecule localization has a direct impact on the resolving power of the reconstructed image. We confirmed in this study of SMLM software packages that the experimental accuracy is one order of magnitude better than the classical diffraction limit, which supports theoretical findings<sup>24,25</sup>. This is the best one can hope for; indeed, a few software packages nearly achieve the Cramér-Rao lower bound.

Notwithstanding its popularity, the accuracy measure may still misrepresent performance. For instance, it does not capture issues related to the spread of the localizations—too few accurate ones, for example, or too many false positives. To avoid reliance on accuracy alone, we therefore considered additional criteria such as the detection rate, which describes the overlap between the set of detected molecules and the set of true molecules, along with a measure of the quality of the rendered image and a measure of its resolution.

Accuracy and detection rate tend to be in opposition—the average accuracy of localization can often be made to artificially increase just by excluding those unreliable molecules that emit a low number of photons. It is therefore enlightening to quantify the tradeoff between accuracy and detection. This idea has led us to propose the efficiency lines or curves (Fig. 2), which should aid microscopy practitioners in selecting software by better allowing them to judge if a particular software will help them meet their own preferred tradeoff.

We proposed a combination of six simple metrics to help users choose an SMLM software package. While no single measure of performance can capture the complexity of this choice, our goal with the combined criterion is to provide guidance to practitioners that is balanced and fair.

Although the correlation (CORR) between the number of photons of the ground truth and the number estimated by the tested software is a parameter of interest, only a few participants provided us with relevant output to obtain these correlations. We therefore decided to exclude CORR from the final score but have encouraged developers to focus their efforts on improving accessibility and usability and to provide an estimate of the number of photons or the uncertainty of measurements for future releases. Also, we did not assess the grouping of

multiple-frame emission from a single molecule, as this is often carried out at the postprocessing stage.

All packages we studied require parameters from the user. Unfortunately, choosing appropriate values is by no means easy or straightforward. More often than not, the tuning of parameters requires a deep knowledge of the algorithmic pipeline; inexperienced users may find that they need to invest a lot of time before they can obtain satisfactory results. For this study, to ensure that each software was properly tuned to our simulated database,

**Table 1 | Description of SMLM software**

Software	Molecule detection	PSF	Method	Platform	Acc.	Affiliation
3D-DAOSTORM <sup>28</sup>	Adaptive threshold—update on residual images	Gauss	LS	Python	+	Harvard Univ., USA
a-livePALM <sup>29</sup>	Denoising, SNR threshold, adaptive histogram equalization	Gauss	MLE	Matlab	+	Karlsruhe IT, Germany
Auto-Bayes	Generalized minimum-error threshold (GMET), local maximum	Gauss, Weibull	LS	Stand-alone	+	NCNST, Beijing, China
B-recs	Detection: n/a; fit: Bayesian inference framework	Arbitrary	MMSE, MAP	Stand-alone	-	Janelia Farm, HHMI, USA
CSSTORM <sup>30</sup>	No explicit localization; convex optimization problem (HD)	Gauss	Compressed sensing	Matlab	+	UCSF, USA
DAOSTORM <sup>31</sup>	Gaussian filtering, local maximum (HD)	Measured, arbitrary	LS	Python	+	Univ. Oxford, UK
FacePALM <sup>32</sup>	No explicit localization; background estimation	—	—	Python	-	Univ. Amsterdam, the Netherlands
FALCON <sup>33</sup>	Deconvolution with sparsity prior, local maximum (HD)	Taylor approx.	ADMM	Matlab	+	KAIST, Daejeon, Republic of Korea
Fast-ML-HD <sup>34</sup>	Sparsity constraint, concave-convex procedure (HD)	Gauss	MLE	Matlab	-	KAIST, Daejeon, Republic of Korea
FPGA <sup>35</sup>	Adaptive threshold	Gauss	MLE, CoMass	Stand-alone	-	Univ. Heidelberg, Germany
Gauss2DCirc <sup>36</sup>	Fixed SNR threshold	Gauss	REG	Matlab	+	Univ. Illinois, USA
GPUgaussMLE <sup>37</sup>	Simple (unspecified) methods to select subregions	Gauss	MLE	Matlab	+	TU Delft, Delft, the Netherlands
GraspJ <sup>38</sup>	Peak finding: fixed threshold value	Gauss	MLE	ImageJ	+	ICFO, Barcelona, Spain
Insight3	Low-pass filtering, local maximum	Arbitrary	LS	Stand-alone	-	UCSF, USA
L1H <sup>39</sup>	No explicit localization; L1 homotopy, FIST deconvolution	Gauss, arbitrary	Compressed sensing	Python	+	Harvard Univ., USA
M2LE <sup>40</sup>	Adaptive threshold	Gauss	MLE	ImageJ	+	Cal Poly Pomona, USA
Maliang <sup>41</sup>	Annular averaging filters, denoising by convolution	Gauss	MLE	ImageJ	+	WUST, Wuhan, China
Micro-Manager LM	Adaptive threshold	Gauss	LS	ImageJ	+	UCSF, USA
MrSE <sup>42</sup>	Band-pass filtering, local maximum	Radial	CoSym	Stand-alone	-	WUST, Wuhan, China
Octane <sup>43</sup>	Watershed maximum	Gauss	LS	ImageJ	+	Univ. Connecticut, USA
PeakFit	Band-pass filtering, local maximum	Gauss	LS	ImageJ	+	Univ. Sussex, UK
PeakSelector <sup>44</sup>	Time-domain filtering, adaptive threshold	Gauss	LS	IDL, Matlab	-	HHMI, USA
PYME <sup>27</sup>	Wiener filtering, adaptive threshold	Arbitrary	LS	Python	+	Univ. Auckland, New Zealand
QuickPALM <sup>45</sup>	Band-pass filtering, fixed SNR threshold	Gauss	CoMass	ImageJ	+	Institut Pasteur, France
RadialSymmetry <sup>46</sup>	Filtering, local max., minimal distance to gradient	Radial	CoSym	Matlab	+	Univ. Oregon, Eugene, USA
rapidSTORM <sup>12</sup>	Low-pass filtering, local maximum	Gauss	LS, MLE	Stand-alone	+	Univ. Würzburg, Germany
SimplePALM <sup>47</sup>	Variance stabilization denoising, DoG, probabilistic threshold	n/a	Mean-shift	Stand-alone	-	Molecular Genetics Center, Gif-sur-Yvette, France
simpleSTORM <sup>14</sup>	Self-calibration, noise normalize, background subtraction, P value	Gauss, measured	Interpolation	Stand-alone	+	Univ. Heidelberg, Germany
SNSMIL	Gaussian filtering, fixed contrast threshold	Gauss	LS	Stand-alone	+	NCNST, Beijing, China
SOSplugin	Wavelet transform, local maximum, Gaussian mixture	Gauss	LS	ImageJ	+	Erasmus MC, Rotterdam, the Netherlands
ThunderSTORM <sup>15</sup>	Extensive collection of methods, preview, filtering, local maximum	Gauss	LS, MLE	ImageJ	+	Charles Univ., Prague, Czech Republic
W-fluoroBancroft <sup>48</sup>	Wavelet, adaptive threshold	Gauss	fb	Matlab	+	Boston Univ., USA
WaveTracer <sup>49</sup>	Wavelet, watershed maximum	Gauss	LS	Metamorph	-	Univ. Bordeaux, France
WTM <sup>50</sup>	Wedge template matching (HD)	Wedge	Match.	Stand-alone	-	Hamamatsu Photonics, Japan

The software packages whose manufacturers participated in our study are listed. The study is ongoing, and this list will be updated at <http://bigwww.epfl.ch/smlm/software/>. Software marked 'ImageJ' runs on compatible products ImageJ, Fiji, Icy and ImageJ2. Abbreviations for PSF: Gauss, Gaussian, elliptical Gaussian or averaged Gaussian. Abbreviations for methods: ADMM, alternating direction method of multipliers; CoMass, center of mass; CoSym, center of symmetry; fb, fluoroBancroft; LS, least-squares; MAP, maximum a posteriori; MLE, maximum-likelihood estimator; MMSE, minimum mean-square error; REG, regression. Abbreviations regarding open access: +, available online (sometimes upon request); -, not available or included in commercial package.

we encouraged the developers themselves to run their own software, guided by the training data. To alleviate the difficulty of presetting parameters, we suggest that developers incorporate

self-calibration capabilities or dynamically tune the parameters<sup>26</sup>. We predict that this will be one of the key factors determining the success of future software<sup>14</sup>.

**Table 2** | Quantitative comparison for long-sequence (LS) and high-density (HD) data

Criteria	Physical values					Grades						Score	Run by
	JAC	ACC	SNR	FRC	CORR	JAC	ACC	SNR	FRC	USA	TIME		
<b>LS data</b>													
Unit	%	nm	dB	nm	%	[0.5]	[0.5]	[0.5]	[0.5]	[0.5]	[0.5]	[0.5]	[0.5]
Weights						1	1	1	1	0.25	0.25		
3D-DAOSTORM	62.5	36.1	6.0	71.1	n/a	3.58	3.67	4.20	3.03	3.00	1.98	3.44	Author
a-livePALM	54.5	35.6	5.1	62.6	n/a	2.02	3.74	3.13	3.71	2.50	3.97	3.09	Author
Auto-Bayes (W)	<b>69.1</b>	45.4	5.6	66.7	n/a	4.83	2.00	3.72	3.38	0.00	0.41	3.05	Author
B-recs	64.2	40.4	5.9	74.1	51.2	3.91	2.89	4.07	2.78	0.00	0.00	2.96	Author
Fast-ML-HD	52.9	44.9	3.7	83.9	60.6	1.72	2.08	1.40	2.00	0.00	0.00	1.43	Author
FPGA	47.8	36.3	4.2	81.3	62.8	0.73	3.63	2.01	2.21	0.00	4.11	2.00	Author
Gauss2dcirc	53.8	71.5	1.1	143.2	64.0	1.90	0.00	0.00	0.00	3.00	2.75	0.69	Expert
GPUgaussMLE	60.9	44.0	4.4	65.5	2.8	3.26	2.25	2.26	3.48	4.00	3.00	2.78	Author
GraspJ	51.7	47.2	4.4	77.2	n/a	1.48	1.67	2.22	2.54	4.50	5.00	2.13	Author
InSight3	53.9	41.8	4.1	74.5	53.5	1.90	2.64	1.91	2.75	2.50	2.50	2.19	Author
Maliang	53.3	35.6	4.4	69.5	60.4	1.80	3.75	2.22	3.16	1.50	0.50	2.44	Author
MicroManager	55.3	34.5	4.9	64.3	57.7	2.18	3.95	2.87	3.57	5.00	5.00	3.28	Author
MrSE	54.6	34.8	4.5	67.6	n/a	2.05	3.89	2.35	3.31	1.50	0.50	2.60	Author
Octane	42.7	53.9	3.2	114.4	n/a	0.00	0.48	0.84	0.00	4.00	3.99	0.62	Expert
PeakFit	60.0	34.9	5.5	64.6	59.5	3.09	3.87	3.61	3.55	4.50	3.07	3.51	Author
PeakSelector	49.8	40.3	5.2	66.9	59.4	1.11	2.91	3.18	3.36	0.00	2.50	2.39	Expert
PYME	48.6	36.5	3.5	73.8	n/a	0.88	3.58	1.16	2.81	3.00	3.97	2.13	Author
QuickPALM	41.9	50.6	3.5	95.4	57.7	0.00	1.05	1.21	1.08	5.00	5.00	1.14	Author
RadialSymmetry	47.3	<b>31.0</b>	4.4	74.4	n/a	0.64	4.57	2.21	2.76	4.00	4.11	2.61	Author
RapidSTORM	54.7	45.4	5.5	68.4	61.7	2.06	1.99	3.60	3.25	5.00	5.00	2.88	Author
SimplePALM	68.8	44.4	5.8	79.1	n/a	4.79	2.17	3.96	2.39	0.00	5.00	3.15	Author
SimpleSTORM	67.9	40.8	5.6	66.3	n/a	4.61	2.81	3.64	3.41	5.00	2.74	3.59	Author
SNSMIL	63.0	45.3	5.0	66.0	n/a	3.66	2.01	3.03	3.44	0.00	2.17	2.73	Author
SOSplugin	59.2	37.8	5.7	70.0	n/a	2.94	3.35	3.77	3.11	2.00	3.69	3.18	Author
ThunderSTORM	68.6	40.0	6.0	<b>60.8</b>	46.5	4.75	2.97	4.14	3.85	5.00	1.41	<b>3.81</b>	Author
W-fluoroBancroft	61.9	56.5	1.5	113.8	n/a	3.45	0.00	0.00	0.00	1.50	3.70	1.02	Author
WaveTracer	60.0	38.8	<b>6.1</b>	69.5	n/a	3.08	3.17	4.28	3.16	2.50	0.00	3.12	Author
WTM	66.0	47.6	4.0	89.7	60.5	4.24	1.61	1.83	1.54	0.00	3.28	2.08	Author
Average on LS	57.0	42.6	4.6	77.7									
Gauss		43.6	4.6	78.1									
Radial		32.9	4.4	71.0									
Generation 1		59.5	2.0	117.5									
Generation 2		40.8	4.9	72.1									
Generation 3		39.9	5.0	75.2									
<b>HD data</b>													
B-recs	<b>63.7</b>	78.4	<b>4.4</b>	93.2	20.2	5.00	1.76	4.44	3.86	0.00	0.00	<b>3.35</b>	Author
DAOSTORM	45.1	82.2	3.9	<b>78.5</b>	27.5	3.99	0.91	3.52	4.60	3.00	0.00	3.06	Author
FALCON <sup>a</sup>	39.1	75.5	3.9	99.2	17.3	3.38	2.42	3.49	3.56	3.00	0.00	3.02	Author
Fast-ML-HD	52.1	80.3	3.4	104.6	19.7	4.70	1.33	2.53	3.29	0.00	0.00	2.63	Author
FPGA	14.3	70.2	3.0	104.9	30.1	0.89	3.59	1.68	3.27	0.00	4.11	2.32	Author
L1H	42.5	76.9	3.6	136.1	n/a	3.73	2.10	2.81	1.71	3.00	1.62	2.56	Author
Octane	18.2	<b>62.9</b>	3.0	124.0	n/a	1.28	5.00	1.83	2.32	4.00	3.99	2.76	Expert
PeakFit	37.3	81.5	3.9	105.9	11.9	3.20	1.07	3.39	3.22	4.50	3.07	2.84	Author
PeakSelector	15.7	84.4	3.5	87.8	n/a	1.03	0.43	2.78	4.13	0.00	2.50	2.00	Expert
RadialSymmetry	11.8	61.5	2.0	164.2	n/a	0.64	5.00	0.00	0.30	4.00	4.11	1.77	Author
SimpleSTORM	27.9	70.5	3.6	131.8	n/a	2.26	3.54	2.90	1.92	5.00	2.74	2.79	Author
SNSMIL	23.3	80.8	3.3	143.2	n/a	1.80	1.23	2.29	1.35	0.00	2.17	1.60	Author
SOSplugin	18.2	71.8	3.6	106.2	n/a	1.28	3.23	2.85	3.21	2.00	3.69	2.67	Author
ThunderSTORM	31.7	70.9	2.9	154.2	15.7	2.64	3.44	1.67	0.80	5.00	1.41	2.26	Author
W-fluoroBancroft	19.2	80.9	0.8	203.5	n/a	1.38	1.19	0.00	0.00	1.50	3.70	0.86	Author
WTM	54.2	85.5	4.4	91.2	21.9	4.91	0.17	4.36	3.96	0.00	3.28	3.16	Author
Average on HD	32.2	75.9	3.3	120.5									

<sup>a</sup>Software version under development.

Performance measures for the indicated software packages are shown. JAC, Jaccard index; ACC, localization error; SNR, image quality; FRC, image resolution; USA, usability; TIME, computational time. Bold numbers indicate top scorers. The correlation of the estimated number of photons (CORR) was excluded from our analysis but is given here for the sake of completeness. The relative grades are normalized on a scale from 0 (worst) to 5 (best). The score is a weighted sum of the six criteria; here, the weights are 1 for the four quantitative criteria, 0.25 for the usability, and 0.25 for the computational time.

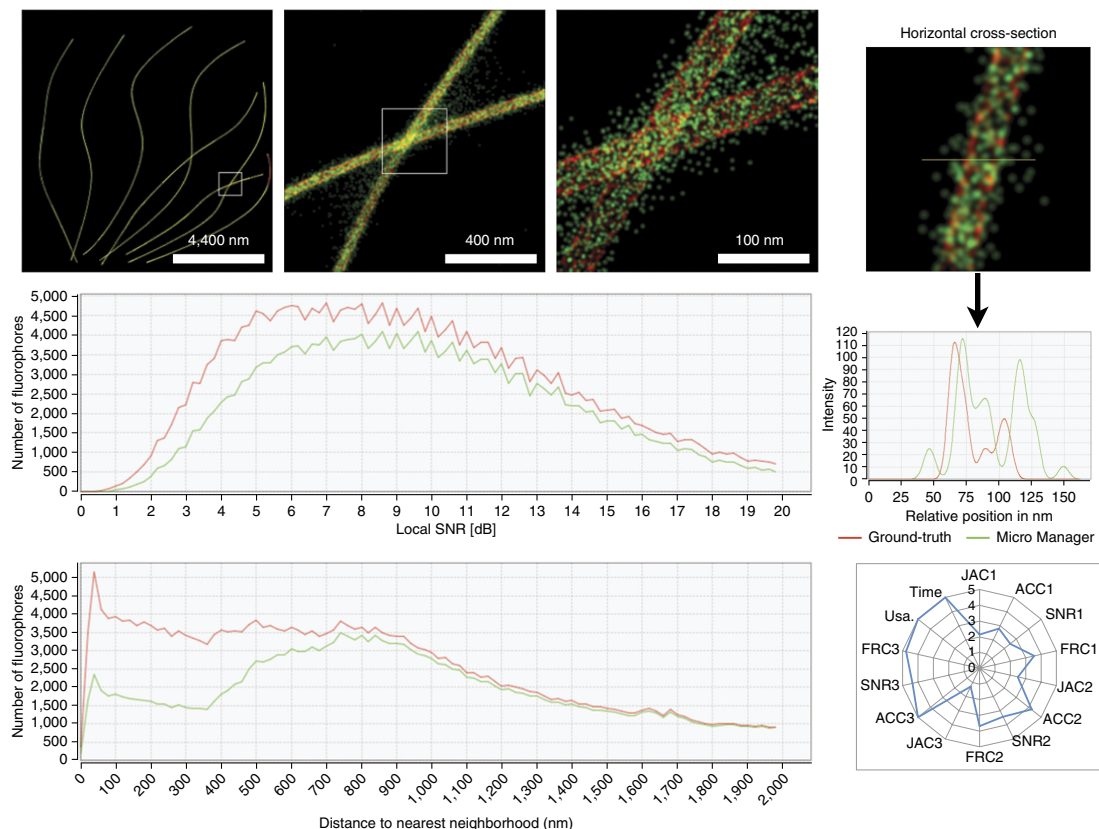


**Figure 4** | Illustration of an assessment report. Every participant to the challenge received a detailed report including figures and plots as shown; the particular instance shown here corresponds to the MicroManager software. Three top left images: renderings (see the caption of **Fig. 3** for explanations). Middle left plot, distribution of the local  $SNR_f$  in the range 0 dB–20 dB; the green and the red curves correspond to the evaluated software and the ground truth, respectively. Bottom left plot, distribution of the distance to the nearest-neighbor  $d_{NN}$  in the range 0 nm–2,000 nm, same color conventions. Top right image, cross-section. Middle right plot, intensity profile along the yellow line seen in the cross-section. Lower right, radar plot of the grades.

The simulated ground-truth data used for our comparison remain accessible to future participants. We pledge to extend this study with new results as they become available and to enrich our collection of data. We plan to include additional features such as several levels of molecule density, 3D (PSF engineering and multiple planes), drift and various noise models for EMCCD cameras and sCMOS (scientific complementary metal-oxide-semiconductor) cameras.

We encouraged all participants to produce output data in common formats to facilitate interoperability and to promote independent rendering software<sup>27</sup> (<https://github.com/PALMsiever/>). A first step in this direction was taken by many participants in the IEEE International Symposium on Biomedical Imaging 2013 (ISBI 2013) challenge.

Our study has shown that a simple Gaussian PSF model is sufficiently accurate for low-density data, whereas the quality of high-density imaging depends strongly on the model of the PSF. We predict that the PSF model will have an even more significant role in 3D SMLM applications. We see great potential in a two-phase reconstruction workflow—a first reconstruction that is fast but has reduced performance, followed by a slower run that yields improved results.

## METHODS

Methods and any associated references are available in the [online version of the paper](#).

*Note: Any Supplementary Information and Source Data files are available in the online version of the paper.*

## ACKNOWLEDGMENTS

We thank N. Olivier for providing the experimental data and R. Nieuwenhuizen for his technical assistance in running the Fourier ring correlation. We thank also P. Thévenaz for critical reading and for his assistance in writing the manuscript. We thank the participants in the ISBI 2013 localization microscopy challenge: S. Anthony, S. Andersson, T. Ashley, D. Baddeley, K. Bennett, J. Boulanger, N. Brede, L. Dai, L. Fiaschi, F. Gruell, G. Hagen, R. Henriques, A. Herbert, S. Holden, E. Hoogendoorn, B. Huang, Z.-L. Huang, A. Kechkar, K. Kim, M. Kirchgessner, U. Koethe, P. Krizek, M. Lakadamyali, Y. Li, K. Lidke, R. McGorty, L. Muresan, R. Parthasarathy, B. Rieger, H. Rouault, M. Sauer, J.-B. Sibarita, I. Smal, A. Small, S. Stahlheber, Y. Tang, Y. Wang, S. Watanabe, S. Wolter, J.C. Ye and C. Zimmer. This work was supported by the Biomedical Imaging Group, the School of Engineering at the Ecole Polytechnique Fédérale de Lausanne, the European Research Council (ERC) FUN-SP project (267439), the ERC Starting Grant PALMassemby (243016) and the Eurobioimaging Project (WP11).

## AUTHOR CONTRIBUTIONS

D.S., H.K., T.P., J.M. and N.S. conceived the project. D.S. developed the project and organized the challenge with contribution from all authors. D.S. and H.K. wrote the code for the simulated data and analyzed the results. S.M. and M.U. directed the project. D.S. and H.K. wrote the manuscript with input from all authors.

## COMPETING FINANCIAL INTERESTS

The authors declare no competing financial interests.

Reprints and permissions information is available online at <http://www.nature.com/reprints/index.html>.

1. Betzig, E. *et al.* Imaging intracellular fluorescent proteins at nanometer resolution. *Science* **313**, 1642–1645 (2006).
2. Rust, M.J., Bates, M. & Zhuang, X. Sub-diffraction-limit imaging by stochastic optical reconstruction microscopy (STORM). *Nat. Methods* **3**, 793–795 (2006).
3. Hess, S.T., Girirajan, T.P. & Mason, M.D. Ultra-high resolution imaging by fluorescence photoactivation localization microscopy. *Biophys. J.* **91**, 4258–4272 (2006).
4. Balzarotti, F. & Stefani, F.D. Plasmonics meets far-field optical nanoscopy. *ACS Nano* **6**, 4580–4584 (2012).
5. Walder, R., Nelson, N. & Schwartz, D.K. Super-resolution surface mapping using the trajectories of molecular probes. *Nat. Commun.* **2**, 515 (2011).
6. Manley, S., Gunzenhäuser, J. & Olivier, N. A starter kit for point-localization super-resolution imaging. *Curr. Opin. Chem. Biol.* **15**, 813–821 (2011).
7. Schermelleh, L., Heintzmann, R. & Leonhardt, H. A guide to super-resolution fluorescence microscopy. *J. Cell Biol.* **190**, 165–175 (2010).
8. Sauer, M. Localization microscopy coming of age: from concepts to biological impact. *J. Cell Sci.* **126**, 3505–3513 (2013).
9. Moerner, W.E. New directions in single-molecule imaging and analysis. *Proc. Natl. Acad. Sci.* **104**, 12596–12602 (2007).
10. Small, A. & Stahlheber, S. Fluorophore localization algorithms for super-resolution microscopy. *Nat. Methods* **11**, 267–279 (2014).
11. Endesfelder, U. & Heilemann, M. Art and artifacts in single-molecule localization microscopy: beyond attractive images. *Nat. Methods* **11**, 235–238 (2014).
12. Wolter, S., Endesfelder, U., van de Linde, S., Heilemann, M. & Sauer, M. Measuring localization performance of super-resolution algorithms on very active samples. *Opt. Express* **19**, 7020–7033 (2011).
13. Kirshner, H., Aguet, F., Sage, D. & Unser, M. 3-D PSF fitting for fluorescence microscopy: implementation and localization application. *J. Microsc.* **249**, 13–25 (2013).
14. Köthe, U., Herrmannsdorfer, F., Kats, I. & Hamprecht, F.A. SimpleSTORM: a fast, self-calibrating reconstruction algorithm for localization microscopy. *Histochem. Cell Biol.* **141**, 613–627 (2014).
15. Ovesný, M., Krízek, P., Borkovec, J., Svindrych, Z. & Hagen, G.M. ThunderSTORM: a comprehensive ImageJ plugin for PALM and STORM data analysis and super-resolution imaging. *Bioinformatics* **30**, 2389–2390 (2014).
16. Ovesný, M., Krízek, P., Svindrych, Z. & Hagen, G.M. High density 3D localization microscopy using sparse support recovery. *Opt. Express* **22**, 31263–31276 (2014).
17. Ma, H., Kawai, H., Toda, E., Zeng, S. & Huang, Z.-L. Localization-based super-resolution microscopy with an sCMOS camera part III: camera embedded data processing significantly reduces the challenges of massive data handling. *Opt. Lett.* **38**, 1769–1771 (2013).
18. Wang, Y. *et al.* Localization events-based sample drift correction for localization microscopy with redundant cross-correlation algorithm. *Opt. Express* **22**, 15982–15991 (2014).
19. Mandula, O., Šesták, I.Š., Heintzmann, R. & Williams, C.K. Localisation microscopy with quantum dots using non-negative matrix factorisation. *Opt. Express* **22**, 24594–24605 (2014).
20. Rieger, B. & Stallinga, S. The lateral and axial localization uncertainty in super-resolution light microscopy. *ChemPhysChem* **15**, 664–670 (2014).
21. Nieuwenhuizen, R.P.J. *et al.* Measuring image resolution in optical nanoscopy. *Nat. Methods* **10**, 557–562 (2013).
22. Mukamel, E.A., Babcock, H. & Zhuang, X. Statistical deconvolution for superresolution fluorescence microscopy. *Biophys. J.* **102**, 2391–2400 (2012).
23. Abraham, A.V., Ram, S., Chao, J., Ward, E.S. & Ober, R.J. Quantitative study of single molecule location estimation techniques. *Opt. Express* **17**, 23352–23373 (2009).
24. Thompson, R.E., Larson, D.R. & Webb, W.W. Precise nanometer localization analysis for individual fluorescent probes. *Biophys. J.* **82**, 2775–2783 (2002).
25. Ober, R.J., Ram, S. & Ward, E.S. Localization accuracy in single-molecule microscopy. *Biophys. J.* **86**, 1185–1200 (2004).
26. Holden, S.J. *et al.* High throughput 3D super-resolution microscopy reveals *Caulobacter crescentus* *in vivo* Z-ring organization. *Proc. Natl. Acad. Sci. USA* **111**, 4566–4571 (2014).
27. Baddeley, D., Cannell, M.B. & Soeller, C. Visualization of localization microscopy data. *Microsc. Microanal.* **16**, 64–72 (2010).
28. Babcock, H., Sigal, Y. & Zhuang, X. A high-density 3D localization algorithm for stochastic optical reconstruction microscopy. *Opt. Nanoscopy* **1**, 1–10 (2012).
29. Li, Y., Ishitsuka, Y., Hedde, P.N. & Nienhaus, G.U. Fast and efficient molecule detection in localization-based super-resolution microscopy by parallel adaptive histogram equalization. *ACS Nano* **7**, 5207–5214 (2013).
30. Zhu, L., Zhang, W., Elnatan, D. & Huang, B. Faster STORM using compressed sensing. *Nat. Methods* **9**, 721–723 (2012).
31. Holden, S.J., Uphoff, S. & Kapanidis, A.N. D.A.O.S.T.O.R.M.: an algorithm for high-density super-resolution microscopy. *Nat. Methods* **8**, 279–280 (2011).
32. Hoogendoorn, E. *et al.* in *Focus on Microscopy (FOM2013)* (Maastricht, the Netherlands, 2013).
33. Min, J. *et al.* FALCON: fast and unbiased reconstruction of high-density super-resolution microscopy data. *Sci. Rep.* **4**, 4577 (2014).
34. Kim, K.S. *et al.* in *Proceedings of the 10th International Conference on Sampling Theory and Applications (SAMPTA)* (Bremen, Germany, 2013).
35. Grüll, F., Kirchgessner, M., Kaufmann, R., Hausmann, M. & Kehschull, U. in *2011 International Conference on Field Programmable Logic and Applications (FPL)* 1–5 (2011).
36. Anthony, S.M. & Granick, S. Image analysis with rapid and accurate two-dimensional Gaussian fitting. *Langmuir* **25**, 8152–8160 (2009).
37. Smith, C.S., Joseph, N., Rieger, B. & Lidke, K.A. Fast, single-molecule localization that achieves theoretically minimum uncertainty. *Nat. Methods* **7**, 373–375 (2010).
38. Brede, N. & Lakadamyali, M. GraspJ: an open source, real-time analysis package for super-resolution imaging. *Opt. Nanoscopy* **1**, 11 (2012).
39. Babcock, H.P., Moffitt, J.R., Cao, Y. & Zhuang, X. Fast compressed sensing analysis for super-resolution imaging using L1-homotopy. *Opt. Express* **21**, 28583–28596 (2013).
40. Starr, R., Stahlheber, S. & Small, A. Fast maximum likelihood algorithm for localization of fluorescent molecules. *Opt. Lett.* **37**, 413–415 (2012).
41. Quan, T. *et al.* Ultra-fast, high-precision image analysis for localization-based super resolution microscopy. *Opt. Express* **18**, 11867–11876 (2010).
42. Ma, H., Long, F., Zeng, S. & Huang, Z.-L. Fast and precise algorithm based on maximum radial symmetry for single molecule localization. *Opt. Lett.* **37**, 2481–2483 (2012).
43. Niu, L. & Yu, J. Investigating intracellular dynamics of FtsZ cytoskeleton with photoactivation single-molecule tracking. *Biophys. J.* **95**, 2009–2016 (2008).
44. Shtengel, G. *et al.* Interferometric fluorescent super-resolution microscopy resolves 3D cellular ultrastructure. *Proc. Natl. Acad. Sci. USA* **106**, 3125–3130 (2009).
45. Henriques, R. *et al.* QuickPALM: 3D real-time photoactivation nanoscopy image processing in ImageJ. *Nat. Methods* **7**, 339–340 (2010).
46. Parthasarathy, R. Rapid, accurate particle tracking by calculation of radial symmetry centers. *Nat. Methods* **9**, 724–726 (2012).
47. Boulanger, J. *et al.* Patch-based non-local functional for denoising fluorescence microscopy image sequences. *IEEE Trans. Med. Imaging* **29**, 29 (2010).
48. Andersson, S.B. Localization of a fluorescent source without numerical fitting. *Opt. Express* **16**, 18714–18724 (2008).
49. Kechkar, A., Nair, D., Heilemann, M., Choquet, D. & Sibarita, J.-B. Real-time analysis and visualization for single-molecule based super-resolution microscopy. *PLoS ONE* **8**, e62918 (2013).
50. Watanabe, S., Bennett, K., Takahashi, T. & Takeshima, T. in *Focus on Microscopy (FOM2013)* (Maastricht, the Netherlands, 2013).

## ONLINE METHODS

**Data.** Establishing reference data is a key point for conducting a fair evaluation of image analysis algorithms; all software packages should use the same benchmark data sets. In microscopy, biologists and practitioners prefer real experimental image sequences, while algorithm developers need simulated data sets with ground-truth information. Here, we provide both: real experimental data sets which are mostly useful for visual inspection and synthetic simulated data sets, which are intensively used for the quantitative evaluation.

**Experimental data.** We acquired two sequences of images of tubulins, one in low-density imaging conditions (ReALLS, a long sequence of 15,000 frames of  $64 \times 64$  pixels) and one in high-density imaging conditions (RealHD, a short sequence of 500 high-density frames of  $64 \times 64$  pixels). The sample is Cos-7 cells fixed in methanol. The microtubules are stained with  $\alpha$ -tubulin primary antibodies and Alexa-647-conjugated secondary antibody fragments.

**Simulated data.** To achieve realistic images, we defined mathematical models for biological structure. We chose microtubules because they are often used to showcase SMLM studies. They are components of most eukaryotic cells which have widths smaller than the diffraction limit of the conventional light microscope. Microtubules are defined with their central axis elongating in a 3D space having an average outer diameter of 25 nm with an inner, hollow tube of 15 nm diameter.

To obtain rendered images at all scales including very high resolution (up to 1 nm/pixel), we represent the continuous-domain 3D curve by means of a polynomial spline. The sample is imaged in a limited field of view, i.e., less than  $20 \times 20 \mu\text{m}^2$ , and the centerlines of the microtubules have limited variation along the  $z$  (vertical) axis, i.e., less than 1  $\mu\text{m}$ . The fluorescent markers are uniformly distributed over the structure according to the required density. We randomly assign each fluorophore with a random photon emission rate and with an active time instant according to a statistical lifetime model. For the synthetic data sets, we developed a simulator that can generate realistic image sequences of thousands frames resulting from the stochastic activation of millions of fluorophores.

The sample structure, fluorophore excitation, and image formation can be completely controlled with a large number of user configurable parameters (**Supplementary Note 3**). We defined the underlying sample structure in a continuous space which allows rendering of digital images at any scale. The exact locations of all fluorophores are therefore stored at high precision, as floating point numbers expressed in nanometers. This ground-truth file is useful for conducting objective evaluations without human bias.

**Photon emission model.** We calculate the photon flux in the following manner<sup>51</sup>:

$$F = \Phi \frac{P}{e} \sigma$$

where  $\Phi$  is the quantum yield of the dye,  $P$  is the excitation laser power in  $\text{W}/\text{cm}^2$ ,  $e$  is the energy of a single photon,  $\sigma = 1,000 \epsilon \ln(10)/\text{NA}$  is the absorption cross section,  $\epsilon$  is the absorptivity coefficient of the dye and NA is the numerical aperture of the lens. The spatial variation of the excitation laser power,  $P$ , is modulated by a unimodal function that produces higher excitation

at the center, rather than the border, of the field of view. The flux  $F$  is given in photons/s, and it is used for randomly determining a flux value for every excited fluorophore under a probability density function of a Poisson random variable.

Once the flux has been determined for the excited fluorophore, we choose an active duration  $A$  and a life-time model for computing the number of photons that would be emitted during the frame acquisition time  $T$ . We proposed three different life-time models: constant, linearly decreasing and exponentially decaying. This last is motivated by photobleaching phenomenon. An additional temporal parameter is a time delay  $\Delta$  between the beginning of the frame and the time the fluorophore starts emitting photons. In this study, we chose  $A$ ,  $\Delta$  and  $T$  to be random variables but we impose that most of the photons of a single molecule are emitted within a single frame.

**Source of photons.** We consider three independent sources of photons: the signal of interest (the activated molecule) modeled as described above, the background signal normally distributed, slowly changes with time, and the autofluorescent signal simulated by introducing deep clusters of intense fluorophores that are constantly in an active mode, slowly changes with time. We sum these three sources of photons to yield the image that impinges on the detector. We then generate the microscopic image of each fluorophore by simulating the image formation process (Fig. 1b). Noise sources and perturbations include: non-homogeneous excitation laser power; random nature of the emission process of the fluorophore; shot noise for small photons count; EMCCD and read-out noise models.

A volumetric density parameter  $\rho$  controls the number of fluorophores per  $\mu\text{m}^3$  that we generate. This parameter, together with the number of frames parameter, controls the total imaging density conditions: low-density, long sequences (LS) and high-density sequences (HD).

**High-density.** A recent trend in the super-resolution localization microscopy is the development of methods to detect multiple overlapping emitters in high density data sets<sup>31,41,52–55</sup>. To benchmark these methods, our generated HD are particularly suitable. Taking advantage of the exact knowledge of the sample structure, we defined three properties to qualify the density of the sequence: the average distance  $d_{\text{NN}}$  of a fluorophore to its nearest fluorophore within the same frame, the average number of fluorophores  $N$  per frame, and the average number of fluorophores  $M$  per  $\mu\text{m}^2$ . We obtained the following properties:  $d_{\text{NN}} = 1,536.1 \text{ nm}$ ,  $N = 26.3 \text{ nm}$ ,  $M = 0.14$  for LS data sets and  $d_{\text{NN}} = 156.9 \text{ nm}$ ,  $N = 562.7 \text{ nm}$ ,  $M = 2.19$  for HD data sets. The high number of fluorophores per frame and the small  $d_{\text{NN}}$  setting induce numerous overlapping of PSFs in the HD data sets.

**Image formation.** We put our effort in implementing a faithful reproduction of the physical reality to produce plausible synthetic images. The individual fluorophores, which are taken to be ideal point source, are convolved with the PSF of the microscope. Here, two models of PSF were considered, the defocussed Gaussian PSF model and the Gibson and Lanni PSF model.

The  $xy$ -Gaussian and  $z$ -exponential PSF model is defined as a 2D Gaussian function in the  $xy$  plane centered at  $(x_c, y_c)$  in

$$f(x, y, z) = A(z) e^{-\frac{(x-x_c)^2 + (y-y_c)^2}{2\sigma^2(z)}}$$

where the variance depends on the axial position of the particle,

$$\sigma(z) = \frac{\lambda}{2NA} e^{\log(2)} \left| \frac{z - z_{\text{focus}}}{z_{\text{defocus}} - z_{\text{focus}}} \right|$$

The amplitude  $A(z)$  is chosen in such a way as to make  $f(x,y,z)$  have a unit norm at every value of  $z$ . The value  $z_{\text{focus}}$  is the axial position of the focal plane and  $z_{\text{focus}}$  allows one to introduce defocusing effects. The  $xy$ -Gaussian and  $z$ -exponential is a common approximation of the main lobe of the Airy pattern.

The scalar Gibson-Lanni model generates a more accurate PSF by using a 3-layer model taking into account refractive index mismatch at each optical interface. We rely on our accurate and fast implementation of the Gibson and Lanni PSF model to evaluate millions of convolution operations in very high resolution (5 nm/pixel) in a reasonable amount of time.

*Conversion of photons to a digital number.* At this stage, the number of electrons is converted to a digital number DN<sup>56</sup> by a simulated A/D converter that is characterized by a linear gain and an offset. Readout noise (Gaussian distributed) and dark noise (Poisson distributed) are added, as well. Final pixel values are calculated by checking for saturation and by quantization into 14-bits. Our simulated EMCCD camera down-samples the high resolution image from 5 nm/pixel to 100 or 150 nm/pixel by means of averaging. We then simulated the electron multiplier component by multiplying every pixel value by the EM noise factor  $2^{1/2}$ .

*Data delivery.* The frames are stored in a standard uncompressed 16-bits TIFF format. While typical experimental data consists of 10,000 frames, we restricted the number of frames so as to have data sets of moderate size, say 300 MB, after lossless compression. Such file sizes are still convenient to download from the Internet. Our data sets are accompanied by metadata information that includes microscope and camera parameters that are usually available in real experiment.

*Level of difficulty.* To produce data sets with different degrees of difficulty, we modified the contribution of autofluorescence, the level of acquisition noise, and the thickness of the sample. At the end of each simulation, we calculated two measures for every fluorophores:  $d_{\text{NN}}$ , the distance of the nearest neighborhood in the same frame;  $\text{SNR}_f$ , the local signal-to-noise ratio of a fluorophore. The  $\text{SNR}_f$  is the ratio of the difference of the peak signal and the mean of the local surrounding background and the standard deviation of the local background. For the HD data,  $d_{\text{NN}}$  is smaller than the size of the PSF, so that frames contain many overlapping PSFs (**Supplementary Note 3**).

*Future directions.* In the future, our reference data will include more features, such as drift, 3D localization (PSF engineering<sup>57,58</sup> and multiple planes<sup>59,60</sup>, additional levels of molecule density, multiple fluorescent channels, asymmetrical PSF due to dipole effect<sup>61</sup>, scattering effects, and a richer variety of noise models associated with various types of cameras, EMCCD, sCMOS<sup>62,63</sup>. It will also be interesting to generate benchmarking data to test the impact of clustering (spatial aggregation) and diffusion for single-particle tracking.

**Evaluation and scoring calculation.** *Theoretical accuracy.* The simplest theoretical localization precision is given by  $s/\sqrt{N}$ , where  $s$  is the size of the PSF and  $N$  is the number of detected

photons<sup>23,25</sup>. This Cramér-Rao lower bound (CRLB) was initially introduced as a fundamental limit of accuracy<sup>23,24,37</sup>. There also exist refined CRLBs that take pixelation, various sources of noise, and fluorescence background into account. A survey of localization accuracy and precision in the SMLM context can be found in Deschout *et al.*<sup>64</sup>, while uncertainties in the lateral localization in super-resolution microscopy were also addressed in Rieger *et al.*<sup>20</sup>.

Some of our data fail to be compatible with the restrictive assumptions needed to establish CRLBs. It is only over LS1 and LS2 that it is valid to compare the experimental accuracy of the tested software packages to the theoretical expectations. Selecting the five best algorithms, we found that the accuracies are 21.05 nm and 32.13 nm for LS1 and LS2, respectively. They are worse than predicted by Thompson's rule (13.98 nm, 15.96 nm), but it is known that Thompson's rule<sup>24</sup> is too optimistic. More-realistic results are obtained with a bound recently proposed that gives (19.10 nm, 25.78 nm)<sup>20</sup>.

*Matching of two sets of localization.* To establish statistical measures of detection rate and the localization accuracy, a pairing must first be found between the molecules localized by the participants and the molecules from the ground-truth. For each frame  $f$ , the pairing is obtained by solving a bi-partite graph-matching problem of minimizing the sum of distances between the two elements of a pair. The matching is enabled when the distance from  $P_{\text{ref}}(f)$  to its closest point  $P_{\text{test}}(f)$  is less than the full-width half-maximum (FWHM) of the PSF. We deployed two matching algorithms: the presorted nearest-neighbor search and the Hungarian algorithm (**Supplementary Software**). Both gave similar results.

*Computation of detection rate using the Jaccard index (JAC).* The localized molecules successfully paired with some ground-truth molecule are categorized as true positives, TP; the remaining localized molecules are farther than  $\rho$ , unpaired, and categorized as false positives, FP; finally, ground-truth molecules that are not associated with any localized molecule are categorized as false negatives, FN.

The detection rate quantifies the framewise fidelity and completeness of the set  $P_{\text{test}}(f)$  of localizations with respect to the ground-truth  $P_{\text{ref}}(f)$ . It involves the positive predictive value (precision  $p$ ), the sensitivity (recall  $r$ ) and the Jaccard index (JAC).

$$p = \frac{\text{TP}}{\text{FP} + \text{TP}}, \quad r = \frac{\text{TP}}{\text{FN} + \text{TP}}, \quad \text{JAC} = \frac{\text{TP}}{\text{FN} + \text{FP} + \text{TP}}$$

In this study, we observed that the precision value  $p$  is high (average 0.956, s.d. 0.09) in comparison to the recall value  $r$  (average 0.487, s.d. 0.25). We thus believe the most relevant measure of similarity between lists of localized molecules is the Jaccard index,  $j$  (i.e., JAC, in %).

*Computation of localization accuracy using the root-mean-square error (RMSE).* Let  $(x_n^{\text{Test}}, y_n^{\text{Test}})$  and  $(x_n^{\text{Ref}}, y_n^{\text{Ref}})$  be the  $n$ th matched pair, and where the superscripts Ref and Test indicate the oracle (ground-truth) and participant's list of localizations, respectively. The root-mean-square error (RMSE) of the matched localizations is

$$a^2 = \frac{1}{N} \sum_{n=1}^N (x_n^{\text{Test}} - x_n^{\text{Ref}})^2 + (y_n^{\text{Test}} - y_n^{\text{Ref}})^2$$

The expectation of  $a^2$  is the sum of the variance (precision) and the square of the bias (accuracy).

Independent computations convinced us that the bias is always negligible (unbiased estimators). Hence, the RMSE represents essentially the standard deviation of the errors, which is truly the precision of the estimator. Confusingly enough, in the specific lingo of the SMLM community, this term is called “accuracy” instead; we shall follow this improper terminology and call RMSE a localization accuracy.

*Computation of the image quality using signal-to-noise ratio (SNR).* To render an image, we let the contribution of each localized molecule take the form of an additive 2D Gaussian circular function with a standard deviation ten times smaller than the standard deviation of the PSF. Correspondingly, we let the resolution of the rendered image be ten times finer than that of the simulated camera with which we collected our synthetic data.

To compare the super-resolved image  $I_{\text{test}}$  to the oracle image  $I_{\text{ref}}$  we compute

$$\text{SNR} = 10 \log_{10} \frac{\|I_{\text{ref}}\|^2}{\|I_{\text{ref}} - I_{\text{test}}\|^2}$$

*Computation of the image resolution using the Fourier ring correlation (FRC).* Fourier-ring correlation (FRC) was recently introduced as a method for measuring the image resolution in the SMLM context<sup>21,65</sup>. In the formalism of FRC, the set of positions is partitioned in two halves to determine the resolution. In our case, we populate the first half with  $P_{\text{ref}}(f)$  and the second half with  $P_{\text{test}}(f)$ . The resolution is determined by applying the threshold  $T = 0.5$  on the spectral correlation curve which typically decays monotonically<sup>66</sup>.

*Parsing the localization files.* Because every software has its own file format, unit, axis and coordinate convention, we asked the participants to report their results in a delimiter-separated values text file (typically CSV), where every localized position in a frame is stored as a single row in this file. For every software, we created a description file (XML) containing the information to univocally parse the localization. The description file contains the type of separator (comma, tab...) the unit of position (nm, pixel), the first row containing fluorophore, the  $x$  and  $y$  shift of the system coordinate (center of the pixel, top-left corner), the unit of shift, the shift in the numbering of the frame (0, 1) and finally the column numbers in which to find the information:  $x$ ,  $y$ , intensity and frame. With this simple procedure, we succeeded in reading all localization files without modifying any software.

*Minimal bound on performance.* We developed a rudimentary ImageJ plugin in Java, called CenterOfGravity, to determine a lower performance bound. This software detects candidate molecules by thresholding the local maximum of the band-pass filter; the accurate position is simply the center of gravity of a local neighborhood window centered on the candidates. Two software packages consistently failed to meet this criteria and were not further evaluated.

*Usability.* For the practitioner, the usability of the software is an important aspect for the daily work. The usability (USA) evaluation cannot be carried out quantitatively because it involves human behavior and multiple interaction factors

between computer, data and users. Here, we follow the strategy of Carpenter *et al.*<sup>67</sup> and evaluate each software using two sources of information: a questionnaire that was filled out by the software developers and some testing of the software. The maximum usability grade is 5 and such a software fulfills the following requirements.

- Accessibility: easy to find and to download from the web. Non-accessible softwares are assigned a usability grade of 0.
- Open-source: free tool or an add-on of a free software (for example, ImageJ), accessible source code, no cost.
- Installation: no dependency of specific hardware, no requirements of additional library, easy to install, binaries for multi-platforms, multiple operation systems, double-click type installation, fast learning curve.
- Usage: user-friendly interface, intuitive parameters, documentation, interoperability.
- Maintenance: continued, long-term support, feedback mechanism.

*Computational time.* At first sight, execution runtime would appear to be measurable objectively. Unfortunately, the participating packages all exhibit some degree of dependence upon specific hardware installations and code-development environments. This prevented us from running every software by ourselves. As a proxy, we determined the computational runtime (TIME) by analyzing the answers we received from the participants and by normalizing it by the power of their machine.

We asked the algorithm developers to report not only their own run-time values but also the main specifications of the run-time machine. There is a large variety of processors among the participants of this study. We therefore weighted the runtime by “normalized” coefficient: 0.75 for relatively slow desktop machine (e.g. 2.70 Ghz Intel Core i5), 1.25 for fast desktop machines (e.g. 3.40 Ghz Intel 4 cores).

For computers that are equipped with additional hardware, like graphical processing unit (GPU) usage, or field-programmable gate array (FPGA), we assign a penalty factor of 3.00. Another aspect we take into account is non comparable tasks between the various packages. Some software measures only the elapsed time of the localization task. Others measure the full processing task: loading frames in memory, localization and rendering. We compensate for that by introducing an advantage factor of 0.75 and we apply it to software that measured the full processing task.

The runtime of every software was normalized by the above coefficients to yield a “normalized runtime” measure,  $T_n$ , which is mapped to a grade scale and clipped to between 0 and 5. We note that our grading should be regarded as a rough indicator of the software efficiency only.

*Grading and ranking.* For all criteria, JAC, ACC, SNR, FRC, USA and TIME, we attributed a normalized grade between 0 (worst case) and 5 (best case); see **Supplementary Data 2**. The values of criteria were normalized to impose an average of 2.5 and a s.d. of 1.5, and they are clipped to 0 and 5.

We computed an overall performance score as a weighted sum of the criteria (average over the 3 data sets if necessary). The final rank is associated with either low-density imaging data sets or

with high-density imaging data sets. We normalize the criteria values to be in the interval [0,5] and define the final score as

$$s = \frac{\lambda_{\text{JAC}} \cdot \overline{\text{JAC}} + \lambda_{\text{ACC}} \cdot \overline{\text{ACC}} + \lambda_{\text{SNR}} \cdot \overline{\text{SNR}} + \lambda_{\text{FRC}} \cdot \overline{\text{FRC}} + \lambda_{\text{USA}} \cdot \overline{\text{USA}} + \lambda_{\text{TIME}} \cdot \overline{\text{TIME}}}{\lambda_{\text{JAC}} + \lambda_{\text{ACC}} + \lambda_{\text{SNR}} + \lambda_{\text{FRC}} + \lambda_{\text{USA}} + \lambda_{\text{TIME}}}$$

We ran a principal-components analysis on the 4 criteria JAC, ACC, SNR and FRC showing that all criteria have an similar importance. We chose to compute an overall performance measure, as weighted sum, namely a score  $s$ , by choosing the following weights (see **Supplementary Fig. 3**).

**Challenge organization.** The organization of a world-wide challenge was an opportunity to get the attention of a large number of the developers working in different fields, including biology, biophysics and computer science. We broadly advertized the challenge trying to ensure coverage of most representative and well-known software and also to attract newcomers to the field. The Localization Microscopy challenge (<http://bigwww.epfl.ch/smlm>) was presented at the IEEE ISBI conference, at San Francisco, in April 2013. The high participation rate of the developers reveals the importance of this study. The localization task was carried out by the software developers themselves with the exception of PeakSelector, Octane and CSSTORM, which were performed by experts. By having the authors or experts use their own algorithms, we believe we obtained the best performance possible. We initially provided them with training data sets that included ground-truth information, allowing them to choose the appropriate mode and to properly tune the parameters of their algorithms. We assumed that developers were at the same time most knowledgeable about their software, and keenest on cranking out the best performance, guided by the training data. We also offered the opportunity to submit three different runs for each data sets with different settings. Only four participants (a-livePALM, Auto-Bayes, SimpleSTORM and SOSplugin) have chosen this option. Finally, we observed that the results were very similar from one run to the next. This is summarized in **Table 2** and reported in **Supplementary Data 2**.

This comparative study was first released at the IEEE ISBI 2013 Symposium (<http://bigwww.epfl.ch/smlm/>). Ever since, it has proved to be a valuable resource to developers and end users alike. The ISBI challenge has now turned into a permanent online

challenge and is referred to in the Grand Challenge in Medical Image Analysis website (<http://www.grand-challenge.org/>).

51. Hinterdorfer, P. & Oijen, A.V. *The Handbook of Single-Molecule Biophysics* (Springer, 2009).
52. Huang, F., Schwartz, S.L., Byars, J.M. & Lidke, K.A. Simultaneous multiple-emitter fitting for single molecule super-resolution imaging. *Biomed. Opt. Express* **2**, 1377–1393 (2011).
53. Wang, Y., Quan, T., Zeng, S. & Huang, Z.-L. PALMER: a method capable of parallel localization of multiple emitters for high-density localization microscopy. *Opt. Express* **20**, 16039–16049 (2012).
54. Babcock, H., Sigal, Y.M. & Zhuang, X. A high-density 3D localization algorithm for stochastic optical reconstruction microscopy. *Opt. Nanoscopy* **1**, 6 (2012).
55. Cox, S. *et al.* Bayesian localization microscopy reveals nanoscale podosome dynamics. *Nat. Methods* **9**, 195–200 (2012).
56. Janesick, J.R. *Photon Transfer* (SPIE Publications, 2007).
57. Huang, B., Wang, W., Bates, M. & Zhuang, X. Three-dimensional super-resolution imaging by stochastic optical reconstruction microscopy. *Science* **319**, 810–813 (2008).
58. Pavani, S.R.P. *et al.* Three-dimensional, single-molecule fluorescence imaging beyond the diffraction limit by using a double-helix point spread function. *Proc. Natl. Acad. Sci. USA* **106**, 2995–2999 (2009).
59. Juette, M.F. *et al.* Three-dimensional sub-100 nm resolution fluorescence microscopy of thick samples. *Nat. Methods* **5**, 527–529 (2008).
60. Ram, S., Prabhat, P., Ward, E.S. & Ober, R.J. Improved single particle localization accuracy with dual objective multifocal plane microscopy. *Opt. Express* **17**, 6881–6898 (2009).
61. Mortensen, K.I., Churchman, L.S., Spudich, J.A. & Flyvbjerg, H. Optimized localization analysis for single-molecule tracking and super-resolution microscopy. *Nat. Methods* **7**, 377–381 (2010).
62. Bennett, K., Takahashi, T., Sage, D. & Huang, Z. in *Fourth Single Molecule Localisation Microscopy Symposium (SMLMS'14)* (London, UK, 2014).
63. Huang, F. *et al.* Video-rate nanoscopy using sCMOS camera-specific single-molecule localization algorithms. *Nat. Methods* **10**, 653–658 (2013).
64. Deschout, H. *et al.* Precisely and accurately localizing single emitters in fluorescence microscopy. *Nat. Methods* **11**, 253–266 (2014).
65. Banterle, N., Bui, K.H., Lemke, E.A. & Beck, M. Fourier ring correlation as a resolution criterion for super-resolution microscopy. *J. Struct. Biol.* **183**, 363–367 (2013).
66. Rosenthal, P.B. & Henderson, R. Optimal determination of particle orientation, absolute hand, and contrast loss in single-particle electron cryomicroscopy. *J. Mol. Biol.* **333**, 721–745 (2003).
67. Carpenter, A.E., Kamentsky, L. & Eliceiri, K.W. A call for bioimaging software usability. *Nat. Methods* **9**, 666–670 (2012).

# Super-Resolution Imaging Strategies for Cell Biologists Using a Spinning Disk Microscope

Neveen A. Hosny<sup>1</sup>✉, Mingying Song<sup>1</sup>, John T. Connelly<sup>2</sup>, Simon Ameer-Beg<sup>3</sup>, Martin M. Knight<sup>4</sup>, Ann P. Wheeler<sup>1</sup>\*

**1** Blizard Institute, Barts and the Royal London School of Medicine and Dentistry, Queen Mary University London, London, United Kingdom, **2** Blizard Institute, Barts and the Royal London School of Medicine and Dentistry, Queen Mary University London, London, United Kingdom, **3** Randall Division of Cell and Molecular Biophysics, Kings College London, London, United Kingdom, **4** School of Engineering and Materials Science, Queen Mary University London, London, United Kingdom

## Abstract

In this study we use a spinning disk confocal microscope (SD) to generate super-resolution images of multiple cellular features from any plane in the cell. We obtain super-resolution images by using stochastic intensity fluctuations of biological probes, combining Photoactivation Light-Microscopy (PALM)/Stochastic Optical Reconstruction Microscopy (STORM) methodologies. We compared different image analysis algorithms for processing super-resolution data to identify the most suitable for analysis of particular cell structures. SOFI was chosen for X and Y and was able to achieve a resolution of *ca.* 80 nm; however higher resolution was possible  $>30$  nm, dependant on the super-resolution image analysis algorithm used. Our method uses low laser power and fluorescent probes which are available either commercially or through the scientific community, and therefore it is gentle enough for biological imaging. Through comparative studies with structured illumination microscopy (SIM) and widefield epifluorescence imaging we identified that our methodology was advantageous for imaging cellular structures which are not immediately at the cell-substrate interface, which include the nuclear architecture and mitochondria. We have shown that it was possible to obtain two coloured images, which highlights the potential this technique has for high-content screening, imaging of multiple epitopes and live cell imaging.

**Citation:** Hosny NA, Song M, Connelly JT, Ameer-Beg S, Knight MM, et al. (2013) Super-Resolution Imaging Strategies for Cell Biologists Using a Spinning Disk Microscope. PLoS ONE 8(10): e74604. doi:10.1371/journal.pone.0074604

**Editor:** Vadim E. Degtyar, University of California, Berkeley, United States of America

**Received** March 22, 2013; **Accepted** August 5, 2013; **Published** October 9, 2013

**Copyright:** © 2013 Hosny et al. This is an open-access article distributed under the terms of the Creative Commons Attribution License, which permits unrestricted use, distribution, and reproduction in any medium, provided the original author and source are credited.

**Funding:** Funding for NAH was provided by an Engineering and Physical Sciences Research Council/Medical Research Council discipline bridging grant. The funders had no role in study design, data collection and analysis, decision to publish, or preparation of the manuscript.

**Competing Interests:** The authors have declared that no competing interests exist.

\* E-mail: a.p.wheeler@qmul.ac.uk

✉ Current address: Department of Chemistry, Imperial College London, London, United Kingdom.

## Introduction

Many biological structures are too small to be resolved by standard confocal microscopy, which has a limit of resolution of approximately 200 nm. Until recently this has restricted the scope of research into small molecular structures and cellular complexes, such as bacteria, viruses, membrane vesicles, nuclear ultrastructure and cytoskeletal filaments. Super-resolution microscopy has circumvented this resolution limit, described by Abbe's law [1,2], permitting observations of structures as small as 30 nm in size. This technological revolution advances our understanding of molecular cell biology as it reveals novel biological phenomena at nanometre resolution.

Super-resolution techniques can be performed by a number of approaches [3]. Structured Illumination microscopy (SIM) is a technique where a grid pattern, generated from diffraction of light, is super-imposed on the specimen and rotated in steps. The output dataset is processed with specialised algorithms giving an improvement in lateral resolution by a factor of two [4]. Other techniques, such as STED, GSD, SSIM, PALM, STORM, FPALM, dSTORM, GSDIM and PAINT rely upon the principles of Reversible Saturable Optical Fluorescence Transitions (RESOLFT) microscopy. In RESOLFT proteins or organic fluorophores are switched between dark and fluorescent states

stochastically, data are captured and processed to give an output image with resolution refined beyond the Abbe limit of 200 nm [2,3,5].

Methods of super-resolution which use stochastic molecular switching, do not require specialised microscopy systems [5]; instead they generate super-resolved images by iteratively activating a set of photo-switchable fluorophores and precisely fitting the point of emission through complex image analysis [6,7]. Techniques such as photo-activation light microscopy (PALM) [6], stochastic optical reconstruction microscopy (STORM) [8] and ground state depletion microscopy (GSDIM) [9,10] all operate on the statistical methods principle. PALM uses photo-switchable fluorescent proteins and STORM/GSDIM photo-switchable fluorescent dyes to generate stochastic fluorescent emissions which are imaged and then processed to refine image resolution [5]. The methodologies employed by image processing algorithms for statistical SR methods fall broadly into two categories; specific identification of spatially separate individual fluorescent emission events and fitting of these events in an reconstructed image, e.g. RainSTORM [11], QuickPALM [12] and GLRT [13] or higher order statistical analysis of intensity fluctuations e.g. SOFI [14,15], 3B [16], Deconvolution-STORM (DeconSTORM) [17] and Faster-STORM [18] (Table S1). These latter group of image analysis methodologies, such as SOFI and Decon-STORM do not

require single molecule activations and were developed for super-resolution imaging of structures which may be more densely labelled by fluorescent dyes [15,17]. For all RESOLFT methods using iterative imaging of stochastic light emission the photon yield of the dye, detector sensitivity and detector resolution play a key role in determining the level of resolution improvement that can be obtained [19].

PALM, STORM and other forms of statistical super-resolution methodology require only a standard light microscope and electron-multiplying charge-coupled device (EMCCD) camera as hardware [5]. For these techniques to work well, image datasets must be acquired at fast frame rates and with good signal-to-noise (S/N). This ensures a sufficient number of stochastic fluorescent emission events are collected for the super-resolution image analysis algorithms to work accurately [1]. It can be challenging to obtain good S/N in PALM/STORM using biological samples in widefield illumination. This is due to photo-bleaching of the fluorophore labelling the epitope of interest, which reduces the number of fluorophores actively emitting light; and artefacts arising from photo-interactions above and below the focal plane. The out of focus light is generated from fluorescent emission of labelled proteins that are not in the desired plane of focus and the viscous nature of the cytoplasm, which scatters light [5]. These photo-interactions, from above and below the focal plane, impede correct reconstruction of the super-resolution image.

Total Internal Reflection Microscopy (TIRF) overcomes these issues by creating an evanescent wave that only illuminates a thin (<100 nm) optical section at the immersion oil and coverslip interface omitting out of focus light [20]. The excellent S/N this achieves makes TIRF the standard method for PALM and STORM imaging. Unfortunately, TIRF visualisation is not appropriate for all biological samples due to the limited imaging depth [20]. This means that structures further away from the coverslip than 100 nm such as; the cells' nucleus and organelles immediately surrounding the nucleus such as the endoplasmic reticulum, mitochondria and Golgi apparatus, are cannot be imaged using TIRF based PALM/STORM. Recent research has tried to overcome this problem by using a TIRF microscope with double objectives to visualise the actin cytoskeleton at the very top and the bottom of the cell [21]. Selective plane illumination microscopy (SPIM) has also been used to generate 3D super-resolution images [22]. Another alternative is 'near TIRF' where a highly inclined laminated optical light sheet (HILO) is generated using an intense laser illumination of light, angled through a high numeric aperture objective [23]. However, HILO only increases the depth of light penetration into the cell to 500 nm, so cellular structures which are 2–3  $\mu$ m inside the cell such as the nucleus, Golgi apparatus, Endoplasmic reticulum and mitotic spindle still cannot be visualised.

In widefield microscopy all of a specimen in the optical path of the microscope is excited by the light source. This means for a point source there will be in focus light and out of focus light present at the detector (Figure 1A). It is particularly important to improve the signal to noise ratio when imaging the nucleus at super-resolution as it is a dense structure in the centre of the cell and so a lot of out of focus light is present which degrades the quality and accuracy of the output image. Spinning disk confocal microscopy (SD) presents an excellent solution to this as it functions as a widefield confocal, selectively illuminating one focal plane with thousands of pinholes and omitting out of focus light (Figure 1A) [24–26]. The spinning disk speeds up the acquisition time, compared with a standard raster scanning confocal and improves the S/N ratio compared with a standard widefield epifluorescence. Combining the spinning disk together with

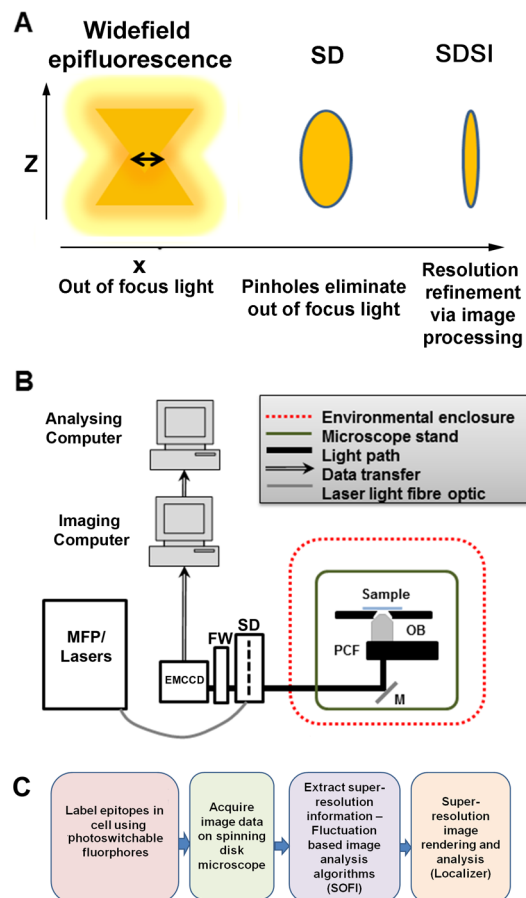


**Figure 1. Setup of spinning disk stochastic imaging (SDSI) system and evaluation of imaging capabilities.** (A) Schematic diagram describing how the point spread function is refined in a selected axial plane by spinning disk confocal microscopy and super-resolution image processing. (B) Diagram showing the configuration of the SDSI microscope, abbreviations are as follows. EMCCD = Electron multiplied Charge Coupled Device camera. FW = Filter wheel. SD = Yokogawa CSUX1 spinning disk, M = mirror. PCF = Piezo coupled focus feedback unit. OB = Objective. (C) Workflow of the SDSI experiments used in this paper. Briefly samples are prepared with probes for either PALM or dSTORM, next samples are imaged and finally SR data is generated using the SOFI image processing algorithm.

doi:10.1371/journal.pone.0074604.g001

super-resolution imaging allows a truly single plane super-resolution image to be acquired at any z-axis (Figure 1A), which allows any plane in the full depth of a cell to be imaged [25].

Here we combined the flexibility of an SD microscope with the simplicity of using PALM/STORM probes to present a novel methodology using spinning disk microscopy for super-resolution imaging (SDSI). We further present a comparative study of several image analysis algorithms available for PALM/STORM to inform potential users of the advantage different image analysis strategies provide for the interpretation of their particular datasets.

## Results

### Spinning disk super-resolution imaging set up

Spinning disk super-resolution imaging (SDSI) was developed to facilitate the super-resolution imaging of proteins or organelles at any single location in the cells axial (z) plane across a large field of view.

To implement SDSI it was necessary to perform the following modifications to our spinning disk set up (Materials and Methods, Figure 1B): Environmental vibrations were minimized by removing all non-essential equipment from the optical table and incorporating active damping legs to the optical bench (Figure 1A and Figure S1A–C) and isolating the system from air currents. This reduced system drift to around 40 nm reasonably consistently in SDSI experiments (Figure S1C). The accuracy of super-resolution image assignment is directly correlated to the number of photons detected and pixel size of the detector [6,19] (materials and methods). The spinning disk unit (CSU) itself is moderately light inefficient [26,27] therefore laser power was increased slightly above levels normally used in routine SD imaging to maximise sufficient photon counts. We investigated different detectors for SDSI and identified that an EMCCD camera with an 70% quantum efficiency and 8  $\mu\text{m}$  pixels was required, as a minimum, to detect sufficient photons for the super-resolution image reconstruction on our system using a  $100\times 1.4\text{NA}$  objective. This is because the number of photons detected and pixel size of the detector determine the amount of resolution refinement as explained in the equation given by Thompson et al [19] (materials and methods). We also found it necessary to use fluorescent probes with high quantum efficiency for data reconstruction, and confirmed that TdEos, mEOS, Dronpa, AlexaFluor555 and AlexaFluor647 performed well in our experiments.

As proof of principle, we performed experiments that visualised cellular structures smaller than the resolution limit of a standard confocal microscope. We also examined two different super-resolution imaging methodologies PALM and STORM to determine if both of these techniques could be used with SDSI. Eos Actin was used to generate PALM images of the actin structure in the lamellipodia of cells (Figure 2A). The Eos Actin dataset was also used to confirm and optimise the occurrence and collection of photo-switching events (Figure S2A and B). Antibodies were used to generate STORM images of Connexins trafficking through the cell (Figure 2B). PALM required cells to be transfected with a photo-convertible probe that switched between the off and on state through illumination from two lasers. To determine if PALM could work with SDSI, HeLa cells were transfected with tdEos-Actin. Actin was imaged using simultaneous imaging of the sample with an activation laser at low power (405 nm laser, 1–5 mW) and an imaging laser at medium power (561 nm laser, 10–12.5 mW). Over the course of the experiment the laser power of both the activation and imaging laser were modulated to ensure only a sparse population of fluorophores were present in each frame (Figure 2A and B). dSTORM microscopy relies on a combination of standard chemical dyes and a bespoke image buffer that is used to reactivate dyes, which are in the fluorescent off-state (i.e. not emitting light but not photo-bleached) (Materials and Methods) [10]. For STORM microscopy the composition of the imaging buffer was modified to account for the dye used [18]. To visualise Alexa Fluor 647 labelled Connexin vesicles cells were again imaged carefully by monitoring the laser power (640 nm laser, 8–16 mW). Laser power was altered to ensure a sparse set of fluorophores were present and that photo-bleaching of the AlexaFluor647 was minimised to ensure sufficient signal was available for image reconstruction (Figure 2B) [10]. All SDSI images were processed using the 3<sup>rd</sup> order SOFI algorithm implemented in the Localizer software suite [13,14] achieving a minimum resolution of 80 nm (Figure S3A). Two colour super resolution imaging was conducted by combining photoswitchable fluorescent proteins and dyes combining PALM and dSTORM sample preparation methodologies, by transfecting cells with

Eos-Histone 2B fluorescent proteins (PALM) and LaminA/C labelled with AlexaFluor647 (dSTORM) (Figure 2C). The presence of the buffer for dSTORM did not perturb photo-conversion events for Eos fluorescent proteins (Figure 2C). For correct image registration of two colour data was correctly 100 nm gold beads were added to the sample as fiduciary marks and left to settle onto the glass. The electrostatic charge on the glass was sufficient to hold the beads in place during imaging. The gold beads were visible in all imaging channels, we also found that 40 nm gold beads could be used if a higher level of resolution accuracy was required. Taken together these data show that both PALM and dSTORM sample preparation methodologies can be used separately and together to acquire super-resolved data on a spinning disk microscope.

### SDSI image analysis

All super-resolution data reconstruction algorithms require a certain minimum number of photo-conversion events to correctly assign structure. Under-sampling of super-resolution data can lead to artefacts where the structure is not completely assigned. To find the best image analysis methodology for SDSI comparative studies between seven different algorithms, (Table S1 and Materials and Methods) were conducted. Three separate datasets were used: a simulated dataset of overlapping emitters [17] (Movie S1) this dataset was chosen to model data from our biological system as it comprises simulated overlapping emission events. A dataset generated using recombinant actin filaments visualised using TIRF (Movie S2) (a kind gift from D.Metcalf, NPL, UK), and Eos-actin filaments in cells generated by SDSI (Movie S3). Analysis of the reconstructed simulated data showed the single molecule fitting algorithms QuickPALM and GLRT could not reconstruct the simulated dataset, this is because it contained overlapping emitters (Figure 3A). Of the algorithms that reconstructed the simulated

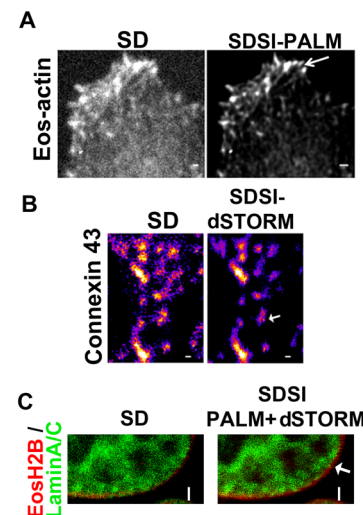


**Figure 2. SDSI super resolution imaging using both PALM and STORM.** (A) Comparison of SD and PALM images (processed by SOFI) of Eos-Actin, (B) Comparison of SD and d-STORM images of Connexin 43, Secondary Fab fragment antibodies conjugated to AlexaFluor647 were used for dSTORM imaging, SR data was generated using 3<sup>rd</sup> order SOFI, in both images bar = 1  $\mu\text{m}$ . (C) Comparison of SD and SDSI combining PALM and dSTORM imaging of Eos-Histone 2B (PALM) and Lamin A/C (dSTORM). Secondary Fab fragment antibodies conjugated to AlexaFluor647 were used for dSTORM imaging. SR data was generated using 3<sup>rd</sup> order SOFI. Arrow indicates individual histone complexes, bar = 2  $\mu\text{m}$ . doi:10.1371/journal.pone.0074604.g002

dataset, FasterSTORM and DeconSTORM gave smoothed results, whereas RainSTORM and SOFI produced results more representative of the sample data (Figure 3A). We also performed comparative analysis with a noisy background sample. We found GLRT, and RainSTORM would on occasion mis-assign the background as a positive signal (Figure 3B). The spatial fitting for both TIRF and SR data varied between the algorithms with QuickPALM and FasterSTORM reported to give the highest accuracy (Figure 3B) [12,18]. However, visual analysis of both the TIRF and SDSI images showed that only SOFI and RainSTORM reconstructed all of the features in the original image (Figure 3A). The partial reconstruction of images is likely due to either overlapping emitters, which the algorithms rejects (Table S1), or a low number of stochastic emitting events occurring in the region reconstructed during data collection; collecting more data could remedy the latter problem. The TIRF dataset did appear to be slightly better resolved; most likely due to more photo-conversion events being detected by TIRF than SDSI due to light inefficiency of the spinning disk or because of increased sensitivity of the camera on the TIRF system (Figure 3A and Figure S3B). This may explain why Deconvolution STORM processed TIRF data well and the SDSI data poorly. FasterSTORM was not able to process SDSI images (Figure 3A), which may be due to the optics of spinning disk not being compatible with the signal processing algorithms of FasterSTORM (Table S1) [18].

In terms of retention of image intensity information: SOFI performed the best with RainSTORM also producing excellent data, (Figure 3A and C). QuickPALM, GLRT, FasterSTORM, Deconvolution STORM images had punctate and broken appearances in the TIRF and SDSI data. This should not be the case as actin is filamentous as transmission electron microscopy studies have shown [28]. There was a considerable variation in speed of processing, which appeared not to correlate to refinement in resolution accuracy or retention of intensity information (Figure 3C). We found that 3B [16] was unable to reconstruct this size of dataset using a standard lab computer as the algorithm crashed and so excluded it from the analysis. We anticipate that with a multicore image processing cluster that the 3B algorithm would perform admirably. In summary SOFI gave the best compromise between refinement of spatial resolution of the image, retention of image intensity information and convincing image rendering for SDSI data. Therefore for the remainder of studies the SOFI algorithm, as implemented in Localizer was used for SR image processing.

### Comparative study between SDSI and SIM

To examine the validity of the SDSI methodology a parallel study was performed using SIM. SIM differs from stochastic SR methods as the sample is visualised using standard widefield illumination and a structured light pattern is projected onto the sample. Superimposing two or more of these patterns on one another causes an interference pattern (termed moiré pattern), containing harmonic frequencies not available in standard microscopy. Data processing is then carried out to generate an image with resolution of around 120 nm, (Figure S3A) [4,29]. For both SDSI and SIM imaging specific cellular components of HeLa cells were labelled with fluorescent probes compatible with PALM and STORM methodologies. SIM was shown to be advantageous for visualising structures in 3D as datasets comprising the whole cell could be collected between 2 and 10 minutes, although resolution was limited to 120 nm. SDSI could only be used to visualise structures in a single plane, using currently available image analysis algorithms, as samples bleached during data acquisitions of longer than 10,000 frames.

Comparing the single plane SDSI image to the SIM showed a resolution enhancement of fine structured microtubules in the mitotic spindle (Figure 4A). Although SIM gave a better 3D reconstructed image of the mitochondria, SDSI images processed using the 3<sup>rd</sup> order SOFI algorithm showed smaller (80 nm) mitochondria (Figure 4B and C). It was found that Alexa-Fluor dyes gave sufficiently high quantum yields to be used in correlative SIM/STORM microscopy experiments as both had high quantum yield and low photo bleaching. Unfortunately, it was more difficult to carry out correlative PALM/SIM studies due to the fluorescent proteins not being photo-stable enough to withstand the intense illumination required for 3D SIM. Eos-FP probes also performed poorly in SIM studies as they were liable to photo-convert in the process of imaging, generating artefacts of intensity in the output image. However, we found that the Dronpa fluorescent protein performed better than Eos, making it possible to visualise mitochondria (Figure 4B). The 150 nm resolution of Dronpa-Mito in SIM studies was substantially worse than the SIM spindle images generated using Mitotracker-Orange due to the Dronpa-Mito signal being degraded during SIM image acquisition (Figure 4C).

### SDSI of the nucleus

The nucleus is a challenging structure to visualise using current super-resolution methodologies as it is above the maximum lateral height of visualisation of both TIRF (100 nm) and HiLo (500 nm) (Figure 5A). To compare SDSI with widefield epi-illumination (WF) super-resolution we visualised HP1 $\alpha$ , a marker of heterochromatin in the nucleus using dSTORM sample preparation. HP1 $\alpha$  is present throughout the nucleus and gives punctate staining which can be seen in 3D (Figure 5B). This caused serious problems with WF as the photo-interactions of the labelled HP1 $\alpha$  were above and below the plane of focus masked photo-switching in the focal plane (Figure 5B). This meant the SR image processing using the SOFI algorithm was unable to enhance the resolution of WF images or correctly assign structures (Figure 5B). The raw image acquired using the spinning disk system had little out of focus light present as the image was confocal (Figure 5B). Therefore photo-interactions from out of focus light were excluded and the whole image could be accurately processed by SOFI (Figure 5B and C). We found WF imaging of actin, on the basal layer of the cell, gave slightly better data as there are no photo-interactions from out of focus light from below the focal plane (Figure S4A and B). However the resolution improvement with actin was still above the Abbe limit (Figure S4C) whereas SDSI can give super-resolved actin data (Figure 2A).

To show the flexibility of the technique two coloured SDSI was used to resolve hetero-chromatin structures in the medial plane of the nucleus (Figure 5A and D). HP1 $\alpha$  and LaminA/C were both prepared using dSTORM sample preparation methodologies, with HP1 $\alpha$  being labelled with AlexaFluor555 and LaminA/C with AlexaFluor647, we ensured that the super-resolution sample buffer was compatible with both fluorophores for dSTORM [10]. The heterochromatin fluorescence appeared more diffuse by SD microscopy, while SDSI super-resolution image analysis revealed several small discrete objects ranging from small foci, most likely less than 100 nm in diameter, to larger agglomerations 600 nm in diameter (Figure 5D and E). In addition the background subtraction achieved by SOFI clearly allowed visualisation at high resolution of structures where heterochromatin was absent, such as the nucleolus and PML bodies. SOFI reconstruction revealed regions which appeared as smaller 'beads' of heterochromatin whereas confocal microscopy showed only large diffuse staining (Figure 5D and E). Detailed analysis of Lamin A/C also

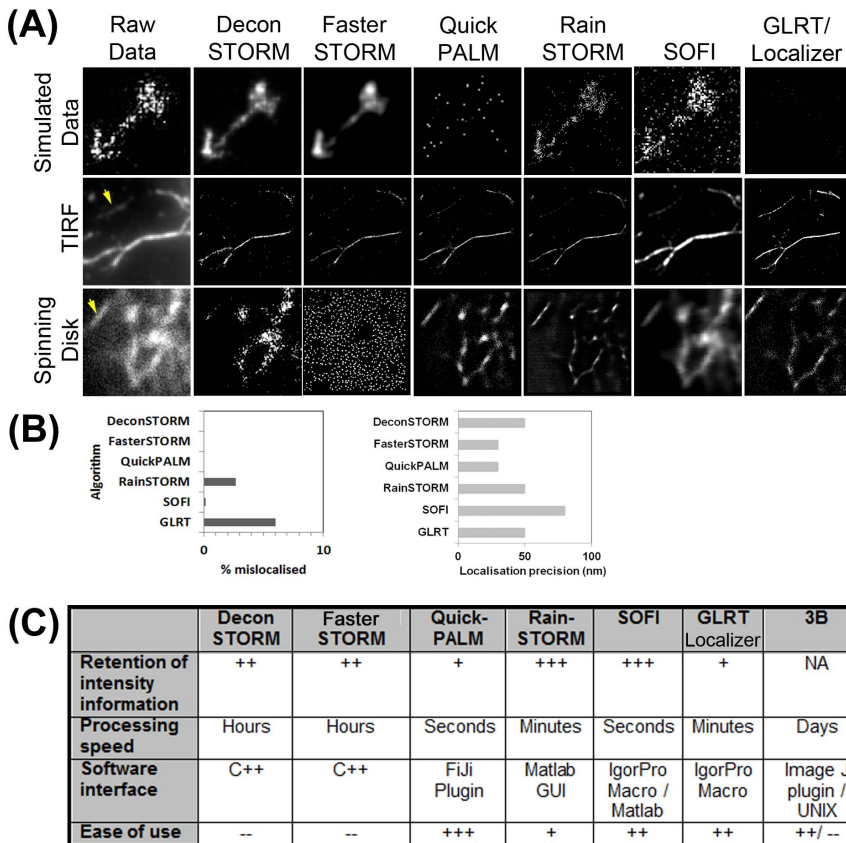


**Figure 3**

**Figure 3. Comparative study of different stochastic super-resolution image processing algorithms.** (A) Reconstructed super-resolution images from: a simulated dataset of 800 frames, a 64×64 pixel, 5000 frame dSTORM dataset of actin filaments labelled with AlexaFluor647 visualised by TIRF microscopy, a 90×90 pixel 5000 frame PALM dataset of HeLa cells transfected with Eos-Actin. SR images were generated using DeconSTORM, FasterSTORM, QuickPALM, RainSTORM, 3<sup>rd</sup> order SOFI and GLRT implemented in the Localizer image analysis package respectively. An image of the raw, unreconstructed, data is shown for comparison. For TIRF and SD this is the average of 8 frames of data, for the simulated data a maximum intensity projection of the whole dataset is shown. (B) Graphs showing the percentage of mislocalized pixels in datasets reconstructed from a noisy background image. The noisy background image was generated by acquiring 5000 frames of images of a red fluorescent Perspex slide. Graph showing the predicted localization precision between all of the investigated algorithms. (C) Chart comparing retention of intensity information, processing speed, software interface and ease of use of the software of all the algorithms in the comparative study.

doi:10.1371/journal.pone.0074604.g003

showed variations in the width of the nuclear membrane between 100–200 nm, SIM studies confirmed this observation [30]. Multicolour analysis of our data showed that small puncta of heterochromatin are found immediately adjacent to the nuclear membrane (Figure 5D, indicated by arrow). This is a significant improvement on the confocal data which shows that the nuclear membrane and heterochromatin are localised, which is an erroneous interpretation of the data. Many scientific studies of colocalization could benefit from super-resolution imaging as it provides better information about the precise localization of proteins and obtains stronger and clearer data about protein–protein interactions or their absence.

## Conclusions

We show that multi-spectral SDSI can collect super-resolution images with good S/N, resolved in any selected axial plane within a cell. We compared both PALM and STORM and found that either these techniques can be used either separately or together for generation of super-resolution data. We examined seven

different algorithms for processing SD data and found SOFI gave the best retention of image intensity information and provide the most accurate data reconstruction, in terms of spatially assigning all of the emission data found in the original images. This decision was aided by the user friendly GUI for SOFI in the Localizer suite of super-resolution algorithms and the fast data processing times [13]. The speed of processing was important as we intended to use SDSI for imaging multiple large image datasets in 2–3 colours. As SOFI only requires 2000 frames of data for accurate assignment of all of the fluorophore used in this study it would be possible to expand SDSI in future work to encompass applications such as high content screening, imaging of multiple epitopes, and live imaging.

SDSI generated data was comparable to or an improvement on, the SIM dataset. In summary, the SDSI technique was flexible enough to analyse a range of cellular structures in a fast and reliable manner. Our comparative study showed that SIM was more appropriate for imaging 3D structures, such as the mitotic spindle as even the fastest super-resolution data collection and

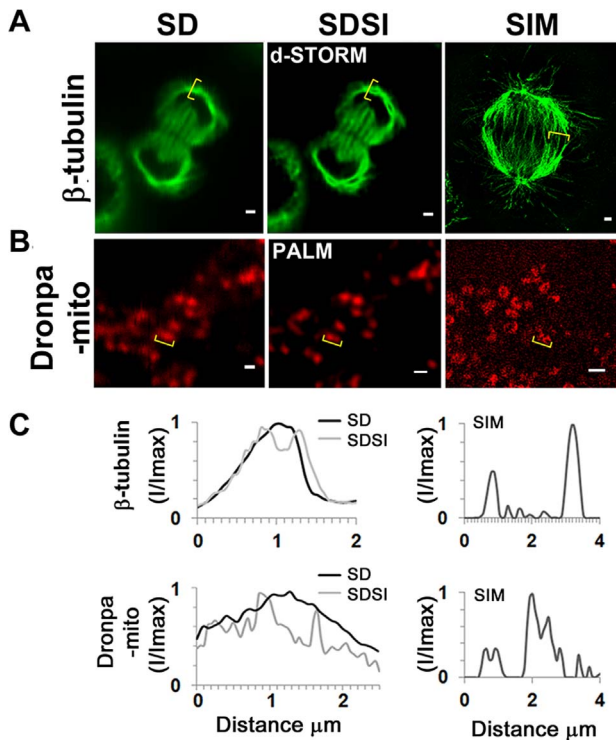


**Figure 4. Comparison between single channel SDSI super-resolution imaging and SIM imaging in a medial plane of HeLa cells.** (A) Comparison of SD, SDSI-dSTORM and SIM images of the mitotic spindle, the spindle was visualised using  $\beta$ -tubulin antibodies. Secondary Fab fragment antibodies conjugated to AlexaFluor647 were used for dSTORM imaging. SR data was generated using 3<sup>rd</sup> order SOFI, bar = 1  $\mu\text{m}$ . (B) Comparison of SD, SDSI-dSTORM and SIM images of the mitochondria, the mitochondria were visualised by transfecting cells using the Dronpa-Mito construct for PALM imaging, SR data was generated using 3<sup>rd</sup> order SOFI, bar = 1  $\mu\text{m}$ . (C) Line-scans (indicated in yellow parenthesis) through the mitotic spindle and mitochondria comparing SD resolution with SDSI and SIM.  
doi:10.1371/journal.pone.0074604.g004

image processing, would still require several hours compared to 10 minutes of SIM imaging. However, PALM/STORM SDSI could generate higher resolved data than SIM for single plane imaging dependant on the image processing algorithm used. Both SIM and PALM/STORM techniques required strong fluorophore labelling and powerful lasers to generate sufficient data for image analysis, due to the signal degradation during data collection and processing.

SDSI is a powerful addition to the range of super-resolution methodologies as it is capable of resolving structures that are located in the centre of the cell where there is a considerable amount of light scattering and densely labelled structures. In the comparative study widefield epi-fluorescence based methodologies could not achieve this (Figure 5B, Figure S4) and TIRF is not able to visualise the nucleus. SDSI has the potential of being applied to visualise multiple epitopes, at high resolution, in the centre of cells instead of cryosectioning or transmission electron microscopy. The increased resolution of SDSI allows accurate interpretation of proteins which are closely connected and are distant neighbours in a disparate group. It also provides an improved assignment of the size and composition of protein-protein complexes. We have shown that multicolour images can be collected and processed in less than two hours using fast image analysis algorithms. This technique provides the utility in multi-parametric biological

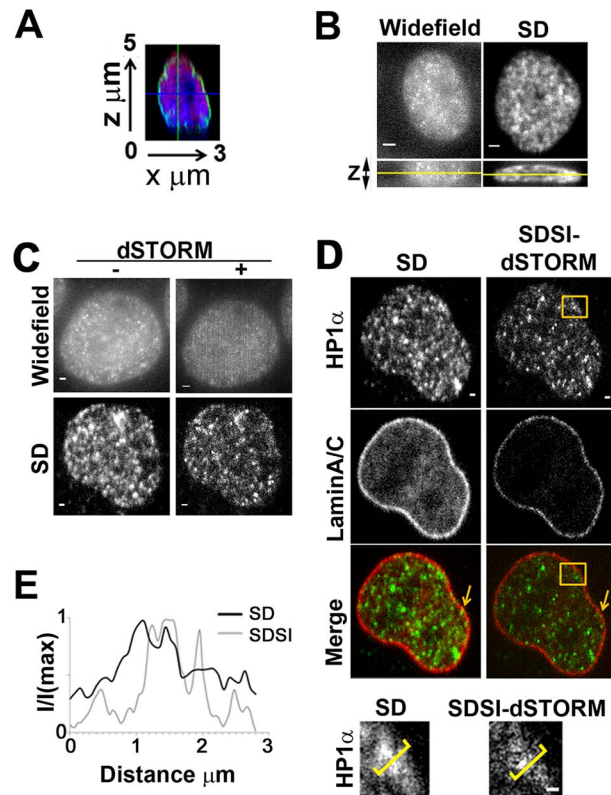


**Figure 5. Multispectral super-resolution imaging of the nucleus.** (A) Point scanned confocal images showing orthogonal axial (x,z) view of Histone H3 (Red), LaminA/C (Green) and Nuclei (Blue). (B) Widefield epifluorescent (WF) and spinning disk (SD) x,y and x,z images. Yellow line in x,z images indicates the plane shown in the x,y image of hetero-chromatin in the nucleus visualised using HP1 $\alpha$ , bar = 2  $\mu\text{m}$ . (C) dSTORM images of hetero-chromatin in the nucleus visualised using HP1 $\alpha$  antibodies acquired by widefield epifluorescence (WF) and spinning disk confocal (SD). SR data from both WF and SD images was generated using 3<sup>rd</sup> order SOFI, bar = 1  $\mu\text{m}$ . (D) Comparison of SD and SDSI images of hetero-chromatin visualised using HP1 $\alpha$  antibodies and the nuclear membrane visualised using LaminA/C antibodies. Secondary Fab fragment antibodies conjugated to AlexaFluor555 and 647 were used for dSTORM imaging, SR data was generated using 3<sup>rd</sup> order SOFI, bar = 1  $\mu\text{m}$ . Lower panel shows high-resolution region (indicated by orange box in upper panel) of heterochromatin, bar = 1  $\mu\text{m}$ . (E) Intensity profiles, through regions indicated by yellow parenthesis in E, comparing SD resolution with SDSI.  
doi:10.1371/journal.pone.0074604.g005

studies and delivers it to within easy reach of the biomedical researchers who are not microscopy specialists. Naturally if a question demanded higher resolution than 80–100 nm further spatial resolution can be obtained by using other algorithms, although these would require collecting a larger dataset with more photo-interactions for accurate image reconstruction making it impossible to carry out 3D or live imaging studies due to photobleaching/phototoxicity. RainSTORM gave better localization accuracy than SOFI and provided better preservation of image intensity information, in addition it has a useful toolkit for registration of multicolour images [11]. However with our implementation of super-resolution on a spinning disk microscopy and SOFI image processing it would be possible to expand the technique to such applications as live cell imaging, high content screening and 3D imaging. Overall we show that this method presents an encouraging step forward for the wider application of super-resolution methodologies for the biological researcher.

## Materials and Methods

### Cellular sample preparation and transfection

HeLa cells were grown as described elsewhere [29]. For transfection, cells were seeded onto glass-bottomed dishes (WPI, UK) at a density of  $2 \times 10^4$  cells  $\text{ml}^{-1}$  and transfected one day after plating using jetPRIME<sup>TM</sup> (Polyplus transfection, France) according to the manufacturers protocol with either 1  $\mu\text{g}$  Eos-actin, Eos-H2B or Dronpa-Mito DNA. Cells were incubated for 48 hours after transfection then fixed in 4% Paraformaldehyde diluted from a 16% EM grade stock (Agar Scientific, UK). For STORM/SIM imaging, cells were permeabilized using 0.1% Triton x100 and incubated with primary antibodies raised against  $\beta$ -Tubulin (Sigma, UK), Connexin 43 (BD, UK), LaminA/C (Santa Cruz Biotech, USA), raised against mouse and HPI $\alpha$  (New England Biolabs, USA) raised against rabbit. For STORM imaging samples were incubated with anti-mouse Fab fragment AlexaFluor647 secondary antibodies or AlexaFluor 555 anti-rabbit antibodies (Invitrogen, UK). For SIM imaging anti-mouse Fab fragment AlexaFluor 594 secondary antibodies were used. For SIM F-actin was labelled with Alexa-Fluor488 phalloidin (Invitrogen, UK) and nuclei were labelled using DAPI (Sigma, UK).

### Imaging buffer

For SDSI samples were placed in imaging medium consisting of PBS containing 100 nM 2-mercapto-ethanol, to promote photo-switching, 10 nm ascorbic acid to reduce reactive oxygen species which may damage fluorophores [31] and an oxygen scavenging system [18]. Prior to imaging the medium was degassed by bubbling through nitrogen for 10 minutes. 100 nm gold beads were added to the sample as fiduciary marks (BBI Gold, UK). These are left to settle onto the cells and coverslip for 1 hour prior to imaging and used for post-hoc drift correction and multispectral image registration.

### Spinning disk super-resolution optical setup

The SDSI system was built on an inverted optical microscope (Nikon TE2000E), with a Yokogawa Nipkow spinning disk unit (CSU X1 DSD, Yokogawa Electric Corporation). Four solid state lasers were used as the excitation source: a 405 nm (100 mW), 488 nm (50 mW), 561 nm (50 mW) and 640 nm (100 mW) (Coherent Inc. CA, USA), all lasers were collimated, combined and coupled into an optical fibre (Andor laser combiner, Andor Technologies, UK). The fluorescence emission was filtered using a quad dichroic mirror (Semrock, USA). All imaging was carried out using a 100 $\times$  1.4N.A Plan Apochromat VC objective (Nikon, UK). Images were collected on a xIon885 EMCCD camera (Andor Technologies, UK).

For SDSI data was acquired using streaming to the camera, images acquisition rates varied between at 4–6 frames per second. Data was collected using IQ2 software (Andor Technologies, UK). Throughout all SDSI experiments laser power was adjusted to ensure a sparse field of stochastic fluctuations were continuously visible (Figure S2). For SDSI PALM probes were simultaneously activated by a 405 nm (0.5–6% power) and imaged and bleached with either a 488 nm or 561 nm laser (15–30% power). For STORM imaging, the dSTORM methodology was used as described elsewhere [10], For dSTORM imaging 8–20% of the 100 mW power of the 647 nm laser was used. Analysis of fluctuation of intensity of individual actin foci throughout the experiment showed these imaging conditions could capture of photo-conversion events (Figure S2A and B).

### Super-resolution image analysis, including algorithm comparison

Data analysis was carried out on a Dell Alienware PC, 12 GB RAM, Core I5 3.0 GHz quad core processor, 500 GB hard disk. Prior to analysis images were reconstructed and re-registered using Fiji (<http://fiji.sc/wiki/index.php/Fiji>). To optimise the number of frames for SDSI imaging a 10<sup>5</sup> frame dataset of 100 nm Tetra speck beads (Invitrogen, UK) was acquired using a 561 nm laser. Data was reconstructed using SOFI algorithms using input datasets of 200, 500, 1000, 2000, 4000, 6000, 8000 and 10,000 frames (Figure S3C). The reconstructed area of the bead was then measured and was repeated for five separate beads. The data analysis showed that a minimum of 2000 frames were required for consistent data reconstruction of the 100 nm beads using SOFI (Figure S3C). An estimate of the localization error along a single axis in the x–y imaging plane showed, for our system, the localization error was 18 nm for single molecule imaging (Materials and Methods). This is due mainly to the small pixel size of our camera, as SDSI detects approximately half the number photo-switching events TIRF does, although individual emission events can be detected (Figure S2A and B and 3B). Using the actin test dataset we found 3<sup>rd</sup> order SOFI was able to obtain a resolution standard of 80 nm (Figure S3A). For the super-resolution image analysis comparison three datasets were used: A simulated dataset, 64 $\times$ 64 pixel and 800 images with some simulated overlapping emission events, taken from Mukamel et al [17] (Movie S1). A dataset of recombinant actin filaments labelled with AlexaFluor 647 obtained by TIRF microscopy: 64 $\times$ 64 pixels, 5000 frames, which was a kind gift from Dr D. Metcalf, NPL, London UK (Movie S2). A dataset of tdEos-Actin from transfected Hela cells obtained by spinning disk microscopy: 90 $\times$ 90 pixels 5000 frames (Movie S3). 3B and QuickPALM image analysis was carried out using the Fiji plugin [12,16]. RainSTORM [11] image analysis was carried out in Matlab, ([www.mathworks.co.uk](http://www.mathworks.co.uk)). FasterSTORM [18] and DeconSTORM [17] analysis were carried out according to published instructions. The Localizer suite of super-resolution image analysis algorithms [13] was used to conduct SOFI [14] and GLRT [32] image analysis. For the comparative studies each separate test dataset was processed by all of the algorithms and the reconstructed images compiled and measured. A 5000 frame ‘noisy background’ set of images was acquired by using a red fluorescent Perspex slide on the SDSI system to determine if the algorithms would incorrectly assign noise as signal. All data analysis of reconstructed images was carried out using Fiji (<http://fiji.sc/Fiji>).

### Drift correction

To determine the SDSI system accuracy 100 nm Tetraspeck fluorescent microspheres (Invitrogen, UK) were dried onto glass bottomed dishes (WPI, FL, USA). Bead samples were imaged continuously for 45 minutes and particles tracked using the Particle Tracker plugin in Fiji ([http://fiji.sc/wiki/index.php/Particle\\_Tracker](http://fiji.sc/wiki/index.php/Particle_Tracker)) (Figure S1A–C). Lateral image drift was reduced by placing the system in an environmental enclosure which maintained a stable temperature. To maximise stability the environmental chamber surrounding the system was pre-warmed for 4–6 hours to 32°C prior to imaging for all experiments (Figure 1A and Figure S1). A lateral drift of around 40 nm is assumed for all experiments, however the gold beads are tracked for each experiment and if lateral drift above 40 nm is observed the experiment is rejected and not processed. Axial drift of the objective was corrected using a capacitive feedback system (Pi-Foc 721, Physik Instruments, UK).

## Spinning disk system calibration

PSFs were measured from 100 nm Tetraspeck beads, images were processed by SOFI or QuickPALM and were fitted using the MetroloJ plugin in ImageJ (<http://imagejdocu.tudor.lu/doku.php?id=plugin:analysis:metroloj:start>) (Figure 1C). The localization accuracy of our system was determined using the standard equation for determination of localization error [6,19]

$$\left(\sigma_{x,y}^2\right)_m \approx \frac{s^2 + a^2/12}{N_m} + \frac{4\sqrt{\pi}s^3b_m^2}{aN_m^2}$$

where,  $s$  is the standard deviation of the PSF,  $a$  is the pixel size in the image (taking into account the system magnification),  $N_m$  is the total number of photons measured from molecule  $m$ , and  $b_m$  is the number of background photons collected in the fitting window used for molecule  $m$ . To determine photon number 5000 frames of data were acquired of td-Eos Actin. Photon number was estimated using Fiji and information from the camera suppliers (<http://www.andor.com/learning-academy/count-convert-quantifying-data-in-electrons-and-photons>). To determine the resolution achieved by SOFI this dataset was also analysed.

## SIM microscopy

3DSIM was performed on a microscope system (OMX version 2; Applied Precision, USA) as described previously [29]. Raw 3DSIM images were processed and reconstructed using algorithms implemented in SoftWoRx software (Applied Precision, USA) [4,33,34].

## Widefield and spinning disk microscopy

Widefield epi-fluorescent microscopy was carried out by removing the spinning disk from the optical path in our system. All other components were identical. For widefield analysis HeLa cells were processed as described above. F-actin was labelled with Alexafluor 555-phalloidin. Spinning disk microscopy images were captured using the same software, laser power, camera gain and exposure time as for SDSI imaging. The widefield and spinning disk images presented are the average of 8 frames of data.

## Supporting Information

**Figure S1 Quantification of axial drift in the super-resolution system.** Drift measurements were obtained from 100 nm Tetraspeck beads (Invitrogen). Imaging conditions were identical to those used in PALM/STORM data acquisition, where data are streamed to the camera at a rate of 4–6 frames per second. Data are pooled from 10 independent tracks, (A) Drift in the x plane in the SDSI system during a 2000 frame data acquisition series. (B) Drift in the y plane in the SDSI system during a 2000 frame data acquisition. (C) Position map showing x, y drift in the SDSI system during a 2000 frame data acquisition. (TIF)

**Figure S2 The photo conversion properties of Eos-FP Actin.** (A) Images taken from a 5000 frame dataset showing stochastic photo-conversion of Eos-FP actin vesicles. Frame number is indicated on bottom left, data are acquired by streaming at a rate of 4–6 frames per second so total time for dataset acquisition is 1250 seconds approximately, bar = 5 Am. (B) Graph indicating the rate of photo conversion of an individual Eos-Actin vesicle. Imaging conditions were identical to those used in PALM/dSTORM data acquisition, 250 frames of data acquired at a rate of 5 frames per second were measured of a representative sample are shown here. (TIF)

## Figure S3 Resolution improvement using the SD-SI system.

(A) Graphs comparing the resolution of SSIM and SDSI using an intensity profile of a 100 nm Tetraspeck fluorescent bead. Fluorescence from the bead was excited using a 488 nm laser, Intensity profiles of the bead were collected. Left hand graph shows the OMX SSIM system, right hand side graph compares raw data from the spinning disk with the resolution enhancement in SR images generated using 3rd order SOFI. On both graphs the full width at half maximal intensity are indicated by a line. Data are pooled from 5 separate beads. (B) Graph comparing the number of photo-switching events detected by QuickPALM software in data collected by TIRF and SD. Test datasets of 64×64 images of AlexaFluor647 labeled F-actin (TIRF) and 90×90 pixel images of tdEos-actin in HeLa cells (SD) were compared. (C) Bar chart showing average area reconstructed from SOFI analysis of 100 nm Tetraspeck beads. Datasets of 200, 500, 1000, 2000, 4000, 6000, 8000 and 10000 frames are measured. Data are pooled from 10 separate beads, error bars show standard deviation.

(TIF)

**Figure S4** (A) Widefield epifluorescent of HeLa cells labeled with AlexaFlour555 Phalloidin. SR data was generated from a Widefield image set using 3rd order SOFI. (B) High-resolution region (indicated by orange box in image (A)) of F-actin bar = 1 Am. (C) Intensity profiles, through regions indicated by yellow parenthesis in E, comparing WF resolution with the super-resolution images generated using 3rd order SOFI.

(TIF)

**Table S1 Table showing how super-resolution algorithms work and any assumptions the algorithms made about the nature of the input image data prior to data processing.**

(DOCX)

**Movie S1 A simulated multiframe fluorescence microscopy data sets in which only a subset of fluorophores was activated in each frame taken from Mukamel et al [17].**

(AVI)

**Movie S2 A 5000 frame dataset of AlexaFluor 647 labelled actin generated using TIRF.**

(AVI)

**Movie S3 A 5000 frame dataset of HeLa cells transfected with Eos-Actin generated using SDSI.**

(AVI)

## Acknowledgments

We thank Dr Jan Pechyl and Dr Andrei Sapelkin for helpful discussions regarding super-resolution theory. Dr Thomas Dertinger, for advice about image analysis and implementation of SOFI. James Wainwright (Andor) for hardware and technical support. Dr Daniel Metcalf for the generous gift of TIRF super-resolution data. The OMX microscope was supported by the Scottish University Life Sciences Alliance and used under the auspices of the Euro-BioImaging Proof-of-concept studies. We thank Dr Markus Posch and Professor Jason Swedlow for their assistance with the OMX system.

## Author Contributions

Conceived and designed the experiments: APW NAH MS SAB MMK. Performed the experiments: NAH MS AW JTC. Analyzed the data: NAH MS AW. Contributed reagents/materials/analysis tools: MMK JTC SAB. Wrote the paper: APW NAH MMK.

## References

- Huang B, Babcock H, Zhuang X (2010) Breaking the diffraction barrier: super-resolution imaging of cells. *Cell* 143: 1047–1058.
- Hofmann M, Eggeling C, Jakobs S, Hell SW (2005) Breaking the diffraction barrier in fluorescence microscopy at low light intensities by using reversibly photoswitchable proteins. *Proc Natl Acad Sci U S A* 102: 17565–17569.
- Hell SW (2009) Microscopy and its focal switch. *Nat Methods* 6: 24–32.
- Gustafsson MG, Shao L, Carlton PM, Wang CJ, Golubovskaya IN, et al. (2008) Three-dimensional resolution doubling in wide-field fluorescence microscopy by structured illumination. *Biophys J* 94: 4957–4970.
- Herbert S, Soares H, Zimmer C, Henriques R (2012) Single-molecule localization super-resolution microscopy: deeper and faster. *Microsc Microanal* 18: 1419–1429.
- Betzig E, Patterson GH, Sougrat R, Lindwasser OW, Olenych S, et al. (2006) Imaging intracellular fluorescent proteins at nanometer resolution. *Science* 313: 1642–1645.
- Bates M, Huang B, Dempsey GT, Zhuang X (2007) Multicolor super-resolution imaging with photo-switchable fluorescent probes. *Science* 317: 1749–1753.
- Rust MJ, Bates M, Zhuang X (2006) Sub-diffraction-limit imaging by stochastic optical reconstruction microscopy (STORM). *Nat Methods* 3: 793–795.
- Fölling J, Bossi M, Bock H, Medda R, Wurm CA, et al. (2008) Fluorescence nanoscopy by ground-state depletion and single-molecule return. *Nat Methods* 5: 943–945.
- van de Linde S, Löschberger A, Klein T, Heidbreder M, Wolter S, et al. (2011) Direct stochastic optical reconstruction microscopy with standard fluorescent probes. *Nat Protoc* 6: 991–1009.
- Erdelyi M, Rees E, Metcalf D, Schierle GS, Dudas L, et al. (2013) Correcting chromatic offset in multicolor super-resolution localization microscopy. *Opt Express* 21: 10978–10988.
- Henriques R, Lelek M, Fornasiero EF, Valtorta F, Zimmer C, et al. (2010) QuickPALM: 3D real-time photoactivation nanoscopy image processing in ImageJ. *Nat Methods* 7: 339–340.
- Dedecker P, Duwe S, Neely RK, Zhang J (2012) Localizer: fast, accurate, open-source, and modular software package for superresolution microscopy. *J Biomed Opt* 17: 126008.
- Dertinger T, Colyer R, Iyer G, Weiss S, Enderlein J (2009) Fast, background-free, 3D super-resolution optical fluctuation imaging (SOFI). *Proc Natl Acad Sci U S A* 106: 22287–22292.
- Dedecker P, Mo GC, Dertinger T, Zhang J (2012) Widely accessible method for superresolution fluorescence imaging of living systems. *Proc Natl Acad Sci U S A* 109: 10909–10914.
- Cox S, Rosten E, Monypenny J, Jovanovic-Talisman T, Burnette DT, et al. (2011) Bayesian localization microscopy reveals nanoscale podosome dynamics. *Nat Methods* 9: 195–200.
- Mukamel EA, Babcock H, Zhuang X (2012) Statistical deconvolution for superresolution fluorescence microscopy. *Biophys J* 102: 2391–2400.
- Zhu L, Zhang W, Elnatan D, Huang B (2012) Faster STORM using compressed sensing. *Nat Methods* 9: 721–723.
- Thompson RE, Larson DR, Webb WW (2002) Precise nanometer localization analysis for individual fluorescent probes. *Biophys J* 82: 2775–2783.
- Wazawa T, Ueda M (2005) Total internal reflection fluorescence microscopy in single molecule nanobioscience. *Adv Biochem Eng Biotechnol* 95: 77–106.
- Xu K, Babcock HP, Zhuang X (2012) Dual-objective STORM reveals three-dimensional filament organization in the actin cytoskeleton. *Nat Methods* 9: 185–188.
- Cella Zanacchi F, Lavagnino Z, Perrone Donnorso M, Del Bue A, Furia L, et al. (2011) Live-cell 3D super-resolution imaging in thick biological samples. *Nat Methods* 8: 1047–1049.
- van 't Hoff M, de Sars V, Oheim M (2008) A programmable light engine for quantitative single molecule TIRF and HILO imaging. *Opt Express* 16: 18495–18504.
- Adams MC, Salmon WC, Gupton SL, Cohan CS, Wittmann T, et al. (2003) A high-speed multispectral spinning-disk confocal microscope system for fluorescent speckle microscopy of living cells. *Methods* 29: 29–41.
- Petran M, Hadravsky M, Benes J, Boyde A (1986) In vivo microscopy using the tandem scanning microscope. *Ann N Y Acad Sci* 483: 440–447.
- Adams MC, Salmon WC, Gupton SL, Cohan CS, Wittmann T, et al. (2003) A high-speed multispectral spinning-disk confocal microscope system for fluorescent speckle microscopy of living cells. *Methods* 29: 29–41.
- Murray JM, Appleton PL, Swedlow JR, Waters JC (2007) Evaluating performance in three-dimensional fluorescence microscopy. *J Microsc* 228: 390–405.
- Urban E, Jacob S, Nemethova M, Resch GP, Small JV (2010) Electron tomography reveals unbranched networks of actin filaments in lamellipodia. *Nat Cell Biol* 12: 429–435.
- Posch M, Khoudoli GA, Swift S, King EM, Deluca JG, et al. (2010) Sds22 regulates aurora B activity and microtubule-kinetochore interactions at mitosis. *J Cell Biol* 191: 61–74.
- Markaki Y, Gunkel M, Schermelleh L, Beichmanis S, Neumann J, et al. (2010) Functional nuclear organization of transcription and DNA replication: a topographical marriage between chromatin domains and the interchromatin compartment. *Cold Spring Harb Symp Quant Biol* 75: 475–492.
- Knight MM, Roberts SR, Lee DA, Bader DL (2003) Live cell imaging using confocal microscopy induces intracellular calcium transients and cell death. *Am J Physiol Cell Physiol* 284: C1083–1089.
- Sergé A, Bertiaux N, Rigneault H, Marguet D (2008) Dynamic multiple-target tracing to probe spatiotemporal cartography of cell membranes. *Nat Methods* 5: 687–694.
- Gustafsson MG (2000) Surpassing the lateral resolution limit by a factor of two using structured illumination microscopy. *J Microsc* 198: 82–87.
- Schermelleh L, Carlton PM, Haase S, Shao L, Winoto L, et al. (2008) Subdiffraction multicolor imaging of the nuclear periphery with 3D structured illumination microscopy. *Science* 320: 1332–1336.



OPEN

# Image artifacts in Single Molecule Localization Microscopy: why optimization of sample preparation protocols matters

SUBJECT AREAS:

SUPER-RESOLUTION MICROSCOPY

SINGLE-MOLECULE BIOPHYSICS

Received  
16 October 2014Accepted  
11 December 2014Published  
21 January 2015Correspondence and requests for materials should be addressed to  
T.D.M.B. (toby.bell@monash.edu)

Donna R. Whelan &amp; Toby D. M. Bell

School of Chemistry, Monash University, Clayton, Victoria 3800, Australia.

Single molecule localization microscopy (SMLM) techniques allow for sub-diffraction imaging with spatial resolutions better than 10 nm reported. Much has been discussed relating to different variations of SMLM and all-inclusive microscopes can now be purchased, removing the need for in-house software or hardware development. However, little discussion has occurred examining the reliability and quality of the images being produced, as well as the potential for overlooked preparative artifacts. As a result of the up to an order-of-magnitude improvement in spatial resolution, substantially more detail is observed, including changes in distribution and ultrastructure caused by the many steps required to fix, permeabilize, and stain a sample. Here we systematically investigate many of these steps including different fixatives, fixative concentration, permeabilization concentration and timing, antibody concentration, and buffering. We present three well-optimized fixation protocols for staining microtubules, mitochondria and actin in a mammalian cell line and then discuss various artifacts in relation to images obtained from samples prepared using the protocols. The potential for such errors to go undetected in SMLM images and the complications in defining a 'good' image using previous parameters applied to confocal microscopy are also discussed.

The recent widespread uptake of new super resolution techniques has revolutionized and invigorated molecular and cellular biology. Methods based on the detection and localization of single molecules such as (f)PALM ((Fluorescence<sup>1</sup>) Photoactivated localization microscopy<sup>2</sup>) and (d)STORM ((Direct<sup>3</sup>) Stochastic optical reconstruction microscopy<sup>4</sup>) have achieved the most superior gains in spatial resolution with live cell measurements reportedly achieving ~30 nm spatial resolution<sup>5</sup> and fixed cell measurements achieving ~10 nm spatial resolution<sup>6</sup>. These techniques take advantage of the ability to fit the emission pattern of a single emitting molecule's point spread function giving a precise localization coordinate. Whereas conventional widefield or confocal fluorescence microscopy views all fluorophores in an emissive state at once, localization techniques achieve temporal separation through one of several (photo)physical or (photo)chemical methods (For a recent comprehensive review see Klein *et al.*<sup>7</sup>).

Extensive protocol and methods papers have been published for PALM, fPALM<sup>8</sup>, STORM<sup>4</sup> and dSTORM<sup>9</sup>, as well as 3D STORM<sup>6,10</sup>, and live cell dSTORM<sup>11,12</sup>. These papers, however, focus on microscope set up and image acquisition and processing providing extensive detail on these matters, but typically provide only outlines of common epifluorescence sample protocols. In an effort to demonstrate the importance of, and stimulate further discussion regarding, sample preparation in SMLM, we share here, optimized fixation and staining protocols for single color, 2D SMLM of microtubules (MTs), mitochondria (MC) and actin in COS-7 cells. More importantly, we detail the optimization process via the systematic investigation of the images produced by varying the fixative used, fixation time, temperature and concentration, permeabilization time and concentration, use of blocking buffers and quenching of glutaraldehyde-related autofluorescence. Overall glutaraldehyde is demonstrated to be the best fixative for structure-preservation, though we also detail highly reproducible paraformaldehyde and methanol protocols for MT staining. The images rendered by our optimized protocols are comparable in localization precision and spatial resolution to the very best SMLM images in the literature and surpass many of those images published of un-optimized samples.

A potentially underappreciated consequence of any gain in resolution is that previously satisfactory protocols (e.g. for confocal imaging) may be insufficient for SMLM. This is because any artifacts present on a distance scale



smaller than that previously imaged have not been visible in fluorescence imaging, due to the overlapping of point spread functions and the resultant blur. In the case of SMLM, cellular structure must be preserved much more accurately because sub-diffraction deviations will be resolved to the same extent as 'real' sub-diffraction detail.

There is not much discussion in the literature about the processes by which sample preparation should be optimized for SMLM and even less research has been conducted into the effects of suboptimal fixation and/or staining on the resulting SMLM image. A handful of publications have endeavoured to highlight some common artifacts seen in SMLM images<sup>10,13,14</sup>, however, those discussed are more often due to acquisition error. Developing a robust understanding and appreciation of the causes and appearance of artifacts in SMLM images is of paramount importance because oftentimes, these artifacts will not be easily identified. This is particularly true in SMLM involving unknown or dispersed target molecules. A stringent degree of benchmarking is therefore needed to assure that cells imaged using SMLM truly reflect the biologically native state as closely as possible. To do this, targets such as microtubules (MTs) and nuclear pore complexes (NPCs) are ideal as has been demonstrated by extensive publication of these structures imaged using SMLM<sup>10,15,16</sup>. In addition to well-defined sub-diffraction width, MTs show decreased SM signal in the center of the two-dimensional projection of their three-dimensional cylindrical structure<sup>17</sup> and NPCs possess an eight-fold symmetry that can be distinctly resolved<sup>15</sup>. These features allow for comprehensive and rigorous assessment of the performance of the experiment including preservation of the cells.

Therefore, along with our discussion of optimized protocols for SMLM, images of sub-optimally prepared samples are discussed in relation to our understanding of super-resolution image artifacts as well as the underlying chemistry of fixation. Particular attention is paid to artifact structures observed only in the super-resolution images and not in the epifluorescence images. We draw attention to the inherent artifactual nature of fixed samples as recently highlighted<sup>18</sup> and demonstrate the importance of widespread and enhanced understanding of the limitations of SMLM.

## Results and Discussion

**Optimized Protocols for Paraformaldehyde, Glutaraldehyde and Methanol Fixation.** The main outcome of the research presented here is the optimization of several protocols using common fixatives for SMLM. Moreover, the crucial steps in the fixation process are pinpointed and discussed in relation to corresponding SMLM images containing artifacts. For all of these fixation protocols to progress well the chambered coverglass must be removed from the incubator and placed immediately on a pre-warmed 37°C surface with the fixation steps proceeding without delay.

**Paraformaldehyde (PFA) fixation.** The majority of the culture medium is aspirated using a glass pipette placed carefully into a corner of each chamber. Simultaneously, 500  $\mu$ l of 37°C 3.7% PFA is added down the side of the chamber using a second glass pipette. This PFA should be freshly prepared from frozen 10% PFA (filtered after thawing and adjusted to pH 7.4) by adding 2X Phosphate buffered saline (PBS) and then the equivalent milli-Q water to make an isotonic solution. This is again pH adjusted using 1 M KOH or HCl to achieve a pH of 7.4.

The 3.7% PFA solution is then left on the cells for 12 minutes with occasional gentle agitation before aspiration using a glass pipette, again positioned in the same corner of each chamber to minimize perturbation damage. 500  $\mu$ l of PBS is added concurrent to the removal of the fixative solution. This PBS wash is aspirated after approximately 30 seconds and replaced with fresh PBS that is removed after another 60 seconds. Three more PBS washes are administered lasting approximately 5, 10 and 15 minutes each. To per-

meabilize the cells Triton X-100 in isotonic PBS at concentrations ranging from 0.1–1% for 10 minutes is used. Following permeabilization, cells are again washed in PBS, once for 30 seconds and then twice for 5 minutes.

Blocking can be achieved using bovine serum albumin (BSA) in PBS at concentrations between 1 and 10%. Immunostaining is then done in BSA/PBS at the same concentration as the blocking step with the antibodies used at dilutions ranging 1 : 100–1 : 2000 primary antibody and 1 : 200–1 : 4000 secondary antibody depending on the antibodies themselves. Three washes of five minutes in PBS follow each staining step.

**Glutaraldehyde (GA) fixation.** For glutaraldehyde fixation, a previously optimized protocol used for electron microscopy (EM) and SMLM experiments that yielded excellent preservation of the cytoskeletal network<sup>6,19,20</sup> was slightly modified. Unlike published SMLM methods using PFA or methanol, which are generally identical to the protocols used for confocal samples, this particular GA protocol was specifically modified for ultrastructure preservation and SMLM measurements and therefore required minimal adjustments. Instead it afforded us the opportunity to investigate what changes to SMLM images resulted from slight deviations from the established, well-developed protocol.

For GA fixation, the culture medium is aspirated and a primary fixative of 0.4% glutaraldehyde and 0.25% Triton X100 in PBS is added simultaneously as detailed in the PFA fixation protocol. After 90 seconds this primary fixative solution is removed, the cells are washed once quickly with 37°C PBS, and a second solution of 3% GA in PBS applied. This solution is removed after 15 minutes. Both the 0.4% and 3% glutaraldehyde are made from frozen 10% glutaraldehyde stock, 2X cytoskeleton stabilizing buffer (CSB)<sup>21</sup> (1 M NaCl, 100 mM PIPES, 30 mM MgCl<sub>2</sub>, 10 mM EGTA, and 10 mM sucrose) and Milli-Q water to form an isotonic solution, pH 6.2.

The cells are washed following fixation as in the PFA protocol prior to addition of a reductant to quench auto-fluorescence from remaining free aldehyde groups. The 500  $\mu$ l aliquots of reductant are either NaBH<sub>4</sub> (0.1–1% w/v) or glycine (0.3 M) in PBS solution and are left for 15 minutes. Cells are then washed extensively with two quick washes (30, 60 seconds) and then three longer washes (5, 10 and 15 minutes). Blocking and staining steps are carried out as outlined in the PFA protocol.

**Methanol(MeOH) fixation.** One hour prior to fixation, the medium of cells for methanol fixation is replaced with pre-warmed medium that does not contain FBS. Cells are then returned to the incubator. After one hour the medium is aspirated and the cells are washed once quickly with PBS (37°C). The PBS is then aspirated and 500  $\mu$ l of –20°C methanol is added to each well. The cells are left in a freezer at –20°C for five minutes and then the methanol is removed and the cells washed with PBS as detailed in the PFA protocol. Cells are then blocked and stained as outlined in the PFA protocol.

**Development of well optimized protocols yield exemplary SMLM images of microtubules, mitochondria and actin.** In the development of the optimized protocols we focussed primarily on microtubules (MTs) and mitochondria (MC) because they have very well defined structures. MTs are polymeric and expected to measure approximately 60–65 nm in width when immunostained and imaged with a localization precision of <10 nm<sup>22</sup>. The structure of MC networks is also well documented using SMLM methods<sup>10</sup> and by targeting the Tom20 protein in the import receptor on the outer membrane we expect to see 40–50 nm clustering as previously detected using STimulated Emission Depletion (STED)<sup>23</sup>. By knowing the structure of our targets prior to SMLM dSTORM measurements we were able to more readily identify deviation from the biologically native state in response to changes in fixation and staining protocols.

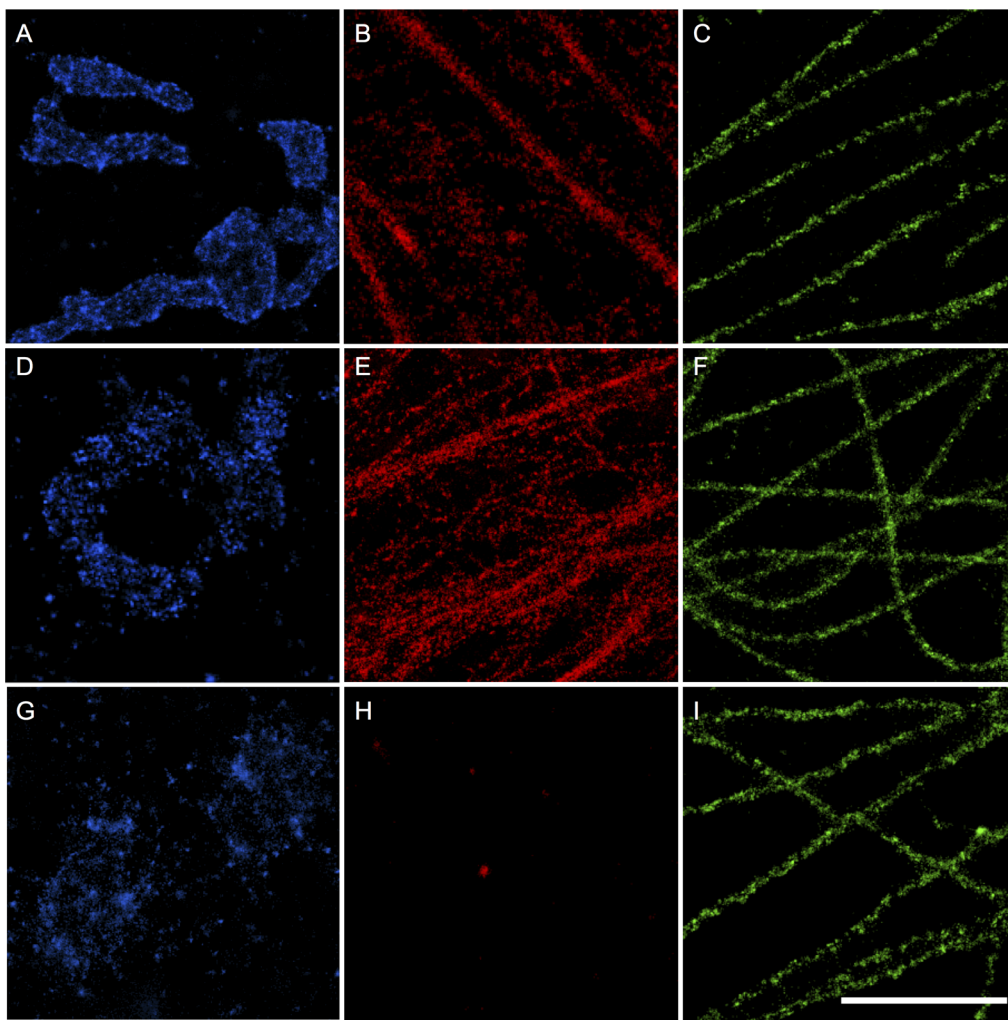


**Figure 1 | Optimized protocols using paraformaldehyde, glutaraldehyde and methanol preserve ultrastructure for SMLM imaging of mitochondria, actin and microtubules.** (A–C) COS-7 cells fixed using the optimized 3.7% paraformaldehyde protocol and stained using Alexa Fluor 647 in conjunction with (A) anti-Tom20, a protein component of the import receptor on the outer membrane of mitochondria, (B) phalloidin which strongly associates with filamentous actin, and (C) anti- $\alpha$ / $\beta$ -tubulin, the unit protein that polymerizes into microtubules. (D–F) Similarly stained mitochondria (D), actin (E) and microtubules (F) in cells fixed using the optimized 3% glutaraldehyde protocol. (G–I) Similarly stained mitochondria (G), actin (H) and microtubules (I) in cells fixed using the optimized  $-20^{\circ}\text{C}$  methanol protocol. All images show sub-diffraction structure with the exception of G–H that show substantial damage. Scale bar: 1  $\mu\text{m}$ .

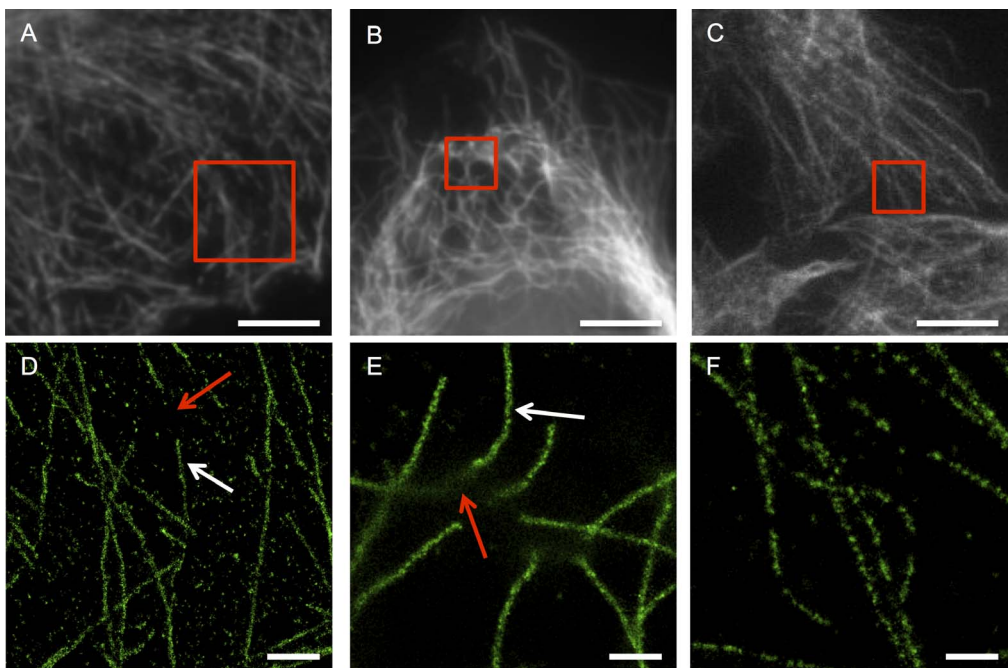
As such, the three optimized protocols detailed above are a result of careful, systematic consideration of many of the different facets and steps of sample preparation and were initially developed specifically for MT fixation. Conclusively, all three fixatives—paraformaldehyde (PFA), glutaraldehyde (GA) and methanol—when used in accordance with the protocols outlined, give exemplary SMLM images of MTs (Figure 1). The PFA fixation protocol also worked well for MC networks but actin microstructure was lost; conversely the GA fixation protocol worked well for actin but MC appeared susceptible to shrinkage as has been observed before<sup>24</sup>. Overall, methanol gave unsatisfactory results for both MC and actin stains as expected based on previous literature and the precipitory action of methanol on the MC membrane<sup>25–27</sup>.

Figure 1 shows these results with highly magnified sections of reconstructed *d*STORM images of COS-7 cells stained to show MTs, the MC membrane, and actin. These images are representative of images taken of cells routinely fixed following the detailed protocols. The top row (a–c) are images of cells fixed using the optimized PFA protocol, the middle row (d–f) depicts cells fixed using the GA protocol, and the bottom row (g–i) shows cells fixed using the methanol protocol. The PFA and GA protocols used to obtain the images

in Figure 1c and 1f included a pre-extraction step (Full protocol parameters can be accessed in SI Methods 1).

The images of PFA and GA fixed cells stained for all three target proteins (Figure 1a–f) show sub-diffraction structural detail whereas the methanol protocol yields very poor images of mitochondria and actin (Figure 1g–h) while maintaining good MT structure (Figure 1i). As each image is of a  $2 \times 2 \mu\text{m}$  area, the sub-diffraction detail present in these images can immediately and clearly be observed. In the case of the Tom20 stains (1a and 1d), the boundaries of the MC are more clearly delineated in the PFA fixed cell than in the GA fixed cell and similarly, a lower level of background/non-specific stain is observed when PFA is used. The previously reported<sup>23</sup> clustering of the import receptor unit on the outer MC membrane is also visible. This clustering is clear evidence of the successful application of SMLM to elucidate sub-diffraction structure as epifluorescence images of identically prepared Tom20 stained cells yield highly homogeneous membrane visualization with no evidence of the underlying clustering.

The successful actin stains (Fig 1b and e) were somewhat more difficult to obtain and cytoskeleton-stabilizing buffers (CSBs) were found to make a significant difference to the preservation of the



**Figure 2 | SMLM microtubule images of sub-optimally fixed cells reveal sub-diffraction artifacts not observable in epifluorescence images.**

(A–C) Epifluorescence images of COS-7 cells stained for tubulin using Alexa Fluor 647 after fixation with PFA (A) for a shorter period than optimal, (B) at a lower concentration than optimal, and (C) for a longer period than optimal. These images are not readily identified as having fixation artifacts. (D–F) Corresponding SMLM images of sub-areas from A–C show clear sub-diffraction scale damage to the microtubule architecture with some areas well preserved and continuously stained in D–E (white arrows) and other long stretches of filament missing or damaged beyond antibody-epitope recognition. Scale bars A–C: 5  $\mu$ m, D: 1  $\mu$ m, E–F: 500 nm.

structure during GA fixation and have accordingly been used throughout. Any perturbation to the architecture of the actin was found to significantly impact the SMLM images. This is because the distribution of actin within cells is far denser, sometimes taking up to 20% of the protein mass in muscle cells and having less defined and more complicated ultrastructure compared to the MT or MC network<sup>28</sup>. Singular microfilaments of actin are only 4–6 nm in diameter, with intermediate filaments  $\sim$  10 nm wide<sup>29</sup>. Larger bundles, known as stress fibres consist of tens of microfilaments and can measure up to 300 nm wide<sup>30</sup> with filaments of various widths often distributed  $<$  10 nm from neighbouring filaments<sup>31</sup>. In epifluorescence and confocal imaging only the large stress fibres can be imaged and identified over the homogeneous signal of actin throughout the rest of the cell. Using the optimized PFA protocol (Fig 1b) we were unable to identify structural features beyond this, although the stress fibres themselves were resolved with much enhanced acuity demonstrating cross sections regularly smaller than those limited by diffraction (50–70 nm).

Using GA (Fig 1e) much of the substructure could be observed with fibres detected at less than 25 nm wide and resolved well from microfilaments less than 30 nm away. In both cases, the average localization precision of the Alexa Fluor conjugated F(ab')<sub>2</sub> fragments was calculated to be approximately 13 nm and so the lack of clear structure in Fig 1b is strong evidence that the limitation to spatial resolution is not the measurement or equipment but rather the sample itself.

Under optimized conditions all three fixatives could produce very high quality MT images (Fig 1c,f,i) with good cross section widths ( $<$  60 nm in all three examples) and very little background/non-specific stain. This low background stain was achieved by adding a pre-extraction step for both the PFA and GA fixations that removed the cytosol (SI Methods 1), and with it, many of the potential sites for non-specific attachment. It should also be noted that for good continuous structures in the methanol fixed cells, a four-fold increase in antibody concentration was necessary as well as the previously men-

tioned careful modulation of the temperature of the fixative. It is important to appreciate that conventional background fluorescence does not manifest directly in a reconstructed SMLM image because only single, bright fluorophore PSFs are fitted to Gaussians and localized using rapidSTORM. Instead, any background fluorescence that is present as homogeneous signal, lowers the localization precision of the measurement and can then worsen the spatial resolution of the resulting image (See SI Figure 1). It is fair to assume then that any localized molecule in these images is an Alexa Fluor and the question becomes whether the fluorophore is specific to the target molecule or not.

**Sub-optimal initial application of the fixative to cells causes sub-diffraction artifacts.** Following optimization of the protocols, we investigated the many artifacts observed in SMLM images of sub-optimally fixed MTs and MC. Worth mentioning but without need for extensive discussion, we observed that temperature, fixative concentration, fixation time, the use of blocking buffers, and the importance of quenching after glutaraldehyde fixation, were all parameters that need to be optimized for each new cell type and target protein. These parameters have previously been discussed in the literature extensively<sup>14,18,32</sup> and artifacts associated with them were often observed in both the epifluorescence and SMLM images.

Interestingly, the steps within our optimized protocols and, indeed, in all trialled protocols, that were observed to produce the most sub-diffraction scale damage were those involved in the initial application of the fixative. This included both the type of fixative used and the technique with which it was introduced into the cells. Examples of the regularly observed sub-diffraction artifacts that resulted are shown in Figure 2. Contrary to widespread practice, we observed best structure preservation when no initial washing step was conducted for the PFA and GA fixations. Application of PBS even at 37°C for 60 seconds caused changes in the clustering distribution on the MC membrane and introduced short unstained/damaged tracts on the MTs like those shown in Fig 2e. Similarly,



any degree of dehydration prior to fixation caused similar artifacts to arise and because of the chamber walls, our samples were particularly susceptible to this if care was not taken. For these reasons we have specified that culture medium be removed from one side of the chamber while 37°C PFA or GA fixative is added simultaneously down the opposite chamber wall. This appears to increase the amount of non-specific aggregated stain on the coverglass outside of the cells but allows very good preservation of the MT, MC and actin substructure.

Often extra-cellular protein was observed to precipitate onto the glass or cells during methanol fixation and was not easily removed by extensive washing following fixation. For this reason we developed a protocol via which FBS was removed from the cell culture environment prior to fixing and then a single warm wash was applied. It is possible that some of the artifacts seemingly omnipresent in our methanol fixed cells and discussed below are due to the inclusion of these extra steps although precipitating fixatives have previously been identified as causing a significant loss of overall cellular structure<sup>27</sup>.

**Temperature, blocking buffer, quenching, washing and tonicity all affect SMLM images.** In the case of the temperature of the applied fixative, the literature values vary from  $-20^{\circ}\text{C}$  to room temperature for methanol<sup>33</sup>, and from  $4^{\circ}\text{C}$  to  $45^{\circ}\text{C}$  for cross linking fixatives<sup>34-36</sup>, depending on the target. Clearly optimization of fixation temperature was required and various temperatures were tested and incorrect temperatures observed often to result in artifacts like those depicted in Figure 2. However for MT, MC and actin,  $37^{\circ}\text{C}$  PFA or GA, and  $-20^{\circ}\text{C}$  methanol were found reproducibly to yield the best structural preservation. Similarly, the concentrations of fixative and permeabilizer listed in the protocols yielded the best SMLM images when compared with other tested concentrations.

We developed washing steps that increased in duration because this was observed to aid in the removal of the majority of the contaminant in the first 2–3 steps and then any remaining strongly-bound contaminant was removed over the final 10–15 minute washes. The tonicity of the solutions used was also found to be very important in preserving sub-diffraction structure, and slightly hyper- or hypotonic solutions resulted in significant changes to the MT architecture and MC size. This was particularly true if the solutions used prior to, or during the fixation and permeabilization steps were not isotonic. This is why we have stressed the use of 2X PBS and CSB to calculate isotonic solutions throughout.

As reported previously<sup>14</sup> blocking buffers were used to lower the degree of antibody binding to non-target proteins. However, the antibodies used were found to have very high specificity for our target proteins with there being only small decreases in non-specific binding upon use of a 2–10% blocking buffer. This slight decrease in non-specific dye localizations was only observed when all subsequent steps including antibody incubations and washes were also conducted in the same concentration of BSA blocking buffer. Finally, quenching of samples with either NaBH<sub>4</sub> or glycine following GA fixation<sup>6</sup> was observed to drastically increase the signal to noise of single Alexa Fluor 647 dyes thus improving overall localization precision. Overall various concentrations of permeabilizing agent (Triton X-100, 0.1–1%), blocking buffer (BSA, 2–10%) and quencher (NaBH<sub>4</sub>, 0.1–1%) were all observed to produce acceptable images with only slight changes in quality and structure. Finally, in optimization of the fixation protocols it was observed that the use of cytoskeleton stabilizing buffers aided in preservation of both MT and actin architecture but did not affect the images of MCs when used in conjunction with GA.

**Over or under exposure of cells to fixative chemicals cause sub-diffraction artifacts.** Fixative concentration and incubation time were found to be key to preserving sub-diffraction structure. Figure 2 depicts epifluorescence and super-resolution images of

MTs in cells that were fixed in GA for less time than optimal (Fig 2a and d), at a lower concentration than optimal (Fig 2b and e), and for longer than optimal (Fig 2c and f) (Full protocols in SI Methods 2). These types of sub-diffraction artifacts were also routinely encountered when different temperatures or pre-fixation washing steps were used. Moreover, the severity of these artifacts was found to vary depending on several parameters. As such they were often seen and represent any number of biochemical changes to the MTs themselves.

Importantly, the epifluorescence images (Fig 2a–c) are not immediately recognisable as having fixation artifacts and would often be considered fit for publication, especially at low levels of magnification such as in images of multiple cells. For comparison epifluorescence images of cells fixed according to the optimized protocols are provided (SI Figure 1a and e) and show similar structures to those in Figure 2a–c. Conversely the damage to the MT structure is readily identifiable in the corresponding super-resolution images (bottom, 2d–f). Figure 2a–b, d–e depict cells that we hypothesize have not been fixed sufficiently so that the MTs themselves have not been immobilized sufficiently and stabilized in place to avoid damage from subsequent steps. This under-fixation occurs when the biochemical changes necessary for successful fixation are not completed to the required degree prior to removal of the fixative solution. Some areas of the MT architecture are well preserved with continuous, well-stained MTs observed over  $>500$  nm (Fig 2d, white arrow) while in other areas, filaments seem to have either been removed or the epitopes damaged over similar length scales (Fig 2d red arrow). Lower concentrations of fixative or less time for incubation were seen to exacerbate this problem as shown in Fig 2e in which long continuous well-stained MTs (white arrow) are observable with gaps in which blur indicates some disruption to the structure or possible movement during image acquisition (red arrow). Even lower concentrations/shorter incubation times were observed to result in large areas of cells being removed during subsequent washing steps.

Conversely, over-fixing occurred when the primary directive of fixation—to secure the native biological structure in place—was achieved but then further chemical modifications were made. In this case it appears that the MTs have been damaged by the GA in some places but not others. More extensive over-fixation (either by leaving the fixative on longer or at a higher concentration) was observed to erode MT structure completely and, in extreme cases, destroy entire cells. These images clearly demonstrate that the first few minutes of any fixation protocol are the most important in preserving sub-diffraction structure.

**Without optimization established protocols often result in artificial SMLM images.** Figure 3 further investigates sub-diffraction artifacts by directly comparing four common protocols used for preparing cells for MT staining and confocal imaging (Full protocols in SI Methods 3). Figure 3a shows a cell fixed using methanol kept at  $-20^{\circ}\text{C}$  throughout the fixation. Some epitope damage is observed since there are discontinuous filaments present, (white arrow) despite the use of increased antibody concentration for methanol fixed stains. Minimal background/nonspecific stain is observed without the use of pre-extraction or blocking steps. Figure 3b shows a cell fixed in methanol at  $-20^{\circ}\text{C}$  but allowed to sit in ambient conditions for the 20 minutes of fixation, thus raising the temperature of the methanol. There is some indication of non-native curvature in these MTs (blue arrow) as well as structure and clustering in the non-specific dyes localized near the filaments (red arrow). This clustering of the non-specific stain is not observed under any of the other trialled or optimized fixation methods. Figure 3c shows MTs fixed using room temperature, 4% PFA: while MT filaments can be observed in this image and the average cross section of these single MTs is comparable with optimized protocols ( $\sim 60$ – $65$  nm), the image suffers from some discon-

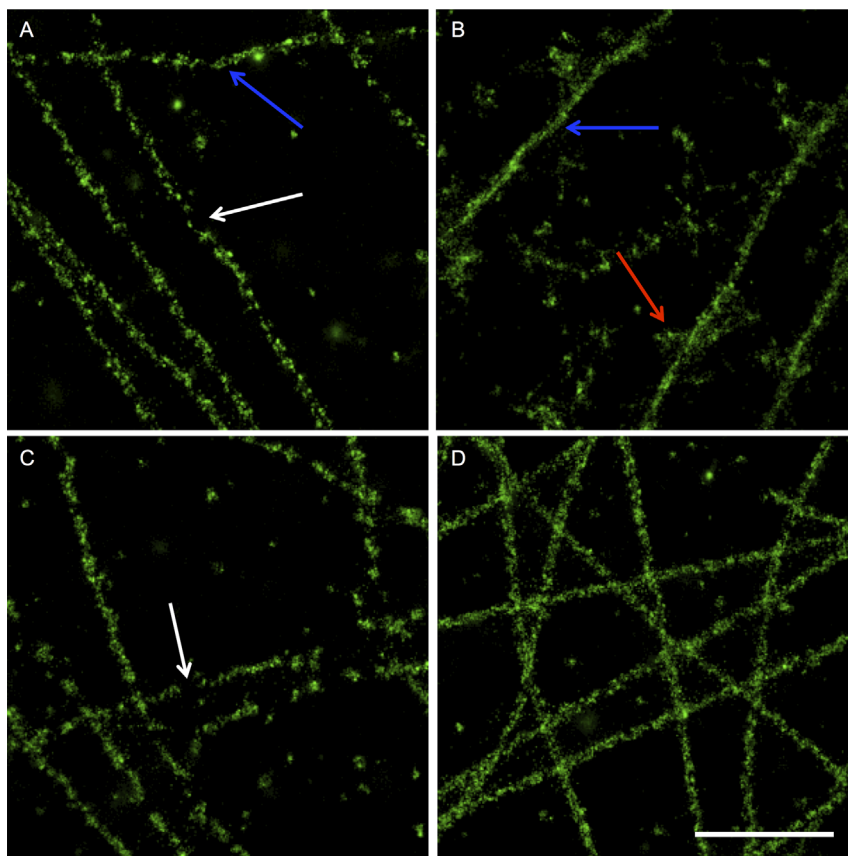


**Figure 3 | SMLM images of microtubules prepared using standard protocols but with careful initial preparation and application of the fixative solutions show some sub-diffraction artifacts but preserve much of the filamentous architecture.** (A–D) COS-7 cells stained for tubulin using Alexa Fluor 647 after fixation with (A)  $-20^{\circ}\text{C}$  methanol following a PBS wash, (B)  $-20^{\circ}\text{C}$  methanol allowed to equilibrate to room temperature during fixation, (C) room temperature 4% paraformaldehyde, and (D) 3% glutaraldehyde following pre-extraction using 0.3% Triton X-100. White arrows indicate discontinuousness of filaments, blue arrows indicate abnormal curvature of the filaments, red arrows indicate structured but non-filamentous localizations. Scale bar: 1  $\mu\text{m}$ .

tinuousness in the MT structures as well as increased background/non-specific stain. Finally, Figure 3d shows MTs in a cell fixed using a pre-extraction step and 3% GA in CSB, demonstrating well-conserved architecture and a low level of background/non-specific stain. While methanol is an often-used fixative for MT structure preservation, these results show that GA is preferable and invite further investigation into the biochemical causes for the differences between methanol and GA fixed cells. They are also an excellent illustration of a previously sufficient protocol yielding unexpected artifacts at a sub-diffraction level.

**Both antibody concentration and permeabilization techniques affect the distribution of fluorophores within the sample.** Like the MTs in Fig 1i, Fig 4a shows a cell fixed in  $-20^{\circ}\text{C}$  methanol. In this cell almost no non-specific stain is detected despite a high antibody concentration used. Similarly, cells pre-extracted with 0.3% Triton X-100 in growth medium have a very low amount of non-specific stain (Fig 4b) (SI Methods 4). Permeabilization of the cells in a pre-fixation step with a low concentration of GA (0.3% with 0.3% Triton X-100) was observed to leave some cytosolic non-specific stain (Fig 4c) while permeabilizing after fixation (2% GA, followed by 0.3% Triton X-100) yielded the highest amount of non-specific localizations (Fig 4d). In all images the MTs themselves have been stained well with continuous filaments intact and yielding average cross-sections of 55–65 nm. These observations led us to hypothesize that the localized fluorophores not associated with polymeric tubulin were associated with cytosolic dimeric tubulin and were not non-specific in the traditional sense. If they were

truly non-specific we would expect to see non-polymeric localizations even with the cytosol removed.

Images supporting this hypothesis are shown in Figure 5 which depicts changes observed in response to different antibody concentrations applied to MTs. As mentioned above, homogeneous background fluorescence does not result in localizations therefore this represents only the Alexa Fluor dyes. These cells were all fixed according to the optimized GA protocol and then stained over the dilution range of 1:50 to 1:2000 primary and secondary antibodies. In all cases the antibody solutions were administered in 200  $\mu\text{l}$  aliquots with a primary incubation time of three hours and a secondary incubation time of one hour. Figure 5a shows heavily overstained MTs with an increased average MT width (91 nm) as well as a very high level of background/non-specific stain. A magnitude less antibody results in the MTs depicted in Fig 5b. These MTs have average widths of 58 nm and a significantly lowered amount of non-specific stain and depict the optimal staining density for SMLM. An image of stained MTs resulting from further dilution of the antibodies is shown in Fig 5c depicting an even lower number of non-specific localizations but also suffering from very discontinuous MT filaments. A control stain in which the primary antibody was not used showed almost no localizations demonstrating that the non-specific stain observed in Fig 5 is not simply non-specific secondary antibody. This suggests that these are not ‘traditional’ non-specific fluorophore attachment but are something specific, most likely dimeric tubulin. Previous SMLM publications featuring MTs have not identified the non-polymeric localizations seen in their published images as dimeric tubulin. Nor has it been discussed that by pre- or simulta-

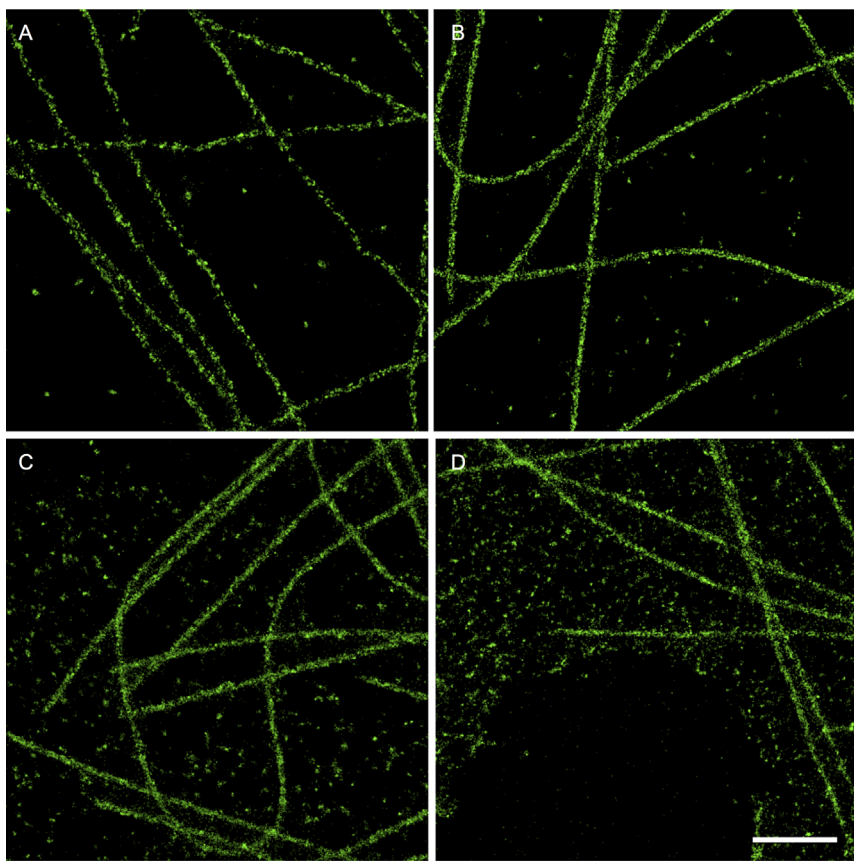


**Figure 4 |** The timing of permeabilization of cells significantly affects the distribution of fluorophores within the cell, resulting in differences in the ‘cleanliness’ of the image as well as the degree to which the image is representative of the biologically native structure and distribution. (A–D) COS-7 cells stained for tubulin using Alexa Fluor 647 after (A) fixation with  $-20^{\circ}\text{C}$  methanol, (B) pre-extraction with 0.3% Triton X-100 in HEPES buffer before 3% glutaraldehyde fixation, (C) simultaneous permeabilization and fixation (0.3% glutaraldehyde with 0.3% Triton X-100), and (D) fixation with 3% glutaraldehyde prior to permeabilization with 0.3% Triton X-100. Scale bar: 1  $\mu\text{m}$ .

neously extracting the cytosol from cells the resulting images appear ‘cleaner’ with less non-filamentous localizations and that this effect is achieved with significant alteration of the biology of the sample, i.e. by removing the cytosol and with it, many ‘real’ tubulin localizations. Diffraction limited confocal or epifluorescence images of MTs in a cell would also detect the dimeric tubulin but as a low-intensity homogeneous background that is easily considered noise below the signal of the MTs themselves.

**Varying fixative and antibody concentration alters the apparent clustering of Tom20 on the mitochondrial membrane.** Our

observations of significant changes in fluorophore distribution and apparent structure in response to permeabilization and antibody dilution prompted us to investigate the impact that similar changes in preparation would have on MC structure. As in Figure 1, the mitochondrial membrane import receptor was imaged by staining the Tom20 subunit after fixation with various protocols. In Figure 6 the first column shows cells fixed using the optimized PFA protocol, the second column shows cells fixed using a mixed PFA/GA (3%/0.5%) (SI Methods 6) protocol, and the right column shows cells fixed according to the optimized GA protocol. The three rows show cells stained with a relatively high concentration of primary

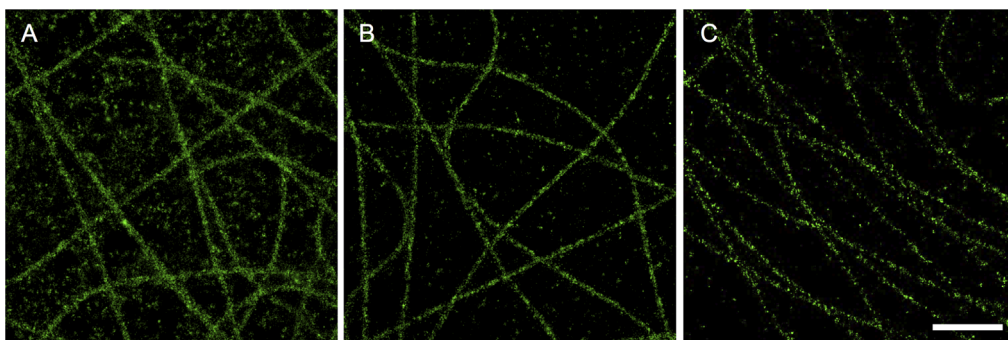


**Figure 5 |** Varying antibody concentration affects apparent microtubule width, non-filamentous stain, and filament continuity—all of which can affect spatial resolution. (A–C) COS-7 cells fixed using the optimized glutaraldehyde protocol and then stained for tubulin using mouse anti- $\beta$ -tubulin and Alexa Fluor 647 conjugated rabbit anti-mouse. (A) Both primary and secondary antibodies were diluted 1:50, (B) 1:500, and (C) 1:2000. Scale bar: 1  $\mu\text{m}$ .

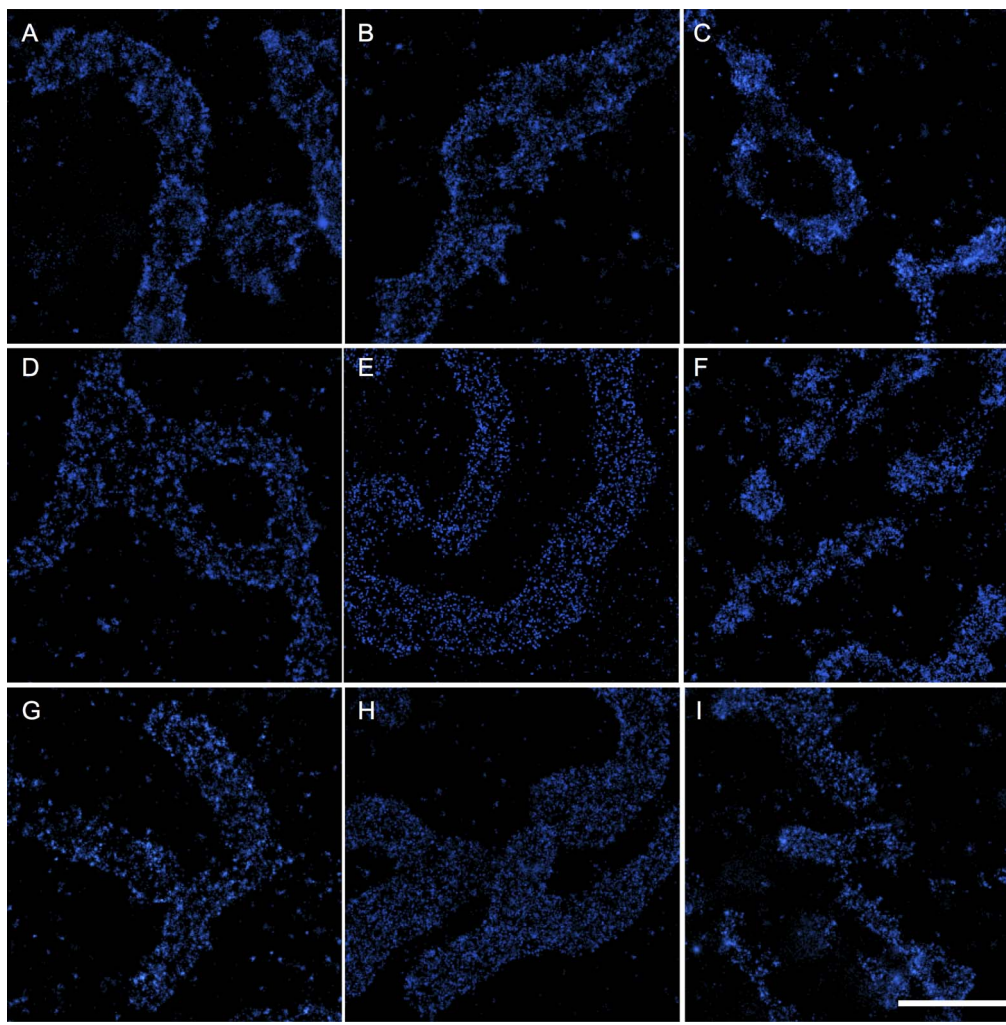


**Figure 6 |** Varying fixative and antibody concentration affects the apparent clustering distribution of import receptors on the mitochondrial membrane. (A–I) COS-7 cells stained using Alexa Fluor 647 primary/secondary antibodies against the Tom20 protein subunit of the import receptor on the outer mitochondria membrane. Cells were stained with a high (A–C, 1 : 50), mid-range (D–F, 1 : 500) or low (G–I, 1 : 2000) concentration of primary and secondary antibodies. Cells were fixed using the optimized paraformaldehyde protocol (A, D, G), a mixed 3% paraformaldehyde, 0.5% glutaraldehyde protocol (B, E, H) or the optimized glutaraldehyde protocol (C, F, I). Scale bar: 1  $\mu$ m.

and secondary antibody (1 : 50, Top, Fig 6a–c), a mid-range concentration of antibody (1 : 500, Fig 6d–f), and a low concentration of antibody (1 : 2000, Fig 6g–i). Cells in the top and middle rows have not been quenched or blocked whereas those depicted in the bottom row (6g–i) were quenched using 1% NaBH<sub>4</sub> and blocked in 3% BSA. Differences in clustering size and distribution are immediately apparent across antibody concentrations as well as fixatives; indeed, upon visual examination differences in all nine protocols can be seen. This is further demonstrated with basic cluster analysis which was performed by scanning the dSTORM images for clustered fluorophores forming features larger than  $2 \times 2$  10 nm pixels (400 nm<sup>2</sup>) and smaller than  $30 \times 30$  10 nm pixels (90,000 nm<sup>2</sup>) and then measuring the size of these clusters. Extensive preprocessing of the data was not necessary, nor was the definition of regions of interest, in order to acquire reasonable estimates of average cluster size. This was found to range from 2020–4330 nm<sup>2</sup> corresponding to a range of average diameters (assuming circular arrangements) from 51–74 nm across all fixation and immunostaining conditions tested. The PFA/GA fixed preparation with 1 : 500 dilution of antibodies showing the smallest clusters (Figure 6e) and the 3.7% PFA fixation with 1 : 50 dilution of antibodies showing the largest clusters (Figure 6a) (Results summarized SI Table 1). In some cases, this analysis returned

clusters larger than previous work which estimated them to be 30–40 nm in diameter. This is a consequence of both the enlargement of the Tom20 clusters by antibodies and fluorophores and the simplicity of the analysis performed. It should not be taken as truly quantitative due to the minimal preprocessing, however the large overall variation in mean size is in good agreement with visual examination of the images and confirms the role of fixation artifacts in the final images. In Figure 6 it can be seen that PFA fixation gives clear clustering at all three antibody concentrations but cluster size decreases as antibody concentration decreases. The mixed PFA/GA fixation yields what appears to be a lower degree of clustering with a more homogeneous distribution of localized dyes irrespective of antibody concentration. GA fixation shows a different pattern of clustering once more as well as some indication of shrinkage of the overall MC structure. This demonstration that slight changes in sample preparation—all of which yielded essentially visually identical epifluorescence images—can alter the sub-diffraction distributions and structures in relation to the known native state<sup>23</sup> is extremely important because in many cases the sub-diffraction structure is unknown prior to SMLM. In the case of the Tom20 subunit of the import receptor, previous work using a PFA-based protocol similar to that depicted in Fig. 6d) has detected and quantified this clustering<sup>23</sup>. Without the reference point of this



previously conducted work it would be more difficult to substantiate any claim that one protocol was more biologically accurate compared to the others. The fact that nine different levels of clustering were observed from nine variations of the protocol once again stresses the importance of determining which resembles the true biological native state most closely and to identify the causes of any artifacts.

**General implications for SMLM.** By focussing on fixation and staining protocols for SMLM we have gained significant appreciation for the importance of speed, hydration and minimal perturbation, particularly in the first steps of fixation, as well as for the necessity of adequate protocol optimization. The importance of carefully made solutions with correct tonicity and concentrations of fixative are also demonstrated. Significantly, all of the SMLM images we have shown here have been of structured targets with well-understood architecture due to extensive previous fluorescence and EM work. In contrast, much of the current and ongoing research using SMLM requires imaging of unknown structures and distributions of biomolecules that have not previously been extensively studied. For such research, the protocols established here are presented as a starting point, in particular the fully optimized double GA and 3.7% PFA protocols, which were found to present good images of all three targets. Following fixation with new or modified protocols, cells should be co-stained to investigate the sub-diffraction preservation of known structures (MTs, MCs, actin, etc.) as this will provide insight into the overall structural preservation of the cell. It is unavoidable that significant work will be required to optimize fixation protocols for new experiments in such a way that the structures and distributions of interest are maintained. However, both efficiency and robustness are maximised by starting with an established protocol and known structures and proceeding to probe in a systematic fashion, the impact of changing the main variables (fixative and fixative concentration, permeabilizer and permeabilizer concentration) on the SMLM images of both known and unknown molecule distributions. Extensive further work is necessary to establish the complicated biochemical effects of fixation on cells and will allow better predictions of fixation damage and artifacts. Live-cell SMLM will also undoubtedly assist in detecting, identifying and minimizing fixation artifacts but at present remains very challenging.

Here, by considering well-known structures, we have been readily able to identify unexpected localizations within the images simply with direct observation. In the case of the MTs, breaks in the filaments were observed as well as non-native curvature after methanol fixation, and dyes that were non-specific for the MT filaments but most likely legitimate localizations of dimeric tubulin. In the case of MC, various clustering distributions were seen across different antibody concentrations and fixation protocols and without a known clustering behaviour<sup>23</sup>, no single result would be identifiable as correct. This demonstrates that careful consideration is required for interpretation of all SMLM images and in SMLM studies of distributions of single proteins in the cell, or of co-localization, a significant amount of benchmarking and protocol development is necessary before the images can be reasonably believed to be a reliable depiction of the native state of the sample. It is also worth noting that while direct observation was sufficient to detect differences in the samples presented here, future development of analytical tools for objective, quantitative appraisal of SMLM images will be crucial for the success of many potential applications.

The identification of fluorophores, such as those attached to dimeric tubulin, which would usually be thresholded out as noise also highlights a key difference between confocal and SMLM images. Specifically, SMLM images are not a true optical rendering rather a coordinate map of single molecule localizations; a distinction which must be continually appreciated when evaluating and interpreting SMLM ‘images’. Moreover, the parameters previously used to judge a

confocal fluorescence image—namely the level of signal-to-noise, background, and non-specific stain—do not readily apply to SMLM images and thus judging an image ‘good’ is complicated. Another interesting point that became apparent during our measurements is that even working with well-known structures, such as MC and MTs, the SMLM images that resemble the expected images, as well as those with highest signal or the lowest level of background stain, are not necessarily the most biologically relevant.

Ample literature exists detailing the various SMLM configurations<sup>4,6,9,37–44</sup> as well as the commercial systems available. Conversely, sample fixation and immunostaining for SMLM has not been well discussed with sample preparation methodologies often published without enough information to be reproduced and with no explanation of optimization or potential artifacts. Our measurements highlight the ability of *d*STORM to image sub-diffraction cellular features at a spatial resolution significantly improved (up to ten-fold) on conventional microscopy. We also stress that this improved resolution also brings a similar increase in the apparent severity of artifacts within the image. The many sub-diffraction artifacts we have encountered raise questions over results obtained from samples that were not fixed under optimal conditions and will hopefully be cause for more explicit detailing of the optimization process. We have aimed to highlight the high degree of variability in resulting SMLM images and the differences between normal fluorescence images and SMLM images. Accordingly, we have stressed the importance of protocol development and benchmarking, as well as furthering our understanding of the mechanisms of fixation.

## Methods

**Cell Culture.** COS-7 cells were cultured routinely in Dulbecco’s modified eagle’s medium (DMEM) containing no phenol red and supplemented with 10% foetal bovine serum (FBS) and penicillin (100 units/ml) and streptomycin (100 µg/ml) at 37°C and 5% CO<sub>2</sub>. Cells were regularly passaged to keep confluence below 70% using TryPLE Express (Life Technologies). For all experiments cells were seeded at very low confluences (<20%) directly into 8 well Lab Tek II chambered coverglass (No. 1.5 borosilicate, Nunc). Prior to seeding, these chambers were cleaned by sonication for 15 minutes in 1 M KOH. Each chamber held 500 µl culture medium and was returned to the incubator for 36–48 hours prior to fixation.

**Antibodies and Variations to Protocols.** For the purposes of the figures and discussion presented in this paper the fully optimized protocols were varied somewhat to induce artifacts (Full protocols for each experiment and Figure available in SI). Stated ranges in concentration indicate that little difference was observed. The concentration and time of the fixation steps themselves were also varied to find the ideal balance (data not shown). Both the PFA and GA fixations were also done with an optional pre-extraction step using 37°C 0.3% Triton X100 in PBS or CB for 30 seconds. For all images of MTs mouse anti-α/β-tubulin (Sigma) and Alexa Fluor 647 rabbit anti-mouse (Life Sciences) were used. For images of MC rabbit anti-Tom20 (Santa Cruz) and Alexa Fluor 647 cow anti-rabbit (Life Sciences) were used. For actin staining Alexa Fluor 647-phalloidin (Life Sciences) was used at a 1:500 dilution of 6.6 µM stock solution.

**dSTORM Measurement and Analysis.** Samples were kept at 4°C in the dark and were imaged within a week of fixation and staining. Switching buffer was made up from stock solutions using 2X PBS and milli-Q water, and pH adjusted immediately before measurements. The stock solutions were 20% w/v glucose in milli-Q water, 1 M mercaptoethylamine (MEA) in milli-Q water, and an enzyme cocktail containing catalase and glucose oxidase in PBS. Switching buffer was made up to a concentration of 10% glucose, 120 mM MEA, 400 µg/mL glucose oxidase, and 35 µg/ml catalase in isotonic PBS and 1 M KOH added to adjust the pH to a starting point of 8. The buffer was measured to shift to a pH of 6 during the experiment before significant distortions to the photophysics of the Alexa Fluor 647 dyes was observed.

All measurements were conducted on a home-built widefield microscope as detailed previously<sup>37</sup>. Briefly, a 150 mW 638 nm (Oxxius) diode laser is expanded and then focused using two lenses (focal lengths 25 and 100 mm) onto the back focal aperture of a 1.49 NA 100X TIRF (total internal reflection fluorescence) objective (Köhler illumination) via a dichroic filter. A quasi-TIRF illumination pattern is achieved by translating the excitation beam so that it is entering the objective off-centre, but parallel to the optical axis. Fluorescence is collected back through the objective and dichroic filter and imaged directly onto an electron-multiplying charge-coupled device (EM-CCD) camera (Andor Ixon Ultra).

All images were obtained using the Andor Solis software with the microscope in Q-TIRF mode using a power density of approximately 3–6 kW cm<sup>-2</sup>. Between ten and twenty thousand frames were collected at a frame rate of 80–100 Hz with the EM-Gain held at 200 (For an example of single frames showing single molecule emissions



see SI Figure 1b-d and f-h). TIFF stacks were directly imported into the rapidSTORM software suite and used to generate super resolution coordinate files that were rendered into SMLM images using  $10 \times 10$  nm pixels. The input pixel size was set at 105 nm and the PSF FWHH diameter found to be 350 nm by using the rapidSTORM 'Estimate PSF form'. Single molecule emissions were identified only when more than 600 photons were detected within a single frame and localized to a single spot. The rapidSTORM software identified single molecule emissions as sufficiently intense local maxima in the noise-reduced (using an average mask) image and localized the centroid using a 350 nm 2D Gaussian function<sup>45</sup>. SI Figure 1b-d and f-h show example frames with well-separated single molecule emissions. Localization precision was estimated using the equation derived by Thompson<sup>46</sup> and MT widths quoted are full width at half maximum of an intensity cross-section averaged over 400 nm. For cluster analysis of the distribution of Tom20 on the MC membrane, the images shown in Figure 6 were smoothed and analysed using "Analyse Particles" in the FIJI software suite<sup>47</sup>.

- Hess, S. T., Girirajan, T. P. K. & Mason, M. D. Ultra-high resolution imaging by fluorescence photoactivation localization microscopy. *Biophys. J.* **91**, 4258–4272 (2006).
- Betzig, E. *et al.* Imaging intracellular fluorescent proteins at nanometer resolution. *Science* **313**, 1642–1645 (2006).
- Heilemann, M. *et al.* Subdiffraction-resolution fluorescence imaging with conventional fluorescent probes. *Angew. Chem. Int. Edit.* **47**, 6172–6176 (2008).
- Rust, M. J., Bates, M. & Zhuang, X. W. Sub-diffraction-limit imaging by stochastic optical reconstruction microscopy (STORM). *Nat. Methods* **3**, 793–795 (2006).
- Jones, S. A., Shim, S.-H., He, J. & Zhuang, X. Fast, three-dimensional super-resolution imaging of live cells. *Nat. Methods* **8**, 499–U496 (2011).
- Xu, K., Babcock, H. P. & Zhuang, X. W. Dual-objective STORM reveals three-dimensional filament organization in the actin cytoskeleton. *Nat. Methods* **9**, 185–188 (2012).
- Klein, T., Proppert, S. & Sauer, M. Eight years of single-molecule localization microscopy. *Histochem. Cell Biol.* **141**, 561–575 (2014).
- Gould, T. J., Verkushava, V. V. & Hess, S. T. Imaging biological structures with fluorescence photoactivation localization microscopy. *Nat. Protoc.* **4**, 291–308 (2009).
- van de Linde, S. *et al.* Direct stochastic optical reconstruction microscopy with standard fluorescent probes. *Nat. Protoc.* **6**, 991–1009 (2011).
- Huang, B., Jones, S. A., Brandenburg, B. & Zhuang, X. W. Whole-cell 3D STORM reveals interactions between cellular structures with nanometer-scale resolution. *Nat. Methods* **5**, 1047–1052 (2008).
- Klein, T. *et al.* Live-cell dSTORM with SNAP-tag fusion proteins. *Nat. Methods* **8**, 7–9 (2011).
- Wombacher, R. *et al.* Live-cell super-resolution imaging with trimethoprim conjugates. *Nat. Methods* **7**, 717–U772 (2010).
- Kamiyama, D. & Huang, B. Development in the STORM. *Dev. Cell* **23**, 1103–1110 (2012).
- Bennett, B. T., Bewersdorf, J. & Knight, K. L. Immunofluorescence imaging of DNA damage response proteins: Optimizing protocols for super-resolution microscopy. *Methods* **48**, 63–71 (2009).
- Loeschberger, A. *et al.* Super-resolution imaging visualizes the eightfold symmetry of gp210 proteins around the nuclear pore complex and resolves the central channel with nanometer resolution. *J. Cell Sci.* **125**, 570–575 (2012).
- Szymborska, A. *et al.* Nuclear pore scaffold structure analyzed by super-resolution microscopy and particle averaging. *Science* **341**, 655–658 (2013).
- Dempsey, G. T., Vaughan, J. C., Chen, K. H., Bates, M. & Zhuang, X. Evaluation of fluorophores for optimal performance in localization-based super-resolution imaging. *Nat. Methods* **8**, 1027–1036 (2011).
- Schnell, U., Dijk, F., Sjollema, K. A. & Giepmans, B. N. G. Immunolabeling artifacts and the need for live-cell imaging. *Nat. Methods* **9**, 152–158 (2012).
- Small, J. V., Rottner, K., Hahne, P. & Anderson, K. I. Visualising the actin cytoskeleton. *Microsc. Res. Techniq.* **47**, 3–17 (1999).
- Xu, K., Zhong, G. S. & Zhuang, X. W. Actin, spectrin, and associated proteins form a periodic cytoskeletal structure in axons. *Science* **339**, 452–456 (2013).
- Small, J. V., Isenberg, G. & Celis, J. E. Polarity of actin at the leading edge of cultured cells. *Nature* **272**, 638–639 (1978).
- Bates, M., Huang, B., Dempsey, G. T. & Zhuang, X. W. Multicolor super-resolution imaging with photo-switchable fluorescent probes. *Science* **317**, 1749–1753 (2007).
- Wurm, C. A. *et al.* Nanoscale distribution of mitochondrial import receptor Tom20 is adjusted to cellular conditions and exhibits an inner-cellular gradient. *Proc. Natl. Acad. Sci. U. S. A.* **108**, 13546–13551 (2011).
- Doughty, M. J., Bergmansson, J. P. G. & Blocker, Y. Shrinkage and distortion of the rabbit corneal endothelial cell mosaic caused by a high osmolality glutaraldehyde-formaldehyde fixative compared to glutaraldehyde. *Tissue Cell* **29**, 533–547 (1997).
- Vielkind, U. & Swierenga, S. H. A simple fixation procedure for immunofluorescent detection of different cytoskeletal components within the same cell. *Histochemistry* **91**, 81–88 (1989).
- Stadler, C., Skogs, M., Brisman, H., Uhlen, M. & Lundberg, E. A single fixation protocol for proteome-wide immunofluorescence localization studies. *J. Proteomics* **73**, 1067–1078 (2010).
- Hoetelmans, R. W. M. *et al.* Effects of acetone, methanol, or paraformaldehyde on cellular structure, visualized by reflection contrast microscopy and transmission and scanning electron microscopy. *Appl. Immunohisto. M. M.* **9**, 346–351 (2001).
- Kim, H. R., Gallant, C., Leavis, P. C., Gunst, S. J. & Morgan, K. G. Cytoskeletal remodeling in differentiated vascular smooth muscle is actin isoform dependent and stimulus dependent. *Am. J. Physiol.-Cell Ph.* **295**, C768–C778 (2008).
- Schroede, T. E. Actin in dividing cells – contractive ring filaments bind heavy meromyosin. *Proc. Natl. Acad. Sci. U. S. A.* **70**, 1688–1692 (1973).
- Kumar, S. *et al.* Viscoelastic retraction of single living stress fibers and its impact on cell shape, cytoskeletal organization, and extracellular matrix mechanics. *Biophys. J.* **90**, 3762–3773 (2006).
- Cooke, P. Filamentous cytoskeleton in vertebrate smooth-muscle fibers. *J. Cell Bio.* **68**, 539–556 (1976).
- Srinivasan, M., Sedmak, D. & Jewell, S. Effect of fixatives and tissue processing on the content and integrity of nucleic acids. *Am. J. Pathol.* **161**, 1961–1971 (2002).
- Noguchi, M., Furuya, S., Takeuchi, T. & Hirohashi, S. Modified formalin and methanol fixation methods for molecular biological and morphological analyses. *Pathol. Int.* **47**, 685–691 (1997).
- Fox, C. H., Johnson, F. B., Whiting, J. & Roller, P. P. Formaldehyde fixation. *J. Histochem. Cytochem.* **33**, 845–853 (1985).
- Bussolati, G., Annaratone, L., Medico, E., D'Armento, G. & Sapino, A. Formalin fixation at low temperature better preserves nucleic acid integrity. *Plos One* **6**, doi:10.1371/journal.pone.0021043 (2011).
- Zakout, Y. M. A., Salih, M. M. & Ahmed, H. G. The effect of fixatives and temperature on the quality of glycogen demonstration. *Biotech. Histochem.* **85**, 93–98 (2010).
- Whelan, D. R., Holm, T., Sauer, M. & Bell, T. D. M. Focus on super-resolution imaging with direct stochastic optical reconstruction microscopy (dSTORM) *Aust. J. Chem.* **67**, 179–183 (2014).
- Lippincott-Schwartz, J. & Manley, S. Putting super-resolution fluorescence microscopy to work. *Nat. Methods* **6**, 21–23 (2009).
- Mortensen, K. I., Churchman, L. S., Spudich, J. A. & Flyvbjerg, H. Optimized localization analysis for single-molecule tracking and super-resolution microscopy. *Nat. Methods* **7**, 377–381 (2010).
- Wolter, S. *et al.* rapidSTORM: accurate, fast open-source software for localization microscopy. *Nat. Methods* **9**, 1040–1041 (2012).
- Holm, T. *et al.* A blueprint for cost-efficient localization microscopy. *Chemphyschem* **15**, 651–654 (2013).
- Dedecker, P., Duwe, S., Neely, R. K. & Zhang, J. Localizer: fast, accurate, open-source, and modular software package for superresolution microscopy. *J. Biomed. Opt.* **17** (2012).
- Henriques, R. *et al.* QuickPALM: 3D real-time photoactivation nanoscopy image processing in ImageJ. *Nat. Methods* **7**, 339–340 (2010).
- Kechkar, A., Nair, D., Heilemann, M., Choquet, D. & Sibarita, J.-B. Real-time analysis and visualization for single-molecule based super-resolution microscopy. *Plos One* **8** doi:10.1371/journal.pone.0062918 (2013).
- Wolter, S., Schüttelpehl, M., Tscherpanow, M., van der Linde, S., Heilemann, M. & Sauer, M. Real-time computation of subdiffraction-resolution fluorescence images. *J. Microsc-Oxford* **237**, 12–22 (2009).
- Thompson, R. E., Larson, D. R. & Webb, W. W. Precise nanometer localization analysis for individual fluorescent probes. *Biophys. J.* **82**, 2775–2783 (2002).
- Schindelin, J. *et al.* Fiji: An open-source platform for biological-image analysis. *Nat. Methods* **9**, 676–682 (2012).

## Acknowledgments

TDMB is grateful for a Monash University Faculty of Science Dean's Strategic Funding Initiative. TDMB and DRW thank the German Laboratory Exchange Program (DAAD). DRW acknowledges an Australian Synchrotron Scholarship.

## Author contributions

D.R.W and T.D.M.B conceived, designed and performed the experiments, analyzed the data and wrote the paper.

## Additional information

Supplementary information accompanies this paper at <http://www.nature.com/scientificreports/>

**Competing financial interests:** The authors declare no competing financial interests.

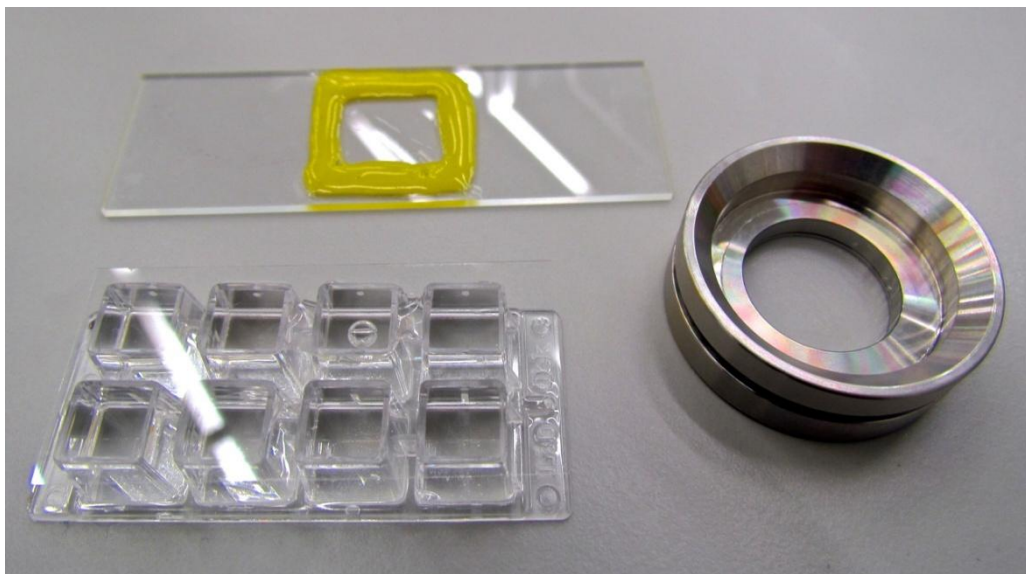
**How to cite this article:** Whelan, D. R. & Bell, T. D. M. Image artifacts in Single Molecule Localization Microscopy: why optimization of sample preparation protocols matters. *Sci. Rep.* **5**, 7924; DOI:10.1038/srep07924 (2015).



This work is licensed under a Creative Commons Attribution-NonCommercial-ShareAlike 4.0 International License. The images or other third party material in this article are included in the article's Creative Commons license, unless indicated otherwise in the credit line; if the material is not included under the Creative Commons license, users will need to obtain permission from the license holder in order to reproduce the material. To view a copy of this license, visit <http://creativecommons.org/licenses/by-nc-sa/4.0/>

# Localisation Microscopy Coverglass Guide

This guide describes 3 different sample formats suitable for (d)STORM, PALM, GSDIM and similar super-resolution microscopy techniques where sample immersion in an aqueous buffer is necessary. In particular this mounting guide is intended for use with dyes or fluorescent proteins that require the use of an oxygen scavenging switching buffer, for example Alexa 647 in glucose oxidase with MEA. Imaging should be possible for 2 to 8 hours without needing to change the switching buffer.



LabTek chambers	2
Coverslips with cavity chambers	3
Coverslips with Attofluor cell chamber	4
Product references	5

## LabTek Chambered Coverglass

1. Fill the chambers to the top with switching buffer (approximately 850 µl).

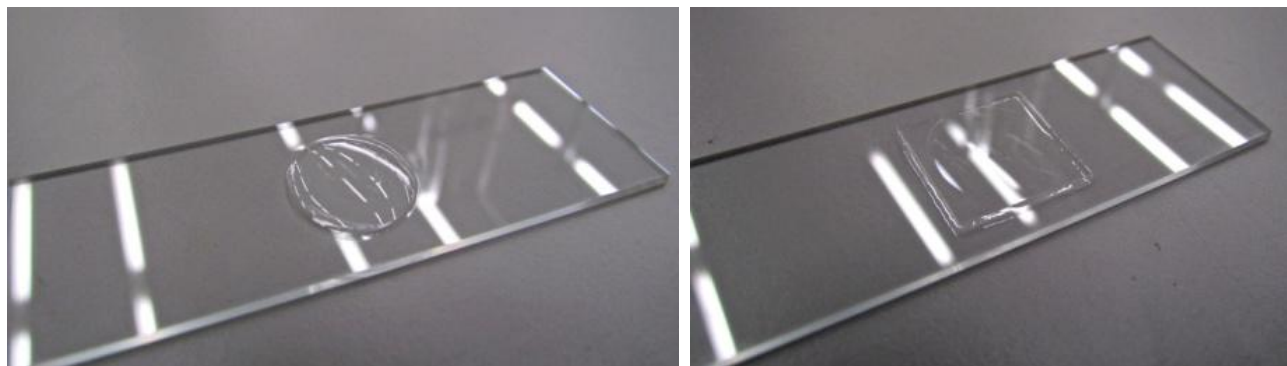


2. Place a coverslip on top of the chambers ensuring that there are no bubbles inside.

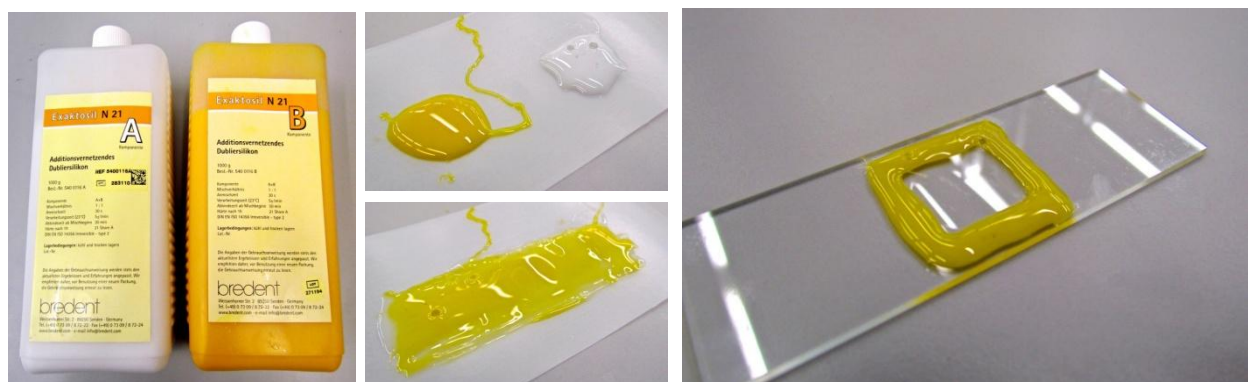


## Coverslips with Cavity Slides

1. Add approximately 150  $\mu$ l of switching buffer to the cavity and place inverted coverslip (18–25 mm diameter circular or square) onto it, with sample side facing down. Push lightly down into place with a pair of forceps or a cocktail stick. Carefully wipe away excess buffer.



2. Mix silicone adhesive components A and B together in a 1:1 ratio and then carefully apply with a cocktail stick around the edges of the coverslip. Wait 15-30 minutes for it to set firmly before imaging.



*Tip: Try and keep the amount of silicone adhesive to a minimum. This results in quicker setting & reduces the chances of the objective lens pushing against the silicone when imaging.*

# Coverslips with Attofluor Cell Chamber

1. Insert 25 mm diameter circular coverslip into cell chamber with sample side facing up.



2. Screw top section down onto coverslip gently to form a seal with red O-ring.



3. Fill with switching buffer, approximately 1.5 ml, and place another 25 mm diameter circular coverslip over the top. Press gently down with forceps or a cocktail stick ensuring that there are no bubbles. Carefully wipe away excess buffer.

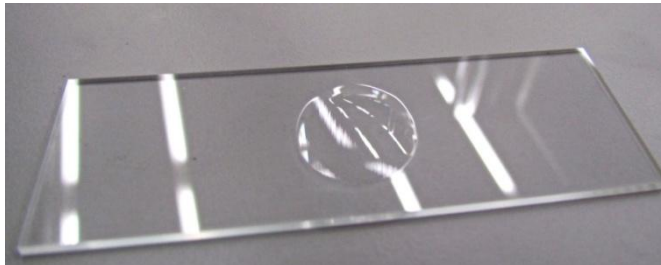


## Product References

LabTek chambered coverglass 8-well (#1)  
Fisher – 11377694\*



Microscope slides with single cavity  
Fisher – 12312158



Certain commercial materials, instruments and equipment are identified in this document in order to specify the experimental procedure as completely as possible. In no case does such identification imply recommendation or endorsement by the National Physical Laboratory, nor does it imply that the material, instrument or equipment identified is necessarily the best available for the purpose.

\*There is a similar product with #1.5 thickness glass available (Fisher – 12812794). Be aware this has a plastic tab on the end of the chamber which is incompatible with some sample holders. It can be cut off with sharp scissors or a scalpel if careful.

### Glass thickness

In most cases coverglass thicknesses of #1 or #1.5 will be suitable for use with high NA oil immersion objective lenses. Match your objective lens, glass thickness and oil refractive index!

Coverglass thickness can vary. Correction collar adjustment is recommended. If there is a mismatch localisation algorithms will not be able to localise molecules as accurately due to spherical aberration. This results in super-resolution images with worse resolution and fewer localisations in the final image.

Attofluor Cell Chambers  
Invitrogen – A-7816



Silicon adhesive (Exactosil N21)  
Bredent UK, 54001147



Number	Thickness (mm)
0	0.08 – 0.13
1	0.13-0.16
1.5	0.16-0.19
2	0.19-0.25

# SCIENTIFIC REPORTS



OPEN

## Light-induced cell damage in live-cell super-resolution microscopy

Sina Wäldchen\*, Julian Lehmann\*, Teresa Klein, Sebastian van de Linde & Markus Sauer

Received: 01 April 2015

Accepted: 22 September 2015

Published: 20 October 2015

Super-resolution microscopy can unravel previously hidden details of cellular structures but requires high irradiation intensities to use the limited photon budget efficiently. Such high photon densities are likely to induce cellular damage in live-cell experiments. We applied single-molecule localization microscopy conditions and tested the influence of irradiation intensity, illumination-mode, wavelength, light-dose, temperature and fluorescence labeling on the survival probability of different cell lines 20–24 hours after irradiation. In addition, we measured the microtubule growth speed after irradiation. The photo-sensitivity is dramatically increased at lower irradiation wavelength. We observed fixation, plasma membrane permeabilization and cytoskeleton destruction upon irradiation with shorter wavelengths. While cells stand light intensities of  $\sim 1 \text{ kW cm}^{-2}$  at 640 nm for several minutes, the maximum dose at 405 nm is only  $\sim 50 \text{ J cm}^{-2}$ , emphasizing red fluorophores for live-cell localization microscopy. We also present strategies to minimize phototoxic factors and maximize the cells ability to cope with higher irradiation intensities.

Fluorescence microscopy is the method of choice for the relatively non-invasive visualization of biomolecules in living cells because it allows selective and specific detection of molecules with high signal-to-background ratio. However, with increasing spatiotemporal resolution the prevention of photodamage effects in live-cell fluorescence microscopy becomes increasingly challenging. This is especially true for single-molecule sensitive fluorescence imaging and tracking experiments where photobleaching of the fluorophores sets the ultimate experimental limit. To use the limited photon budget efficiently in live-cell experiments and reduce photobleaching and phototoxicity, low irradiation intensities confined to micron-thin planes<sup>1</sup>, e.g., light-sheet and Bessel beam plane illumination microscopy, have been used also in combination with super-resolution structured illumination microscopy<sup>2–4</sup>.

Super-resolution microscopy by single-molecule detection and precise position determination (localization microscopy)<sup>5–8</sup> achieves a higher spatial resolution but requires higher irradiation intensities in the  $\text{kW cm}^{-2}$  range, because switching and activation rates of fluorophores are mainly a function of the laser power applied<sup>9</sup>. Total-internal reflection fluorescence (TIRF) microscopy can be used to lower the penetration depth to merely the basal cell membrane. In order to image cell's interior, on the other hand, epi- or highly inclined and laminated optical sheet (HILO)<sup>10</sup> illumination are required. Nevertheless, independent of the excitation method used high irradiation intensities generate reactive oxygen species (ROS) through excited-state reactions of endogenous and exogenous chromophores that have a high potential to damage cellular components<sup>11</sup>.

If the cell cannot handle, i.e., repair, accumulating phototoxic events during irradiation, it will ultimately die. Unfortunately, so far live-cell localization microscopy largely ignored possible phototoxic effects<sup>12</sup> or treated them only superficially likely due to the nonexistence of appropriate instrumentation for automated long term live-cell observation. Hitherto, in most studies it was investigated whether the cells are still adherent, changed their shape, or showed other apparent ill effects directly after super-resolution microscopy experiments<sup>13–15</sup>. Recently, it has been shown that yeast cells that appeared healthy directly after irradiation with a very low light-dose failed to divide when left overnight, whereas their non-imaged neighbors divided normally<sup>16</sup>. Even though the exact mechanism behind light-induced cell damage is still unclear and the irradiation sensitivity will undoubtedly vary among different cell types

Department of Biotechnology and Biophysics, Biocenter, University of Würzburg, Am Hubland, 97074 Würzburg, Germany. \*These authors contributed equally to this work. Correspondence and requests for materials should be addressed to M.S. (email: m.sauer@uni-wuerzburg.de)

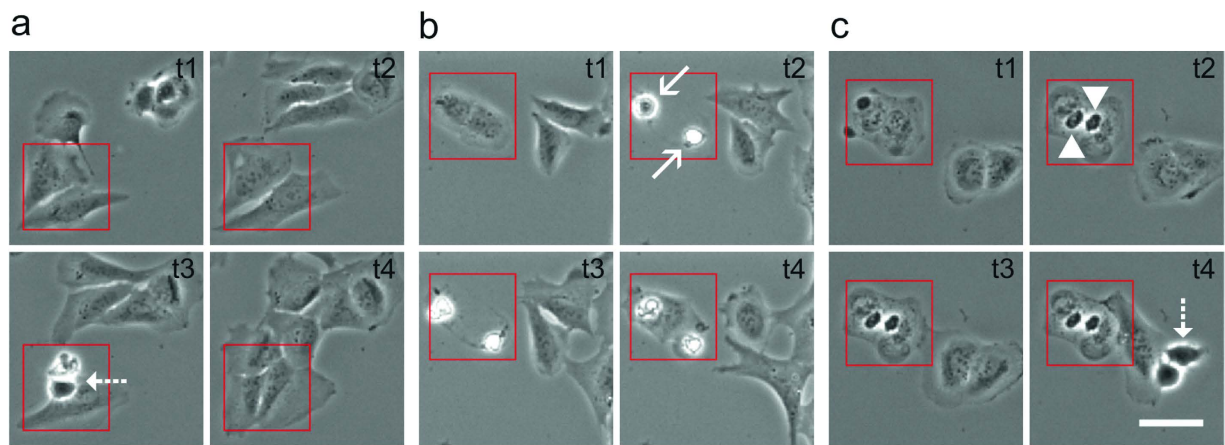


**Figure 1. Classification of photodamage effects using U2OS cells in three categories.** (a) Non-irradiated healthy cells (Supplementary Video 1), (b) apoptotic cells irradiated with an intensity of  $0.49 \text{ kW cm}^{-2}$  at 514 nm for 240 s (Supplementary Video 2), and (c) frozen cells irradiated with an intensity of  $1.5 \text{ kW cm}^{-2}$  at 514 nm for 240 s (Supplementary Video 3). Images were taken 1.15 h (t1), 6.15 h (t2), 10.30 h (t3), and 16.30 h (t4) after irradiation. The red rectangle in (b) and (c) shows the irradiated cells. Dashed arrows mark dividing cells, continuous arrows apoptotic cells, and arrowheads frozen cells. Scale bar,  $50 \mu\text{m}$ .

and irradiation wavelengths<sup>17–19</sup>, the reported results clearly demonstrate that the simple observation of the cell's appearance directly after irradiation cannot be used as a meaningful photodamage marker.

A variety of non-radioactive cell proliferation assays can be used to estimate the number of viable eukaryotic cells<sup>20,21</sup>. The MTT assay<sup>22</sup> is one of the most popular assays, which can be used to probe cellular metabolism. Here, the tetrazolium salt MTT (3-(4,5-dimethylthiazol-2-yl)-2,5-diphenyltetrazolium bromide) is reduced by cellular reducing equivalents, such as NADH and NADPH, to a blue formazan product<sup>23</sup>. The latter is used as indicator for cell viability and measurable via quantitative absorption spectroscopy, e.g., with a plate reading spectrophotometer<sup>21</sup>.

Here, we used an alternative approach to probe the cell viability after super-resolution microscopy experiments where typically single or only a few cells are irradiated with the required high intensities. We monitored cell survival of irradiated and non-irradiated cells for 20–24 hours and observed microtubule growth after wide-field illumination in epi- and HILO-mode with typical irradiation intensities ( $0–3 \text{ kW cm}^{-2}$ ) and wavelengths (405–640 nm) used in PhotoActivated Localization Microscopy (PALM)<sup>5,13</sup> and *direct* Stochastic Optical Reconstruction Microscopy (dSTORM)<sup>14,15,24</sup>. We investigated the influence of irradiation intensity, wavelength, light-dose, fluorescence labeling, temperature, and reducing agent (ascorbic acid) on the viability of various labeled and unlabeled cultured cell lines.

## Results

**Degree of photodamage.** We used U2OS, COS-7 and HeLa cells seeded in petri dishes with an imprinted  $500 \mu\text{m}$  relocation grid, irradiated them under localization microscopy conditions ( $0–3 \text{ kW cm}^{-2}$ ) and observed them afterwards for 20–24 hours under standard culture conditions using an automated cell observation system. As irradiation time we used 240 s, a typical acquisition time in localization microscopy, sufficient to record 12,000 frames with 20 ms integration time. We used high-power laser light sources to generate the required intensities over a large field of view ( $65.5 \times 65.5 \mu\text{m}$ ) in order to irradiate a few cells per experiment (Online Methods). The laser beams were confined with a rectangular field stop to ensure that only the cells present within the field of view are irradiated. Photodamage analysis was based simply on the fact whether the irradiated cells appear healthy and show cell division during the next 20–24 hour after irradiation or not. We classified the cells in three different photodamage categories. First, cells that appear healthy and show cell division after irradiation, termed 'healthy' (Fig. 1a and Supplementary Video 1), second, cells that show no or slowed cell division and detachment from the cover slip followed by cell death, termed 'apoptotic' (Fig. 1b and Supplementary Video 2), and third, cells that do not divide but appear completely immobile attached to the surface, termed 'frozen' (Fig. 1c and Supplementary Video 3). Frozen cells represent the most damaged type of cells through irradiation. For the sake of convenience we do not differentiate between apoptotic and frozen cells in the following. We simply count cells that survived irradiation and did further progress through the cell cycle like un-irradiated cells and cells that did not further divide and died.

**Effect of transfection, dye labeling, and cellular environment.** In each experiment we irradiated 20–50 cells and counted the number of 'dead' (apoptotic + frozen) cells (Table 1). First, we performed irradiation experiments with U2OS cells at different irradiation intensities ( $0–3 \text{ kW cm}^{-2}$ ) at 514 nm for 240 s (Fig. 2 and Supplementary Fig. 2). We compared wildtype U2OS cells (Fig. 2a), U2OS cells stably

	Conditions	$I_{50}$ (kW cm $^{-2}$ ) <sup>a</sup>		LD50 (kJ cm $^{-2}$ )		Number of cells	
		'dead'	'frozen'	'dead'	'frozen'	total	per data point <sup>b</sup>
U2OS	untreated	0.43 ± 0.01	1.06 ± 0.02	104.4	254.1	404	36.7 ± 19.2
	transfected	0.34 ± 0.02	1.31 ± 0.06	81.6	313.9	707	22.1 ± 17.7
	transfected+TMR	0.24 ± 0.01	1.38 ± 0.03	58.4	331.6	599	20.7 ± 10.8
	transfected+37°C	0.58 ± 0.05	1.06 ± 0.03	138.4	253.6	385	42.8 ± 14.1
	transfected+AA	0.54 ± 0.06	n.d.	129.6	n.d.	458	28.6 ± 21.7
COS-7	untreated	0.53 ± 0.01	0.88 ± 0.04	126.5	211.6	239	26.6 ± 3.5
HeLa	untreated	2.82 ± 0.62	n.d.	677.5	n.d.	256	32.0 ± 8.8

**Table 1. Effects of intracellular and environmental conditions on photo-sensitivity of cells.** If not otherwise stated, cells were irradiated at 21 °C.  $I_{50}$  value is the intensity where 50% of the irradiated cells died after imaging at 514 nm for 240 s. U2OS cells were transfected with CLIP-H2B and optionally imaged with TMR, at 37 °C, or supplemented with 100 μM ascorbic acid (AA). <sup>a</sup>Errors are standard errors from data fits. <sup>b</sup>Errors are given as one standard deviation. n.d., not determined.

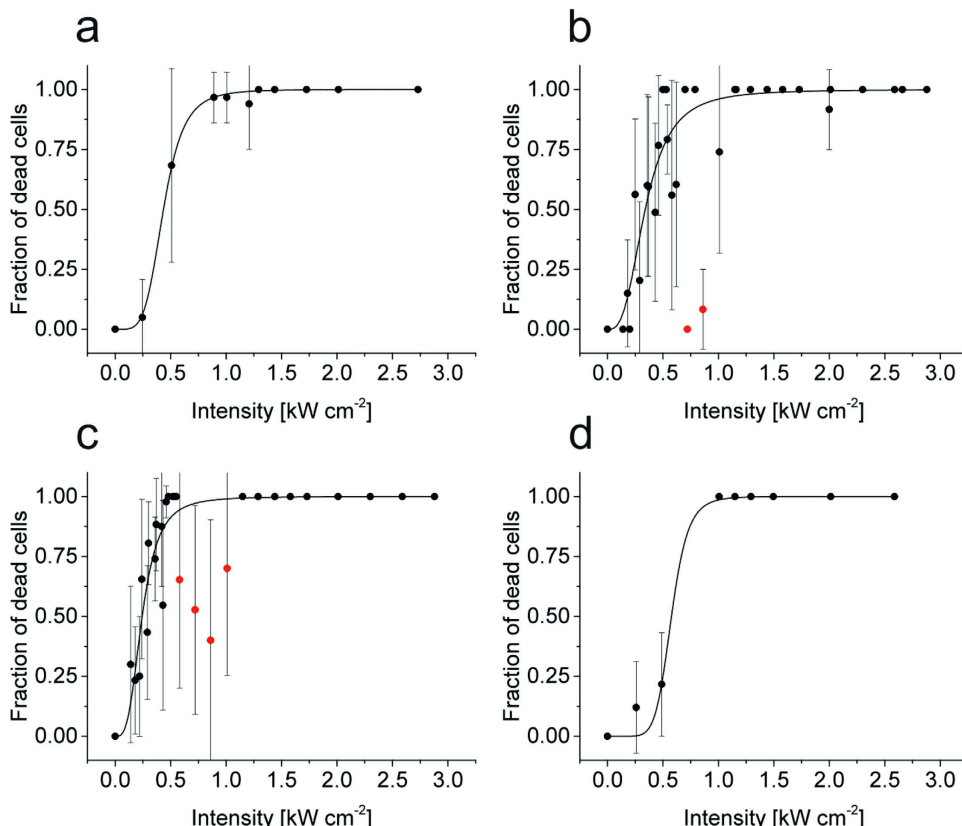


**Figure 2. Dependence of cell survival on irradiation intensity at 514 nm for 240 s of differently modified U2OS cells.** (a) Wildtype cells irradiated at 21 °C, (b) cells stably transfected with CLIP-H2B irradiated at 21 °C, (c) cells stably transfected with CLIP-H2B and labeled with TMR, irradiated at 21 °C and (d) cells stably transfected with CLIP-H2B irradiated at 37 °C. Red dots are masked data points and were not considered for fitting. Error bars are given as one standard deviation. For each data point 20–50 cells were irradiated (Table 1).

transfected with CLIP-H2B (Fig. 2b), and U2OS cells stably transfected with CLIP-H2B and labeled with tetramethylrhodamine (TMR) (Fig. 2c), all irradiated at 21 °C. An additional experiment with U2OS cells stably transfected with CLIP-H2B was conducted at 37 °C (Fig. 2d). From the titration curves (Fig. 2) we determined the intensity where 50% of all irradiated cells died within 20–24 h after an irradiation time of 240 s ( $I_{50}$ ) and calculated the corresponding lethal dose LD50 (Table 1). These results indicate that transfection of cells increases the photodamage sensitivity already in the absence of fluorophores.

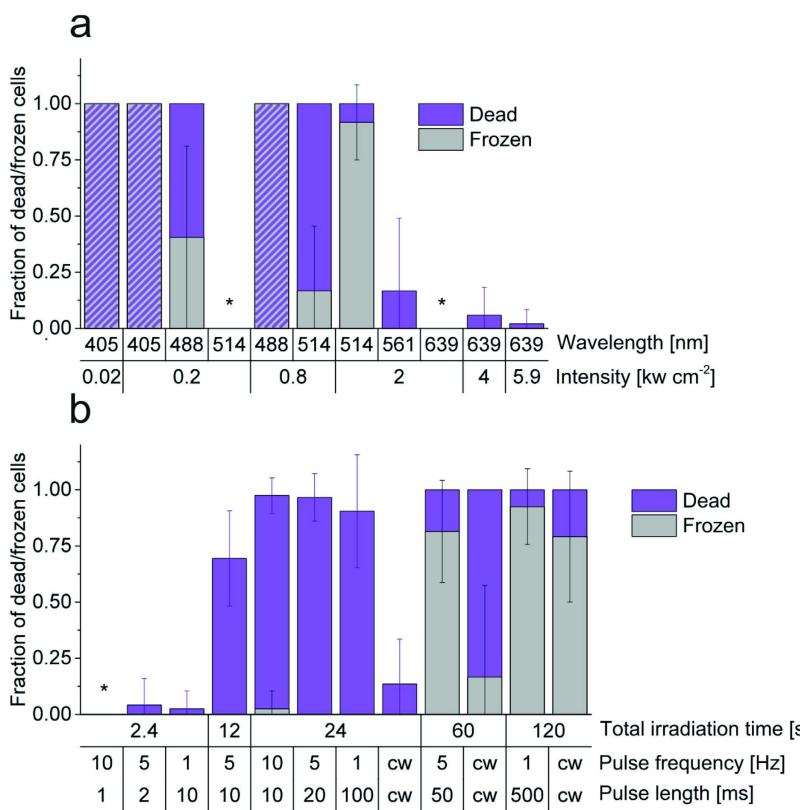


**Figure 3. Wavelength, intensity, and irradiation-mode dependent phototoxicity.** (a) Wavelength and intensity based phototoxicity upon cw irradiation for 240 s. (b) Cell death as a function of the irradiation light dose at 405 nm with an irradiation intensity of  $0.02 \text{ kW cm}^{-2}$  (pulsed vs. cw mode). Under pulsed irradiation conditions the total acquisition time was always 240 s. \*No dead cells were observed. Error bars are given as one standard deviation. For each data point 10–50 cells were irradiated (Supplementary Table 1 and 2).

Labeling with fluorophores further promotes phototoxic effects. (Fig. 2c and Table 1). Transfection and labeling with an organic fluorophore (here TMR) that absorbs at the irradiation wavelength exhibit comparable photodamage efficiency using U2OS cells. Both, transfection and labeling lower the  $I_{50}$  irradiation intensity by 20–25% (Table 1) stepwise from 0.43 (untreated) via 0.34 (transfected) to  $0.24 \text{ kW cm}^{-2}$  (transfected and labeled). This implies that genetically modified fluorescently labeled cells require lower irradiation intensities to survive live-cell fluorescence imaging experiments. Furthermore, our finding demonstrates that besides ROS generation by fluorophore triplet states and additional toxicity potentially induced through the attachment of fluorophores to cellular molecules other important phototoxic sources exist.

In addition, our experiments show that cells have mechanisms to repair phototoxic effects when irradiated under ideal conditions at  $37^\circ\text{C}$  and thus can stand higher irradiation intensities. Thereby,  $I_{50}$  increases by 35% to  $0.58 \text{ kW cm}^{-2}$ . (Fig. 2d and Table 1). Furthermore, the photo-resistance of cells can be further improved by the addition of  $100 \mu\text{M}$  ascorbic acid (AA) as a supplement to the imaging medium, thus increasing  $I_{50}$  by 26% to  $0.54 \text{ kW cm}^{-2}$  ( $21^\circ\text{C}$ ) (Table 1 and Supplementary Fig. 1). After irradiation, the AA buffer was replaced by standard medium and the cells were observed in the live-cell recorder for the next 20–24 h.

**Wavelength and illumination-mode dependent phototoxicity.** The energy of photons used to irradiate cells has a dramatic impact on phototoxicity (Fig. 3a and Supplementary Table 1). In particular, the photodamage efficiency increases with decreasing irradiation wavelength with the strongest phototoxic effect observed at 405 nm irradiation even at very low intensities, e.g., as typically used for photo-activation of fluorescent proteins in PALM experiments ( $0.02\text{--}0.05 \text{ kW cm}^{-2}$ )<sup>13</sup>. While at  $0.2 \text{ kW cm}^{-2}$  488 nm irradiation for 240 s cells do not survive, 100% of cells survive when the wavelength is redshifted to 514 nm although the cells experienced the same light dose of  $\sim 48 \text{ kJ cm}^{-2}$  (Fig. 3a and Supplementary Table 1). This small shift of 26 nm shows that cells exhibit a very distinct sensitivity related to the irradiation wavelength. But increasing the intensity at 514 nm to  $2 \text{ kW cm}^{-2}$  ( $\sim 480 \text{ kJ cm}^{-2}$ ) kills all cells, whereas 85% and 100% of all cells survive when irradiating with the same intensity and dose at 558 and

640 nm, respectively. Even when irradiating at 640 nm with intensities of 4–6 kW cm<sup>−2</sup> (960–1,410 kW cm<sup>−2</sup>) only weak effects on the cell survival rate are observed (<5% dead cells, Fig. 3a).

Next, we studied the effect of the irradiation dose at 405 nm. Irradiation with 0.02 kW cm<sup>−2</sup> was applied at different pulse frequencies (continuous wave (cw), 10, 5, and 1 Hz) and pulse lengths (cw, 500, 100, 50, 20, 10, 2, and 1 ms) resulting in total irradiation times of 2.4–120 s (Fig. 3b and Supplementary Table 2). For pulsed irradiation the total acquisition time has been kept constant at 240 s. Our data show that pulsed and cw irradiation at 405 nm with 0.02 kW cm<sup>−2</sup> corresponding to a total irradiation time of 60 seconds (1.2 kJ cm<sup>−2</sup>) is sufficient to kill virtually all irradiated U2OS cells (Fig. 3b). On the other hand, U2OS cells stand a 10<sup>3</sup>-times higher irradiation dose (1,410 kJ cm<sup>−2</sup>) at 640 nm undamaged (cw, 6 kW cm<sup>−2</sup> for 240 s, Fig. 3a).

Interestingly, the strength of phototoxic effects for cw irradiation is lower than for pulsed excitation applying the same total irradiation time of 24 s, i.e., the same light dose. After cw irradiation with 0.02 kW cm<sup>−2</sup> at 405 nm for 24 s (0.48 kJ cm<sup>−2</sup>) the survival fraction of cells is ~85%. In contrast, applying the same dose by pulsing the laser with 1 Hz pulse frequency and 100 ms pulse length, i.e., a recovery time of 900 ms between subsequent 100 ms irradiation pulses, decreases the survival fraction to ~10% (Fig. 3b). Increasing the pulse frequency and shortening the pulse length at constant total irradiation time of 24 s does not change the situation (Fig. 3b). This implies that U2OS cells rather withstand phototoxic stress through constant but short irradiation periods of 24 s (irradiation time/acquisition time: 24 s/24 s, 0.48 kJ cm<sup>−2</sup>) than repetitive irradiation pulses over a longer total acquisition time (24 s/240 s, 0.48 kJ cm<sup>−2</sup>) (Fig. 3b and Supplementary Table 2).

However, if cells are irradiated only for a total irradiation time of 2.4 s, short pulse lengths of 1 ms at a pulse frequency of 10 Hz allow total acquisition times of 240 s (corresponding to 48 J cm<sup>−2</sup>) and thus the observation of dynamic processes without any obvious phototoxic effect (Fig. 3b). Maintaining the light dose constant but increasing the pulse length only slightly, e.g., to 2 ms at 5 Hz pulse frequency, phototoxic effects are again detectable (Fig. 3b). These findings indicate that live-cell single-molecule localization microscopy experiments using 405 nm photoactivation can be performed for short total irradiation times using pulse frequencies of 10 Hz and pulse lengths of 1 ms or less at an irradiation intensity of 0.02 kW cm<sup>−2</sup>.

Irradiating cells for 60 or 120 s (1.2–2.4 kJ cm<sup>−2</sup>) leads to 100% dead cells, no matter whether cw or pulsed irradiation was applied. But pulsing increases the fraction of frozen cells, i.e., from 17% (60 s, cw) to 81% (60 s, 5 Hz) and 79% (120 s, cw) to 93% (120 s, 1 Hz). For the 24 s irradiation scenario, a small fraction of frozen cells (3%) was only observed when the pulse frequency was increased to 10 Hz (Fig. 3b and Supplementary Table 2). To summarize, our results demonstrate that the total irradiation time especially for 405 nm light has to be kept as short as possible in order to minimize phototoxic effects.

**Cell lines.** Since it is expected that the photodamage sensitivity will vary between different cell lines, we performed additional experiments with COS-7 and HeLa cells (Fig. 4, Table 1). The results show that COS-7 cells exhibit a photo-sensitivity comparable to U2OS cells, whereas HeLa cells are substantially more resistant (Fig. 4d). The  $I_{50}$  value is about 0.5 kW cm<sup>−2</sup> at 514 nm (120 kJ cm<sup>−2</sup>) for U2OS and COS-7 cells. The transition area between the lower and upper saturation levels—usually accompanied with huge variability in cell sensitivity (i.e., large standard deviations, compare Figs 2 and 4)—of U2OS and COS-7 are in the range of 0.25–0.75 kW cm<sup>−2</sup>. Here, the increased fluctuation in photo-sensitivity might be due to the fact that cells reside in different stages of the cell cycle. With the applied irradiation intensities at 514 nm, we were unable to achieve 100% dead HeLa cells (Fig. 4b). Even at the highest applied irradiation intensity of 2.5 kW cm<sup>−2</sup> half of the irradiated HeLa cells survived. This demonstrates that HeLa cells exhibit the highest resistance to phototoxicity among all tested cell lines. The transition point  $I_{50}$  was determined to 2.8 kW cm<sup>−2</sup> and is ~5–7 times higher than for COS-7 and U2OS.

**'Frozen' cells.** So far, we hardly differentiated between 'frozen' and apoptotic cells (Fig. 1b,c). While in apoptotic cells too many phototoxic effects lead the cell to initiate cell death, frozen cells appear to die instantaneously without any residual mobility as if they would have been fixed by light (Fig. 1c). In fact, upon irradiation at 405 nm with an intensity of 0.24 kW cm<sup>−2</sup> for 240 s (57.6 kJ cm<sup>−2</sup>) cells are not only fixed but additionally the membrane and cytoskeleton is destroyed (Fig. 5a).

Labeling of cells with Alexa Fluor 647 phalloidin followed by fluorescence imaging directly after irradiation without any additional fixation and permeabilization step demonstrates that only non-irradiated parts of the cell show typical actin filaments, irradiated parts show diffusive background fluorescence (Fig. 5a). Furthermore, the structure was super-resolved using *d*STORM (Fig. 5c). Here, it can be seen that at the edge of the illumination area actin filaments and bundles are sharply disrupted. Labeling of  $\beta$ -tubulin in suchlike irradiated cells shows similar results, i.e., the membrane and microtubule network is depolymerized upon irradiation of cells at 405 nm with 0.05 kW cm<sup>−2</sup> for 240 s at 37°C (Fig. 5b).

**Microtubule dynamics as light sensor.** To identify already first signs of light-induced cell damage beyond the crude dead or alive criterion, we performed additional experiments tracking microtubule dynamics after irradiation. To this end, we used HeLa cells stably expressing YFP-tagged end binding protein 1 (EB1). EB1 localizes to microtubule plus ends and modulates their dynamics and interactions with intracellular organelles<sup>25–27</sup>. Hence, by tracking the movement of EB1-N-YFP the microtubule

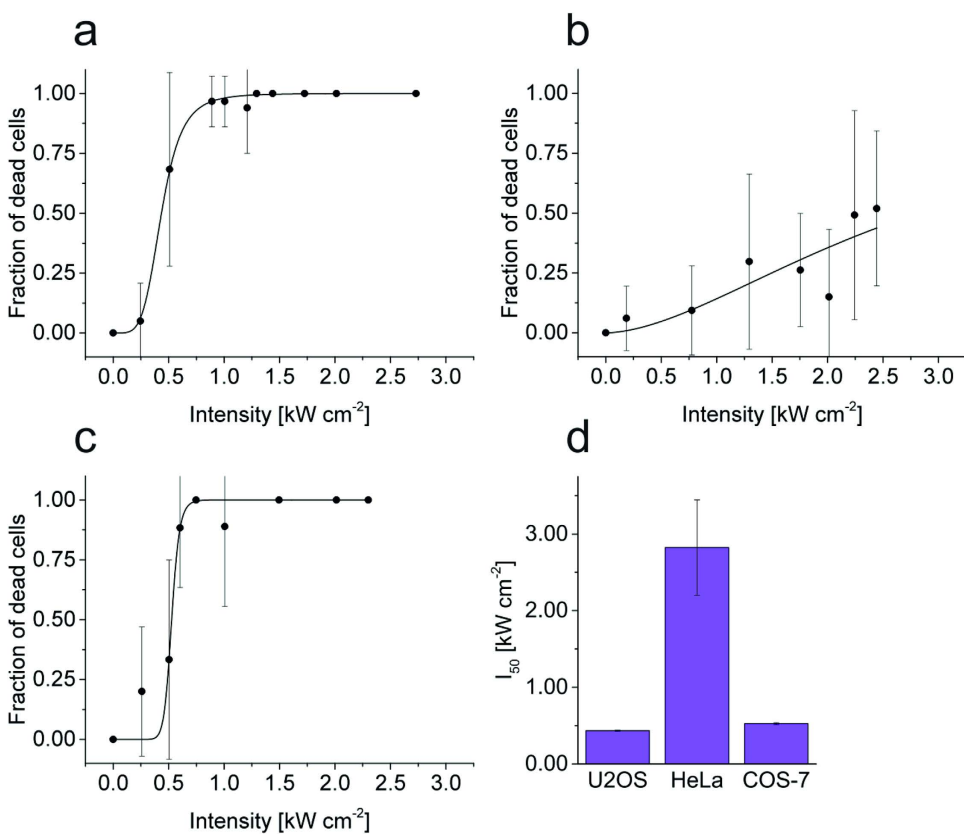


**Figure 4. Cell line dependent photodamage efficiency.** (a) U2OS, (b) HeLa, and (c) COS-7 cells were irradiated at 514 nm with varying intensity. (d) Corresponding  $I_{50}$  where 50% of the cells died (LD50). Error bars are given as one standard deviation. For each data point 20–50 cells were irradiated (Table 1).

growth can be monitored (Fig. 6a). Here it has to be considered that the HeLa cells have been stably transfected and microtubule growth represents a central element of cell viability. Therefore, the irradiation resistance of the HeLa cells may be strongly affected (Fig. 2b and Table 1).

The speed of microtubule growth was measured with weak 488 nm irradiation, with an overall irradiation intensity  $< 10 \text{ W cm}^{-2}$  for 10 s ( $< 100 \text{ J cm}^{-2}$ ), before and after additional irradiation at 558 nm or 640 nm (Fig. 6b and Supplementary Fig. 5). The low irradiation dose allowed us to balance efficient read out of the YFP signal and phototoxic effects. All cells merely irradiated under these conditions survived ( $n = 15$ ; Supplementary Table 3 and Supplementary Fig. 3). However, we observed a mean deceleration of microtubule growth from  $59 \text{ to } 53 \mu\text{m min}^{-1}$  upon irradiation solely at 488 nm i.e., a deceleration by 11%. Additional irradiation with  $0.03 \text{ kW cm}^{-2}$  at 640 nm for 225 s decelerates microtubule growth by 19% (Fig. 6b). Albeit strong phototoxic effects for irradiation at 640 nm are not expected (Fig. 3a), these results demonstrate that microtubule growth is sensitive to much weaker irradiation intensities. Upon further increase of irradiation intensity at 640 nm microtubule growth slows down by 40–50% of its initial speed (Fig. 6b). This value remains unaffected up to irradiation intensities of  $10 \text{ kW cm}^{-2}$  at 640 nm (Supplementary Table 3). For 558 nm irradiation microtubule growth speed decreases to a plateau with 70 to 76% of the initial speed applying irradiation intensities of up to  $\sim 2 \text{ kW cm}^{-2}$  (Fig. 6b). After irradiation with intensities of  $\sim 5 \text{ kW cm}^{-2}$  at 558 nm and higher, microtubule growth could not be measured anymore, because of the loss of microtubule primary structure and cell death, respectively (Supplementary Fig. 4).

## Discussion

In previous live-cell single-molecule localization microscopy studies the effect of irradiation and potential light-induced damage was judged after irradiation by the immediate appearance of the cells<sup>13–15</sup>. In this work, phototoxic effects were studied by observing cell viability after irradiation for a period of 20–24 h. Here, we discovered two different cell death mechanisms (Fig. 1). Apoptotic cells still showed motility directly after irradiation, but died some hours later, whereas frozen cells died instantaneously through irradiation. Therefore, it is hard to judge to which extent apoptotic cells were already damaged during imaging. However, it is certain that through imaging they were damaged to an extent that out-reached the cells' repair mechanisms, resulting in cell death later on.

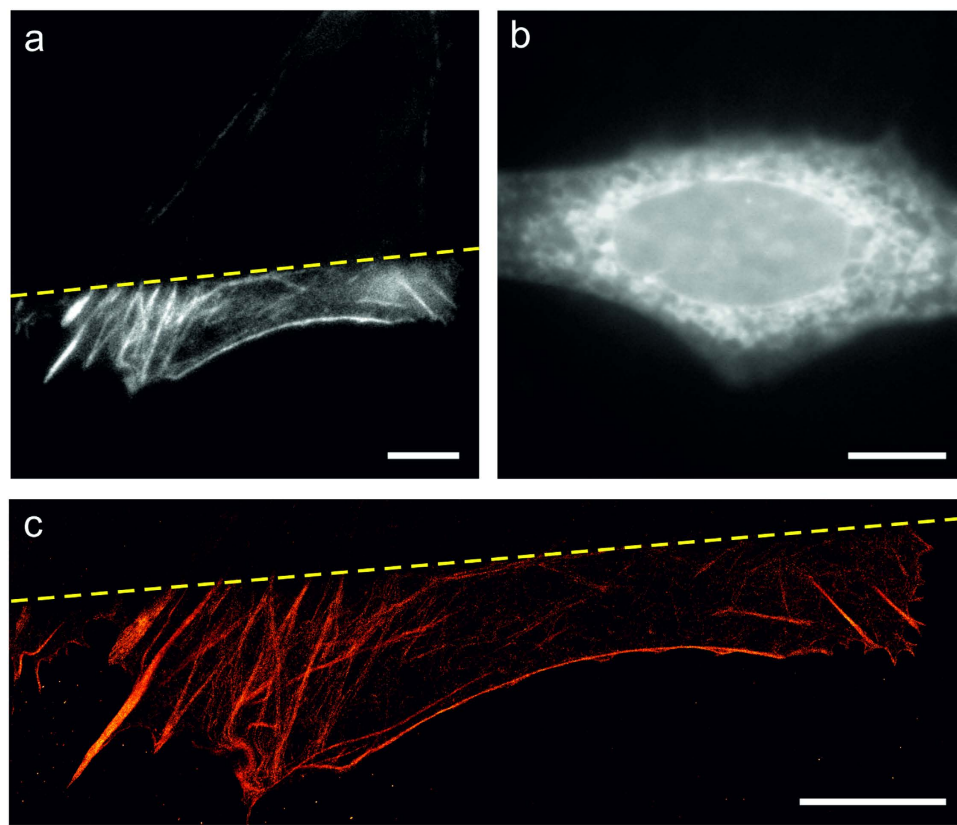


**Figure 5. Imaging the cytoskeleton of a frozen U2OS cell without additional chemical fixation and permeabilization.** (a) Epi-fluorescence image of f-actin. The upper part of a U2OS cell (yellow dashed line) was irradiated with  $0.24\text{ kW cm}^{-2}$  at 405 nm for 240 s at  $37^\circ\text{C}$  and stained with Alexa Fluor 647 phalloidin. Only the unirradiated lower part of the cell shows an intact actin network. F-actin in the upper part is completely destroyed. (b) Epi-fluorescence image of microtubules. The U2OS cell was irradiated with  $0.05\text{ kW cm}^{-2}$  at 405 nm for 240 s at  $37^\circ\text{C}$  and stained with SiR-Taxol<sup>46</sup>. (c) dSTORM image of the actin structure shown in a). Scale bars,  $10\mu\text{m}$ .

Our results demonstrate that stable transfection of cells reduces photoresistance (Fig. 2 and Table 1), at which the degree depends on the transfected protein and its importance for cell viability. Thus, it has to be considered that genetically modified fluorescently labeled cells might require lower irradiation intensities to survive live-cell fluorescence imaging experiments. As expected, irradiation experiments with labeled cells indicate that ROS generated through fluorophore triplet states and subsequent singlet oxygen generation damage cells and reduce their photoresistance (Fig. 2 and Table 1)<sup>28,29</sup>. However, the degree of photodamage remains reasonable at least for standard organic fluorophores with low triplet quantum yields as used in our experiments. Thus, other processes such as the absorption of light by endogenous cellular chromophores and subsequent excited state reactions accompanied by generation of toxic substances, have to be taken into account to explain the observed phototoxic effects.

Generally, cells exhibit a very distinct irradiation sensitivity, i.e., the phototoxicity increases dramatically with decreasing irradiation wavelength (Fig. 3a)<sup>30</sup>. This is most impressively illustrated comparing the photodamage efficiency through irradiation at 488 nm and 514 nm with an intensity of  $0.2\text{ kW cm}^{-2}$  (Fig. 3a). Here, a wavelength shift of only 26 nm suffices to dramatically change the survival rate. Fortunately, irradiation of fluorophores in the near infrared region at, e. g., 640 nm with an intensity  $<6\text{ kW cm}^{-2}$  without additional activation at 405 nm, can be considered innocuous<sup>14</sup>. However, after irradiation at 640 nm we observed a deceleration of microtubule growth speed (Fig. 6b) indicating that monitoring of microtubule growth speed is a very sensitive photodamage parameter.

Our data also clearly show that the fraction of apoptotic and frozen cells is particularly high at 405 nm irradiation even at a very low intensity of  $0.02\text{ kW cm}^{-2}$  (Fig. 3a), the wavelength at which most photoactivatable fluorescent proteins have to be activated over time periods of several tens of minutes in PALM experiments<sup>13,31</sup>. Furthermore, we discovered that especially shorter wavelength photons can fix cells, permeabilize the plasma membrane and depolymerize the cytoskeleton (Fig. 5). If one would succeed to fix and permeabilize cells without any further cellular destruction by application of a short UV-light pulse one would have an elegant method at hand to freeze a specific cellular state during live-cell fluorescence imaging under low irradiation conditions.

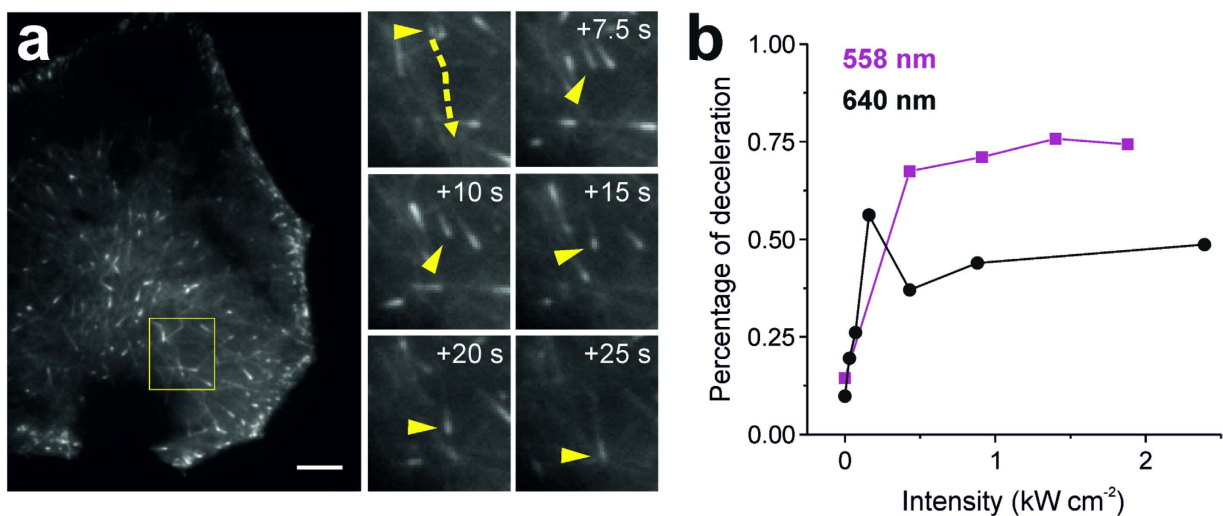


**Figure 6.** (a) Live-cell recording of EB1-N-YFP transfected HeLa cells. Movement of a single EB1-N-YFP molecule is shown. Dashed arrow in yellow indicates individual EB1 track, arrow heads depict the same EB1 molecule (Supplementary Fig. 5). (b) Deceleration of EB1 movement depends on the irradiation intensity at 558 nm (magenta) and 640 nm (black) (median). In absence of additional irradiation at 558 nm and 640 nm the microtubule growth speed decreases due to irradiation at the excitation wavelength of EB1-N-YFP at 488 nm with an intensity of  $<0.1\text{ kW cm}^{-2}$ . Solid lines were used to guide the eye. Cells were irradiated at  $37^\circ\text{C}$  for 225 s. The number of tracks analyzed per data point is given in Supplementary Table 3. Scale bar,  $5\text{ }\mu\text{m}$ .

One way to minimize phototoxic effects in PALM experiments is pulsed activation at 405 nm with short pulse lengths of 1 ms at 10 Hz pulse frequency applied for short total irradiation times of only a few seconds (Fig. 3b). In addition, TIRF microscopy can be used to confine irradiation to the cell's basal membrane<sup>13</sup>. Therefore, phototoxic effects are reduced when irradiation is performed in TIRF mode<sup>19</sup>.

Recently, the question how much light biological specimen can withstand was addressed by Ernst Stelzer who suggested the solar constant ( $\sim 100\text{ mW cm}^{-2}$ , central Europe) as a reference<sup>32</sup>. After 600 s sunlight, the energy density is about  $0.6\text{ }\mu\text{J }\mu\text{m}^{-2}$  ( $60\text{ J cm}^{-2}$ ). Albeit half of the sun's irradiation energy is in the infrared spectral range, the estimated value is in general accordance with our result of a maximum dose of  $48\text{ J cm}^{-2}$  at 405 nm irradiation (Fig. 3b, Supplementary Table 2) and the result reported by Wagner *et al.* of  $\sim 25\text{ J cm}^{-2}$  at 375 nm<sup>19</sup>.

However, our experiments using pulsed irradiation (Fig. 3b) reveal that the irradiation dose alone does not determine the degree of photodamage. For a total irradiation time of 24 s at 405 nm with an intensity of  $0.02\text{ kW cm}^{-2}$  our data unravel that substantially less U2OS cells survive pulsed irradiation than cw irradiation albeit they experienced the same light dose of  $480\text{ J cm}^{-2}$  (Fig. 3b). On the other hand, all cells survive pulsed irradiation at 405 nm with pulse lengths of 1 ms at 10 Hz applied for a short irradiation time of 2.4 s (Fig. 3b). This indicates that cells can cope with the concentration of phototoxic molecules generated during 2,400 1 ms irradiation periods. For longer irradiation periods and irradiation times more toxic molecules are generated surpassing the cells' repair capacity.

Whether our results can be applied to other fluorescence and super-resolution microscopy methods remains to be experimentally verified but can be carefully estimated. Confocal laser scanning microscopy operates typically at irradiation intensities of  $10\text{--}50\text{ kW cm}^{-2}$  yet focuses the energy on a very small spot and uses short irradiation times typically in the range of  $10\text{--}500\text{ }\mu\text{s}$  per pixel and frame<sup>33</sup>. Using these values and a pixel size of  $\sim 120\text{ nm}$  we estimate that cells experience a light dose of less than  $500\text{ J cm}^{-2}$  per image. That is, according to our studies, cells should survive confocal laser scanning microscopy at irradiation wavelengths of  $\geq 488\text{ nm}$  as long as the total light dose experienced does not exceed a few  $\text{kJ cm}^{-2}$  (Fig. 3a and Supplementary Tables 1 and 2). On the other hand, it is very likely that live-cell laser scanning microscopy at irradiation wavelengths  $< 488\text{ nm}$  causes severe photodamage.

Stimulated emission depletion (STED) microscopy uses an additional depletion laser with an irradiation wavelength usually in the red to near-infrared spectral region (typically at 647 or 800 nm), i.e., in a wavelength range where cells survive irradiation intensities of  $\text{kW cm}^{-2}$  applied for a few minutes (Fig. 3a). However, the irradiation intensity of the depletion laser is typically three to five orders of magnitude higher than the excitation laser because the resolution of STED microscopy scales with the depletion laser intensity<sup>34,35</sup>. Thus, the total light dose impinging on the cells might easily approach  $10^4\text{--}10^6\text{ kJ cm}^{-2}$  and potentially induce photodamage effects even by irradiation with wavelengths  $> 600\text{ nm}$  (Fig. 3a and Supplementary Table 1).

Parameter	Recommendation	Example
Wavelength	High	640 nm
Intensity	Low	$< 6 \text{ kW cm}^{-2}$ (640 nm)
Activation	No	ATTO 655 <sup>*</sup>
Cell type	Photo-insensitive	HeLa
Illumination type	Reduced penetration depth	TIRF
Temperature	Physiological	37 °C
Switching buffer	No	cell culture medium
Protecting agents	Depending	AA

**Table 2. Recommendations for live-cell single-molecule localization microscopy experiments.** AA, ascorbic acid. <sup>\*</sup>Ref. 14.

RESOLFT nanoscopy uses photoswitchable fluorescent proteins such as rsEGFP<sup>36</sup> and Dreiklang<sup>37</sup> as photoswitches. Hence, the applied laser power for activation, readout and photoswitching are reduced to  $0.1\text{--}10 \text{ kW cm}^{-2}$ , but lasers in the (ultra)blue and blue spectral range are required, e.g., Dreiklang at wavelengths of 355 nm for activation ( $0.3 \text{ kW cm}^{-2}$ , 1 ms), 405 nm for photoswitching ( $10 \text{ kW cm}^{-2}$ , 17 ms), and 491 nm for readout ( $0.8 \text{ kW cm}^{-2}$ , 2 ms) (Fig. 3a)<sup>38</sup>. Thus, the corresponding light doses exceed the  $48 \text{ J cm}^{-2}$  level determined in our study for 405 nm irradiation and induce photodamage (Fig. 3b, Supplementary Table 2). A way out of this problem offer new improved photoswitchable fluorescent proteins such as rsEGFP2, which require a light dose of only  $2\text{--}10 \text{ J cm}^{-2}$  for photoswitching at 405 nm<sup>39</sup>, and thus enable photodamage-free super-resolution imaging over longer time periods.

To minimize photodamage problems induced by high peak irradiation intensities in confocal live-cell fluorescence microscopy schemes, light-sheet microscopy is usually applied enabling fascinating studies about the development of living organism also over longer time periods at cellular level<sup>1,3</sup>. To achieve subcellular resolution, lattice light-sheet microscopy in combination with structured illumination has been developed<sup>4</sup>. The method uses ultrathin light sheets which are scanned plane-by-plane through the specimen to generate a 3D image. The laser power of  $1\text{--}100 \mu\text{W}^4$  used for excitation of living cells and organisms is similar to confocal microscopy but distributed over substantially larger areas in the focal plane. Therefore, the light dose impinging on the cells is substantially lower than in confocal microscopy approaches and accordingly light-induced cell damage significantly reduced.

Generally, it is assumed that the resolution of wide-field super-resolution microscopy methods comes along with the irradiation intensity. For example, single-molecule localization microscopy achieves typically a lateral resolution of  $\sim 20 \text{ nm}^{5\text{--}8}$  but requires naturally also higher irradiation intensities ( $1\text{--}5 \text{ kW cm}^{-2}$ ) than methods which achieve a lower spatial resolution, e.g., structured illumination microscopy (SIM)<sup>40</sup>. However, our data clearly demonstrate that living cells can tolerate such high irradiation intensities if excitation is performed at 640 nm or longer wavelengths (Fig. 3a).

As we have seen that HeLa cells withstand much higher irradiation intensities than U2OS cells (Fig. 4) it remains to be tested whether all findings can be directly transferred to other cell lines or living organisms. In addition, cell cycle dependent mechanisms have to be considered. Even within the same population individual cells might respond differently to excessive irradiation<sup>41</sup>. This also might explain fluctuations in the photodamage data found in our study (Fig. 2 and Fig. 4).

Nevertheless, our results give important advice how to perform live-cell super-resolution microscopy experiments (Table 2). The use of switching buffers that include enzymatic oxygen scavenging systems and thiol containing reducing agents will add additional stress to cells in live cell single-molecule localization microscopy experiments (Fig. 6) and should therefore be avoided. Since living cells contain the thiol glutathione at millimolar concentration levels as native reducing agent live-cell dSTORM in standard media is possible with selected organic fluorophores without addition of external thiols<sup>11,14,24,42-44</sup>. Strategies to maintain cell health can be either achieved by reducing the illumination depth through TIRF or single-plane illumination<sup>1</sup>, or increasing the photodamage resistance, e.g., by imaging at 37 °C and the addition of  $\mu\text{M}$  concentrations of ascorbic acid (Table 2). At the same time, ascorbic acid could also serve as photoswitching reagent<sup>45</sup>. On the other hand, phototoxic effects at high irradiation intensities can be substantially reduced when exciting fluorophores at  $> 600 \text{ nm}$ , motivating the development of new (near infra-) red absorbing photoswitchable FPs and live-cell compatible organic dyes<sup>46-48</sup>. Independent of the method and the wavelength used, live-cell super-resolution microscopy experiments require stringent tests to verify that the cellular processes observed are not influenced by the high irradiation intensities.

## Online Materials and Methods

**Cell culture.** All cell lines were cultured at 37 °C and 5% CO<sub>2</sub>. U2OS cells (human osteosarcoma cell line) and COS-7 cells (monkey kidney fibroblast cell line) were grown in DMEM F12 with L-glutamine (Sigma, cat. D8062) supplemented with 10% FBS (Sigma, cat. F7524) and 1% penicillin-streptomycin (Sigma, cat. P4333). HeLa cells (human cervical adenocarcinoma cell line) were cultured in RPMI-1640

medium with L-glutamine (Sigma, cat. R8758) supplemented with 1% MEM Non-essential Amino Acid Solution (Sigma, cat. M7145), 1 mM sodium pyruvate (Sigma, cat. S8636), 10% FBS (Sigma, cat. F7524) and 1% penicillin-streptomycin (Sigma, cat. P4333). All cell lines have been passaged more than 25 times before experiments. Live-cell imaging and irradiation were performed in medium without phenol red: DMEM F12 with 15 mM HEPES (Sigma, cat. D6434) and RPMI-1640 medium (Sigma, cat. R7509). The U2OS CLIP-H2B cell line stably expressing CLIP-H2B was transfected using the transfection reagent FuGENE® HD (Promega, cat. E2311) and selected by 0.3 mg/ml G418 (Sigma, cat. G8168). Cells were stained with 0.2  $\mu$ M CLIP-Cell™ TMR-Star (New England Biolabs, cat. S9219S) for 30 minutes at 37 °C. Afterwards cells were washed three times with medium. Ascorbic acid (100  $\mu$ M) was added one hour before the experiments. After irradiation, the AA buffer was replaced by standard medium.

**dSTORM.** Irradiation and imaging were performed on a widefield setup<sup>42</sup>. As laser light sources we used 405 and 488 nm diode lasers (iBeam smart Family, TOPTICA Photonics) with 120 mW and 200 mW total output power, respectively, as well as three optically pumped semiconductor lasers (OPSL, Genesis MX STM-Series, Coherent), i.e., 514 nm, 558 nm and 640 nm with 500, 500, and 1000 mW total output power, respectively. Laser beams were cleaned-up by bandpass filters (Semrock/Chroma) and combined by appropriate dichroic mirrors (LaserMUX, Semrock). Afterwards, they were focused onto the back focal plane of a high numerical oil-immersion objective (Olympus APON 60XO TIRF, NA 1.49), which is part of an inverted fluorescence microscope (Olympus IX71). To separate the excitation light from the fluorescence light, suitable dichroic beam splitters (Semrock) were placed into the light path before the laser beams enter the objective. Fluorescence light collected by the objective was filtered by appropriate detection filters (Semrock/Chroma) and imaged with additional optical magnification by an EMCCD camera with  $512 \times 512$  pixels (iXon Ultra 897, Andor Technology). The achieved pixel size was 128 nm/px.

**Irradiation and determination of photodamage.** For irradiation experiments cells were seeded in petri dishes with an imprinted 500  $\mu$ m relocation grid (ibidi, cat. 81168) one or two days before the experiment. Cells were irradiated with the desired wavelength at 21 °C unless otherwise stated, a defined laser intensity and for a particular time (240 s unless stated otherwise) in EPI or in HILO mode. The experiments duration was kept constant at 2.5 hours. Using a rectangular field stop (OWIS) irradiation was restricted to cells present in the defined field of view of  $65.5 \mu$ m  $\times$   $65.5 \mu$ m. To achieve virtually homogeneous irradiation over the entire field of view the laser beams were largely expanded. The irradiation intensity varied between 6 and 12% from the center to the edge of the field of view (Supplementary Fig. 7). The laser power was measured above the objective using a laser power meter (LabMax-TO, Coherent). The illuminated intensity in HILO mode was ascertained as described by Tokunaga *et al.*<sup>10</sup>. According to errors in the adjustment of the field stop, the determination of the incidence angle and the measurement of the laser power we assume an uncertainty in intensity assignment of about 5–6%. For experiments at 37 °C a custom build incubation chamber was used, which was put on the x-y stage of the microscope.

After illumination of several cells, the medium was changed against fresh medium and irradiated cells were observed in a live cell recorder (BioStation IM, Nikon) for the following 20–24 hours (0.2 images  $\text{min}^{-1}$ ). The recorded images were assembled to an image stack for cell damage analysis.

**Microtubule and actin staining.** Cells of the stable U2OS CLIP-H2B cell line were seeded in petri dishes with an imprinted 500  $\mu$ m relocation grid (ibidi, cat. 81168) one or two days before the experiment. They were irradiated at 405 nm for 240 s at 37 °C with an intensity of 0.05 kW/cm<sup>2</sup> for microtubule staining and 0.24 kW cm<sup>-2</sup> for actin staining. Microtubules were stained with 1  $\mu$ M SiR-taxol<sup>44</sup> in medium for 30 minutes at 37 °C. Actin was stained with 33 nM Alexa Fluor 647 phalloidin (Molecular Probes, cat. A22287) in PBS for 30 minutes at room temperature. Cells were washed with PBS and imaged at 640 nm using a 679/41 single-band bandpass filter (Semrock). For dSTORM imaging phosphate buffered saline (pH 7.4) containing the following components was used as switching buffer: 100 mM  $\beta$ -mercaptoethylamine (AppliChem, cat. A1546), 4% glucose (w/v) (Merck, cat. 108337), 10 U ml<sup>-1</sup> glucose oxidase (Sigma, cat. G2133), 200 U ml<sup>-1</sup> catalase (Sigma, cat. C100)<sup>49</sup>.

**Microtubule tracking.** The stable cell line HeLa EB1-N-YFP was given to us by the Medical University of Innsbruck (Molecular Pathophysiology, Prof. Dr. Stefan Geley). All measurements were conducted at the setup described above at 37 °C. MT-growth was recorded for 50 s by exciting EB1-N-YFP with 488 nm at minimal intensities ( $< 10 \text{ W cm}^{-2}$ ) within the HILO mode before and after irradiation of the cell. In these measurements, the 488 nm laser and the EMCCD camera were synchronized by a pulse generator (DG645, Stanford Research Systems, Gilching, Germany), i.e., 2 Hz pulse frequency and 100 ms integration time to minimize irradiation effects. Cells were irradiated for 225 s with 558 nm and 640 nm laser excitation in the Epi mode with different intensities, respectively (0–4.48 kW cm<sup>-2</sup> and 0–10.09 kW cm<sup>-2</sup>). Tracking of the EB1-spots and computation of the microtubule growth speed were performed using the software Imaris (Bitplane, Zurich, Switzerland). The median of the MT-growth speed before and after irradiation were subtracted and the percentage of deceleration calculated.

## References

- Huisken, J., Swoger, J., Del Bene, F., Wittbrodt, J. & Stelzer, E. H. Optical sectioning deep inside live embryos by selective plane illumination microscopy. *Science* **305**, 1007–1009 (2004).
- Gao, L. *et al.* Noninvasive imaging beyond the diffraction limit of 3D dynamics in thickly fluorescent specimens. *Cell* **151**, 1370–1385 (2012).
- Keller, P. J. *et al.* Fast, high-contrast imaging of animal development with scanned light sheet-based structured-illumination microscopy. *Nat. Methods* **7**, 637–642 (2010).
- Chen, B. C. *et al.* Lattice light-sheet microscopy: imaging molecules to embryos at high spatiotemporal resolution. *Science* **346**, 1257998 (2014).
- Betzig, E. *et al.* Imaging intracellular fluorescent proteins at nanometer resolution. *Science* **313**, 1642–1645 (2006).
- Hess, S. T., Girirajan, T. P. & Mason, M. D. Ultra-high resolution imaging by fluorescence photoactivation localization microscopy. *Biophys. J.* **91**, 4258–4272 (2006).
- Rust, M. J., Bates, M. & Zhuang, X. W. Sub-diffraction-limit imaging by stochastic optical reconstruction microscopy (STORM). *Nat. Methods* **3**, 793–795 (2006).
- Heilemann, M. *et al.* Subdiffraction-resolution fluorescence imaging with conventional fluorescent probes. *Angew. Chem. Int. Ed. Engl.* **47**, 6172–6176 (2008).
- van de Linde, S. & Sauer, M. How to switch a fluorophore: from undesired blinking to controlled photoswitching. *Chem. Soc. Rev.* **43**, 1076–1087 (2014).
- Tokunaga, M., Imamoto, N. & Sakata-Sogawa, K. Highly inclined thin illumination enables clear single-molecule imaging in cells. *Nat. Methods* **5**, 159–161 (2008).
- van de Linde, S., Heilemann, M. & Sauer, M. Live-cell super-resolution imaging with synthetic fluorophores. *Annu. Rev. Phys. Chem.* **63**, 519–540 (2012).
- Editorial: Artifacts of light. *Nat. Methods* **10**, 1135 (2013).
- Shroff, H., Galbraith, C. G., Galbraith, J. A. & Betzig, E. Live-cell photoactivated localization microscopy of nanoscale adhesion dynamics. *Nat. Methods* **5**, 417–423 (2008).
- Wombacher, R. *et al.* Live-cell super-resolution imaging with trimethoprim conjugates. *Nat. Methods* **7**, 717–719 (2010).
- Jones, S. A., Shim, S. H., He, J. & Zhuang, X. Fast, three-dimensional super-resolution imaging of live cells. *Nat. Methods* **8**, 499–505 (2011).
- Carlton, P. M. *et al.* Fast live simultaneous multiwavelength four-dimensional optical microscopy. *Proc. Natl. Acad. Sci. USA* **107**, 16016–16022 (2010).
- Khodjakov, A. & Rieder, C. L. Imaging the division process in living tissue culture cells. *Methods* **38**, 2–16 (2006).
- Manders, E. M. M., Kimura, H. & Cook, P. R. Direct imaging of DNA in living cells reveals the dynamics of chromosome formation. *J. Cell Biol.* **144**, 813–821 (1999).
- Wagner, M. *et al.* Light Dose is a Limiting Factor to Maintain Cell Viability in Fluorescence Microscopy and Single Molecule Detection. *Int. J. Mol. Sci.* **11**, 956–966 (2010).
- Berridge, M. V., Herst, P. M. & Tan, A. S. Tetrazolium dyes as tools in cell biology: new insights into their cellular reduction. *Biotechnol. Annu. Rev.* **11**, 127–152 (2005).
- Riss, T. L. *et al.* In Assay Guidance Manual. (eds. G. S. Sittampalam *et al.*) (Bethesda (MD); 2004).
- Mosmann, T. Rapid colorimetric assay for cellular growth and survival: application to proliferation and cytotoxicity assays. *J. Immunol. Methods* **65**, 55–63 (1983).
- Berridge, M. V. & Tan, A. S. Characterization of the cellular reduction of 3-(4,5-dimethylthiazol-2-yl)-2,5-diphenyltetrazolium bromide (MTT): subcellular localization, substrate dependence, and involvement of mitochondrial electron transport in MTT reduction. *Arch. Biochem. Biophys.* **303**, 474–482 (1993).
- Klein, T. *et al.* Live-cell dSTORM with SNAP-tag fusion proteins. *Nat. Methods* **8**, 7–9 (2011).
- Schuyler, S. C. & Pellman, D. Microtubule “plus-end-tracking proteins”: The end is just the beginning. *Cell* **105**, 421–424 (2001).
- Vitre, B. *et al.* EB1 regulates microtubule dynamics and tubulin sheet closure *in vitro*. *Nat. Cell Biol.* **10**, 415–421 (2008).
- Akhmanova, A. & Steinmetz, M. O. Microtubule plus TIPs at a glance. *J. Cell Sci.* **123**, 3415–3419 (2010).
- Ochsner, M. Photophysical and photobiological processes in the photodynamic therapy of tumours. *J. Photochem. Photobiol. B* **39**, 1–18 (1997).
- Castano, A. P., Mroz, P. & Hamblin, M. R. Photodynamic therapy and anti-tumour immunity. *Nat. Rev. Cancer* **6**, 535–545 (2006).
- Coohill, T. P., Peak, M. J. & Peak, J. G. The effects of the ultraviolet wavelengths of radiation present in sunlight on human cells *in vitro*. *Photochem. Photobiol.* **46**, 1043–1050 (1987).
- Izeddin, I. *et al.* Super-Resolution Dynamic Imaging of Dendritic Spines Using a Low-Affinity Photoconvertible Actin Probe. *PLoS ONE* **6** e15611 (2011).
- Stelzer, E. H. K. Light-sheet fluorescence microscopy for quantitative biology. *Nat. Methods* **12**, 23–26 (2014).
- Pawley, J. B. *Handbook of Biological Confocal Microscopy*. (Springer, Heidelberg; 2006).
- Hein, B., Willig, K. I. & Hell, S. W. Stimulated emission depletion (STED) nanoscopy of a fluorescent protein-labeled organelle inside a living cell. *Proc. Natl. Acad. Sci. USA* **105**, 14271–14276 (2008).
- Hein, B. *et al.* Stimulated emission depletion nanoscopy of living cells using SNAP-tag fusion proteins. *Biophys. J.* **98**, 158–163 (2010).
- Grotjohann, T. *et al.* Diffraction-unlimited all-optical imaging and writing with a photochromic GFP. *Nature* **478**, 204–208 (2011).
- Brakemann, T. *et al.* A reversibly photoswitchable GFP-like protein with fluorescence excitation decoupled from switching. *Nat. Biotechnol.* **29**, 942–947 (2011).
- Jensen, N. A. *et al.* Coordinate-targeted and coordinate-stochastic super-resolution microscopy with the reversibly switchable fluorescent protein Dreiklang. *ChemPhysChem* **15**, 756–762 (2014).
- Grotjohann, T. *et al.* rsEGFP2 enables fast RESOLFT nanoscopy of living cells. *eLife* **1**, e00248 (2012).
- Shao, L., Kner, P., Rego, E. H. & Gustafsson, M. G. L. Super-resolution 3D microscopy of live whole cells using structured illumination. *Nat. Methods* **8**, 1044–+ (2011).
- Magidson, V. & Khodjakov, A. Circumventing photodamage in live-cell microscopy. *Methods Cell Biol.* **114**, 545–560 (2013).
- van de Linde, S. *et al.* Direct stochastic optical reconstruction microscopy with standard fluorescent probes. *Nat. Protoc.* **6**, 991–1009 (2011).
- Shim, S. H. *et al.* Super-resolution fluorescence imaging of organelles in live cells with photoswitchable membrane probes. *Proc. Natl. Acad. Sci. USA* **109**, 13978–13983 (2012).
- Carlini, L. & Manley, S. Live intracellular super-resolution imaging using site-specific stains. *ACS Chem. Biol.* **8**, 2643–2648 (2013).
- Vogelsang, J., Cordes, T., Forthmann, C., Steinhauer, C. & Tinnefeld, P. Controlling the fluorescence of ordinary oxazine dyes for single-molecule switching and superresolution microscopy. *Proc. Natl. Acad. Sci. USA* **106**, 8107–8112 (2009).

46. Lukinavicius, G. *et al.* Fluorogenic probes for live-cell imaging of the cytoskeleton. *Nat. Methods* **11**, 731–U168 (2014).
47. Grimm, J. B. *et al.* A general method to improve fluorophores for live-cell and single-molecule microscopy. *Nat. Methods* **12**, 244–250 (2015).
48. Uno, S. N. *et al.* A spontaneously blinking fluorophore based on intramolecular spirocyclization for live-cell super-resolution imaging. *Nat. Chem.* **6**, 681–689 (2014).
49. Schafer, P., van de Linde, S., Lehmann, J., Sauer, M. & Doose, S. Methylene blue- and thiol-based oxygen depletion for super-resolution imaging. *Anal. Chem.* **85**, 3393–3400 (2013).

### Acknowledgments

This work was supported by the Deutsche Forschungsgemeinschaft (DFG, grant SA 829/8) and the Bundesministerium für Bildung und Forschung (BMBF grant 13N12781). We are grateful to Stefan Geleys (Division of Molecular Pathophysiology, Innsbruck Medical University, Austria) for the HeLa EB1-N-YFP cell line and Kai Johnsson (Institute of Chemical Sciences and Engineering, École Polytechnique Fédérale de Lausanne, Switzerland) for providing us with SiR Taxol.

### Author Contributions

T.K., S.vdL. and M.S. designed research; S.W. and J.L. performed experiments; S.W., T.K., J.L. and S.vdL. analysed the data; S.vdL. and M.S. wrote the manuscript with contributions from all authors.

### Additional Information

**Supplementary information** accompanies this paper at <http://www.nature.com/srep>

**Competing financial interests:** The authors declare no competing financial interests.

**How to cite this article:** Wäldchen, S. *et al.* Light-induced cell damage in live-cell super-resolution microscopy. *Sci. Rep.* **5**, 15348; doi: 10.1038/srep15348 (2015).



This work is licensed under a Creative Commons Attribution 4.0 International License. The images or other third party material in this article are included in the article's Creative Commons license, unless indicated otherwise in the credit line; if the material is not included under the Creative Commons license, users will need to obtain permission from the license holder to reproduce the material. To view a copy of this license, visit <http://creativecommons.org/licenses/by/4.0/>